

# Optical Signal Processing with Reduced Power Consumption

by

Prashant P. Baveja

Submitted in Partial Fulfillment

of the

Requirements for the Degree

Doctor of Philosophy

Supervised by

Prof. Govind P. Agrawal

The Institute of Optics  
Arts, Sciences and Engineering

Edmund A. Hajim School of Engineering and Applied Sciences

University of Rochester  
Rochester, New York

2012

*To Ruchita, Pankaj, Sushma, and Tarun.*

**There is no Gene for Human Spirit.**

—A single thought which guides me.

# Curriculum Vitae

Prashant P. Baveja was born in Faridabad, Haryana, India, in 1984. He began his undergraduate studies in 2002 at the Electronics and Communications Engineering department at Delhi College of Engineering (DCE), University of Delhi, India and received his Bachelors in 2006. His undergraduate major was on fiber optics and optical communication systems. Between 2004-2006, he was an undergraduate researcher at the TIFAC CORE (Technology Information Forecasting and Assessment Council: Center of research and Excellence) labs at the Department of Applied Physics at DCE. He then started his graduate studies in fall 2006 at The Institute of Optics at University of Rochester and obtained his Masters of Science in Optics in 2009. He has carried out his doctoral research under the supervision of Professor Govind P. Agrawal since the summer of 2007. Since fall 2009, he has been a visiting researcher at Photonic Systems Laboratory at Rochester Institute of Technology where as part of a small team, he implemented a brand new laboratory specializing in nonlinear fiber optics and photonics. He was briefly (fall 2010-spring 2011) a Swedish Institute Guest Scholar at the Photonics Laboratory at the Department of Microtechnology and Nanoscience (MC2), Chalmers University of Technology, Göteborg, Sweden. His research interests include nonlinear optics in semiconductor optical amplifiers, thermal effects in vertical cavity surface emitting lasers, all-optical signal processing, nonlinear fiber optics, optical communication and raman amplification.

# Publications

## *Journal Articles*

- (1) **P. P. Baveja**, D. N. Maywar, and G. P. Agrawal, “Interband four-wave mixing in semiconductor optical amplifiers with ASE-enhanced gain recovery,” *IEEE J. Sel. Topics Quantum Electron.* **18**, 899–908 (2012).
- (2) **P. P. Baveja**, B. Kögel, P. Westbergh, J. S. Gustavsson, Å. Haglund, D. N. Maywar, G. P. Agrawal, and A. Larsson, “Impact of device parameters on thermal performance of high-speed, oxide-confined, 850 nm VCSELs,” *IEEE J. Quantum Electron* **48**, 17–26 (2012).
- (3) **P. P. Baveja**, B. Kögel, P. Westbergh, J. S. Gustavsson, Å. Haglund, D. N. Maywar, G. P. Agrawal, and A. Larsson, “Assessment of VCSEL thermal rollover mechanisms from measurements and empirical modeling,” *Opt. Express* **19**, 15490–15505 (2011).
- (4) **P. P. Baveja**, D. N. Maywar, A. M. Kaplan, and G. P. Agrawal “Self-phase modulation in semiconductor optical amplifiers: Impact of amplified spontaneous emission,” *IEEE J. Quantum Electron.* **46**, 1396–1403 (2010).
- (5) **P. P. Baveja**, D. N. Maywar, A. M. Kaplan, and G. P. Agrawal, “Spectral broadening in ultrafast semiconductor optical amplifiers induced by gain dynamics and self-phase modulation,” *Opt. Lett.* **35**, 294–296 (2010).
- (6) **P. P. Baveja**, D. N. Maywar, and G. P. Agrawal, “Optimization of all-optical 2R regenerators operating at 40 Gb/s: Role of dispersion,” *J. Lightw. Technol.* **27**, 3831–3836 (2009).

## ***Conference Presentations***

- (1) A. Larsson, J. S. Gustavsson, Å. Haglund, B. Kögel, J. Bengtsson, P. Westbergh, E. Haglund, **P. P. Baveja**, “High-speed tunable and fixed-wavelength VCSELs for short-reach optical links and interconnects,” in *Vertical-Cavity Surface-Emitting Lasers XVI*, edited by Chun Lei, Kent D. Choquette, Proceedings of SPIE Vol. 8276 (SPIE, Bellingham, WA 2012) 82760H.
- (2) **P. P. Baveja**, B. Kögel, P. Westbergh, J. S. Gustavsson, Å. Haglund, D. N. Maywar, G. P. Agrawal, and A. Larsson, “Impact of photon lifetime on thermal rollover in 850 nm high-speed VCSELs,” in *Vertical-Cavity Surface-Emitting Lasers XVI*, edited by Chun Lei, Kent D. Choquette, Proceedings of SPIE Vol. 8276 (SPIE, Bellingham, WA 2012) 82760V.
- (3) **P. P. Baveja**, D. N. Maywar, and G. P. Agrawal, “Efficient interband four-wave mixing in semiconductor optical amplifiers with fast gain recovery,” in *Frontiers in Optics*, OSA Technical Digest (CD) (Optical Society of America, 2010), paper FTuC6.
- (4) **P. P. Baveja**, A. M. Kaplan, D. N. Maywar, and G. P. Agrawal “Pulse amplification in semiconductor optical amplifiers with ultrafast gain recovery times,” in *Optical Components and Materials VII*, edited by Shibin Jiang, Michel J. F. Digonnet, John W. Glesener, J. Christopher Dries, Proceedings of SPIE Vol. 7598 (SPIE, Bellingham, WA 2010) 759817.
- (5) **P. P. Baveja**, D. N. Maywar, and G. P. Agrawal, “Scaling rules for optimizing 2R regenerators,” in *Conference on Lasers and Electro-Optics/International Quantum Electronics Conference*, OSA Technical Digest (CD) (Optical Society of America, 2009), paper CMC3. .

# Acknowledgements

As I start to write my thesis and procrastinate to begin on both the hard and juicy parts of this document, I face the arduous task of thanking people who have helped me on this journey. I call this a journey as the last six years have been long and hard, with their own shares of ups and downs, laughters and cries, joys and sorrows, friendships made and lost. In these six years, I feel I have been in a time dilation field, where six years have been shrunk into six months. Thanking is the least one can do for someone who has been with you on such a roller-coaster. So I take this opportunity to thank all these important people before I even write a word of my thesis.

The thesis advisor comes the first and the foremost on this list. Professor Govind P. Agrawal is much more than a thesis advisor for me. He has been a beacon guiding my life long before I even came to Rochester. I was a 19 year old lost in the crowd of millions more like me in India trying to figure out what I wanted to do with my life. I came across Professor Agrawal's book on Optical Communications while I was randomly book browsing in my college library. That book also contained his brief autobiography. The fact that he was born in a small town not too far from my own and not too different either, and has achieved and done so many wonderful things inspired me to walk down the same path. As an undergraduate student, I learnt the basics of fiber optics and optical amplification before applying to graduate schools all across US for fall 2006. And believe it or not, I was accepted to the optics program at the University of Rochester, where I

had applied for the only reason to have an outside chance of working with a small group of 3–4 Professors, with Professor Agrawal being at the top of that list.

Being a man of science, I do not believe in destiny or fate. Yet, this life example stares at me, telling me that sometimes if you really want something to happen, the universe conspires to make it happen. As a thesis advisor, he has been kind, understanding, flexible, supportive of whatever I wish to do and yet mildly vocal and critical of anything I do which is against my best interests. I thank you Professor for being my guiding beacon and I hope that you will continue to be a source of inspiration for me and the generations of young scientists to come.

I am, also, greatly indebted to my experimental mentor Prof. Drew N. Maywar. Professor Maywar is an alumnus of my research group. He has his own distinctive strengths from which I have learnt immensely. He is one of the most organized people I have met. Our discussions have ranged from how to best write a paper to how to best arrange lab equipment. They have helped me immensely in sorting out the way my chaotic mind thinks. I would also like to thank him for letting me work on setting up his lab space at RIT. It has given me a much needed perspective on what goes into running a laboratory.

I would also like to thank Professor Miguel Alonso for his extremely popular and helpful math class, Professor James Fienup for the toughest class I ever took. My failings with Matlab in his advanced imaging class were extremely important for me in that I sat back, took stock of my weaknesses and addressed them in time to have a rewarding graduate experience. Professor Duncan Moore for his extremely interesting entrepreneurship class. His class made me realize the importance of playing well with others. That and the fact that dressing sharply does make an impression. Professor Wayne H. Knox for being the constant source of infectious energy, motivation and encouragement to pursue excellence in my endeavors. Finally, I would like to thank the remainder of my thesis committee, Prof Gary Wicks and Prof. Thomas Brown for critical comments on this document.



I take this opportunity to thank Prof. Anders Larsson for hosting me as a Swedish Institute Guest Scholar at Chalmers University of Technology. He was an exceptional host and a patient teacher and thanks largely to him, I am a better researcher after my experiences at the Photonics Lab. I would also take this opportunity to thank my Swedish Collaborators: Dr. Benjamin Kögel for being a constant source of guidance, encouragement, learning, VCSELs and fine German liquor, Dr. Petter Westbergh for showing me the ropes around photonics lab, Dr. Johan S. Gustavsson for his insights and theoretical calculations of temperature dependence of distributed bragg-reflector (DBR) reflectivities, Dr. Åsa Haglund for the VCSELs and Erik Haglund for critical comments and discussions on my work.

I also take this opportunity to thank my group members and office mates, Dr. Lianhong, Brian, Yuzhe and Jordan for putting up with me all this time. My heartfelt gratitude goes out to fellow graduate students, Amber, Abbie, Mike, Rahul, Krishanu to name a few for amazing company, anecdotes and valuable life lessons. I would also like to thank the administrative and support staff at the Institute of Optics including but not limited to Per Adamson for maintaining and organizing excellent optics lab modules, Lissa Cotter for always being kind, sweet and patient through a slew of requests I sent her way, Joan Christian for showing me the ropes when I first started here, Gayle Thomson for the awesome summer schools and industrial associates program, Noelene Votens, Lori Russell and Gina for keeping the wheels well oiled and the clock ticking around here.

Last but certainly not least I acknowledge the role played by my family. My mother and father both for the endless support, inspiration and encouragement. My brother Tarun for the healthy dose of sibling rivalry, medical consults and general discussions on life questions. My wife Ruchita for always being there for me, for all the love and encouragement. I would also like to acknowledge her for proof-reading this manuscript. Dr Narendra Nath, Prof. R.K. Sinha, Sh. N.K.

Bhagat, Prof. Malin Premaratne, Prof. Hoojon Lee, Scott Householder, Aaron, Sumeeta, and others whose names escape me. I thank you all for playing a positive role in helping me reach where I am.

The work in this thesis was financially supported by the National Science Foundation award ECCS-1041982. The support from the Swedish Institute Guest Scholarship, Swedish Foundation for Strategic Research (SSF), the Swedish Research Council (VR), and the European Union through the project VISIT (FP7-224211) for the VCSEL work is acknowledged. Financial support from SPIE through student scholarship and travel grant support for attending various conferences is acknowledged. Finally the administrative and infrastructure support at the Institute of Optics, Rochester Institute of Technology and Chalmers University of Technology is also acknowledged.

# Abstract

Due to an exponential increase in the number of consumers using the voice, video and data services associated with modern optical transport systems, the footprint of these systems can no longer be ignored. To that end, this thesis focuses on studying the nonlinear effects in highly nonlinear fibers (HNLFs) and semiconductor optical amplifiers (SOAs) along with thermally induced power saturation effects in vertical-cavity surface-emitting lasers (VCSELs) from the standpoint of reducing power consumption associated with wavelength converter and optical signal regenerator topologies based on these devices. This thesis begins with a numerical investigation into the interplay between dispersion and nonlinearity for optimizing the performance and reducing the input power requirement of an all-optical re-amplification and re-shaping (2R) regenerator based on self-phase modulation (SPM) and spectral filtering at 40 Gb/s. Careful dispersion optimization leads to 30% reduction in input power required for HNLF-based 2R-regenerator without significant performance degradation. However, there are some associated trade-offs and watt level input optical powers are still required.

This thesis therefore shifts focus towards amplified spontaneous emission (ASE)-induced enhancement in nonlinear effects [SPM and four-wave mixing (FWM)] in SOAs. Traditionally, SOAs have required few tens of milliwatts (mWs) of input powers for optical signal processing. The modern SOAs investigated in this thesis achieve high internal ASE at high bias currents which reduces the effective carrier lifetime down to  $\approx 10$  ps. A simplified numerical model is developed for these

devices which is used to study SPM and FWM. For the case of SPM, a trade-off between spectral broadening and spectral symmetry due to ASE-mediated gain dynamics is demonstrated. This thesis also investigates the conversion efficiency (CE) and optical signal to noise ratio (OSNR) properties of ASE-assisted FWM in SOAs and demonstrates that in the presence of high internal ASE, the requirement on input optical powers for wavelength conversion is reduced from 10s of mWs to less than 1 mW. A proof of concept 10 Gb/s L-band wavelength converter is demonstrated.

While ASE-enhanced nonlinear effects in SOAs do relax the requirements on input signal powers, the requirement of high bias currents places a serious question mark on the scalability of this technique. VCSELs or vertical cavity SOAs (VCSOAs) (low-Q version of standard VCSELs) consume a fraction of electrical power as compared to SOAs. However the high speed operation of these devices is limited to a great extent by the thermally-induced power saturation effects. This thesis develops an empirical thermal model which can be used for studying mechanisms contributing to thermally induced optical power rollover in VCSELs.

The model is applied to four oxide-confined, 850 nm VCSEL designs. For all these devices, it is demonstrated that the power dissipation due to linear power dissipation exceeds power dissipation across the series resistance at any ambient temperature and bias current. The dominant contributors to device heating for these devices are the power dissipated across series resistance and carrier leakage. Absorption heating is also quite significant in the absence of a shallow surface-etch in the top DBR. Carrier leakage places the ultimate limit on the thermal performance for this entire class of devices. Further, a trade-off between power dissipated due to optical absorption and carrier leakage in these devices is demonstrated and investigated. The empirical thermal model proposed in this thesis is universally applicable for identifying the mechanisms limiting the thermal performance and for formulating the design strategies to ameliorate them .

# Table of Contents

<b>Curriculum Vitae</b>	<b>iii</b>
<b>Acknowledgements</b>	<b>vi</b>
<b>Abstract</b>	<b>x</b>
<b>List of Tables</b>	<b>xvii</b>
<b>List of Figures</b>	<b>xviii</b>
<b>Foreword</b>	<b>1</b>
<b>1 Introduction</b>	<b>3</b>
1.1 Footprint of Optical Transport Systems . . . . .	3
1.2 Optical Signal Regeneration . . . . .	4
1.3 Optical Wavelength Conversion . . . . .	7
1.4 Highly Nonlinear Fibers . . . . .	9
1.5 Semiconductor Optical Amplifiers . . . . .	11
1.6 Vertical-Cavity Surface-Emitting Lasers . . . . .	16
1.7 Footprint of Optical Signal Processing . . . . .	19
1.8 Thesis Outline . . . . .	22

<b>2</b>	<b>Dispersion Optimization in 2R Regenerators</b>	<b>26</b>
2.1	Introduction . . . . .	26
2.2	Details of the Numerical Scheme . . . . .	27
2.3	Role of Dispersion and the Resulting Scaling Rule . . . . .	30
2.4	Impact of Large Dispersion Variations . . . . .	35
2.5	Conclusions . . . . .	39
<b>3</b>	<b>Theoretical Framework for Fast Carrier-Lifetime SOAs</b>	<b>41</b>
3.1	Theoretical Framework . . . . .	41
3.1.1	Propagation of Optical Fields in SOAs . . . . .	41
3.1.2	Approximate Model for ASE . . . . .	42
3.1.3	CW Small Signal Gain Measurements . . . . .	44
3.1.4	SOA Gain and Gain Recovery . . . . .	47
3.2	Self-Phase Modulation . . . . .	50
3.2.1	Modified Equations . . . . .	50
3.2.2	Nonlinear Phase and Chirp . . . . .	51
3.2.3	Pulse Shapes and Spectra . . . . .	54
3.3	Four-Wave Mixing . . . . .	57
3.3.1	Introduction to Interband and Intraband FWM . . . . .	57
3.3.2	Modified Equations for FWM in SOAs . . . . .	58
3.3.3	Numerical Simulations . . . . .	61
3.4	Conclusions . . . . .	65
<b>4</b>	<b>ASE-Assisted SPM in SOAs: Experimental Results</b>	<b>67</b>
4.1	Introduction . . . . .	67

4.2	Experimental Setup . . . . .	67
4.3	Experimental Results . . . . .	69
4.3.1	Spectral Evolution . . . . .	69
4.3.2	Spectral Symmetry and Broadening . . . . .	70
4.4	Conclusions . . . . .	74
<b>5</b>	<b>ASE-Assisted FWM: Experiments and Applications</b>	<b>75</b>
5.1	Introduction . . . . .	75
5.2	Experimental Setup . . . . .	76
5.3	Wavelength Conversion Optimization . . . . .	77
5.3.1	Device Characterization . . . . .	77
5.3.2	Drive Current . . . . .	79
5.3.3	Pump-Signal Detuning $\Delta\lambda$ . . . . .	81
5.3.4	Optimization of Pump and Signal Powers . . . . .	82
5.3.5	Comparison with Theoretical Predictions . . . . .	87
5.4	10 Gb/s, Sub-mW Input-Optical Pump, L-Band Wavelength Converter . . . . .	90
5.4.1	Experimental Setup . . . . .	92
5.4.2	Spectral Analysis . . . . .	93
5.4.3	Experimental Results . . . . .	97
5.5	Concluding Remarks . . . . .	101
<b>6</b>	<b>Empirical VCSEL Thermal Model and Applications</b>	<b>103</b>
6.1	Introduction . . . . .	103
6.2	Theoretical Model . . . . .	104
6.2.1	Extraction of Parameters from Measurements . . . . .	109

6.3	Impact of Ambient Temperature on Thermal Rollover Mechanisms	111
6.3.1	Device Under Test . . . . .	111
6.3.2	Experimental Setup and Measurements . . . . .	112
6.3.3	Extraction of VCSEL Parameters . . . . .	115
6.3.4	Performance Predictions from Thermal Model . . . . .	117
6.4	Thermal Analysis . . . . .	122
6.5	Concluding Remarks . . . . .	125
<b>7</b>	<b>Dimensional Analysis of Thermal Effects in 850 nm VCSELs</b>	<b>128</b>
7.1	Introduction . . . . .	128
7.2	CW Measurements for the Four VCSELs . . . . .	130
7.2.1	Experimental Setup and Measurements . . . . .	133
7.3	Thermal Modelling . . . . .	139
7.4	Impact of Device Parameters . . . . .	144
7.4.1	Photon Lifetime . . . . .	144
7.4.2	Inner Aperture Diameter . . . . .	147
7.5	Concluding Remarks . . . . .	150
<b>8</b>	<b>Concluding Remarks</b>	<b>153</b>
8.1	Overview . . . . .	153
8.2	Optical Signal Processing Based on HNLFs . . . . .	153
8.3	ASE-Assisted Nonlinear Effects in SOAs . . . . .	155
8.4	Wavelength Conversion in SOAs . . . . .	158
8.5	Self-Heating Effects in VCSELs . . . . .	159
8.6	Summary of Contributions . . . . .	164



<b>A</b>	<b>Optiwave OptiSystem Software</b>	<b>166</b>
A.1	Description and Capabilities of OptiSystem 6.0 . . . . .	167
A.2	Optiwave Tutorial . . . . .	168
A.3	Parameter Sweeps . . . . .	173
<b>B</b>	<b>Gain-Switching in Semiconductor Lasers</b>	<b>175</b>
B.1	Numerical Model . . . . .	176
B.2	Gain-Switching Experiments . . . . .	179
<b>C</b>	<b>10 Gb/s NRZ and RZ OOK data generation.</b>	<b>183</b>
C.1	Experimental Setup . . . . .	184
C.2	Experimental Results . . . . .	186
	<b>Bibliography</b>	<b>189</b>

# List of Tables

1.1	Parameter Values for Different Nonlinear Fibers [53, 57]	10
1.2	Comparison of Total Dissipated Power	22
2.1	HNLF Parameters for the Three MTR Configurations Analyzed for Demonstration of the Scaling Rule	30
2.2	Parameters for the Four MTR Configurations with Different HNLFs	35
3.1	Manufacturer's Optical Specifications of the SOA at 500 mA	44
3.2	Assumed Parameter Values for the SPM Simulations	46
3.3	Deduced Parameter Values for the SPM Simulations	47
3.4	Parameter Values Used in the FWM Numerical Simulations	61
5.1	Calculated and Observed Values of $\Delta\lambda$ for $\eta = 1$ and $P_0 = 0.47$ mW	89
6.1	Room Temperature Values of VCSEL Parameters	115
6.2	Linear Temperature Dependence of VCSEL Parameters ( $\Delta = \frac{\partial}{\partial T}$ )	117
7.1	Summary of Devices Under Test	131
7.2	Parameter values at $T_a = 55$ °C for the four VCSELs and their linear temperature dependence ( $\Delta = \frac{\partial}{\partial T}$ ).	137

# List of Figures

1.1	Schematic of (a) a 2R regenerator, and (b) a re-amplification, re-shaping and re-timing (3R) regenerator . . . . .	5
1.2	Schematic of an optical WC . . . . .	7
1.3	Techniques for accelerating SOA gain recovery. . . . .	13
1.4	Schematic of a generic optical WC based on XPM. . . . .	20
2.1	Components of an MTR. Noise in the output signal is reduced when the signal spectrum, broadened nonlinearly inside the HNLF, is filtered by an OBPF that is spectrally offset by $\delta\lambda_0$ . . . . .	27
2.2	Setup used for simulating numerically the operation of an MTR. . . . .	29
2.3	(a) Improvement in the Q-factor as a function of average input power $P_{in}$ and (b) the corresponding transfer function for three MTRs listed in Table 2.1. . . . .	32
2.4	Input and output eye diagrams for the 40 Gb/s RZ bit stream at the power level corresponding to the peak in Fig. 2.3(a). . . . .	33
2.5	Improvement in the Q-factor (a) as a function of $Q_{in}$ and (b) as a function of $\delta$ for three MTRs listed in Table 2.1. . . . .	34
2.6	Characteristic power transfer function shapes of a MTR [18] . . . . .	36
2.7	a) Power transfer functions and (b) $\Delta Q$ as a function of average input power for the four MTRs listed in Table 2.2. . . . .	37

2.8	Improvement in the Q-factor (a) as a function of $Q_{\text{in}}$ and (b) as a function of $\delta$ for the four MTRs listed in Table 2.2. The peak powers correspond to optimum $P_0$ in Table 2.2. . . . .	39
3.1	(a) Experimental setup and (b) measured values of G(I) (dB) as a function of drive current. The solid line corresponds to the best estimate of $D$ from the experimental data (circles). . . . .	45
3.2	Calculated values of (a) $P_{\text{ASE}}$ and $P_{\text{sat}}$ , and (b) $\tau_{\text{eff}}$ as a function of drive current for the SOA used to obtain the data in Fig. 3.1. Experimental measurements of $P_{\text{ASE}}$ are shown as circles. . . . .	49
3.3	(a) Nonlinear phase shift and (b) frequency chirp induced on a 20 ps wide Gaussian pulse by an SOA with large ASE. Dashed lines show the case for which ASE is negligible. The double arrows indicate the maximum value of the nonlinear phase shift and red and blue chirp for both the cases. . . . .	52
3.4	Output pulse shapes (a) at low drive currents ( $r \leq 0.13$ ) and (b) high drive currents ( $0.3 < r < 1.1$ ). . . . .	54
3.5	Output pulse spectrum (a) at relatively low drive currents ( $r \leq 0.13$ ) and (b) at high drive currents ( $0.3 < r < 1.1$ ) . . . . .	56
3.6	Conversion Efficiency as a function of pump-signal detuning (a) at three drive currents for 1 mW pump power and (b) at three input pump powers at 500 mA drive current. . . . .	63
3.7	Conversion Efficiency as a function of effective carrier lifetime ( $\tau_{\text{eff}}$ ) for different pump-signal detuning $\Delta\lambda$ . Device gain $G_0 = 30$ dB . . . . .	64
4.1	(a) Experimental setup. (b) Pulse shape and (c) pulse spectrum produced by the gain-switched DFB laser. . . . .	68

4.2	Observed spectra of amplified pulses at drive current (a) up to 100 mA and (b) beyond 100 mA. . . . .	70
4.3	Relative amplitudes of the three main spectral lobes seen in Fig. 4.2 as a function of drive current. . . . .	71
4.4	(a) Spectral broadening factor (SBF) and (b) measured small signal amplification factor as a function of drive current. . . . .	72
5.1	Experimental setup used for studying interband FWM. PC: polarization controller; PBS: polarization beam splitter; PM: power meter; ISO: isolator; VOA: variable optical attenuator; OSA: optical spectrum analyzer; $\Delta\lambda$ : pump-signal detuning. . . . .	76
5.2	(a) The ASE spectra at 100, 300 and 500 mA. (b) Net device gain as a function of pump power. Input signal power and pump-signal detuning $\Delta\lambda$ were $-20.3$ dBm and 2.5 nm, respectively. . . . .	78
5.3	FWM spectra measured at three currents for a pump-signal detuning of (a) 0.5 nm and (b) 2.6 nm at a pump power of $-3.3$ dBm. The input signal level ( $-20.3$ dBm) is marked by an arrow. . . . .	79
5.4	Conversion efficiency and OSNR as a function of $I_{\text{SOA}}$ for $\Delta\lambda = 0.5$ nm at a pump power of $-3.3$ dBm (dashed curves) and $+3.3$ dBm (solid curves). Input signal power was $-10$ dBm. . . . .	80
5.5	Conversion efficiency and OSNR as a function of $\Delta\lambda$ at a pump power of (a) $-3.3$ dBm and (b) $+3.3$ dBm for input signal power of $-20.3$ dBm. Dashed and solid curves correspond to 100 and 500 mA drive currents, respectively. . . . .	82
5.6	FWM spectra observed at three input pump powers for pump-signal detunings of (a) 0.5 nm and (b) 2.5 nm. The SOA current is 500 mA and the signal level ( $-20.3$ dBm) is marked by an arrow. . . . .	83

5.7	Conversion efficiency (circles) and estimated OSNR (squares) measured as a function of $P_0$ at 500 mA drive current. Solid lines represent a fit to the experimental data. Input signal power was 10 $\mu$ W at a pump-signal detuning of 2.5 nm. . . . .	85
5.8	Conversion efficiency and OSNR measured as a function of $P_1$ at (a) $P_0 = -2.2$ dBm and (b) $P_0 = +3.3$ dBm for $\Delta\lambda = 5$ nm. Dashed and solid lines correspond to drive currents of 300 and 500 mA, respectively. . . . .	86
5.9	Power transfer function for the two pump powers at 500 mA SOA current. The WS is 5 nm. . . . .	87
5.10	Conversion efficiency as a function of $\Delta\lambda$ at SOA currents of 100 and 300 mA. Solid lines are obtained from the numerical model, whereas symbols represent experimental data. $P_0$ and $P_1$ are $-3.3$ and $-20.3$ dBm, respectively. . . . .	89
5.11	Experimental setup used for proof of concept demonstration of 10 Gb/s wavelength converter for RZ-50 signals based on ASE-assisted interband FWM in SOA. PC: Polarization Controller; PBS: Polarization Beam Splitter; PM: Power Meter; 50/50: 3 dB Splitter; 99/1: 1% power tap; RF AMP: RF Amplifier; EDFA: Erbium-Doped Fiber Amplifier; FIL: Optical Filter; MOD: 10 Gb/s Intensity Modulator; VOA: Variable Optical Attenuator; ISO: Isolator; OSA: Optical Spectrum Analyzer. . . . .	91
5.12	FWM spectra for L-Band wavelength conversion measured at the 1% power tap for four different input pump powers. The pump wavelength corresponds to channel no. 45 of L-Band ITU grid with 100 GHz grid spacing [178]. Part (a) corresponds to wavelength conversion from channel no. 44 to 46, (b) channel no. 43 to 47, and (c) channel no. 40 to 50. . . . .	94

5.13	Converted signal spectra measured at the output of (a) Output Filter (b) ASE Filter corresponding for four different input pump powers at 1000 GHz WS (corresponding to Fig. 5.12(c)). . . . .	96
5.14	(a) Conversion efficiency and (b) OSNR measured as a function of $P_0$ at $P_1 = -11.7$ dBm and 500 mA drive current. The solid lines correspond to 200 GHz, the dashed lines 400 GHz and the dotted lines 1000 GHz WS respectively. . . . .	98
5.15	(a) Eye-diagram for input data channel ( $P_1 = -11.7$ dBm). Eye diagrams for converted data channel at $P_0 =$ (b) $-6$ dBm, (c) $-4$ dBm, and (d) $-2$ dBm. The converted data channel was measured at the output of FIL2 and corresponds to 1000 GHz WS. . . . .	99
6.1	Schematic illustration of the capture $\eta_i(T)I_b$ and leakage $(1-\eta_i(T))I_b$ of injected carriers in strained InGaAs quantum wells. $E_B(T)$ , $E_L(T)$ and $\eta_i(T)$ are the temperature dependent barrier bandgap energy, lasing bandgap energy and internal quantum efficiency, respectively. This Fig. depicts three out of the four LPD mechanisms; absorption losses in the top and the bottom DBRs are not shown here. . . . .	106
6.2	Schematic cross section of the high-speed 850 nm VCSEL used in the experiment. Benzo-Cyclo-Butene is employed to reduce parasitic capacitance. Six layers are used for forming an oxide aperture (dark shading region). Other details of the device design can be found in Ref. [190]. . . . .	112

6.3	Measurements used to extract temperature dependence of VCSEL parameters. (a) Output power and (b) voltage as a function $I_b$ at five ambient temperatures. The inset in (b) shows variations of differential resistance $R_s$ with $I_b$ . (c) Wavelength of the (LP <sub>01</sub> ) mode versus $T_a$ (circles); the linear fit is used to estimate the device temperature. . . . .	113
6.4	(a) Threshold current as a function of $T_a$ ; the numerical fit is used in the thermal model. (b) Dissipated power as a function of $I_b$ for five $T_a$ values used in Fig. 6.3(a). (c) SE versus output power at three different $T_a$ values. The inset shows the derived dependence of $\eta_i$ on temperature; the numerical fit is used in the thermal model.	114
6.5	Comparison of simulated (solid lines) and measured (symbols) values of (a) output power, (b) total dissipated power, and (c) device temperature as a function of $I_b$ at three different ambient temperatures $T_a = 25, 55$ and $85^\circ\text{C}$ . . . . .	118
6.6	(a) Internal quantum efficiency and (b) threshold current as a function of $I_b$ . The inset in (b) shows the derivative $dI_{\text{th}}/dI_b$ . . . . .	119
6.7	(a) LPD coefficient $K$ versus bias current at three ambient temperatures. (b) Dependence of four individual LPD coefficients on bias current at $25^\circ\text{C}$ . Total $K$ is also shown for comparison. Vertical dotted lines mark the region where $K$ is relatively small. . . . .	120
6.8	Comparison of the various VCSEL heating mechanisms at three ambient temperatures. (a) Total LPD and QPD as a function of $I_b$ , (b) dependence of individual LPD contributions on $I_b$ , and (c) contributions of LPD and QPD mechanisms to the increase in device temperature as a function $I_b$ . The Figs. with asterisk* refer to the fragments of the corresponding part. These Figs. have been split into two to achieve desired clarity. . . . .	123



7.1	Calculated (a) top DBR loss rate and (b) photon lifetime as a function of etch depth into the top DBR. The experimental etch depths are indicated using dots and correspond to 0, 25, 40 and 55 nm. These Figs. have been adapted from Ref. [127]. . . . .	132
7.2	$P_{\max}$ as a function of $T_a$ for the four VCSELs. . . . .	134
7.3	(a) $P_{\text{opt}}$ , (b) $V_b$ and (c) $P_{\text{tot}}$ as a function of $I_b$ at $T_a = 55$ °C. The inset in (a) shows a two-segment line-fit on device D for estimating threshold current and inset in (b) shows the differential resistance $R_s$ . . . . .	135
7.4	Thermal impedance as a function of inner aperture diameter. The dashed line represents analytical prediction and symbols correspond to values extracted using the thermal model presented in Chapter 6.	138
7.5	Comparison of predicted (colored lines) and measured values (indicated by gray lines and symbols) of (a) $P_{\text{opt}}$ , (b) $P_{\text{tot}}$ , and (c) $T$ as a function of $I_b$ at $T_a = 55$ °C for the four VCSELs. . . . .	140
7.6	(a) Changes in $\eta_i$ (solid lines) and $I_{\text{th}}$ (dashed lines, right scale) with bias current at $T_a = 55$ °C for four VCSELs. (b) LPD coefficient $K$ versus $I_b$ for four VCSELs; inset shows $K$ and $P_{\text{opt}}$ for device A as a function of $I_b$ . An increase in $K$ marks the onset of thermal rollover. . . . .	142
7.7	Internal quantum efficiency $\eta_i$ as a function of $T_a$ for device A (solid lines) and device C (dotted lines). The lines show a numerical fit to the measured data. . . . .	143

7.8	Impact of photon lifetime on the LPD and QPD mechanisms. (a) $P_{\text{LPD}}$ and $P_{\text{QPD}}$ as a function of $I_b$ , (b) individual LPD contributions versus $I_b$ , and (c) contributions of LPD and QPD mechanisms to $\Delta T$ for device A (solid lines) and device C (dotted lines). The Figs. with asterisk* refer to the fragments of the corresponding part. These Figs. have been split into two to achieve desired clarity.	145
7.9	Impact of inner aperture diameter on the LPD and QPD mechanisms. (a) $P_{\text{LPD}}$ and $P_{\text{QPD}}$ as a function of $I_b$ , (b) individual LPD contributions versus $I_b$ , and (c) contributions of LPD and QPD mechanisms to $\Delta T$ for device B (dashed lines), device C (dotted lines), and device D (dot-dashed lines). The Figs. with asterisk* refer to the fragments of the corresponding part. These Figs. have been split into two to achieve desired clarity. . . . .	148
A.1	OptiSystem implementation of the simulation schematic shown in Fig. 2.2. . . . .	168
A.2	Setting the global simulation parameters in OptiSystem Software.	171
A.3	Calculation Output Window for the OptiSystem Software. . . . .	172
A.4	Calculation Output Window for the OptiSystem Software while running a parameter sweep. . . . .	173
B.1	Gain-switching simulations snapshot. Part (a) shows the total current applied to the diode laser in one RF-signal cycle. Part (b) shows the simulated gain-switched pulse with $T_{FWHM} = 44$ ps. . .	178
B.2	Experimental setup used for characterizing gain-switched pulse source.	179

B.3	(a) Shapes and (b) spectra of the picosecond optical pulses from the gain-switched source. For all these measurements, the DFB laser is biased at 15 mA. The series resistance of the mount is 50 $\Omega$ . The modulation currents corresponding to the four peak-peak voltages are 38.8, 43.4, 48.6, and 55 mA, respectively. . . . .	181
C.1	Experimental setup used for generating 10 Gb/s NRZ and RZ-50 bit streams. For generating 10 Gb/s NRZ bit-stream, MOD2 is swapped out of the setup. PC: Polarization Controller; PRBS: Pseudo Random Bit Sequence Generator; 99/1: 1% power tap; RF AMP: RF Amplifier; TL: Tunable Lase; MOD1: 10 Gb/s Data Modulator; MOD2: Synchronous Pulse Carver; OSA: Optical Spectrum Analyzer; PD: Photodiode; OSC: Sampling Scope. . . . .	185
C.2	Experimentally optimized 10 Gb/s NRZ and RZ-50 optical bit streams. (a) Spectrum (b) Eye Diagram for 10 Gb/s NRZ bit stream. (c) Spectrum and (d) Eye Diagram for 10 Gb/s RZ-50 bit stream. . . . .	187

## List of Abbreviations

2R	Reamplification and Reshaping
3R	Reamplification, Reshaping and Retiming
ASE	Amplified Spontaneous Emission
CE	Conversion Efficiency
CW	Continuous Wave
DBR	Distributed Bragg-Reflector
DFB	Distributed-Feedback
DWDM	Dense Wavelength Division Multiplexed
EDFA	Erbium-Doped Fiber Amplifier
FOM	Figure of Merit
FP	Fabry Perot
FWHM	Full-Width at Half Maximum
FWM	Four-Wave Mixing
GUI	Graphical Users Interface
HNLF	Highly Nonlinear Fiber
IL	Insertion Loss
ISO	Optical Isolator
ITU	International Telecommunication Union
LPD	Linear Power Dissipation
MQW	Multi Quantum-Well
MTR	Mamyshev-Type Regenerator
MZM	Mach-Zehnder Modulator

mW	Milliwatt
NF	Noise Figure
NOLM	Nonlinear Optical Loop Mirror
NRZ	Non-Return-to-Zero
OBPF	Optical Bandpass Filter
OEO	Optical-to-Electrical-to-Optical
OOK	On-Off Keying
OSA	Optical Spectrum Analyzer
OSNR	Optical Signal to Noise Ratio
PBS	Polarization Beam Splitter
PC	Polarization Controller
PD	Photodiode
PM	Power Meter
PRBS	Pseudo-Random Bit Sequence
QPD	Quadratic Power Dissipation
QW	Quantum-Well
RF	Radio-Frequency
RZ	Return-to-Zero
SBF	Spectral Broadening Factor
SBS	Stimulated Brillouin Scattering
SCH	Separate-Confinement Heterostructure
SE	Slope Efficiency
SMF	Single Mode Fiber
SOA	Semiconductor Optical Amplifier

SPM	Self-Phase Modulation
TE	Transverse-Electric
TEC	Thermo-Electric Cooler
VCSEL	Vertical-Cavity Surface-Emitting Lasers
VCSOA	Vertical-Cavity Semiconductor Optical Amplifier
VOA	Variable Optical Attenuator
XGM	Cross-Gain Modulation
XPM	Cross-Phase Modulation
WC	Wavelength Converter
WDM	Wavelength Division Multiplexed
WS	Wavelength-Shift

# Foreword

The following is a snapshot of contributions from my collaborators to the work documented in this thesis

1. Prof. Drew N. Maywar provided valuable comments for finalizing the manuscripts based on Chapter 2, Chapter 6, and Chapter 7.
2. Prof. Drew N. Maywar helped shape the content of the manuscripts based on Chapters 4 and 5.
3. The experiments presented in Chapter 4 and Chapter 5 were performed at Prof. Drew N. Maywar's laboratories; both at Laboratory of Laser Energetics and Rochester Institute of Technology.
4. Aaron M. Kaplan assisted with the experiments and data collection pertaining to Chapter 4.
5. Sumeeta Arora and Yuzhe Xiao assisted with the experiments presented in Chapter 5, section 4 (10 Gb/s L-Band wavelength converter) and Appendix C. While Sumeeta Arora assisted with initial experimental setup and building the 10 Gb/s test-bed, Yuzhe Xiao assisted with experimental optimization of 10 Gb/s NRZ and RZ bit streams.
6. Scott Householder constructed the power sources for the RF amplifiers used in the experiments documented in Chapter 5, section 4.

7. Dr. Benjamin Kögel assisted with the experiments presented in Chapter 6 and 7 and also helped with writing portions of manuscripts based on Chapter 6 and 7.
8. Dr. Petter Westbergh provided critical comments on the manuscripts based on Chapter 6 and Chapter 7. He also helped me train on some of the laboratory equipment at Photonics Laboratory, MC2 department, Chalmers University of Technology. He also provided the experimental data for the temperature dependence of the internal optical loss, a key aspect of the VCSEL thermal model presented in Chapter 6.
9. Prof Johan S. Gustavsson provided valuable insight and gave instructions for the work presented in Chapter 6. He also provided with the theoretical calculations of temperature dependence of distributed bragg-reflector (DBR) reflectivities, a key aspect of the VCSEL thermal model presented in Chapter 6.
10. The four VCSELs analyzed in this thesis were fabricated at the Photonics Laboratory, MC2 department, Chalmers University of Technology. Dr. Benjamin Kögel, Dr. Petter Westbergh, Prof. Johan S. Gustavsson, Prof. Åsa Haglund and Prof. Anders Larsson were behind the design and fabrication of these devices.



# 1 Introduction

## 1.1 Footprint of Optical Transport Systems

The advent of communications technologies has truly changed the way we lead our lives. The smart phones, cable TV, online banking and e-trading, internet, teleconferencing, tele-medicine etc are all necessities of present times which were inconspicuous less than a decade ago. The driving force behind all these innovations has been an enormous increase in the telecom system capacity and a dramatic reduction in the cost of associated components and devices. While increasing capacity and reducing cost have traditionally been the driving force behind innovations in this area, a third key aspect, that is the energy consumption of optical transport systems, has traditionally taken a back seat [1,2].

The energy consumption of optical transport systems is a key concept and has been around for a while. Many innovations, both in device and systems domain, have been made possible due to dramatic improvement in energy efficiency associated with them. However, in the past decade or so, it has become increasingly clear that our society is constrained by the total amount of energy at its disposal. The growing energy consumption of the global optical communication network is now a real cause for concern [3].

Data wavelength converters (WCs) and optical signal regenerators are the two key functionalities of the future, high-speed, transparent, optical transport systems. Their implementation usually requires a gain element, a nonlinear element and an output optical bandpass filter (OBPF), either spectrally aligned or spectrally offset with respect to the input wavelength [4, 5]. If the nonlinear element is a passive HNLF, then the energy consumption for the associated gain element becomes quite severe. On the other hand, employing an active nonlinear element such as a SOA or a VCSEL can potentially relax the energy consumption of the associated gain element to the point that it could be rendered redundant. This reduction in power consumption of the gain element comes at the cost of increase in power consumption for the nonlinear element.

The focus of this thesis is on reducing the power consumption of WCs and optical signal regenerators using HNLFs and SOAs as nonlinear elements. While VCSELs or vertical-cavity SOAs are prime candidates for replacing SOAs in future energy-efficient optical-signal processing techniques, the scope of this thesis is limited to investigating the thermal effects which currently limit the high-speed operation of these devices. A brief primer on wavelength conversion, optical-signal regeneration, the three nonlinear elements and power consumption calculations is presented in the following sections.

## 1.2 Optical Signal Regeneration

Optical signal regeneration can restore the quality of transmitted signals that has been degraded by transmission over long distances due to ASE, fiber nonlinearities, group velocity dispersion and polarization mode dispersion [4, 5]. Of all the signal-impairment mechanisms, ASE noise is one of the most significant impairments as it grows proportionally with the number of cascaded erbium-doped fiber amplifiers (EDFAs) in an optical communication link [4]. It manifests itself as fluctuation in

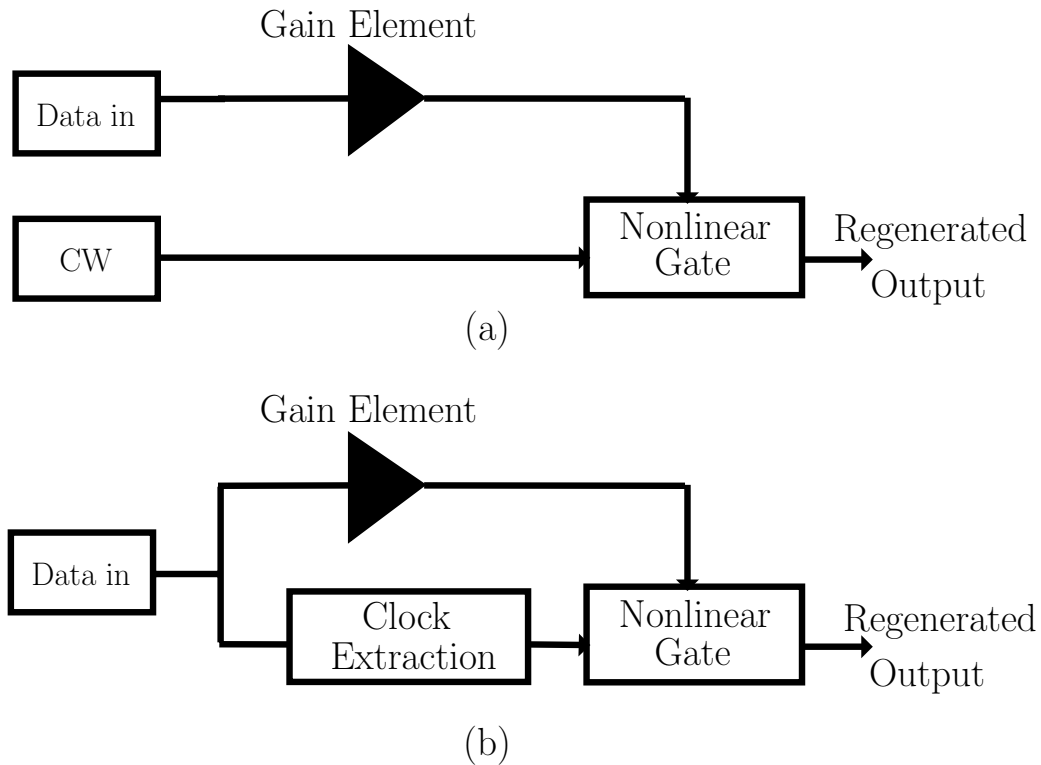


Figure 1.1: Schematic of (a) a 2R regenerator, and (b) a re-amplification, re-shaping and re-timing (3R) regenerator

power level of “1” bits and as noisy ghost pulses in “0” bits. ASE can also induce timing jitter in the optical bit stream by shifting optical pulses from their original location within the time slot in a random fashion [4]. To restore the signal quality, signal regeneration needs to be performed periodically.

All-optical regenerators provide an attractive alternative for regeneration of degraded optical signals in future transparent, high-speed optical networks. Figure 1.1(a) shows the schematic of a 2R regenerator. It consists of a local continuous wave (CW) source and an optical amplifier which amplifies the incoming noisy data signal. This amplified signal is used to drive a nonlinear gate which impresses the data pattern on the local CW beam [6]. A nonlinear gate is nothing but a nonlinear element (for e.g. HNLF, SOA or VCSEL) in combination with

an OBPF. Figure 1.1(b) shows the basic schematic of an all-optical 3R regenerator. The incoming noisy data signal is split into two parts. One part is used for clock extraction and the other part is amplified and drives a nonlinear optical gate which impresses the data pattern on the recovered clock signal [6]. In cases where timing jitter is not an issue, 2R regeneration is sufficient to restore signal quality.

Early attempts at designing 3R regenerators used mode-locked fiber ring lasers for clock recovery, followed by phase modulation in a HNLF [7]. Ito et. al. [8] used a self-pulsating distributed-feedback (DFB) laser for clock recovery, with cross-phase modulation (XPM) in HNLF for signal reshaping to obtain 3R regeneration at 40 Gb/s. Early attempts at designing 2R regenerators include nonlinear optical loop mirrors (NOLMs) [9], two-pump parametric processes [10], similariton generation [11], FWM [12], and XPM [13] in HNLFs.

Among various regenerator configurations, the 2R regenerator based on SPM-induced spectral broadening, followed by spectrally offset filtering, also known as the Mamyshev-Type Regenerator (MTR) [13], has received much attention [14–20] because it is relatively easy to implement as compared to other HNLF-based configurations. It is also scalable to high bit rates as it utilizes the quasi-instantaneous response time of the Kerr nonlinearity in optical fibers [18]. It has reduced sensitivity to environmental instability as well as reduced polarization sensitivity as compared to systems employing interferometric effects. A retiming stage can be integrated with MTR to provide 3R regeneration [8, 21]. Recent advances in fiber designs, which include chalcogenide fibers [22], bismuth-oxide fibers [23] and holey fibers [24], have further enhanced interest in MTRs. These fiber designs have a high nonlinear coefficient and are, therefore, potentially attractive for reducing the required optical power and increasing the compactness of this class of devices [18].

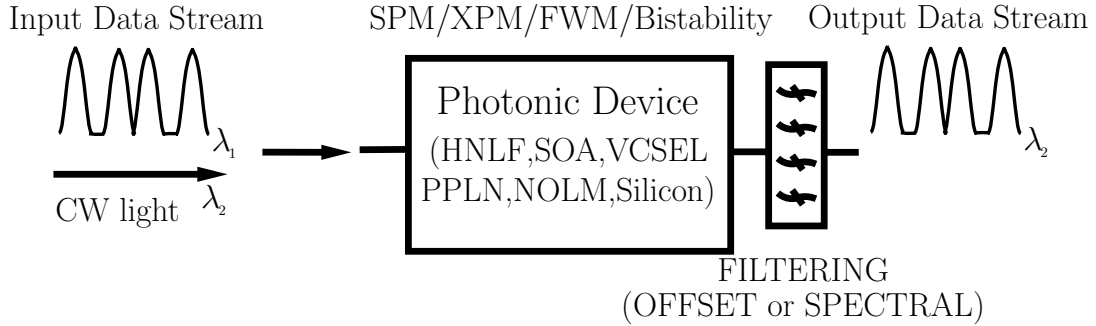


Figure 1.2: Schematic of an optical WC

### 1.3 Optical Wavelength Conversion

Currently deployed high-speed, high-capacity optical transport systems extensively employ wavelength division multiplexing (WDM) along with phase and polarization multiplexing for achieving capacity enhancement [25]. Further, wavelength-based routing is a key functionality in reconfigurable multi-point networks [26]. A combination of wavelength-based routing together with WDM signals means that wavelength blocking at the optical-cross connects and reconfigurable add-drop multiplexers becomes a critical issue [27–29]. Wavelength converters are therefore an essential part of modern optical transport systems. Conventional wavelength conversion method is the power inefficient optical-to-electrical-to-optical (OEO) conversion for each data channel. This technique has the advantage of being regenerative in nature but suffers from high cost associated with scalability, besides being extremely power inefficient [26, 27]. Further, the ease of implementation of OEO WC progressively worsens as the data rates are increased beyond 10 Gb/s.

Optical wavelength conversion techniques have shown tremendous promise from the standpoint of reduced cost, capability to process multiple channels in one device, bit-rate transparency, and reduced power consumption compared to

traditional OEO converters [27]. As a consequence, there has been a tremendous amount of work done to achieve efficient and wherever possible regenerative optical wavelength conversion [25, 27, 30–47]. Figure 1.2 shows a schematic of a generic optical WC topology. An incoming optical bit stream at wavelength  $\lambda_1$  is mixed with a CW signal at  $\lambda_2$ . Depending on the specifics of the converter design and the nonlinear element used, either the data or CW signal could be designated as probe or pump respectively. As indicated in the Fig., there are various nonlinear interactions in the six nonlinear elements that have historically been studied for implementation of optical WCs. Phase-matched second harmonic generation in periodically poled lithium niobate waveguides [30], FWM in silicon waveguides and resonators [31–33], XPM in NOLMs [34, 35], XPM and FWM in HNLFs [36–39] and SOAs [25, 27, 40–45] and XPM in VCSELs [46, 47] have been investigated for realization of high-speed, low-cost optical WCs.

The requirement of phase-matching condition limits the usability of the periodically poled lithium niobate waveguides. NOLM-based WCs suffer from stability issues. While silicon waveguides have become quite popular recently, they are currently plagued by high input power requirements (typically in excess of a few 100 mW), poor conversions efficiencies (typically 10% or less) and free-carrier effects limiting their high speed response [48]. FWM and XPM in HNLFs and SOAs are the most promising techniques and nonlinear elements respectively from the standpoint of realizing practical optical WCs. While HNLF-based techniques are easy to implement, have low coupling losses and bit rate transparency, they suffer from high input optical power requirements (typically in excess of a few watts). Further, narrowband optical filtering at the output implies that most of the optical power is wasted. SOA-based techniques consume less power but are limited in speed due to slow gain recovery dynamics of the device. FWM in SOAs however has the additional advantage of being transparent to the modulation format of the incoming data stream.

## 1.4 Highly Nonlinear Fibers

Nonlinear effects in optical fibers have been known to have adverse effects limiting the data capacity of fiber-optic communication systems [4]. However, positive utilization of these effects have led to the development of various important photonic devices such as fiber lasers [49, 50], parametric oscillators [51], tunable lasers [52], all-optical regenerators, tunable optical delay and all-optical wavelength conversion [34, 39, 53–55].

The origin of nonlinear effects in any glass is due to its nonlinear refractive index  $n_2$ . The nonlinear refractive index for bulk silica is extremely low ( $2.7 \times 10^{-20} m^2/W$ ) and as a consequence, nonlinear effects in bulk silica are negligible. However in case of optical fibers, enhancement in nonlinear effects is achieved due to tight confinement of optical power in the fiber core. An approximate expression for the nonlinear coefficient  $\gamma$  of an optical fiber is [56]:

$$\gamma = \frac{2\pi n_2}{\lambda_0 A_{\text{eff}}}. \quad (1.1)$$

Here  $\lambda_0$  is the free space wavelength and  $A_{\text{eff}}$  is the effective mode area taking into account the optical confinement. Further, the strength of nonlinear interaction in an optical fiber is quantified by a dimensionless parameter known as maximum nonlinear phase shift ( $\phi_0$ ). This parameter is defined as:

$$\phi_0 = \gamma P_0 L_{\text{eff}}. \quad (1.2)$$

where  $P_0$  is the peak optical power, and  $L_{\text{eff}}$  is the effective nonlinear interaction length defined as:

$$L_{\text{eff}} = \frac{1 - \exp(-\alpha L)}{\alpha}. \quad (1.3)$$

where  $L$  is the length of fiber [in kilometers] and  $\alpha$  is the linear propagation loss [in  $\text{km}^{-1}$ ]. It can be seen from Eq. (1.2) that for a fixed input power  $P_0$ , the strength of nonlinear interaction is determined by the product  $\gamma L_{\text{eff}}$ . Indeed this product

Table 1.1: Parameter Values for Different Nonlinear Fibers [53,57]

Fiber	$\gamma$ ( $W^{-1}km^{-1}$ )	$\alpha$ ( $dBkm^{-1}$ )
SMF	1.5	0.2
HNLF	25	0.5
As <sub>2</sub> Se <sub>3</sub> Fiber	1200	1000
Bismuth Oxide Fiber	1100	800

is the conventional figure of merit (FOM) used to characterize the strength of nonlinear interaction in an optical fiber [39,57].

Table 1.1 summarizes the different values of  $\gamma$  and  $\alpha$  reported in the literature for the various nonlinear fibers. It can be seen that even though the value of nonlinear coefficient for non-silica glasses such as chalcogenide [53] and bismuth oxide [55] is much higher than the silica-based single mode fiber (SMF) and HNLF, the increase in the value of  $\alpha$  by nearly four orders of magnitude negates the gains in nonlinear coefficient. Enhancement in the value of  $\gamma$  for silica-based HNLF while maintaining almost constant  $\alpha$  is achieved by heavily doping the fiber core with GeO<sub>2</sub> [39].

This simplistic analysis ignores the effects of stimulated brillouin scattering (SBS) [58]. To include the effects of SBS, the nonlinear FOM for HNLFs is modified as:

$$FOM_{SBS} = \gamma P_{th} L_{eff}. \quad (1.4)$$

where  $P_{th}$  is the SBS threshold power. In the presence of SBS, non-silica glasses demonstrate superior nonlinear response on account of higher SBS threshold. However low splicing loss to the conventional SMF, high reliability, and durability means that silica-based HNLFs are preferred even though they require SBS suppression, chromatic dispersion management and zero-dispersion wavelength equalization [37–39,59].



## 1.5 Semiconductor Optical Amplifiers

The origin of modern semiconductor laser technology can be traced back to the first evidence of coherent radiation from a GaAsP p-n junction, the end facets of which were cleaved to form a Fabry-Perot (FP) cavity [60,61] and the development of semiconductor quantum-well (QW) lasers [60,62]. The development of SOAs was initiated in between these two landmarks in the history of optoelectronic devices [63]. The applications that motivated the initial research into SOAs were optical-repeaters and pre-amplifiers for fiber-optic communication systems [5,63–65]. However with the advent of EDFAs [66] and fiber Raman amplifiers [67], the SOAs were effectively replaced as the optical amplifier of choice for optical transport systems. This was primarily due to their relatively poor noise figure (NF), highly polarization-sensitive gain, high insertion loss (IL), high nonlinearity and severe ripple in the gain spectrum arising due to residual reflectivity from the cavity mirrors [63].

Since early 1990s, there has been a renewed interest in SOAs. This time around however, the focus was to utilize the enhanced nonlinearity in SOAs and use it as a nonlinear block for a variety of optical signal processing applications. These applications included wavelength conversion [40–45], 2-R [27] and 3-R [68] regeneration, optical logic [69–71], optical flip-flop and memory [72–75], data-format conversion [76,77], optical switching [72,78,79], multiplexing/demultiplexing [80–82], all-optical routing [83], tunable-optical filtering [63], pulse compression [84], dispersion compensation [85] and clock generation and recovery [63,72,86,87]. It is important to note that an SOA will also considerably amplify the optical signals apart from performing its intended purpose of signal processing. This dual functionality makes them much more attractive than the passive HNLFs which always require an additional gain element. Further, significant design improvements in the past 2 decades have led to devices with low IL (2–3 dB per device),

considerably less gain-ripple ( $\leq 3$  dB) at moderate injection levels [88], enhanced differential gain coefficient [89,90] and extremely low polarization dependent gain ( $\leq 0.2$  dB) [91]. Further, with the advancement in optical filter technology, out-of-band ASE can effectively be eliminated with low IL ( $\leq 3$  dB). However, the in-band ASE is still a concern with these devices.

The origin of nonlinear effects in SOAs can be traced to the linewidth enhancement factor  $\alpha$ , first derived for the semiconductor lasers [92], which relates the temporal changes in gain to the temporal chirping of the optical signal. It has been demonstrated that a SOA exhibits SPM with an effective nonlinear index  $n_2 = 1 \times 10^{-9} \text{cm}^2/W$ . Comparing that to the nonlinear coefficient of silica glass ( $n_2 = 3 \times 10^{-16} \text{cm}^2/W$ ), it can be seen that the nonlinear response of an SOA is much stronger than that of a silica-based HNLFF. In fact, nonlinear effects have been observed in these devices for input peak powers of the order of 1 mW [93]. However this enhanced nonlinear response comes at a price. Since the origin of this nonlinearity is the time-dependent device gain, the response time of this nonlinearity is limited by the carrier lifetime ( $\tau_c$ ) of the SOA which can be expressed as:

$$\frac{1}{\tau_c} = A_{nr} + B_{sp}N + C_a N^2, \quad (1.5)$$

where  $A_{nr}$  is the intrinsic nonradiative recombination rate,  $B_{sp}$  is the radiative spontaneous recombination coefficient,  $C_a$  is the nonradiative Auger recombination coefficient and  $N$  is the injected carrier density. Each of these coefficients themselves depend on  $N$  [94]. This results in an SOA carrier lifetime strongly dependent on injected carrier density. Typically it varies between 750–200 ps with increasing bias current [95]. However, even at 200 ps, the carrier lifetime is nearly not fast enough to even respond to 10 Gbit/s signals. This in turn leads to nonlinear patterning effects [96] in high-speed signals propagating through these devices.

The limitations imposed by the slow gain recovery dynamics of SOAs were first

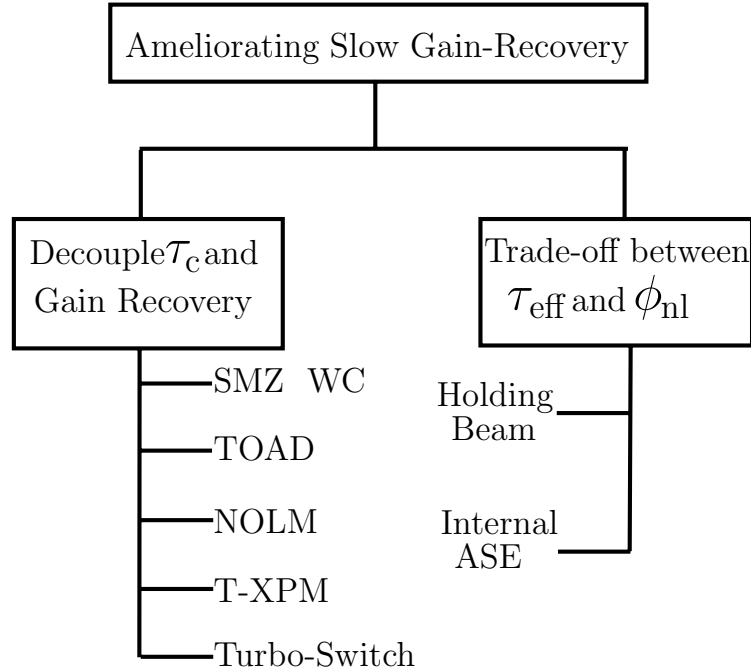


Figure 1.3: Techniques for accelerating SOA gain recovery.

identified in the early 1990s [95] and ever since then there has been considerable amount of work done to enhance the response time of the nonlinearities induced by the SOA gain dynamics [27, 97–109]. All the work that has been done can be classified into two categories summarized in Fig. 1.3. The first category involves decoupling the carrier lifetime and the rate of gain recovery. This in turn is achieved by using SOAs in interferometric configurations and/or cascading them to effectively cancel out the slow gain recovery dynamics [27, 97–102]. The examples for this technique are single Mach-Zehnder all-optical switch and WC [69, 97], terahertz optical asymmetric demultiplexer (TOAD) [81], delayed-interference WC [97, 98], NOLM [80, 97], transient-XPM [27, 99, 100] and turbo-switch [101, 102].

Of all these techniques, transient-XPM and turbo-switch are the two techniques that are simple to implement, robust and practical. In transient-XPM, the CW signal acts as a probe whereas the incoming data signal acts as the pump.

The OBPF at the SOA output is either blue-shifted [99] or red-shifted [27] w.r.t probe wavelength. This implies that, in the absence of data signal or “0” bit, the CW signal at the OBPF output gets suppressed. However when there is a “1” bit in the bit slot of data signal, it imposes a chirp on the CW signal and this chirped signal then passes through the offset output OBPF giving a corresponding “1” bit at the converted wavelength [100]. Indeed, error-free wavelength conversion at data rates as high as 320 Gbit/s have been demonstrated using this technique [99]. However, it is important to note that this technique does not help speed up the intrinsic response time of the SOA. Further, the maximum speed achievable from this technique depends on the intrinsic carrier lifetime of SOA [99] and the OSNR of the converted signal is severely degraded especially with the blue-shifted optical filtering [102]. Turbo-switch is an interesting technique which employs a cascade of two SOAs with an intermediate OBPF. The combination of the two slow SOAs mimics the response of one extremely fast SOA resulting in wavelength conversion at data rates upto 170 Gbit/s with appreciable OSNR [102]. However, it is important to note that even in this case the combined speed of this cascade strongly depends on the individual SOA carrier lifetime.

The second category involves utilization of trade-off between maximum nonlinear phase shift and the rate of phase recovery which in-turn is tied to carrier lifetime [93]. Since the gain-saturation induced nonlinear effects are extremely strong, maximum nonlinear phase shift achievable from these devices at moderate injection levels and input optical powers is typically  $5-7 \pi$  [90,97]. However the rate of recovery of this extremely large phase shift is limited by the carrier lifetime and is extremely slow. Typically,  $1-3 \pi$  nonlinear phase shift is required for most switching and wavelength conversion applications. It was, therefore, theorized that if by certain mechanism, the equilibrium device gain is reduced, the time required to recover to that value of equilibrium gain will also be reduced [72,95].

This trade-off was first investigated by injecting a CW light different from

the pump and the probe into the SOA. The absorption of this so called CW holding beam, which is fairly intense, generates new carriers which in-turn rapidly replenish the carriers depleted due to gain saturation caused by the relatively modest, time-dependent, incoming data stream. In this initial experiment both the holding beam wavelength and the data wavelength were within the SOA gain bandwidth [110] which had a serious drawback in that the holding beam and the incoming time-dependent data stream interact in a nonlinear fashion mediated by the carrier density  $N$ . However, in 2000, optical speed up at transparency (OSAT) was reported [103] and since then, the area of holding beam assisted recovery speed enhancement has seen a lot of activity [104–107]. Injecting assist beam at SOA transparency is advantageous because lower powers need to be injected, there is very little to no impact on device gain and consequently, moderate device injection levels can be maintained [103]. Other aspects of this configuration such as holding beam propagation configurations [105] and analysis of gain saturation and recovery dynamics in the presence of holding beam [107] have been investigated in detail. Further, considerable enhancement in the nonlinear effects in the presence of holding beam have been reported [111–113].

An alternative way of invoking this trade-off involves using the ASE within the SOA as a holding beam, to saturate its gain and to reduce its gain recovery time [40, 88, 90, 108, 109]. Such SOAs are now available commercially with a gain recovery time as short as 10 ps. They are designed carefully so that they can be driven at high drive currents (up to 500 mA for the device investigated in this thesis), and high ASE and short gain recovery times are realized only at these high operating currents [88, 108]. Since these devices are fairly recent, ASE-induced enhancement in nonlinear effects is a fairly unexplored area. A significant portion of this thesis is, therefore, devoted to studying ASE-enhanced SPM and FWM in modern SOAs.

It is important to note that the preceding discussion does not take into account

the fast intraband nonlinear effects in SOAs which respond at sub-picosecond time scales [70, 114]. Carrier heating, spectral hole burning and two-photon absorption are the nonlinear effects governing the ultrafast dynamics of the SOA. They are also responsible for highly non-degenerate FWM in SOAs [115]. In the strong pulse amplification case, ultrafast nonlinear refraction leading to fiber-like symmetric SPM has also been observed [116]. However, the associated nonlinear coefficient ( $n_2 = -2 \times 10^{-11} \text{cm}^2/\text{W}$ ) is about two orders of magnitude smaller than the nonlinear coefficient corresponding to gain saturation induced nonlinearities.

## 1.6 Vertical-Cavity Surface-Emitting Lasers

VCSELs are low cost light sources with amazing capabilities such as monolithic fabrication, ease of testing, low power consumption, capability for high speed at low drive currents and a nice circular output beam for easy coupling into optical fibers [117]. VCSELs were invented in 1979 with a vision that a laser with light output perpendicular to the gain medium could considerably ease the fabrication of a laser array [118]. The VCSELs spent the next decade or so in the laboratory where issues such as DBR design and reflectivity, current confinement, high threshold current and other issues related to device fabrication were ameliorated [119].

The first step towards translation of VCSELs from laboratory curiosities to commercial devices was taken in 1996 when a massive study regarding device reliability was published [120]. This was followed by inclusion of VCSELs as part of multimode fiber standard in the Gigabit Ethernet (GbE) and the Fiber Channel technologies [117]. This in-turn led to commercialization of GaAs-based 850 nm VCSELs for multimode transceivers [121]. Other applications that enhanced the popularity of short-wavelength VCSELs include future high-speed optical interconnects, high-performance computing and consumer electronics [121–125]. One

example of extremely popular consumer electronics application of commercial VCSELs is the increasingly popular, high-performance optical mouse. VCSELs are an ideal replacement for light emitting diodes in optical mice as a VCSEL driven mouse can operate on a wider range of surfaces, have higher resolution, and increased battery lifetime [121].

In the years subsequent to the commercialization of first 850 nm VCSEL, significant work had to be done to enhance both the data transmission rates and output optical power for devices operating in this wavelength regime [122, 126–131]. For example, a high differential gain has required the use of strained QWs by adding indium to the GaAs material. This causes a red shift of the gain peak, which in turn has to be compensated by increasing the Al content in the barrier layers and by reducing the QW width [126]. High speed operation of VCSELs is achieved by reducing the cavity photon lifetime [127], increasing the differential gain [122], and reducing the gain-compression coefficient by optimizing the separate-confinement heterostructure (SCH) for a short carrier capture time [128]. High-speed, oxide-confined VCSELs commonly employ multiple oxide layers [127] for reducing the oxide capacitance. Pad capacitance is reduced by using low-k dielectric material such as Benzo-Cyclo-Butene [129] or polyimide [130, 131]

Compared to their short-wavelength counterparts, the developments in the field of long-wavelength VCSELs has been much slower [132]. At the very minimum, development of any VCSEL needs high-gain material in the wavelength region of interest in combination with the cavity mirrors with high reflectivity, low optical absorption and high thermal conductivity [132]. Traditionally, for long-wavelength VCSELs, the optimum semiconductor materials have been: InP/InAlGaAs quantum wells for gain and GaAs/AlGaAs DBRs respectively [132]. However, InP and GaAs-based structures are incompatible from the standpoint of epitaxial growth, which makes the realization of long-wavelength VCSELs using all epitaxial growth virtually impossible. Attempts for developing long-wavelength

VCSELs have focused on finding solutions to the fabrication problem, improving current transport and reducing absorption losses in the DBRs [132–134]. Recent work on short-cavity buried tunnel junction VCSELs with dielectric top DBR and a hybrid bottom DBR has demonstrated significant improvement in device performance [135]. Single mode operation with upto 11  $\mu\text{m}$  active diameter and single mode powers in excess 6 mW have been demonstrated. These recent improvements make these devices very attractive for telecommunication applications. Further, these devices have recently shown promising results in fields trials pertaining to optical transport systems [136].

One of the major factors limiting the static [137] and dynamic performance [122, 127, 138] of both long and short-wavelength vertical-cavity devices is the current induced self-heating. Self-heating manifests itself as the premature saturation of the output power with increasing bias current, under CW operation. Subsequent saturation of the photon density in the active region limits VCSEL's modulation speed. The phenomena responsible for self-heating have received a great deal of attention, both experimentally [126, 129–131] as well as theoretically [126, 139–144]. Experimental studies on improving the thermally-limited dynamic performance have focused on reducing resistance [122, 129, 130, 133, 134], internal optical absorption [127, 134] and thermal impedance [131, 132]. Theoretical modeling of self-heating effects is a complex problem and involves taking into account various optical, electrical and thermal interactions for the specific VCSEL design under consideration [139, 143, 144].

Previously used thermal models either address the electrical aspects of self-heating effects through an equivalent electrical circuit [140] or employ a detailed physical model by incorporating spatial hole burning, carrier diffusion, and surface recombination [141]. Combined with the laser rate Eqs., the electrical circuit approach can predict dynamic VCSEL characteristics with appreciable accuracy. However, it uses higher order polynomials to describe the V-I characteristics, and



multiple measurements are required to extract values of all parameters associated with such a model. Moreover, it provides little insight into VCSEL design optimization for improving thermal performance. The model of Scott et. al. is important from the standpoint of physical understanding as it incorporates microscopic details of various relevant processes [141]. However, it requires the knowledge of a large number of parameters whose values may not precisely be known for a specific VCSEL, and it also needs to be modified depending on the current injection mechanism.

There is, therefore, a need for an empirical model which, when coupled with the data from basic measurements, can identify major heat sources and quantify their contributions to the total heat load and also relate them to the VCSEL design parameters. Such a model will be useful not only for predicting the thermal performance of a VCSEL, but also for providing design guidelines capable of enhancing the thermally limited device performance. An important contribution of this thesis is development of an empirical thermal model that can be used to study the thermal rollover mechanisms for both long and short-wavelength VCSELs. In particular, in this thesis, this thermal model is used to investigate self-heating effects in 850 nm, high-speed, oxide-confined VCSELs.

## 1.7 Footprint of Optical Signal Processing

In Section 1.1, the concept of footprint of optical transport systems was introduced. Here that concept is extended for assessment of power consumption of optical signal processing techniques. However, a slightly different metric is used than those previously used to estimate the footprint of optical transport systems [1,2]. Instead of applying the concept of energy/bit/km, the total electrical power consumption of a XPM-based WC using HNLF, SOA and a VCSEL as a nonlinear element is estimated. Figure 1.4 shows the generic schematic of such

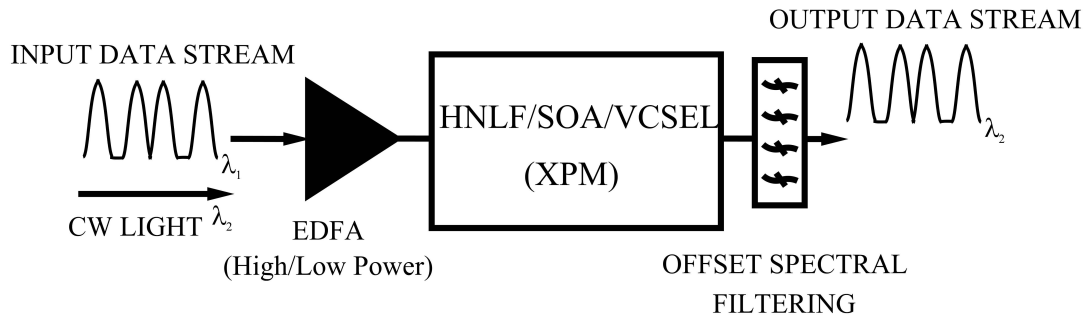


Figure 1.4: Schematic of a generic optical WC based on XPM.

a WC topology. As discussed in section 1.3, the XPM nonlinearity is used for the purposes of footprint comparison as it is the only nonlinear effect that can be employed for practical wavelength conversion using the three nonlinear devices studied in this thesis.

The EDFA shown in the Fig. 1.4 can either be a high power or a standard EDFA depending on the requirements placed on the input signal and the pump power. For the purposes of calculations shown here, it is assumed that for the input average power  $\leq 10$  dBm, standard EDFA is employed and if the average input power exceeds 10 dBm, then the high power EDFA is employed. For average powers below 0 dBm, EDFA deployment is assumed to be unnecessary. These assumptions are based on the fact that the current state of the art high power EDFAs rate 30–33 dBm saturation output power at 0 dBm input. The corresponding number for a typical low power device is 23 dBm at the same input level [145]. Further, power conversion efficiency for these devices, defined as the ratio of output optical power at signal wavelength to total electrical power supplied is 4% and 2% respectively [145]. It is further assumed that separate EDFAs are required for both CW and the data signal. There are other components such as polarization controllers, ASE noise rejection filters and isolators that are typically used in any WC topology [34]. For the purposes of calculations presented here, it is assumed

that only passive renderings of these components are used and hence there is no power consumption associated with them.

Considering the case of WC based on HNLF, the typical average input powers for signal and CW light are in excess of 33 and 15 dBm respectively [36]. Therefore for a HNLF-based WC, it can be assumed that one high power EDFA and one standard EDFA is required. The total electrical power dissipated in the implementation of such a WC exceeds 50 W. It is important to note that these calculations assume a typical silica-based HNLF with  $\gamma$  in the vicinity of 10–20  $\text{W}^{-1}\text{km}^{-1}$  and  $\alpha$  of the order of 0.5 dB/km. The requirements on input optical power and consequently the electrical power dissipated can vary quite a bit depending on the HNLF used as discussed in Section 1.4.

For a WC based on SOA which uses transient-XPM [27, 99, 100] discussed in Section 1.5, the typical average input powers for the signal and the CW light is in the vicinity of 10 dBm. Additional holding beam for gain recovery acceleration is not included [104–107]. Assuming that two low power EDFAs are used to amplify the input signal levels from 0 to 10 dBm, the total electrical power dissipated for amplification is  $\leq 1$  W. In the active nonlinear medium (SOA), there are two sources of power dissipation, one is across the device series resistance and the other is the power dissipated in the thermo-electric cooler (TEC). For a typical nonlinear SOA at typical bias currents [146], the power dissipated across series resistance is 0.3 W and the power dissipated in the TEC is 0.5 W. The total power dissipated in the nonlinear medium is 0.8 W. Therefore the total electrical power dissipated in implementing a WC based on SOA is  $\approx 2$  W. It is important to note that this is the upper bound on electrical power dissipation in WCs based on SOAs. With the advent of SOAs with high differential gain coefficient [89], input signal amplification for WCs based on these devices may not be required [99].

For WCs based on VCSEL or a VCSEA, input amplification is usually not required as nonlinear effects are observed at sub-mW power levels [147]. However,

Table 1.2: Comparison of Total Dissipated Power

Nonlinear Element	HNLF	SOA	VCSSOA
Total Power Dissipation (W)	$\geq 50$	$\approx 2$	$\approx 0.2$

optical pumping is routinely used to improve output saturation power [148, 149]. Further, VCSSOAs are biased below lasing threshold when used as a nonlinear element. Typical threshold current for 1550 nm vertical cavity devices is about 5 mA and the corresponding bias voltage is  $\approx 1$  V [133]. The total electrical power dissipated in implementing a WC based on VCSSOA is about 200 mW which includes the electrical power dissipated for 980 nm optical pumping. Table 1.2 summarizes the electrical power dissipation in WCs based on XPM in the three nonlinear elements. It can be seen that if the nonlinear element is switched from HNLF to SOA, there is more than one order-of-magnitude reduction in the total electrical power dissipation.

A switch from SOA to VCSEL or VCSSOA can potentially lead to a further one order-of-magnitude improvement in the electrical footprint. The goal of this thesis is to investigate various techniques by which total power consumption associated with optical signal processing in HNLFs and SOAs can be reduced. While VCSELs/VCSSOAs are extremely promising candidates for implementation of extremely low power consumption WCs, deleterious thermal effects in these devices need to be mitigated before they can be used for signal processing applications. To this end, this thesis develops an empirical thermal model that can be used to study self-heating effects in VCSELs.

## 1.8 Thesis Outline

The rest of the thesis is organized as follows: Chapter 2 takes a look at the performance optimization of 2R regenerators based on SPM-induced spectral broadening

followed by offset spectral filtering. This class of optical regenerators for on-off keying (OOK) signals has received a lot of attention in the literature but the impact of dispersion on its performance was not clearly understood. We propose a scaled parameter ( $\mathcal{S}$ ) which takes into account the dispersive and nonlinear effects in the MTR in a balanced manner and can be used to predict its performance. We further demonstrate that optimizing HNLF dispersion can reduce the input optical power required for 2R-regeneration.

Chapter 3 presents the theoretical framework that is used to study the nonlinear effects (SPM and FWM) in SOAs with ASE-enhanced gain recovery. The modified Eqs. for gain and phase are derived and are used to numerically investigate SPM and FWM in these devices. For the case of SPM, the impact of internal ASE on nonlinear phase shift and chirp are studied. The resulting impact on pulse shape and spectrum are also investigated. For the case of FWM, the impact of pump-probe detuning, pump power and the effective carrier lifetime on the CE is investigated.

Chapter 4 presents the experimental investigation of SPM in SOAs with ASE-enhanced gain recovery. To study pulse amplification in SOAs, gain switching of Multi Quantum-Well (MQW) DFB laser is used to produce optical pulses with the full width at half maximum of 57 ps at a wavelength of 1594.41 nm. We demonstrate that the experimental measurements agree quite well with the predictions from the numerical model reported in the previous section. We also experimentally study the trade-off between spectral broadening and spectral symmetry mediated by the internal ASE.

Chapter 5 deals with experimental optimization of ASE-Assisted FWM in SOAs. Simple device characterization results are presented followed by a detailed experimental investigation using CW pump and probe signals. The impact of drive current, pump-probe detuning, input pump and signal powers on FWM CE and OSNR is studied from the standpoint of optimizing them. The numerical

model for FWM presented in Section 3 is validated and sources of mismatch between experiments and numerical predictions are discussed. A proof of concept 10 Gb/s wavelength converter for L-Band, return-to-zero (RZ) OOK signals with 50% duty-cycle is also demonstrated.

Chapter 6 presents an empirical thermal model which together with experimental measurements, can be used for studying mechanisms contributing to thermal rollover in VCSELs. The model is based on extraction of the temperature dependence of threshold current, internal quantum efficiency, internal optical loss, series resistance and thermal impedance from measurements of output power, voltage and lasing wavelength as a function of bias current over an ambient temperature range of 15–100°C. This model is applied to a 850 nm oxide-confined VCSEL, fabricated with a 9  $\mu\text{m}$  inner-aperture diameter and optimized for high-speed operation. For this specific device, it is demonstrated that the power dissipation due to linear power dissipation (sum total of optical absorption, carrier thermalization, carrier leakage and spontaneous carrier recombination) exceeds power dissipation across the series resistance (quadratic power dissipation) at any ambient temperature and bias current. It is further demonstrated that the dominant contributors to self-heating for this particular VCSEL are quadratic power dissipation, internal optical loss, and carrier leakage. A rapid reduction of the internal quantum efficiency at high bias currents (resulting in high temperatures) is identified as being the major cause of thermal rollover. The proposed method is applicable to any VCSEL and is useful for identifying the mechanisms limiting the thermal performance of the device and for formulating the design strategies to ameliorate them.

In Chapter 7, this thesis explores the impact of VCSEL design parameters such as inner-aperture diameter and photon lifetime on the thermal rollover mechanisms of 850 nm VCSELs designed for high-speed operation. Using the empirical thermal model presented in Chapter 6, the evolution of power dissipated due to

optical absorption, carrier thermalization, carrier leakage, spontaneous carrier recombination and power dissipated across the series resistance with bias current for four different 850 nm VCSEL designs is calculated. This in-turn demonstrates the universal validity of the proposed numerical model. A trade-off between power dissipated due to optical absorption and carrier leakage is demonstrated in that over compensating for optical absorption can enhance carrier leakage and vice-versa. It was further demonstrated that the carrier leakage places the ultimate limit on the thermal performance for this entire class of devices. The analysis presented in this chapter yields useful design optimization strategies for mitigating the impact of carrier leakage thereby enhancing the performance of 850 nm, high-speed VCSELs.

Chapter 8 summarizes the main results and conclusions of the work presented in this thesis. Possible avenues for extending the work presented in this thesis are also discussed.

Appendix A provides a brief overview of the Optiwave Optisystem 6.0 software. This commercial software was used for numerical simulation of the MTR. This tutorial will focus on the capabilities of this software as applied to the research presented in Chapter 2. Appendix B provides a brief tutorial on gain-switching in semiconductor lasers. A brief theoretical background together with experimental optimization of gain-switched pulses is presented. Finally, Appendix C presents the experimental setup for generation and optimization of 10 Gb/s non-return-to-zero (NRZ) and RZ OOK signals used in 10 Gb/s L-Band wavelength conversion experiments.

## 2 Dispersion Optimization in 2R Regenerators

### 2.1 Introduction

In section 1.2, the 2R regenerator based on SPM-induced spectral broadening, followed by spectrally offset filtering, also known as the MTR, was briefly introduced. While the basic topology of this device is quite simple, leveraging this simple topology to achieve practical all-optical signal regeneration involves optimization of various parameters associated with this device. There have been several studies that have focused on the optimization of SPM-based 2R regenerator parameters. For example, optimization on the basis of soliton number [17], followed by the proof of principle experiment, demonstrated the dependence of the Q-factor improvement on input parameters such as the peak input power, fiber dispersion and pulse width. Numerical simulations for MTRs have been used to deduce scaling rules [18] and to show how its performance depends on the device and signal parameters [19].

In spite of these studies, much less attention has been paid to the role played by the HNLF dispersion in optimizing the regenerator performance. It has been commented that fiber dispersion affects the launched input power needed for optimum regeneration [17]. It has also been claimed that high normal dispersion



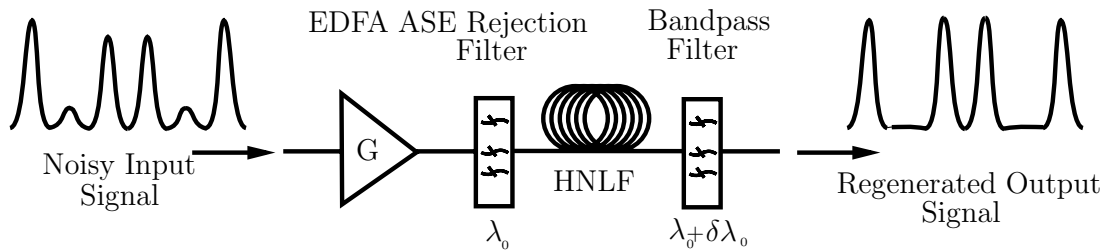


Figure 2.1: Components of an MTR. Noise in the output signal is reduced when the signal spectrum, broadened nonlinearly inside the HNLF, is filtered by an OBPF that is spectrally offset by  $\delta\lambda_0$ .

of the HNLF improves the regenerative capability of an MTR [22]. In another study [20], spectral offset of the output OBPF for a given value of pulse width has been optimized as function of the accumulated dispersion and maximum nonlinear phase shift. However none of the studies have focussed on optimization of HNLF dispersion and the resulting impact on MTR performance.

In this chapter, the results from numerical investigation into the role of HNLF dispersion in optimizing the performance of an MTR are presented. In particular, it is demonstrated how the magnitude of fiber dispersion affects the shape of transfer function and the operating point of an MTR. Based on this numerical work, some design rules that should prove useful in reducing the input power required for 2R regeneration are proposed.

## 2.2 Details of the Numerical Scheme

The schematic of a single-stage MTR, first proposed in [13], is shown in Fig. 2.1. It employs a high power EDFA to boost the peak power of the incoming noisy signal to the power level (denoted by  $P_0$ ) that is high enough to cause spectral broadening through SPM. The amplified signal is first passed through an ASE rejection filter that rejects the out-of-band ASE noise added by the high power

EDFA. The ASE filter is centered at the signal wavelength ( $\lambda_0$ ). The bandwidth of the filter is chosen to be wider than the signal bandwidth [16]. The filtered signal is then injected into the HNLF where it experiences SPM and its spectrum broadens considerably. The HNLF is characterized by its length  $L$ , loss  $\alpha$ , dispersion  $D$ , and the nonlinear parameter  $\gamma$ . The OBPF placed after the HNLF is offset from the signal wavelength  $\lambda_0$  by a certain amount  $\delta\lambda_0$  so that it lets pass only a slice of the signal spectrum. The bandwidth of the output OBPF sets the output pulse width and needs to be optimized in practice. The filtered signal is a cleaned up version of the input with reduced noise, but it is offset from the original wavelength by an amount  $\delta\lambda_0$ .

The propagation of the optical signal through the HNLF is governed by the well-known nonlinear schrödinger Eq. [34]:

$$\frac{\partial A(z, t)}{\partial z} + \frac{i\beta_2}{2} \frac{\partial^2 A(z, t)}{\partial t^2} = i\gamma |A(z, t)|^2 A(z, t) - \frac{\alpha}{2} A(z, t), \quad (2.1)$$

where  $A(z, t)$  is the complex amplitude of the optical signal,  $\beta_2$  is the second order dispersion parameter,  $\gamma$  is the nonlinear coefficient and  $\alpha$  is the fiber propagation loss. In the absence of the dispersive effects, Eq. (2.1) can be solved analytically. The result shows that the optical power,  $|A(z, t)|^2$ , decays as  $\exp(-\alpha z)$  because of propagation losses, while the nonlinear phase shift induced by SPM is given by [4]:

$$\phi(L, t) = \gamma \int_0^L |A(z, t)|^2 dz. \quad (2.2)$$

A parameter that plays a crucial role for the MTR operation is the maximum nonlinear phase shift,  $\phi_0$ , occurring at the center of the pulse where the optical power is at its maximum. This parameter is defined in Eq. (1.2) and governs the extent of spectral broadening experienced by the optical signal inside the HNLF. In the presence of dispersive effects, the spectral broadening inside HNLF depends both on the nonlinear and dispersion parameters. Since Eq. (1.5) cannot be solved analytically in this case, it is numerically solved using the well known split-step

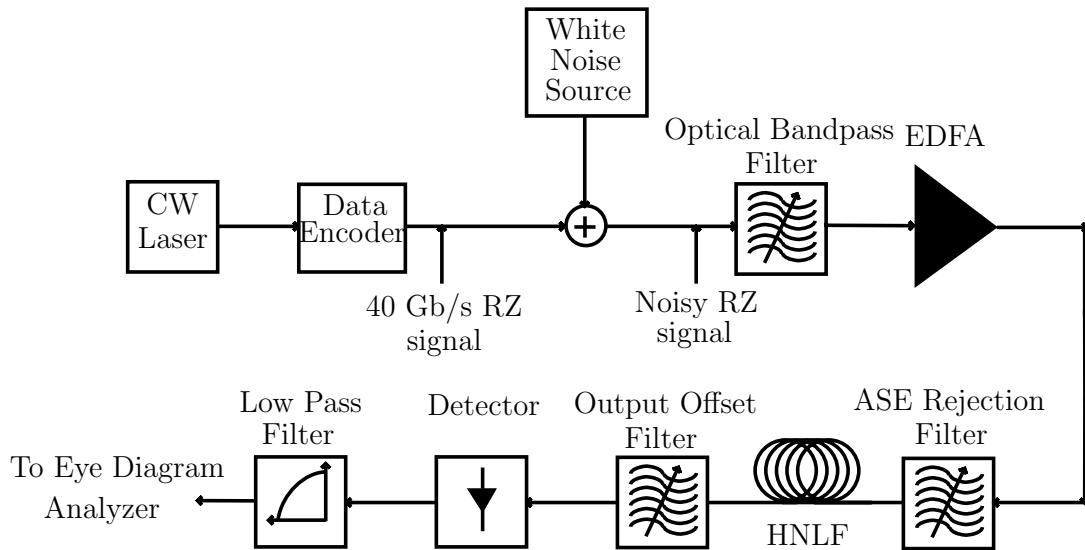


Figure 2.2: Setup used for simulating numerically the operation of an MTR.

fourier method [4]. The nonlinear phase rotation method [150] is used for the required step size estimation.

The numerical simulations in this chapter are carried out for a 40 Gb/s signal, in the form of a RZ-OOK bit stream, with the OptiSystem software (supplied by Optiwave). An overview and a brief tutorial for this commercial software and its capabilities is provided in Appendix A. Figure 2.2 shows the block diagram used for numerical simulations. The CW laser and the data encoder create the data in the form of a pseudo-random bit sequence (PRBS) consisting of 64 bits. Each “1” bit contains a Gaussian pulse with a full-width at half maximum (FWHM) of 7.5 ps (a 30% duty cycle) at a carrier wavelength of 1550 nm. A white noise source adds broadband noise to the incoming RZ signal to simulate the degradation of the Q-factor associated with the bit stream. This approach is similar to that used in [16]. The bandwidth of the input OBPF is adjusted to achieve the desired Q-factor degradation. This filter is a fourth order super gaussian filter with a bandwidth of 1.33 nm. The EDFA NF is 5.5 dB. The ASE rejection filter shown in Fig. 2.2 is identical to the OBPF used before the EDFA and its role is to

Table 2.1: HNLF Parameters for the Three MTR Configurations Analyzed for Demonstration of the Scaling Rule

MTRs	L (m)	$\gamma$ (W <sup>-1</sup> /km)	$\alpha$ (dB/km)	D (ps/nm/km)
MTR 1	1500	5	1	-2
MTR 2	150	50	10	-20
MTR 3	15	500	100	-200

suppress the ASE noise over the passband of the output OBPF [16]. The output OBPF selects a part of optical spectrum at the HNLF output. It is chosen to be a first-order Bessel filter with a spectral width of 0.47 nm and a spectral offset of 0.6 nm. The filtered optical bit stream is converted into an electrical bit stream using a detector, followed with a low-pass electrical Bessel filter with a cut off frequency of 30 GHz. The resulting electrical signal is used to calculate the Q-factor of the regenerated optical bit-stream.

## 2.3 Role of Dispersion and the Resulting Scaling Rule

In this section, the performance of an MTR is analyzed by considering the interplay between the dispersive and nonlinear effects taking place simultaneously inside the HNLF. Further, a simple design scaling rule is deduced. In practice, as discussed in the previous section, the HNLF length can vary from a few meters to a few kilometers, depending on the fiber design and material used to fabricate the HNLF. In particular, the required length is much smaller for non-silica glass and/or micro-structured fibers because the nonlinear parameter  $\gamma$  is much larger

for them (Chapter 1). With this in mind, three different types of HNLFs with the parameter values listed in Table 2.1 are considered.

The choice of fiber parameters for the three HNLFs requires some thought. Through extensive simulations, it was discovered that the combined effects of dispersion and nonlinearity on the MTR performance depend on the ratio between accumulated dispersion and maximum nonlinear phase shift defined as  $\mathcal{S} = |DL|/\phi_0$ , or

$$\mathcal{S} = \frac{|DL|}{\gamma P_0 L_{\text{eff}}}, \quad (2.3)$$

For this reason, the HNLF dispersion  $D$ , nonlinear parameter  $\gamma$ , length  $L$  and propagation loss  $\alpha$ , in Table 2.1 are scaled by the same factor such that the product  $DL$  and  $\phi_0$ , given by Eq. (1.2), remain the same for all the three fibers at a fixed value of the peak power  $P_0$ . For the three HNLFs, the new scaling ratio has a value of  $\mathcal{S} \approx 0.46$  ps/km when  $P_0 = 1$  W and scales inversely with  $P_0$ .

To demonstrate the effectiveness of the proposed scaling rule, the performance of the three MTRs listed in Table 2.1 has been analyzed by varying the average input power  $P_{\text{in}}$  of the 40 Gb/s bit stream from 0 to 500 mW. The corresponding peak power  $P_0$  of the 7.5 ps Gaussian input pulses was varied between 0 to 3 W. The amount of noise added by the white noise source was controlled to set the input value  $Q_{\text{in}}$  of the Q-factor to 13. For each value of  $P_{\text{in}}$ , the average output power  $P_{\text{out}}$  at the output of the MTR is obtained and also the output Q-factor is calculated. The improvement in the Q-factor is quantified by the ratio:

$$\Delta Q = 10 \log(Q_{\text{out}}/Q_{\text{in}}). \quad (2.4)$$

Figure 2.3(a) shows  $\Delta Q$  as a function of  $P_{\text{in}}$  for the three MTRs listed in Table 2.1. The power transfer functions for the three MTRs are shown in Fig. 2.3(b). In each case, the three curves almost coincide and cannot be distinguished from each other, indicating that the three MTRs behave in an identical manner in

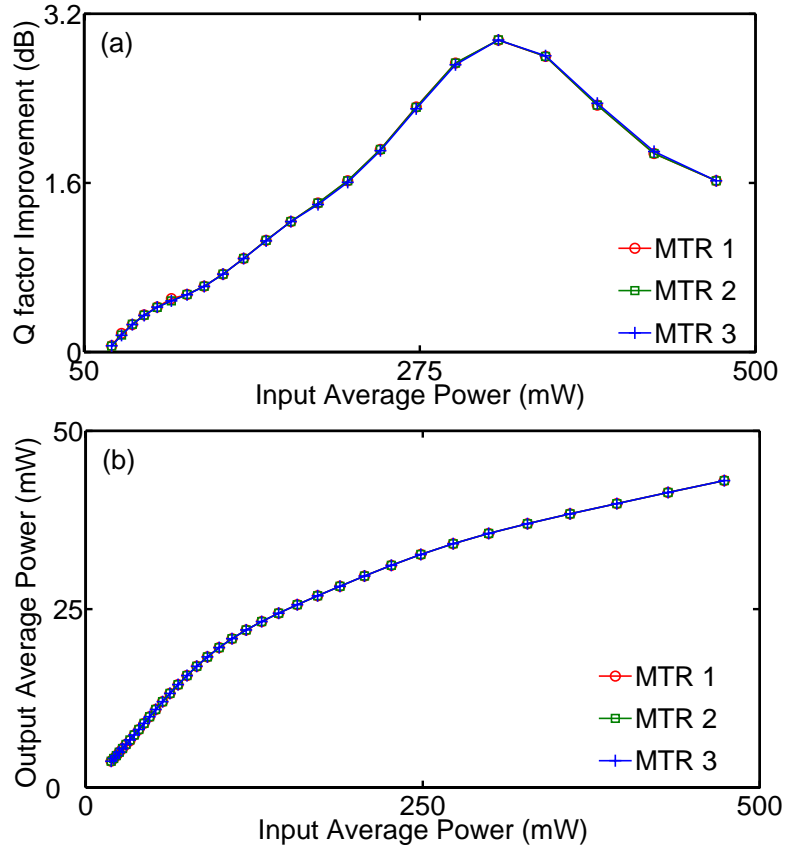


Figure 2.3: (a) Improvement in the Q-factor as a function of average input power  $P_{\text{in}}$  and (b) the corresponding transfer function for three MTRs listed in Table 2.1.

spite of very different HNLFs used inside them. These results provide support for the claim that the ratio between accumulated dispersion and maximum nonlinear phase shift defined by  $\mathcal{S}$  introduced in Eq. (2.3) sets the performance of an MTR because it accounts for the interplay between the dispersive and nonlinear effects in a balanced manner. Figure 2.3(a) shows that the maximum improvement in the Q-factor occurs for an optimum value of  $P_{\text{in}}$  close to 320 mW (or an input peak power  $P_0$  close to 2 W). The maximum nonlinear phase shift for this value is  $\phi_0 \approx 13$  and exceeds  $4\pi$ . Although, in the absence of dispersion,  $\phi_0$  values of  $< 2\pi$  are sufficient to operate an MTR, much larger values are needed when dispersive effects are included. The extent of noise reduction realized at the optimum input

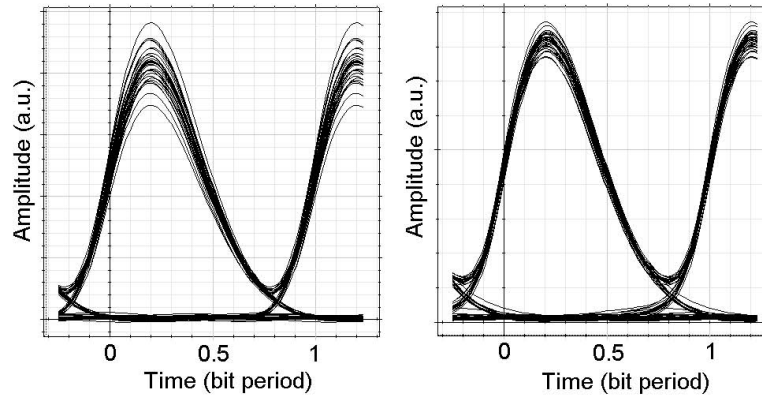


Figure 2.4: Input and output eye diagrams for the 40 Gb/s RZ bit stream at the power level corresponding to the peak in Fig. 2.3(a).

power level of 320 mW is evident from Fig. 2.4 where the input and output eye diagrams for the 40 Gb/s RZ-OOK signals are shown.

One may wonder how sensitive the scaling rule proposed in this chapter is to the deviations in the parameter values from those used for Fig. 2.3. It turns out that the scaling rule is quite robust to such variations. As an example, Fig. 2.5(a) shows  $\Delta Q$  as a function of  $Q_{\text{in}}$  for the three MTRs listed in Table 2.1. Even though  $\Delta Q$  varies considerably with  $Q_{\text{in}}$ , the three curves again coincide, indicating that the three MTRs behave identically. A rapid decrease in  $\Delta Q$  for  $Q_{\text{in}}$  values below 6 shows that an MTR becomes less effective if the input bit stream becomes too degraded. A similar behavior has been observed in earlier studies [19].

Next question is how much the performance of a regenerator changes when  $D$  deviates from its value listed in Table 2.1. The magnitude of the relative change in the  $D$  parameter is quantified by a dimensionless ratio defined as:

$$\delta = (D' - D)/D. \quad (2.5)$$

where  $D'$  is the modified value of  $D$ . Figure 2.5(b) shows how  $\Delta Q$  varies with  $\delta$  in the range  $-0.5 < \delta < 0.5$ . The input average power was kept fixed at 320 mW, a value that corresponds to the peak in Fig. 2.3(a). As one may expect,  $\Delta Q$  changes

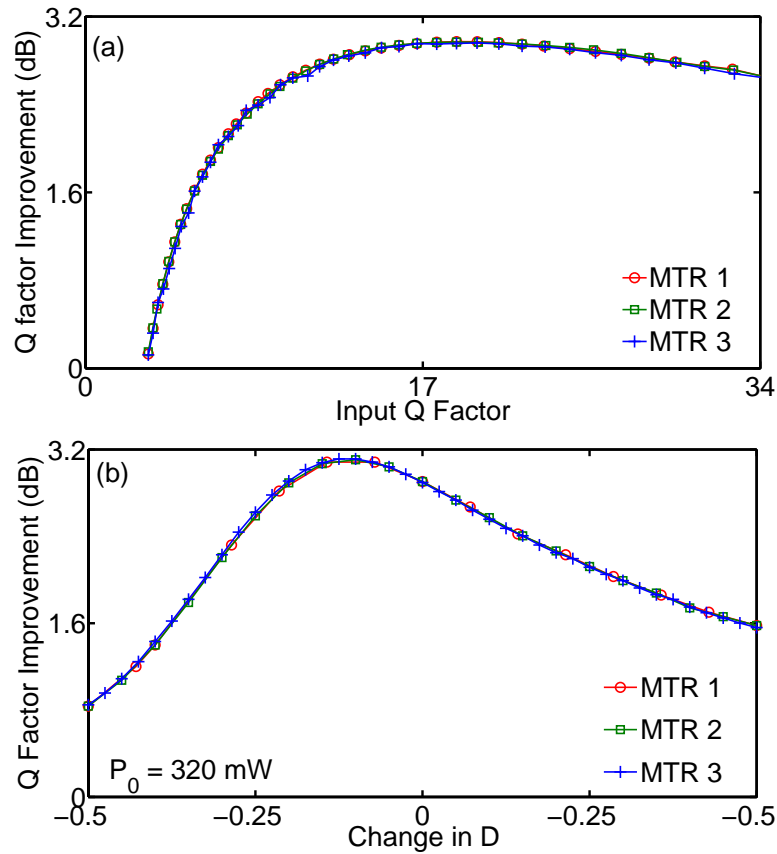


Figure 2.5: Improvement in the Q-factor (a) as a function of  $Q_{in}$  and (b) as a function of  $\delta$  for three MTRs listed in Table 2.1.

when the dispersion of the HNLFF deviates from its original value. However, it was found that the Q-factor can be improved even beyond the peak value seen in Fig. 2.3(a) if the dispersion is lowered by about 10% compared to the values of  $D$  listed in Table 2.1. It appears that there exists an optimum value of  $D$  for a given value of the nonlinear parameter associated with the HNLFF. Note also that the three curves again coincide in Fig. 2.5(b), indicating that the scaling rule works even when  $D$  changes. The reason is because a change in the value of  $D$  just amounts to changing the value of the scaled parameter  $\mathcal{S}$  when all the other parameters are kept fixed.



Table 2.2: Parameters for the Four MTR Configurations with Different HNLFs

MTRs	D (ps/nm/km)	$\delta\lambda_o$ (nm)	Optimum $P_0$ (W)	$\mathcal{S}$ (ps/nm)
MTR 4	-12	0.61	3.0	0.206
MTR 5	-6	0.61	2.1	0.160
MTR 6	-4	0.37	1.2	0.171
MTR 7	-2	0.37	1.1	0.0935

## 2.4 Impact of Large Dispersion Variations

A design question that must be asked is how important is the role of dispersion in realizing optimum performance of an MTR. As mentioned earlier, it has been claimed that high normal dispersion of the HNLF improves the regenerative capability of an MTR [22], but this claim is based on the use of a short length HNLF with a relatively high value of  $\gamma$ . With the introduction of the scaling parameter  $\mathcal{S}$ , it is evident that large  $D$  is required for fibers with high  $\gamma$  to maintain the same value of  $\mathcal{S}$ . The question then arises: What is the optimum value of  $\mathcal{S}$  for an MTR? This question is answered by considering MTRs with different values of  $\mathcal{S}$  and evaluating numerically their relative regenerative capabilities.

Table 2.2 summarizes the parameter values for four different MTRs that are employed for this purpose. In particular, the values of the nonlinear parameter ( $\gamma = 20 \text{ W}^{-1}/\text{km}$ ), fiber propagation loss ( $\alpha = 1 \text{ dB}/\text{km}$ ), and the fiber length ( $L = 250 \text{ m}$ ) are kept constant but  $D$  is varied from  $-2$  to  $-12 \text{ ps}/\text{nm}/\text{km}$ . The value of  $Q_{\text{in}}$  is set at 13 for the results discussed in this section. The wavelength

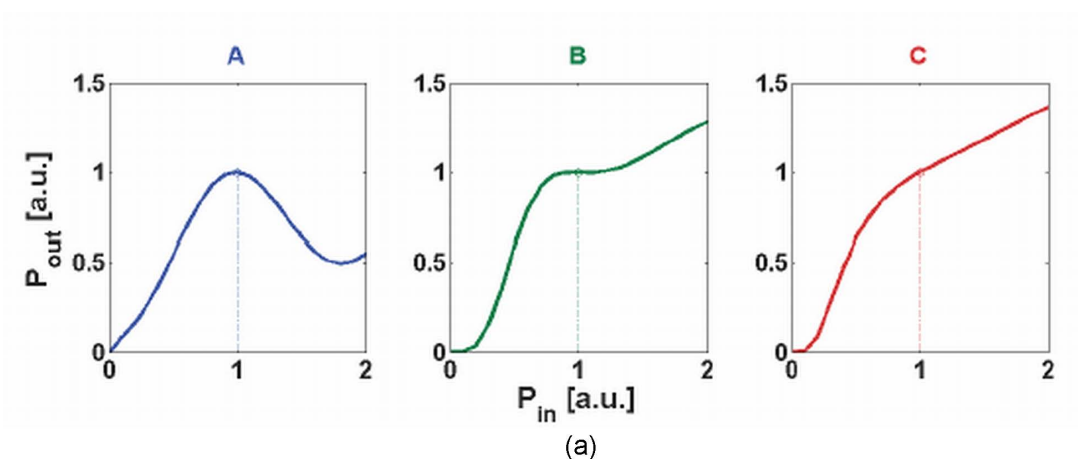


Figure 2.6: Characteristic power transfer function shapes of a MTR [18]

offset for the output filter was optimized for each configuration and its optimum value is listed in Table 2.2.

Authors of [18] have employed the shape of the power transfer function as a predictive measure of the regenerative capacity of an MTR. In particular, they classify different MTRs as type A, B or C depending on whether the output power evolves with the input power in a non-monotonic, locally flat, or monotonic fashion, respectively. These shapes are demonstrated in Fig. 2.6. Among these, type B is found to be the most effective as it tends to equalize the peak power of various “1” bits. Figure 2.7(a) displays the power transfer functions for the four MTRs listed in Table 2.2. From the shape of the curves, it can be concluded that MTR 4 with  $D = -12$  ps/nm/km is of type C, while the other three have a locally flat region and are type B. However, these curves do not provide sufficient guidance to let one decide which MTR is the best among the last three, and at what input power level each one should be operated. To answer these questions, the extent of noise reduction through the improvement in the Q-factor has to be considered.

Figure 2.7(b) shows the extent of the Q-factor improvement ( $\Delta Q$ ) as a function

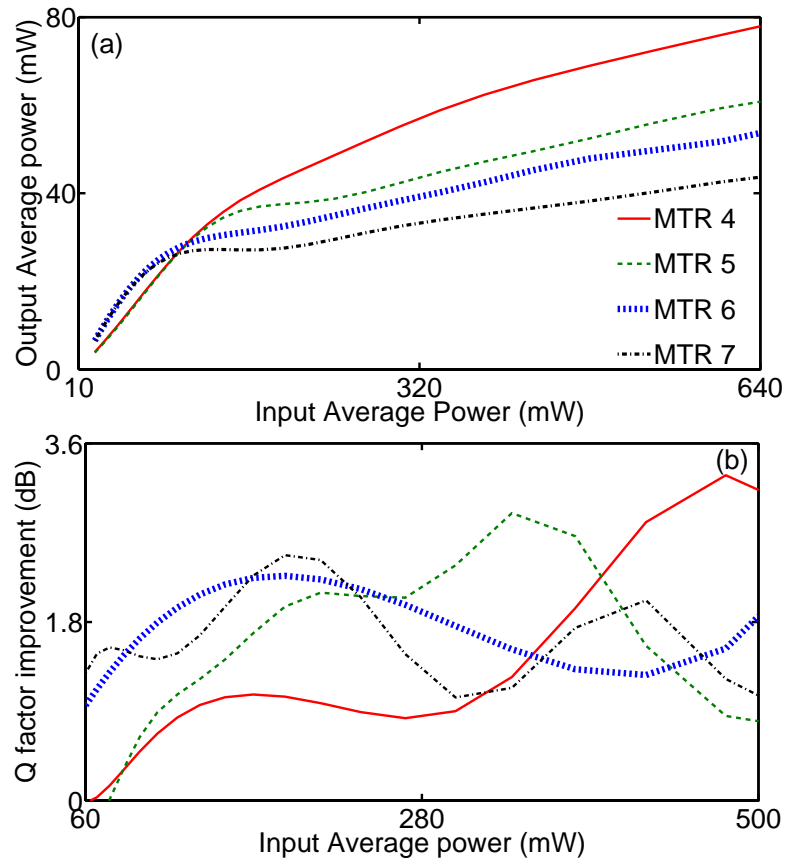


Figure 2.7: (a) Power transfer functions, (b)  $\Delta Q$  as a function of average input power for the four MTRs listed in Table 2.2.

of average input power  $P_{in}$  for the four MTRs listed in Table 2.2. In each case,  $\Delta Q$  peaks at a certain input power, indicating that the noise reduction is largest at that power; these values and the resulting values of the scaling parameter  $\mathcal{S}$  are listed in Table 2.2. Since the peak value of  $\Delta Q$  is different for different MTRs, it provides some guidance in picking the best configuration. Another practical matter that is often relevant must be considered. In practice, it is desirable that an MTR works at relatively low power levels over as wide range of input powers as possible. The operating range of an MTR is defined as the range of  $P_{in}$  for which  $\Delta Q$  exceeds 2 dB. As seen in Fig. 2.7(b), the required input power is reduced with decreasing  $D$ , but the working range of MTR is also reduced. Thus, a lower

value of  $D$  allows one to operate at a lower power level, but only at the expense of a reduced operating range and reduced performance because  $\Delta Q$  is also lowered. In contrast, a higher value of  $D$  provides a larger value of  $\Delta Q$  and wider operating range, but the required input power is also considerably larger. Clearly, a trade-off exists between the HNLF dispersion, regenerator performance and the average input power required for signal-regeneration. If input power level is not of much concern, HNLFs with large dispersion provide the best performance. However, comparing MTR configurations 4 and 5, it can be seen that through careful dispersion optimization, a significant reduction (upto 30%) in input optical power required for optimum signal regeneration can be achieved without significantly altering the MTR performance.

The sensitivity of the preceding conclusion to deviations in the parameter values from those used for Fig. 2.7 is of interest and hence is also investigated. Figure 2.8(a) shows  $\Delta Q$  as a function of  $Q_{\text{in}}$  for the the four MTRs listed in Table 2.2. Even though  $\Delta Q$  varies considerably with  $Q_{\text{in}}$ , the four curves display similar qualitative features. In particular, a rapid decrease in  $\Delta Q$  for  $Q_{\text{in}}$  values below 6 shows that an MTR becomes less effective if the input bit stream becomes too degraded. It should be noticed again that the MTR with the largest value of  $D$  displays the best performance over a wider range of  $Q_{\text{in}}$ . Finally, Fig. 2.8(b) shows the improvement in the Q-factor as a function of variations in the  $D$  value from the value listed in Table 2.2. The most noteworthy feature of this Fig. is that MTRs with smaller values of  $D$  are much more tolerant to variations in the value of the dispersion parameter. This could be attributed to the fact that the value of  $\mathcal{S}$  is lower for MTRs with lower values of  $D$  (see Table 2.2). Note that the nonlinear phase shift due to SPM and the extent of spectral broadening is also reduced in this case because of the reduced input power at the operating point.

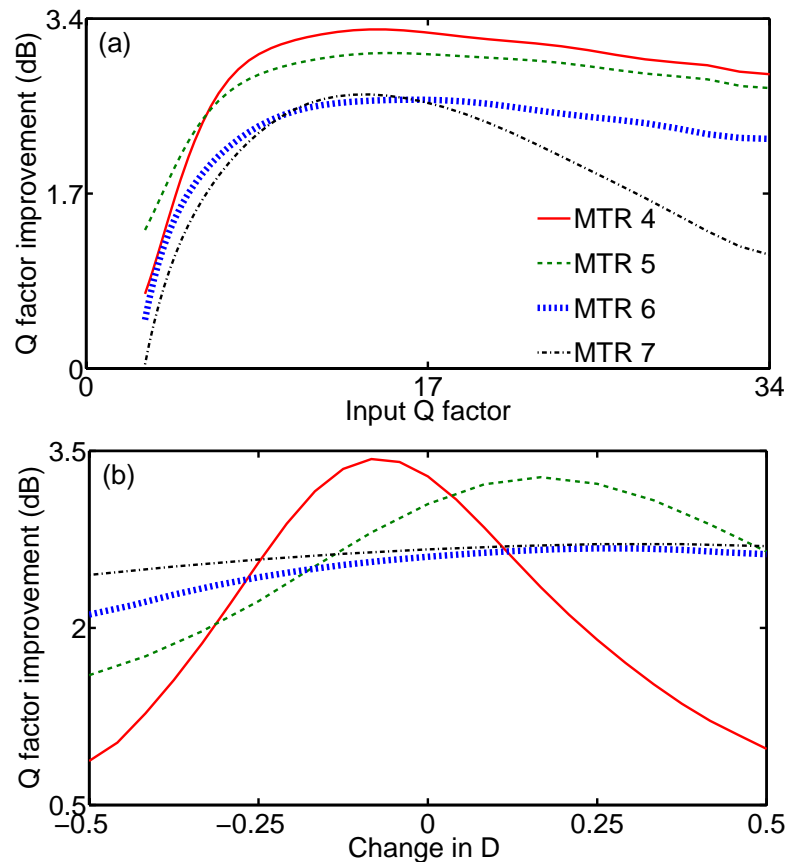


Figure 2.8: Improvement in the Q-factor (a) as a function of  $Q_{in}$  and (b) as a function of  $\delta$  for the four MTRs listed in Table 2.2. The peak powers correspond to optimum  $P_0$  in Table 2.2.

## 2.5 Conclusions

In this chapter, numerical investigation into the role of fiber dispersion in improving the regenerative capability of an MTR operating at 40 Gb/s is presented. This investigation was carried out by studying several different MTR configurations. The focus of this work was on studying the impact of interplay between the dispersive and nonlinear effects that occur simultaneously inside the HNLF used to make the MTR. By considering the extent of improvement in the Q-factor (related to level of noise reduction in the 40 Gb/s RZ-OOK bit stream), it was

concluded that a single scaled parameter  $\mathcal{S}$ , defined in Eq. (2.3) and representing the ratio of accumulated dispersion to the maximum nonlinear phase shift, can be used to predict the performance of MTRs making use of fibers with very different lengths, dispersion, and nonlinear parameters.

Optimization of the value of this scaling parameter was carried out by varying the dispersion over a wide range of values for a 250 m long fiber while keeping the HNLFFOM ( $\gamma L_{\text{eff}}$ ) constant. The simulation results demonstrate that the fiber dispersion plays an important role and needs to be optimized in practice. In general, MTRs with larger fiber dispersion perform better but require higher input powers. Careful optimization of the HNLFF dispersion can reduce the input peak powers by upto 30 % without significant degradation of MTR performance. The impact of fluctuations in dispersion from their nominal value was investigated and it was found that their impact is much less severe for MTRs designed to operate at a smaller value of  $\mathcal{S}$ .

# 3 Theoretical Framework for Fast Carrier-Lifetime SOAs

## 3.1 Theoretical Framework

In this section, a simple yet physically accurate numerical model is developed to study the effects of high internal ASE on the nonlinear effects in SOAs. The experimental verification of the simulation results discussed in this chapter will be presented in the subsequent chapters.

### 3.1.1 Propagation of Optical Fields in SOAs

When an optical signal is launched into a SOA, its amplitude and phase change because of the gain provided by the SOA and the associated changes in the refractive index. To describe this process, the model developed in Ref. [93] is adopted and the signal's electric field is written in the form:

$$\mathbf{E}(\mathbf{r}, t) = \text{Re}[\hat{x}F(x, y)A(z, t)e^{i(\beta_0 z - \omega_0 t)}], \quad (3.1)$$

where  $\hat{x}$  is the polarization unit vector,  $F(x, y)$  is the transverse optical mode distribution,  $A(z, t)$  is the complex amplitude,  $\omega_0$  is angular carrier frequency, and  $\beta_0 = \bar{n}\omega_0/c$  is the propagation constant of the optical mode with the effective index  $\bar{n}$ , and  $c$  is the speed of light in vacuum.

As discussed in Ref. [93], the signal amplitude evolves inside the SOA as:

$$\frac{\partial A}{\partial z} + \frac{1}{v_g} \frac{\partial A}{\partial t} = \frac{g(z, t)}{2} (1 - i\alpha) A, \quad (3.2)$$

where  $v_g$  is the group velocity,  $g(z, t)$  is the SOA gain, and  $\alpha$  is the linewidth enhancement factor responsible for changes in the mode index with changes in the carrier density. The temporal evolution of carrier density satisfies a rate equation of the form [94]:

$$\frac{\partial N}{\partial t} = \frac{I}{qV} - \frac{N}{\tau_c} - \frac{g(N)}{\hbar\omega_0} |A|^2, \quad (3.3)$$

where  $V$  is the active volume and  $\tau_c$  is the carrier lifetime. The injection of current into an SOA creates electrons and holes, the density  $N$  of which provides optical gain as  $g(z, t) = \Gamma a(N - N_0)$ , where  $\Gamma$  is the mode confinement factor,  $a$  is a material parameter (referred to as the gain cross section), and  $N_0$  is the value of carrier density at which the SOA becomes transparent. The rate Eq. (3.3) can be used to obtain the following Eq. for the optical gain  $g(z, t)$  [93]:

$$\frac{\partial g}{\partial t} = \frac{g_0 - g}{\tau_c} - \frac{g|A|^2}{E_{\text{sat}}}, \quad (3.4)$$

where  $E_{\text{sat}} = \hbar\omega_0\sigma/a$  is the saturation energy,  $\sigma$  is the mode cross section, and the unsaturated gain  $g_0$  depends on the injected current  $I$  as:

$$g_0(I) = \Gamma a N_0 (I/I_0 - 1), \quad (3.5)$$

where  $I_0 = qVN_0/\tau_{c0}$  is the current required for transparency and  $\tau_{c0}$  is the carrier lifetime at  $N = N_0$ .

### 3.1.2 Approximate Model for ASE

In modern SOAs designed for ultrafast gain recovery, ASE becomes large enough at high injection currents that it can itself saturate the SOA gain, and the Eqs.



governing the propagation of optical fields in an SOA should be adapted to incorporate the effects of ASE. A general theory should consider the amplification of the spontaneous emission in both the forward and the backward directions over the entire SOA gain bandwidth. Because of the stochastic nature of ASE, such a theory is quite complicated. For the purpose of studying the nonlinear effects in these devices, a simple approach is adopted by ignoring the random nature of the amplified signal and treat  $A(z, t)$  as the average signal amplitude. However, the ASE induced gain saturation is taken into account by replacing  $|A|^2$  in Eq. (3.4) with  $|A|^2 + P_{\text{ASE}}$ , where  $P_{\text{ASE}} = P_{\text{f}} + P_{\text{b}}$  represents the sum of ASE powers in the forward and backward directions. The resulting modified gain Eq. can be written as:

$$\frac{\partial g}{\partial t} = \frac{g_0 - g}{\tau_c} - \frac{g(|A|^2 + P_{\text{ASE}})}{E_{\text{sat}}}. \quad (3.6)$$

Even though  $P_{\text{f}}$  and  $P_{\text{b}}$  change considerably along the SOA length because of exponential amplification of spontaneous emission, their sum is relatively constant. The following analysis is simplified by treating  $P_{\text{ASE}}$  as a constant whose value depends only on the current  $I$  injected into the SOA.

The total ASE power can be quantified by studying the amplification of CW optical fields in the SOA. For the case of CW signal injected in the SOA, it is assumed that the input power  $P_{\text{in}}$  is injected into the device. Using  $A(z) = \sqrt{P}e^{i\phi}$  in Eq. 3.2, the CW signal power,  $P$ , and phase,  $\phi$  satisfy:

$$\frac{dP}{dz} = g(z)P, \quad \frac{d\phi}{dz} = -\frac{\alpha}{2}g(z). \quad (3.7)$$

Setting the time derivative to zero in Eq. (3.6), the signal power  $P(z)$  is found to depend on  $P_{\text{ASE}}$  as:

$$\frac{dP}{dz} = \frac{g_0(I)P}{1 + (P + P_{\text{ASE}})/P_{\text{sat}}}, \quad (3.8)$$

where the saturation power  $P_{\text{sat}}$  is defined as [93]:

$$P_{\text{sat}} = \frac{E_{\text{sat}}}{\tau_c} = \frac{\hbar\omega_0\sigma}{a\tau_c}. \quad (3.9)$$

Table 3.1: Manufacturer's Optical Specifications of the SOA at 500 mA

Parameter	Value
Small signal gain	30 dB
Saturated output power	12.5 dBm
Wavelength of the gain peak	1570 nm
Saturated gain recovery time (1/e)	10 ps
3-dB bandwidth of the gain spectrum	35 nm

In the small-signal regime, SOA gain is saturated only by  $P_{\text{ASE}}$ . Equation (3.8) can then be integrated easily to obtain  $G(I) = P_{\text{out}}/P_{\text{in}}$ , where  $P_{\text{out}} = P(L)$  and  $L$  is the SOA length. The final result is given by:

$$G(I) = \exp\left(\frac{g_0(I)L}{1 + P_{\text{ASE}}/P_{\text{sat}}}\right), \quad (3.10)$$

where both  $P_{\text{ASE}}(N)$  and  $P_{\text{sat}}(N)$  also depend on  $I$  because the carrier density  $N$  changes with  $I$ . The expression for the CW amplification factor  $G(I)$  [Eq. (3.10)] is fitted to the measurements to extract the variation of  $P_{\text{ASE}}$  with drive current. This process, applied to the highly nonlinear SOA used in the experimental work presented in this thesis, is described next.

### 3.1.3 CW Small Signal Gain Measurements

Figure 3.1(a) shows the experimental setup used for measuring the small signal gain of a weak CW signal as a function of drive current using a commercial SOA (CIP [Center for Integrated Photonics] Technologies, model SOA-XN-OEC-1550). Table 3.1 shows the manufacturer's specifications of this SOA used when it amplifies a 1550 nm signal at 500 mA drive current. A 1594.4 nm signal with 2  $\mu\text{W}$  power was launched to ensure that it does not saturate the SOA. The power

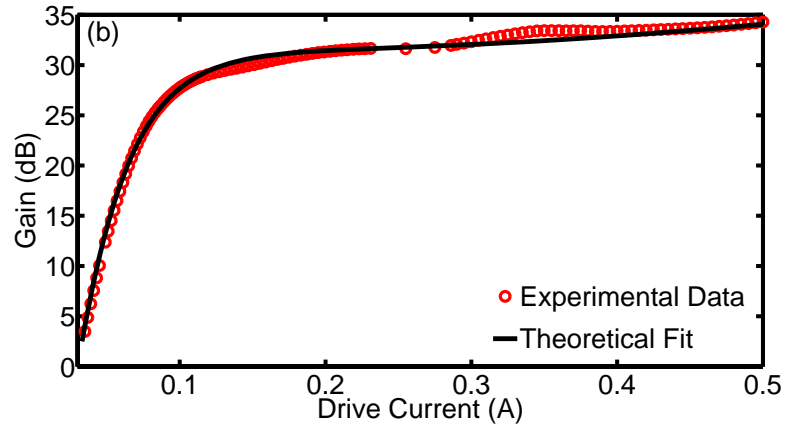
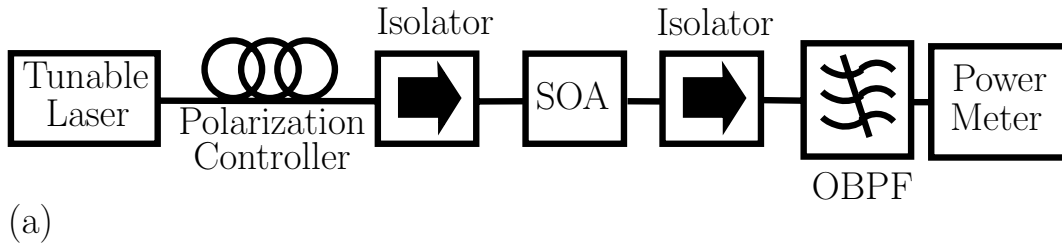


Figure 3.1: (a) Experimental setup and (b) measured values of  $G(I)$  (dB) as a function of drive current. The solid line corresponds to the best estimate of  $D$  from the experimental data (circles).

of the amplified signal was measured after passing it through an OBPF with a 3 dB bandwidth of 1 nm to reject the out of band portion of the ASE.

The symbols in Fig. 3.1(b) show the measured values of  $\log G$  as a function of drive current  $I$ . The coupling and other losses are included by adding 2 dB to the fiber-to-fiber gain values measured in the experiment. It is evident from this Fig. that the CW signal is amplified exponentially (or linearly on the semilog plot) for currents of up to about 100 mA, but this exponential growth is reduced dramatically at higher currents. This behavior is because of gain saturation induced by the increasing ASE.

To fit the expression of amplification factor to the experimental data [Eq. (3.10)], the low current regime [ $I < 60$  mA] is considered. The time derivative is set to

zero in Eq. (3.3), the last term is neglected,  $N$  at a given value of  $I$  is calculated by solving:

$$\frac{I}{qV} = \frac{N}{\tau_c}, \quad (3.11)$$

where the carrier lifetime,  $\tau_c$  [Eq. (1.5)], itself depends on  $N$ . Combining Eqs. (3.11) and (1.5), the carrier density  $N$ , at a drive current  $I$ , is the real and positive root of the cubic polynomial  $P(N)$  which can be written as:

$$P(N) = C_a N^3 + B_{sp} N^2 + A_{nr} N - \frac{I}{qV} \quad (3.12)$$

The dimensionless constant  $\Gamma a N_0 L$  and transparency current  $I_0$  in Eq. (3.5) are uniquely determined from the experimental data by using the gain values at low drive currents, at which ASE can be neglected. They are found to be 7 and 30 mA respectively. For the device under consideration,  $L = 1$  mm. Using the assumed parameter values from table 3.2, the values listed in table 3.3 are deduced.

Table 3.2: Assumed Parameter Values for the SPM Simulations

Parameter	Our value	Typical values
$\Gamma$	0.4	0.3–0.7
$a$ (m <sup>2</sup> )	$10.5 \times 10^{-20}$	$2.5\text{--}4.5 \times 10^{-20}$
$A_{nr}$ (s <sup>-1</sup> )	$3.9 \times 10^9$	$0.1\text{--}4.5 \times 10^9$
$B_{sp}$ (m <sup>3</sup> /s)	$8.5 \times 10^{-16}$	$1\text{--}9 \times 10^{-16}$
$C_a$ (m <sup>6</sup> /s)	$3.3 \times 10^{-40}$	$1\text{--}97 \times 10^{-40}$

Considering the ASE-saturated regime in Fig. 3.1(b), it can be seen that the ASE power also depends on the carrier density  $N$ . It is important to note that since the spontaneous emission noise increases linearly with injected carrier density  $N$  and optical gain also increases linearly with  $N$ , ( $g(z, t) = \Gamma a(N - N_0)$ ), the

Table 3.3: Deduced Parameter Values for the SPM Simulations

Parameter	Description	Deduced value
$N_o$ ( $\text{m}^{-3}$ )	Transparency carrier density	$1.64 \times 10^{23}$
$V$ ( $\text{m}^3$ )	Active volume	$2.83 \times 10^{-16}$
$\sigma$ ( $\text{m}^2$ )	Mode cross-section	$7.07 \times 10^{-13}$
$E_{sat}$ (pJ)	Saturation energy	0.824

product of the two, i.e. the amplified spontaneous emission noise or ASE power is expected to scale as  $N^2$ , where both electron and hole densities are proportional to  $N$  [94]. The total ASE power can therefore be written as:

$$P_{\text{ASE}} = DN^2. \quad (3.13)$$

where  $D$  is a constant of proportionality.

The procedure outlined above allows us to calculate  $P_{\text{ASE}}(N)$  and  $P_{\text{sat}}(N)$ , and consequently  $G(I)$ , at any drive current. The value of  $D$  was estimated by using it as a fitting parameter for the experimental data shown in Fig. 3.1(b). Its value was found to be  $2.32 \times 10^{-50} \text{ m}^6\text{W}$ . Table 3.2 shows the values of parameters used for curve fitting together with typical values employed in the literature for different SOAs [94, 96, 101, 106, 108, 109, 113, 151–153]. As seen there, the value of  $a$  is larger for the SOA, resulting in a smaller value of  $N_0$  at the same optical gain.

### 3.1.4 SOA Gain and Gain Recovery

In this section, the numerical model is used to study how the gain recovery time is shortened at high drive currents by increasing the ASE. Although pump-probe measurements are often performed to measure gain recovery time, here the objective is to deduce it from the CW data in Fig. 3.1.

For this purpose, Eq. (3.6) can be rewritten as:

$$\frac{\partial g}{\partial t} = \frac{g_0}{\tau_c} - \frac{g}{\tau_{\text{eff}}} - \frac{g|A|^2}{E_{\text{sat}}}, \quad (3.14)$$

where the effective gain recovery time is defined as:

$$\frac{1}{\tau_{\text{eff}}} = \frac{1}{\tau_c} + \frac{1}{\tau_{\text{ASE}}}, \quad (3.15)$$

and the ASE-related recombination time can be written as:

$$\frac{1}{\tau_{\text{ASE}}} = \frac{P_{\text{ASE}}}{E_{\text{sat}}} = \frac{DN^2}{E_{\text{sat}}} = D_{\text{sp}}N^2, \quad (3.16)$$

Using Eqs. (1.5), (3.15) and (3.16),  $\tau_{\text{eff}}$  can be written in the form:

$$\frac{1}{\tau_{\text{eff}}} = A_{nr} + B_{\text{sp}}N + (C_a + D_{\text{sp}})N^2. \quad (3.17)$$

This relation shows that the ASE contribution has the same functional dependence on  $N$  as the Auger contribution and can be included in practice by increasing the value of the Auger parameter  $C_a$ . Using the calculated value of  $E_{\text{sat}}$ ,  $D_{\text{sp}}$  is found to be  $2.75 \times 10^{-38}$  m<sup>6</sup>/s. Comparing the value of  $D_{\text{sp}}$  to the value of  $C_a$  in Table 3.2, it can be seen that the ASE contribution to  $\tau_{\text{eff}}$  for this SOA exceeds the Auger contribution by a factor of 83. Clearly, the presence of ASE shortens the gain recovery time drastically.

Figure 3.2(a) shows the calculated values of  $P_{\text{ASE}}$  and  $P_{\text{sat}}$  as a function of drive current together with the experimental measurements of  $P_{\text{ASE}}$  on the same SOA used for Fig. 3.1. For  $I < 70$  mA,  $P_{\text{ASE}} < P_{\text{sat}}$ , which justifies the assumption that the ASE effects are small at low drive currents. The experimental measurements of  $P_{\text{ASE}}$  were carried out by recording the ASE spectrum with an optical spectrum analyzer (OSA) at various drive currents. The ASE spectrum had a 20 dB bandwidth of over 50 nm and its peak shifted towards shorter wavelengths with increasing drive currents. The power data in Fig. 3.2(a) was obtained from spectral data by integrating over the entire bandwidth and assuming constant

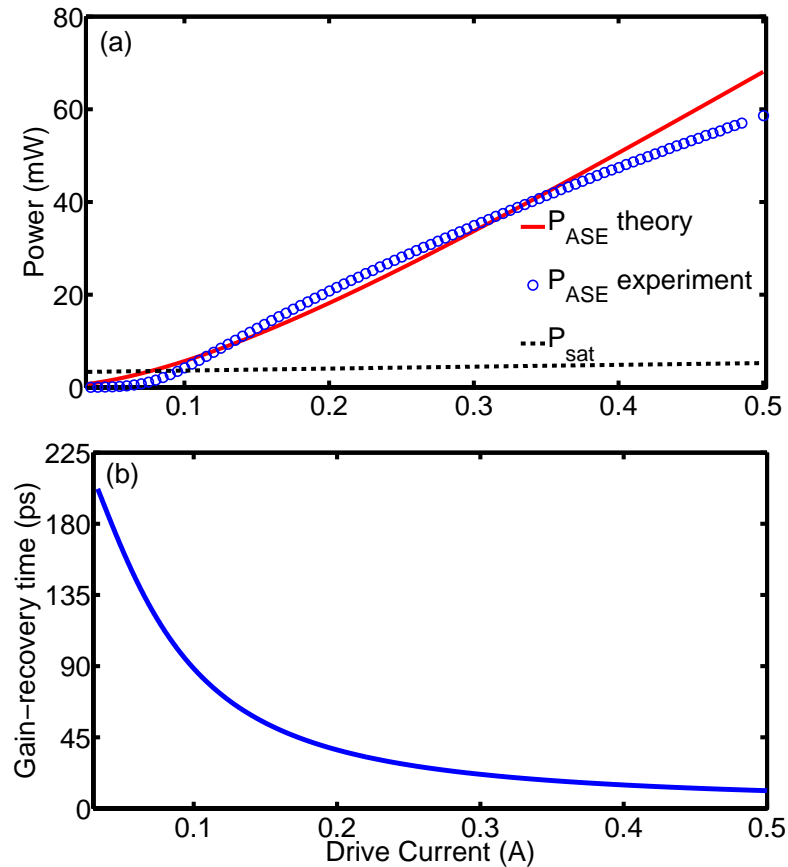


Figure 3.2: Calculated values of (a)  $P_{\text{ASE}}$  and  $P_{\text{sat}}$ , and (b)  $\tau_{\text{eff}}$  as a function of drive current for the SOA used to obtain the data in Fig. 3.1. Experimental measurements of  $P_{\text{ASE}}$  are shown as circles.

coupling losses and IL. Because of a wide ASE spectrum and wavelength dependence of losses associated with some of the components being used, the power data has an uncertainty of about 10% when converted to internal ASE power. With this in mind, the agreement with the model is reasonable at drive currents of up to 400 mA. Larger deviations at higher currents are due to the saturation of the ASE itself. This is due to the saturation of the SOA gain, a second order effect not included in the numerical model.

Figure 3.2(b) shows the calculated values of  $\tau_{\text{eff}}$  as a function of drive current. At low drive currents, the ASE contribution is negligible, and the SOA has an

approximate gain recovery time of 200 ps ( $\tau_{\text{eff}} = \tau_c$ ). As current increases, ASE builds up, as shown in Fig. 3.2(a), and it leads to a monotonic reduction in the value of  $\tau_{\text{eff}}$ , resulting in a value of about 10 ps at  $I = 0.5$  A. This behavior is in agreement with previous studies on this kind of SOAs [89, 108] and also agrees with the quoted value of 9 ps at  $I = 0.5$  A for this particular device.

## 3.2 Self-Phase Modulation

In this section, the numerical model developed in the previous section is used to study the impact of gain dynamics induced by ASE on SPM-induced spectral broadening suffered by picosecond optical pulses propagating in the SOA.

### 3.2.1 Modified Equations

To study the SPM suffered by the optical pulses in the presence of ASE, it is useful to rewrite the amplitude [Eq. (3.2)] in a frame moving with the pulse. Introducing the reduced time as  $\tau = t - z/v_g$  together with  $A = \sqrt{P}e^{i\phi}$  in Eq. (3.2), the signal power  $P(z, \tau)$  and the phase  $\phi(z, \tau)$  are found to satisfy [93]:

$$\frac{\partial P}{\partial z} = g(z, \tau)P, \quad \frac{\partial \phi}{\partial z} = -\frac{\alpha}{2}g(z, \tau). \quad (3.18)$$

These Eqs. look similar to their CW part in Eq. (3.7) except that all variables depend on the time  $\tau$  implicitly. They can be integrated over the SOA length  $L$  to obtain:

$$P_{\text{out}}(\tau) = P_{\text{in}}(\tau) \exp[h(\tau)], \quad \phi_{\text{nl}}(\tau) = -\frac{\alpha}{2}h(\tau), \quad (3.19)$$

where  $h(\tau) = \ln G(\tau) = \int_0^L g(z, \tau)dz$  represents the integrated gain at time  $\tau$ ,  $P_{\text{in}}(\tau)$  represents the power profile of the input pulse,  $P_{\text{out}}(\tau)$  represents the power profile of the output pulse, and the nonlinear phase shift due to SPM is defined as  $\phi_{\text{nl}}(\tau) = \phi(L, \tau) - \phi(0, \tau)$ .



An Eq. for  $h(\tau)$  is obtained by integrating the gain [Eq. (3.14)] over the SOA length [93]. The result can be written as:

$$\frac{dh}{d\tau} = \frac{g_0 L}{\tau_c} - \frac{h}{\tau_{eff}} - \frac{P_{in}(\tau)}{E_{sat}}(e^h - 1). \quad (3.20)$$

Once this Eq. is integrated numerically, both the power and phase profiles of the amplified pulse are calculated. The frequency chirp  $\Delta\nu_0$  imposed on the pulse is related to the nonlinear phase as [93]:

$$2\pi\Delta\nu_0 = -d\phi_{nl}/d\tau \quad (3.21)$$

Using  $\phi_{nl}(\tau)$  from Eq. (3.19), the chirp is given by

$$\Delta\nu_0(\tau) = \frac{\alpha}{4\pi} \frac{dh}{d\tau}, \quad (3.22)$$

where  $dh/d\tau$  is obtained from Eq. (3.20). It is important to note that the significant modification in the above set of Eqs. comes in Eq. (3.20) where the term  $\frac{h}{\tau_c}$ , in the absence of ASE [93] is replaced by  $\frac{h}{\tau_{eff}}$ , in the presence of ASE. Next, the impact of gain saturation and gain recovery acceleration due to ASE on the phase and the chirp profiles of optical pulses will be investigated.

### 3.2.2 Nonlinear Phase and Chirp

SPM is employed for many all-optical signal processing applications including wavelength conversion [27], pulse compression [85], channel multiplexing or demultiplexing [81, 82], and bit-level logic [100]. The nonlinear phase shift and the resulting chirp imposed on the optical pulses is extremely important for such SOA-based applications.

To illustrate the impact of ASE on the nonlinear phase and the frequency chirp, a 20 ps FWHM Gaussian input pulse is considered with the power profile  $P(t) = P_0 \exp(-t^2/\tau_p^2)$ . When the FWHM is 20 ps, the parameter  $\tau_p \approx 12$  ps. We assume that the input pulse energy corresponds to  $E_{in}/E_{sat} = 0.3$ . The linewidth

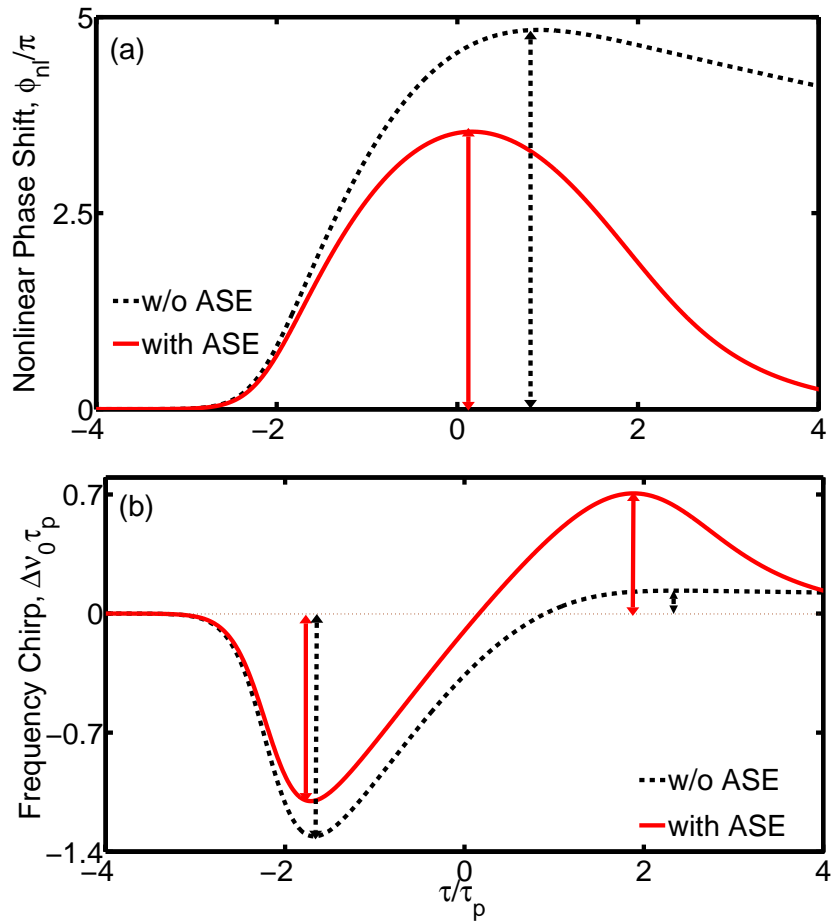


Figure 3.3: (a) Nonlinear phase shift and (b) frequency chirp induced on a 20 ps wide Gaussian pulse by an SOA with large ASE. Dashed lines show the case for which ASE is negligible. The double arrows indicate the maximum value of the nonlinear phase shift and red and blue chirp for both the cases.

enhancement factor  $\alpha$  is taken to be 5. The SOA is operated at  $I = 0.5$  A at which the small signal CW amplification factor corresponds to  $G = e^{7.8} = 33.9$  dB in Fig. 3.1(a). The solid curves in Fig. 3.3 show the temporal profiles for the nonlinear phase shift  $\phi_{nl}(\tau)$  and for the chirp  $\Delta\nu_0(\tau)$  using  $\tau_{\text{eff}} = 10$  ps, the value deduced in the previous subsection. For comparison, the dashed lines show the case of an SOA with negligible ASE by using  $\tau_{\text{eff}} = \tau_c = 200$  ps. Clearly, ASE affects the SPM process considerably, both qualitatively and quantitatively.

When the ASE effects are negligible, the proposed numerical model reduces to that of ref [93] because the pulse width is a small fraction of the gain recovery time of 200 ps. The nonlinear phase shows a rapid increase as the leading edge of the pulse saturates the SOA gain, and a reduction in the carrier density increases the mode index. Since the gain cannot recover much over the pulse duration, the nonlinear phase saturates with only slight reduction in the trailing part of the pulse. The situation changes considerably when ASE reduces the gain recovery time to 10 ps. Now, the saturated gain can recover within the pulse duration. As a result, the carrier density begins to increase in the trailing region of the pulse. The resulting decrease in the mode index then leads to a rapid decrease in the pulse phase as well. The net result is that the phase profile becomes much more symmetric and begins to mimic the shape of the amplified pulse. This is precisely what occurs in the case of optical fibers, the nonlinearity of which responds to femtosecond time scale [56]. The fiber-like features of SPM in SOAs is potentially attractive for designing SOA-based devices such as all-optical regenerators and switches. The nonlinear phase shifts can also be used in an interferometric configuration for ultrafast all-optical signal processing applications [97].

The chirp profiles in Fig. 3.3(b) show how the changes in the gain dynamics due to ASE affect the frequency chirp imposed by the SPM on an amplifying pulse. In the absence of ASE, the pulse experiences a red shift over its leading edge but a negligible blue chirp is imposed on its trailing edge. In the presence of ASE, the extent of red chirp is reduced slightly but there is a significant increase in blue chirp due to the ASE-induced faster gain recovery. The net result is an almost linear chirp across the center part of the pulse, a behavior similar to that occurring in optical fibers [56]. This linear chirp is very attractive for compressing the amplified pulse [34]. It is worth noting that the required peak power of pulses is smaller by a factor of 1000 or more when SOAs are compared with HNLFs.

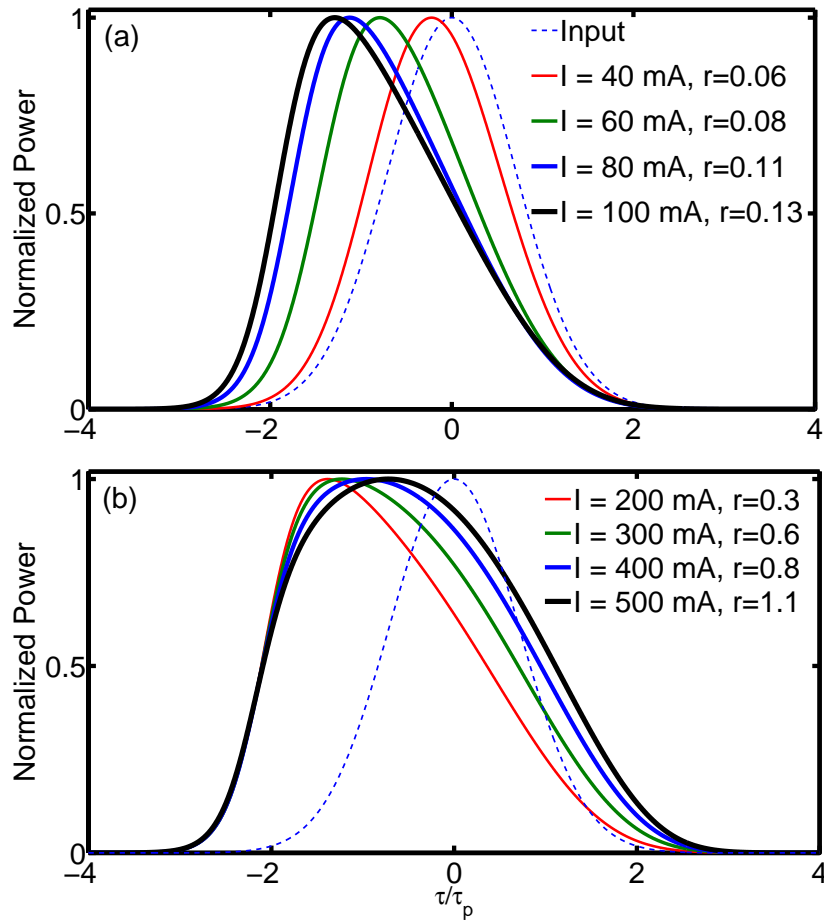


Figure 3.4: Output pulse shapes (a) at low drive currents ( $r \leq 0.13$ ) and (b) high drive currents ( $0.3 < r < 1.1$ )

### 3.2.3 Pulse Shapes and Spectra

Changes induced by ASE in the frequency chirp also affects the spectrum of the amplified pulse. In this section, the variation of the shapes and the spectra of the output pulses at different drive currents is studied. Since the gain recovery time  $\tau_{\text{eff}}$  is reduced with the increasing currents, a dimensionless parameter  $r$  as the ratio  $r = \tau_p/\tau_{\text{eff}}$  is introduced. For a constant input pulse width,  $r$  increases with increasing drive current.

The output pulse shape is obtained from Eq. (3.18), and the corresponding results for different values of  $r$  (or  $I$ ) are shown in Fig. 3.4. All other parameters are identical to those used for simulating the phase and chirp profiles. At low drive currents below 100 mA (or  $r \leq 0.13$ ), ASE power is negligible, and the gain recovery time is much longer than the pulse width, a situation similar to that studied in Ref. [93]. As shown in Fig. 3.4(a), the amplified pulse acquires an asymmetric shape with a leading edge sharper than the trailing edge. This occurs because the leading edge of the pulse experiences full gain, but gain is reduced substantially near the trailing edge, because pulse's leading part saturates the SOA gain. However, at drive currents in the range 200 to 500 mA corresponding to  $0.3 < r < 1.1$ , increasing ASE power begins to saturate the gain and reduce the gain recovery time, making it comparable to the pulse width at currents near 500 mA. As seen in Fig. 3.4(b), the pulse becomes more symmetric as the drive current increases, with no visible changes near the leading edge of the pulse. Physically, the gain begins to recover so quickly that the trailing edge begins to experience as much gain as the leading edge of the pulse.

The pulse spectrum is obtained by taking the fourier transform of the output field  $A(L, \tau)$ , and the results are shown in Fig. 3.5 for the drive currents ranging from 40 to 500 mA and corresponding to  $0.06 < r < 1.1$ . At low drive currents of up to 100 mA ( $r < 0.13$ ), output spectrum is highly asymmetric with most of the pulse energy contained in the red-shifted spectral lobe. This kind of spectrum is associated with the gain recovery time much longer than the pulse width [93]. At high drive currents seen in Fig. 3.5(b), with  $r$  in the range 0.3 to 1.1, the energy is transferred from the red to the blue side of the pulse spectrum, and the blue-shifted spectral lobes increase in amplitude progressively.

These changes in the pulse spectra can be understood in terms of a faster gain recovery induced by increasing ASE. At low drive currents ( $r < 0.1$ ), the trailing part of the pulse does not experience much blue chirp [see Fig. 3.3], resulting in

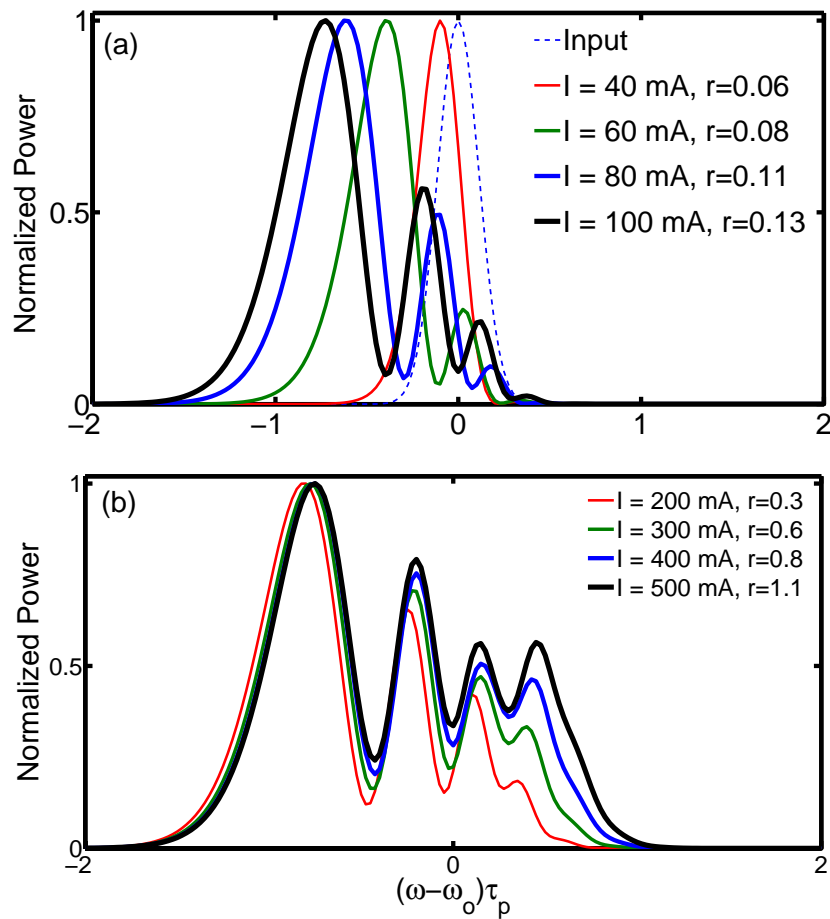


Figure 3.5: Output pulse spectrum (a) at relatively low drive currents ( $r \leq 0.13$ ) and (b) at high drive currents ( $0.3 < r < 1.1$ )

an asymmetric red-shifted pulse spectrum. At drive currents beyond 200 mA, ASE power becomes so large that the gain recovery time is reduced considerably. This enhanced gain recovery imposes a blue chirp on the trailing part of the pulse and increases spectral symmetry in the output spectrum. This situation is similar to that occurring in optical fibers in which SPM is due to a quasi-instantaneous, Kerr nonlinearity [56].

### 3.3 Four-Wave Mixing

In this section, the modified numerical model developed in this chapter is extended to numerically study the ASE-enhanced, interband FWM in SOAs. The impact of pump-signal detuning, effective carrier lifetime ( $\tau_{\text{eff}}$ ) and pump power on FWM CE is investigated.

#### 3.3.1 Introduction to Interband and Intraband FWM

FWM in SOAs has been studied and used for wavelength conversion for almost 25 years and two mechanisms responsible for FWM in SOAs are known as *interband* and *intraband* FWM [115]. Interband FWM requires carrier density modulation involving electron-hole recombination at relatively high frequencies and is typically limited by the carrier lifetime. This limits its usefulness to small wavelength shifts of  $<0.1$  nm [115, 154]. In contrast, intraband FWM involving modulation of occupational probability within an energy band can respond on a time scale of  $<1$  ps and provides wavelength shifts larger than 10 nm [155–157]. For this reason, intraband FWM has been used for practical implementation of WCs, even though required pump powers exceed 10 mW and the CE is typically  $<10\%$  [156–170].

The practical aspects of wavelength conversion for intraband FWM, such as the impact of input pump and signal powers on the CE [156, 157], and the resulting OSNR of the converted signal [160, 161], have been investigated both theoretically and experimentally. Apart from the high input pump powers and a poor CE, such WCs also operate over a limited range of signal powers, mainly because of slow gain recovery in the SOAs [160]. An optical beam at a wavelength near the transparency point of the SOA (called the assist or holding beam) with powers in excess of 40 mW has been used to reduce the SOA gain recovery time to as low as 60 ps [105] and to enhance the performance of the SOA-based WCs [166–168].

Recently, commercial SOAs have become available the gain recovery time of which can be reduced to close to 10 ps at high drive currents [88, 89, 108, 109, 171]. The physical mechanism behind fast gain recovery is related to saturation of the SOA gain at high drive currents through ASE, together with a reduced saturation energy realized by suitable doping of QWs. Such a small value of the gain recovery time implies that these SOAs should exhibit interband FWM with wavelength shifts  $>10$  nm, provided that the pump does not become intense enough to saturate the gain along the SOA length. Efficient FWM at high drive currents was first reported in 1997 in a 1.5 mm long SOA [171]. More recently, SOAs with ASE-enhanced gain recovery were used to observe efficient FWM at small pump-signal detunings (0.02 nm or less) [172]. Simultaneous wavelength conversion of two data channels has also been reported in a 2010 study [41]. In this section the previously developed theoretical framework for SPM is extended to study the ASE-assisted interband FWM.

### 3.3.2 Modified Equations for FWM in SOAs

The origin of interband FWM in the presence of ASE lies in the gain saturation term in Eq. (3.14). More specifically, when a signal field at frequency  $\omega_1$  is launched together with the pump, the amplitude  $A$  contains three terms

$$A = A_0 + A_1 \exp(-i\Omega t) + A_2 \exp(i\Omega t), \quad (3.23)$$

where the subscripts 0, 1, and 2 stand for the pump, signal, and idler fields respectively and  $\Omega = \omega_1 - \omega_0$  represents pump-signal detuning. The idler frequency  $\omega_2 = \omega_0 - \Omega$  is generated such that the FWM condition  $2\omega_0 = \omega_1 + \omega_2$  is automatically satisfied.

Because the total intensity  $|A|^2$  contains terms oscillating at the beat frequency  $\Omega$ , the gain is also modulated at this frequency, and the modified gain



equation [Eq. (3.14)] has an approximate solution of the form:

$$g = \bar{g} + [\Delta g \exp(-i\Omega t) + c.c], \quad (3.24)$$

where the average gain  $\bar{g}$  is given by:

$$\bar{g} = \frac{g_0}{r' + (|A_0|^2 + |A_1|^2 + |A_2|^2)/P_{\text{sat}}}, \quad (3.25)$$

and the amplitude  $\Delta g$  of gain modulations created by the beating of the pump with the signal is given by:

$$\Delta g = -\frac{\bar{g}(A_1 A_0^* + A_0 A_2^*)}{P_{\text{sat}}(r' - i\Omega\tau_c)}. \quad (3.26)$$

In writing the preceding solution for the gain two parameters have been introduced. These can be defined as:

$$r' = \tau_c/\tau_{\text{eff}}, \quad P_{\text{sat}} = E_{\text{sat}}/\tau_c. \quad (3.27)$$

The dimensionless parameter  $r' \geq 1$  represents the factor by which the gain recovery time is reduced by the ASE-induced gain saturation. For  $r' = 1$ , Eqs. (3.25) and (3.26) reduce to the standard solution for carrier density modulation discussed in [115] in the absence of ASE. It can be seen from Eq. (3.25) that as the gain recovery time is shortened, the small signal gain  $g_0$  is reduced by a factor of  $r'$  because of gain saturation induced by ASE [90]. Fortunately, this reduction is accompanied by a considerable enhancement of the bandwidth over which gain modulations can occur. This is apparent from the presence of the factor  $r'$  in Eq. (3.26) and is the origin of large wavelength shifts that can be realized in such SOAs through interband FWM.

The final step is to use Eqs. (3.23) and (3.24) in Eq. (3.2) and separate the oscillating and non-oscillating terms. In the CW case studied here, the time

derivative in Eq. (3.2) can be dropped. The following are the three derived coupled differential Eqs. for the pump, signal, and idler fields:

$$2\frac{dA_0}{dz} = (1 + i\alpha)[\bar{g}A_0 + (\Delta g A_2 + \Delta g^* A_1)], \quad (3.28)$$

$$2\frac{dA_1}{dz} = (1 + i\alpha)(\bar{g}A_1 + \Delta g A_0), \quad (3.29)$$

$$2\frac{dA_2}{dz} = (1 + i\alpha)(\bar{g}A_2 + \Delta g^* A_0). \quad (3.30)$$

Equations (3.28)–(3.30) can be solved analytically in the undepleted pump approximation [157]. However, since the pump is amplified considerably inside the SOAs operating at high currents, this approximation is not valid near the output end. For this reason, the three coupled Eqs. are solved numerically. Further, all pump depletion effects are also included. To further improve the numerical accuracy, the saturation of the average gain  $\bar{g}$  in Eq. (3.25) is allowed by all three optical fields. However, it is assumed that the wavelength dependence of the gain and the  $\alpha$  factor is negligible over the pump-signal detuning range of interest (about 10 nm). These assumptions are reasonable for most SOAs [173, 174]

The CE and the OSNR are the two critical FOMs for FWM-based WCs [25, 160, 164]. They are defined as:

$$\eta = P_2(L)/P_1(0), \quad \text{OSNR} = P_2(L)/P_n, \quad (3.31)$$

where  $L$  is the SOA length,  $P_1 = |A_1(0)|^2$  is the input signal power, and  $P_2 = |A_2(L)|^2$  is the output idler power. The noise power  $P_n$  used to define the OSNR is obtained by using  $P_n = p_n N_{BW}$ , where  $p_n$  is the noise spectral density and  $N_{BW}$  is the reference bandwidth. For telecommunication signals, OSNR is commonly defined over a 0.1 nm noise bandwidth [99, 164]. Presently, since both pump and probe are CW signals, for the sake of consistency, it is assumed that the input signal power represents the average power of a WDM channel containing RZ Gaussian pulses with a 50% duty cycle.

Table 3.4: Parameter Values Used in the FWM Numerical Simulations

Parameter	symbol	Value
Device length	$L$	1 mm
Gain cross section	$a$	$10.2 \times 10^{-20} \text{ m}^2$
Linewidth enhancement factor	$\alpha$	3
Mode confinement factor	$\Gamma$	0.47
Current at transparency	$I_0$	47.5 mA
Carrier density at transparency	$N_0$	$2.7 \times 10^{23} \text{ m}^{-3}$
Carrier lifetime at transparency	$\tau_c$	200 ps
Nonradiative recombination rate	$A_{nr}$	$4.3 \times 10^9 \text{ s}^{-1}$
Spontaneous recombination rate	$B_{sp}$	$4.7 \times 10^{-16} \text{ m}^3/\text{s}$
Auger recombination coefficient	$C_a$	$2.0 \times 10^{-40} \text{ m}^6/\text{s}$
Saturation energy	$E_{\text{sat}}$	0.7 pJ

### 3.3.3 Numerical Simulations

In this subsection, the results from the numerical simulations are presented. The focus of these simulations is on calculating the CE  $\eta$ , using the device and input parameters listed in Table 3.4 for a commercial SOA (CIP [Center for Integrated Photonics] Technologies, model SOA-XN-OEC-1550) designed for high internal ASE at high drive currents. The optical specifications of this device are summarized in Table. 3.1. Using the procedure outlined in the previous subsection, device parameters are estimated from the experimental measurements of the SOA gain (under low input power conditions) as a function of drive current. The parameters listed in table 3.4 are calculated for 1575 nm pump wavelength. Further,

the output OBPF used for measuring optical power [Fig. 3.1(a)], is the Alnair Labs BVF-200, with its tunable bandwidth set to 0.1 nm. This filter has out-of-band suppression in excess of 50 dB, which leads to much more efficient rejection of out of band ASE. As a consequence the estimated device parameters are more accurate compared to those derived for the SPM simulations. It is important to note that the accuracy of the numerical model developed in this thesis for studying ASE-mediated nonlinear effects is dependent on the quality of OBPF used for the small signal gain measurements. The ASE power  $P_{\text{ASE}}$ , is assumed to be constant all along the SOA length. The ASE power is calculated by using the relation  $P_{\text{ASE}} = DN^2$  with  $D = 1.32 \times 10^{-50} \text{ m}^6\text{W}$ , a value deduced based on the experimental measurements [90].

Figure 3.6(a) shows changes in  $\eta$  as a function of pump-signal detuning [ $\Delta\lambda = (\lambda_0^2/2\pi c)\Omega$ ] at three different drive currents for fixed input pump and signal powers (0 and  $-25$  dBm, respectively). As expected,  $\eta$  decreases rapidly with  $\Delta\lambda$  at any drive current. However,  $\eta$  increases by more than 20 dB, at any pump-signal detuning, as the drive current is increased from 100 to 500 mA. This enhancement of CE is due to the ASE-induced shortening of the gain recovery time. From a practical standpoint, the important question is how large is the  $\Delta\lambda$  range over which the interband FWM can provide wavelength conversion with a net gain ( $\eta > 0$  dB). This range is only 0.3 nm at 100 mA but it increases to almost 7.5 nm at 500 mA. Noting that the wavelength shift (WS) is  $2\Delta\lambda$ , the model predicts that the SOA can provide wavelength shifts of up to 15 nm when driven at high current levels. Physical mechanism for the large improvement is a reduction of the gain recovery time at high currents (or high ASE levels). If a 10% CE is acceptable, wavelength shifts can exceed 25 nm. It is remarkable that this kind of performance can be realized at a relatively low 1 mW pump power.

One may wonder whether higher pump powers would make the situation even better because pump powers  $>10$  mW are routinely used in the case of intraband

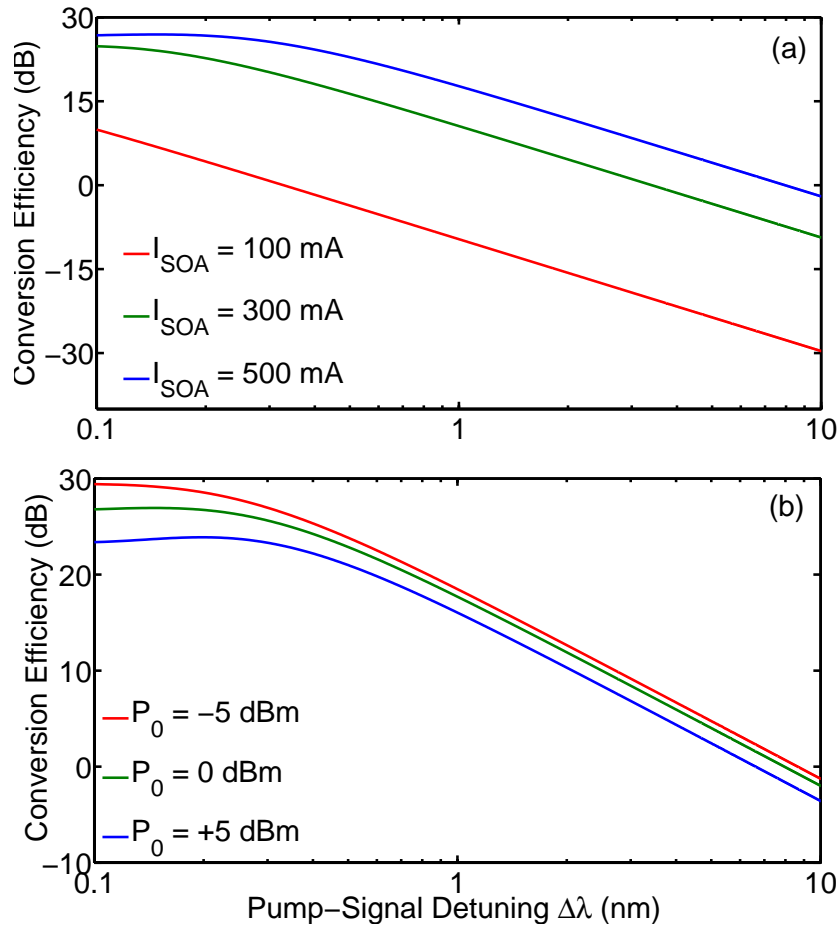


Figure 3.6: Conversion Efficiency as a function of pump-signal detuning (a) at three drive currents for 1 mW pump power and (b) at three input pump powers at 500 mA drive current.

FWM [25, 169, 170]. It is, therefore, important to see the effect of input  $P_0$  on interband FWM. In Fig. 3.6(b),  $\eta$  as a function of  $\Delta\lambda$  is plotted for three input pump powers while keeping the SOA drive current fixed at 500 mA and input signal power at  $-25$  dBm. As the pump power increases, the CE at any  $\Delta\lambda$  is actually reduced. This is somewhat counterintuitive but can be understood by noting that, if the gain is saturated considerably by the pump, the impact of ASE is reduced. Physically speaking, as the pump is amplified by the SOA, its power increases and becomes comparable to the ASE power near the output

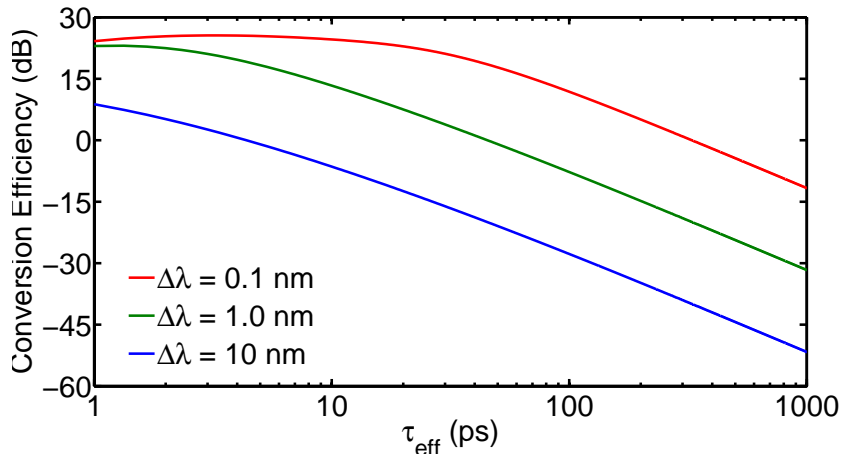


Figure 3.7: Conversion Efficiency as a function of effective carrier lifetime ( $\tau_{\text{eff}}$ ) for different pump-signal detuning  $\Delta\lambda$ . Device gain  $G_0 = 30$  dB.

SOA end. Gain saturation by such an intense pump decreases the ASE power, which increases the gain recovery time and reduces the CE. This is the reason why higher input pump powers should be avoided for WCs, making use of ASE-induced gain saturation. This is not a limitation because the use of low pump powers is desirable from the standpoint of low electrical power consumption for telecommunication applications. Figure 3.6(b) shows that the pump power should be kept below 1 mW to avoid pump-induced gain saturation. We will discuss experimental optimization of pump and signal powers in Chapter 5.

To establish that the CE is indeed enhanced by the ASE-induced shortening of the gain recovery time, the changes in the  $\eta$  as a function of  $\tau_{\text{eff}}$  are studied. It is assumed that the SOA has a carrier lifetime of 1000 ps and is biased to provide a gain of 30 dB, both in the presence and absence of internal ASE ( $g_0L = 6.908$ ). Figure 3.7 shows  $\eta$ , calculated numerically as a function of  $\tau_{\text{eff}}$  for three values of  $\Delta\lambda$ . In all three cases,  $\eta$  improves dramatically as  $\tau_{\text{eff}}$  becomes shorter. For a relatively small detuning ( $\Delta\lambda = 0.1$  nm), a net idler gain can be obtained for  $\tau_{\text{eff}} < 300$  ps. This is consistent with the earlier results on nearly degenerate FWM [115, 157]. However, for a large 10 nm detuning,  $\eta$  is below  $-30$  dB if  $\tau_{\text{eff}}$

exceeds 100 ps. This is the reason why interband FWM was not found to be suitable for wavelength conversion. However, if  $\tau_{\text{eff}}$  can be reduced to below 10 ps,  $\eta > 1$  can be realized even for  $\Delta\lambda = 10$  nm. These results clearly show how the ASE-induced shortening of  $\tau_{\text{eff}}$  can extend the usefulness of interband FWM for wavelength conversion.

### 3.4 Conclusions

In this section, the impact of ASE on the nonlinear effects (SPM and FWM) in SOAs is studied theoretically. The CW gain measurements were used along with a detailed theoretical model to deduce how ASE shortens the effective gain recovery time of the SOA under consideration to near 10 ps. The model assumed that the total ASE power is constant along the length of the amplifier and increases with the current injected into the SOA. A numerical model [175] incorporating the changes with current in counter-propagating ASE spectral components is certainly more accurate than the semi-analytical model proposed in this thesis. A more quantitative comparison however is not possible because the work presented here focuses on modeling recovery speed as function of drive current.

The current dependence of  $\tau_{\text{eff}}$  and the SOA gain was incorporated into the proposed model which was used to study the impact of ASE on the SPM induced spectral broadening of picosecond pulses inside the SOA. It is demonstrated that a shorter gain recovery time affects the SPM induced spectral broadening in several ways. The SPM induced nonlinear phase shift becomes more symmetric and consequently, frequency chirp becomes much more linear across the pulse. These features are attractive for designing SOA-based, all-optical signal processing devices such as WCs, regenerators, and switches.

The shape and spectrum of the optical pulses were calculated over a range of drive currents to study how they change with shortening of the gain recovery time.

The pulse shape becomes much more symmetric at high drive currents because a reduction in the value of  $\tau_{\text{eff}}$  causes the gain to recover fast enough that both the leading and trailing edge of the pulse experience nearly the same dynamic gain profile. For the same reason, the output spectrum becomes more symmetric and resembles that obtained in the case in optical fibers where SPM occurs due to a nearly instantaneous Kerr nonlinearity.

The numerical model developed in this chapter was extended to study interband FWM in SOAs driven at currents high enough that ASE itself begins to saturate the SOA gain. Across a broad range of wavelength shifts (as large as 20 nm), an increase in the CE of over 20 dB is observed, as the SOA current was increased from 100 to 500 mA. The impact of pump-power, pump-signal detuning and  $\tau_{\text{eff}}$  on FWM CE is investigated. A trade-off between average device gain  $\bar{g}$  and the bandwidth of gain-modulations, mediated by a dimensionless parameter  $r' = \tau_c/\tau_{\text{eff}}$ , is demonstrated. The increase in pump-signal detuning over which interband FWM dominates comes at the cost of reduced device small signal gain.



# 4 ASE-Assisted SPM in SOAs: Experimental Results

## 4.1 Introduction

In this chapter, the theory developed in the previous chapter to simulate the impact of internal ASE on the spectrum of picosecond pulses broadened through SPM [90] is experimentally verified. The pulse spectra of the picosecond optical pulses at the SOA output, whose measured gain under CW conditions is shown in Fig. 3.1(a), are recorded at different bias currents and compared to results from numerical simulations reported in the previous chapter. Remarkable evolution of the central and blue-shifted spectral lobes over a wide range of SOA drive currents is demonstrated. Over these drive currents, the SOA small signal gain is nearly constant. A trade-off between spectral broadening and spectral symmetry is inherent to how the recovery-speed enhancement is achieved in this class of devices.

## 4.2 Experimental Setup

Figure 4.1(a) shows the experimental setup used to study spectral broadening of picosecond pulses inside SOAs. We use gain-switching [176] of a MQW DFB laser

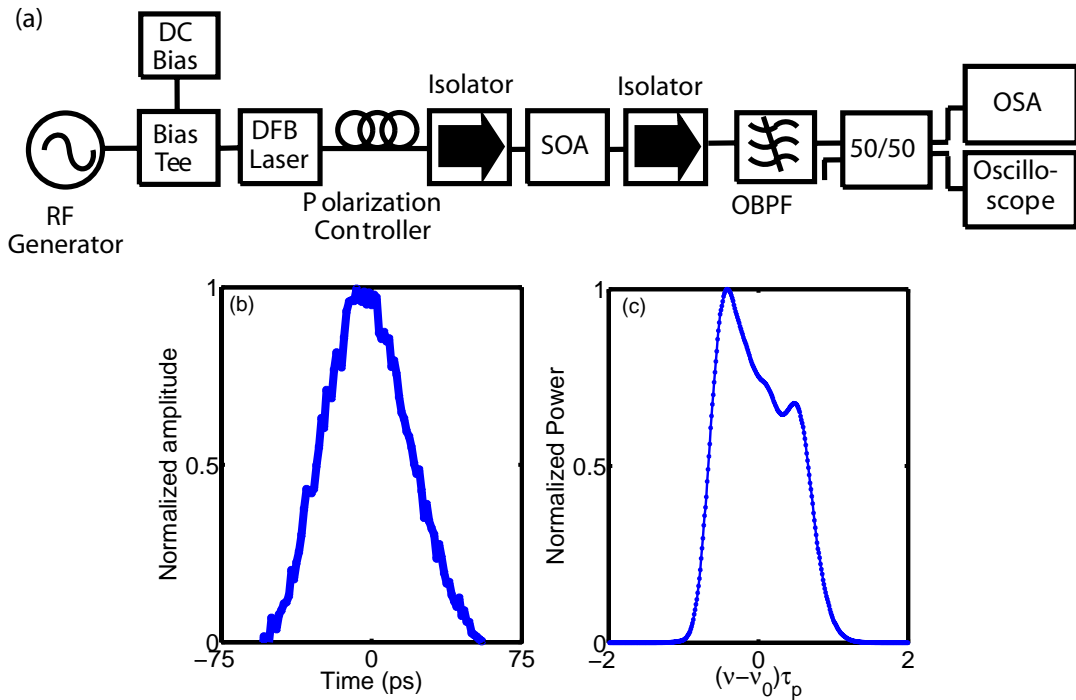


Figure 4.1: (a) Experimental setup. (b) Pulse shape and (c) pulse spectrum produced by the gain-switched DFB laser.

to produce optical pulses with FWHM of 57 ps at a wavelength of 1594.41 nm. Further details on gain-switching and the setup used to generate gain-switched pulses and their optimization can be found in Appendix B. The DFB laser module is part of an ILX lightwave mount whose bias-T circuitry accepts radio-frequency (RF) signals up to 2.5 GHz. The threshold current of the laser was 25 mA at 25°C. To obtain gain-switched pulses, the laser was biased at 14.89 mA and driven with a 1 GHz RF signal with 64.4 mA peak amplitude. Figure 4.1 shows (b) the shape and (c) the spectrum of the resulting gain-switched pulses. The central frequency  $\nu_0 = 188.23$  THz is defined using the first moment of the spectrum. The pulse shape is fitted to a Gaussian function,  $P(t) = P_0 \exp(-t^2/\tau_p^2)$ , resulting in  $\tau_p = 34.2$  ps for a 57 ps pulse. The peak power  $P_0$  of the gain-switched pulses was close to 3 mW. The observed spectrum is asymmetric due to a negative

chirp imposed on the pulse during the gain-switching process. In the notation of Ref. [56], the chirp parameter is estimated to be  $C = -4.91$ .

On the diagnostic end of the experiment setup, an OBPF with a 3 dB bandwidth of 1 nm was used to reject the out of band portion of ASE noise. A 50/50 splitter was employed to send the amplified pulses simultaneously into an OSA with resolution of 0.01 nm and into a PD with a 22 GHz bandwidth. The temporal signal was then captured by a 70 GHz sampling scope (resolution 1.25 ps). The experiments employed an SOA, the optical specifications and characteristics of which, have been presented in Chapter 3.

## 4.3 Experimental Results

### 4.3.1 Spectral Evolution

Figure 4.2 shows the remarkable evolution of the optical spectrum of amplified pulses at the SOA output as the drive current is varied from 40 to 500 mA. For the relatively low drive currents [Fig. 4.2(a)], as the drive current is increased, the spectrum shifts towards the red side with more energy in the red-shifted lobe at the expense of much reduced relative energy in the blue-shifted spectral region. This kind of SPM induced spectral change is associated with SOAs the gain recovery time of which is much longer compared to the pulse width [93]. Until recently, only these kinds of SOAs were available commercially. However, the SOA shows a dramatically different behavior for currents beyond 100 mA, as evident from Fig. 4.2(b). The relative energy of the red-shifted spectral lobe decreases, and at the same time the relative energies in the central lobe and the blue-shifted spectral lobe increase. As a result of these changes, the output spectrum progressively becomes more symmetric at higher currents and acquires features that are typical of SPM in optical fibers [56]. These experimental observations

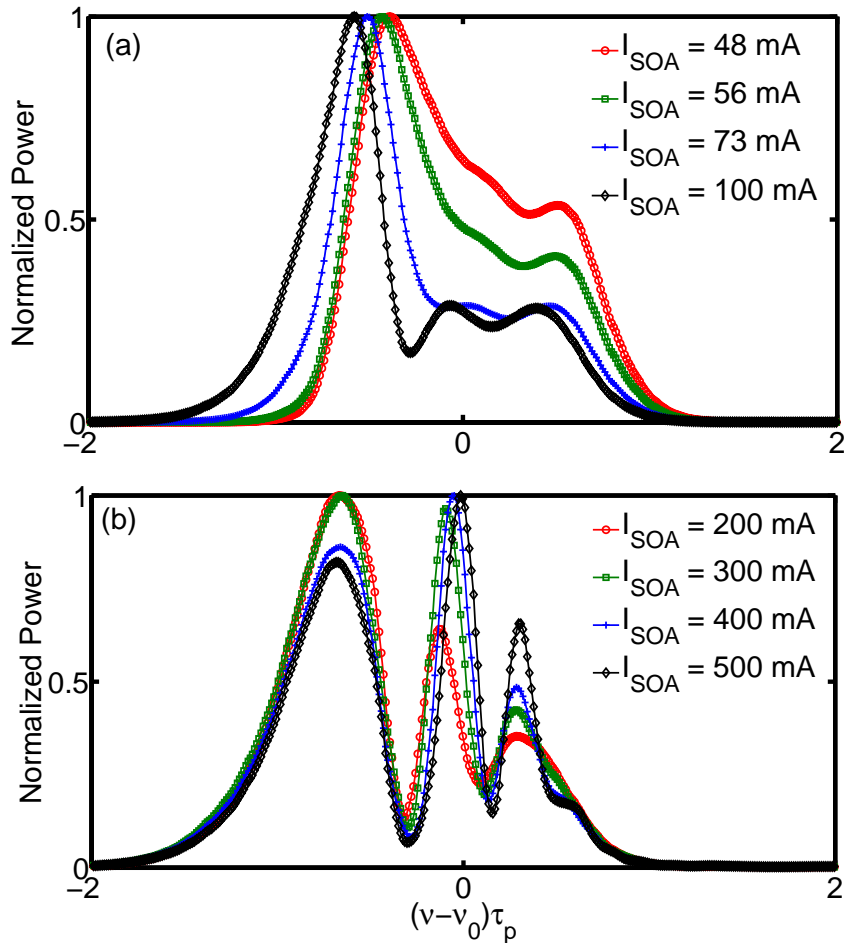


Figure 4.2: Observed spectra of amplified pulses at drive current (a) up to 100 mA and (b) beyond 100 mA.

are consistent with the theoretical results given in Fig. 3.5 and confirm that the ASE-induced reduction in the gain recovery time is responsible for the observed changes at high drive currents.

### 4.3.2 Spectral Symmetry and Broadening

To quantify the extent of spectral changes with the increasing drive current, the amplitudes of the three spectral lobes relative to the maximum spectral power corresponding to each spectral measurement as a function of the drive current are

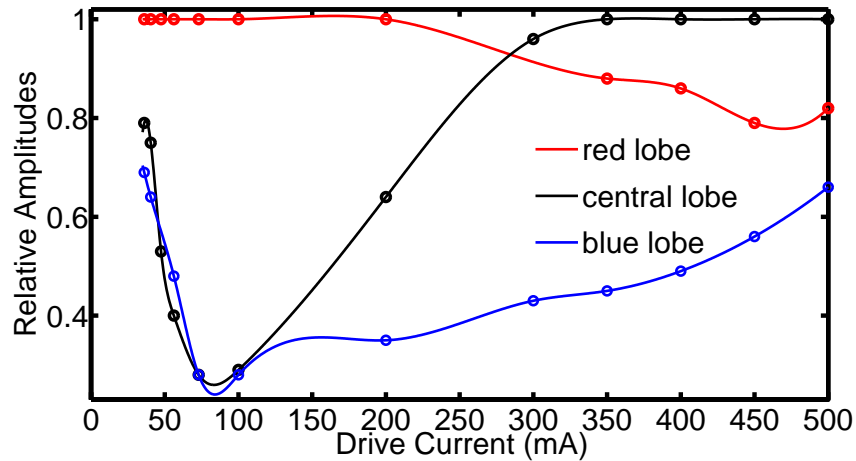


Figure 4.3: Relative amplitudes of the three main spectral lobes seen in Fig. 4.2 as a function of drive current.

plotted in Fig. 4.3. At the lowest drive current of 48 mA, the amplitudes of the blue and central lobes are smaller than the red peak but still so much large that the spectrum can be classified as a three peak spectrum. With increasing drive currents, but below the 100 mA level so that ASE power is relatively small, relative amplitudes of the blue and central lobes decrease rapidly, and the spectrum is dominated by a single red-shifted peak. At drive currents beyond 100 mA, the ASE power level begins to significantly increase the gain recovery time of the SOA. This feature causes a remarkable change in the amplitudes of the three spectral peaks: the relative amplitudes of the central and blue spectral lobes increase rapidly. Beyond a 300 mA drive current, the amplitude of the red-shifted spectral lobe becomes lower than that of central spectral lobe, which evolves to become the highest spectral peak, resulting in a much more symmetric pulse spectrum. As is known from the case of optical fibers [56], a symmetric spectrum is the sign of a nonlinear process that responds almost instantaneously. For this case, the gain recovery time of 9 ps at the maximum drive current becomes much shorter than the width of optical pulses (57 ps), and the spectrum thus begins to exhibit features that correspond to a fast nonlinear process.

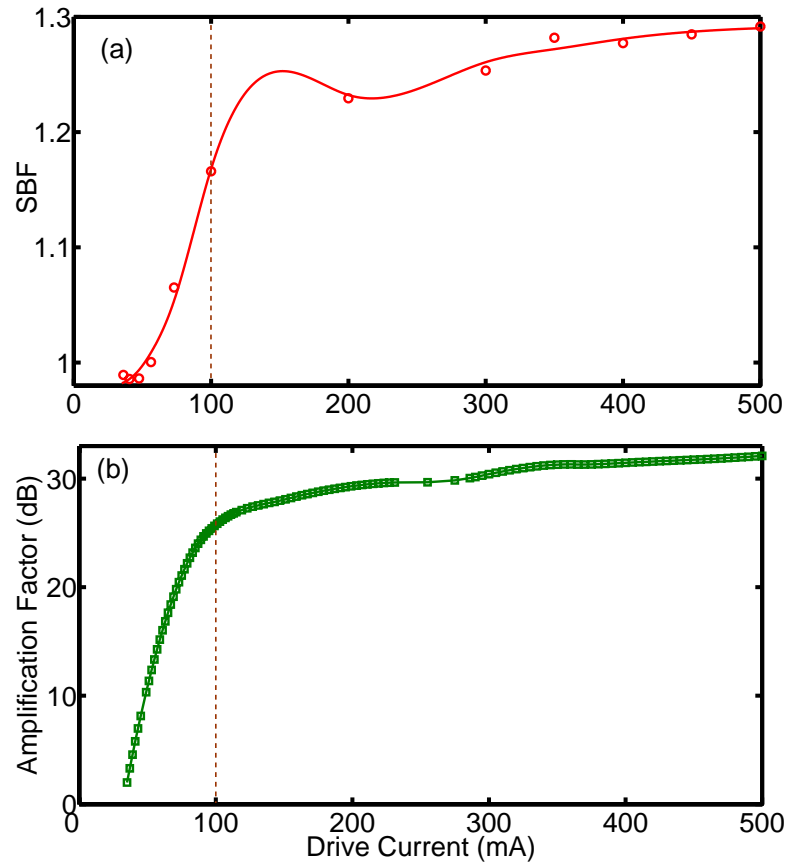


Figure 4.4: (a) Spectral broadening factor (SBF) and (b) measured small signal amplification factor as a function of drive current.

While ASE reduces gain recovery time which improves spectral symmetry, it was observed that the extent of SPM induced spectral broadening is also affected. To quantify the impact on spectral broadening, the first and second moments of the experimentally observed spectrum  $S(\nu)$  are employed. These moments are defined as:

$$\mu_n = \frac{\int_{-\infty}^{\infty} (\nu - \nu_n)^n S(\nu) d\nu}{\int_{-\infty}^{\infty} S(\nu) d\nu}, \quad (4.1)$$

where  $n = 1$  or  $2$ . The two moments can be used to find the spectral width  $\delta\nu = (\mu_2 - \mu_1^2)^{1/2}$ . We define the spectral broadening factor (SBF) as  $\text{SBF} = \delta\nu_{\text{out}}/\delta\nu_{\text{in}}$  and calculate its value as a function of the drive current.

Figure 4.4(a) shows how SBF changes with current. At low drive currents

( $I < 100$  mA), SBF increases almost linearly with the drive current but it begins to saturate at higher drive currents. To understand this saturation behavior, it is important to understand the impact of ASE on the SOA's amplification factor defined as  $G = 10 \log_{10}(P_{out}/P_{in})$ . The experimental setup shown in Fig. 4.1(a) was used to carry out this measurement with minor modifications to accommodate CW light injection. To ensure that the CW signal, launched at the SOA input at a wavelength of 1594.4 nm, does not saturate the amplifier gain, its power,  $P_{in}$ , was limited to only  $2 \mu\text{W}$ . Figure 4.4(b) shows the measured small signal amplification factor as a function of drive current. This curve shows that the signal is amplified exponentially (or linearly on the dB scale used) for currents up to 100 mA, but this exponential growth is reduced dramatically at higher currents because of gain saturation induced by the increasing ASE. The extent of SPM induced spectral broadening achievable from any SOA depends on the SOA amplification factor, in addition to other parameters such as the linewidth enhancement factor [93]. Thus the ASE-induced gain saturation limits the SBF, and at the same time it improves spectral symmetry by reducing the gain recovery time. This trade-off cannot be avoided in SOAs that employ ASE for faster gain recovery.

Note the significance of the 100 mA drive current. This drive current, at which the amplification factor in Fig. 4.4(b) saturates, partitions the gain recovery dynamics of the 9 ps gain recovery time SOA into two regimes. Conventional or slow regime marked by low internal ASE levels and fast regime punctuated by high internal ASE  $\approx 60$  mW [Fig. 3.2(a)]. Further, as seen in Figs. 4.3 and 4.4, the nonlinear response of the SOA changes remarkably at a current level around 100 mA. More specifically, the SOA behaves like a traditional slow gain recovery SOA below this level but its gain recovery time shortens above 100 mA, reaching a value of 9 ps at 500 mA. The simultaneous saturation of small signal gain and gain recovery acceleration controls the device nonlinear response at different injection levels.

## 4.4 Conclusions

In this chapter, it is experimentally demonstrated that the ASE-induced gain saturation changes the gain dynamics in such a way that the SPM features in SOAs begin to resemble those found in optical fibers, but they occur at peak-power levels that are three orders of magnitude lower than those required for optical fibers. Theoretical predictions regarding ASE-assisted SPM in SOAs are verified with an experiment in which the output optical pulse spectra of gain-switched input pulses is measured. The experimental results agree well with the theoretical predictions. While the study presented in this chapter has been done for one particular device length ( $L = 1$  mm), the impact of this important device parameter can be understood by noting that increasing the device length increases the ASE power which potentially can further reduce the recovery-speed. A trade-off between improvement in spectral symmetry and the extent of spectral broadening, mediated by the internal ASE, has also been demonstrated. Understanding this trade-off is important for designing ultrafast, SOA-based, signal-processing techniques such as wavelength conversion and regeneration.



# 5 ASE-Assisted FWM: Experiments and Applications

## 5.1 Introduction

In this chapter, experimental results designed to optimize the device performance for wavelength conversion using FWM in SOAs with ASE-assisted gain recovery acceleration are presented. Further, selected device characterization results are presented and discussed in detail. The CE and the OSNR are the two FOMs used to characterize the FWM process. They are used to study the impact of drive current, pump-signal detuning, input pump and signal powers on wavelength conversion process. In particular, the issue of optimum input pump and signal powers is analysed in detail. The feasibility of all-optical regeneration using FWM in this device is investigated. The experimental results are compared to the numerical results presented in Chapter 3 and the sources of mismatch between the two are identified. Further, a proof of concept demonstration of energy efficient 10 Gb/s wavelength converter for intensity modulated RZ signals with 50% duty cycle is presented. The work presented in this chapter is useful for implementation of energy-efficient, modulation-format transparent WCs for future transparent optical networks.

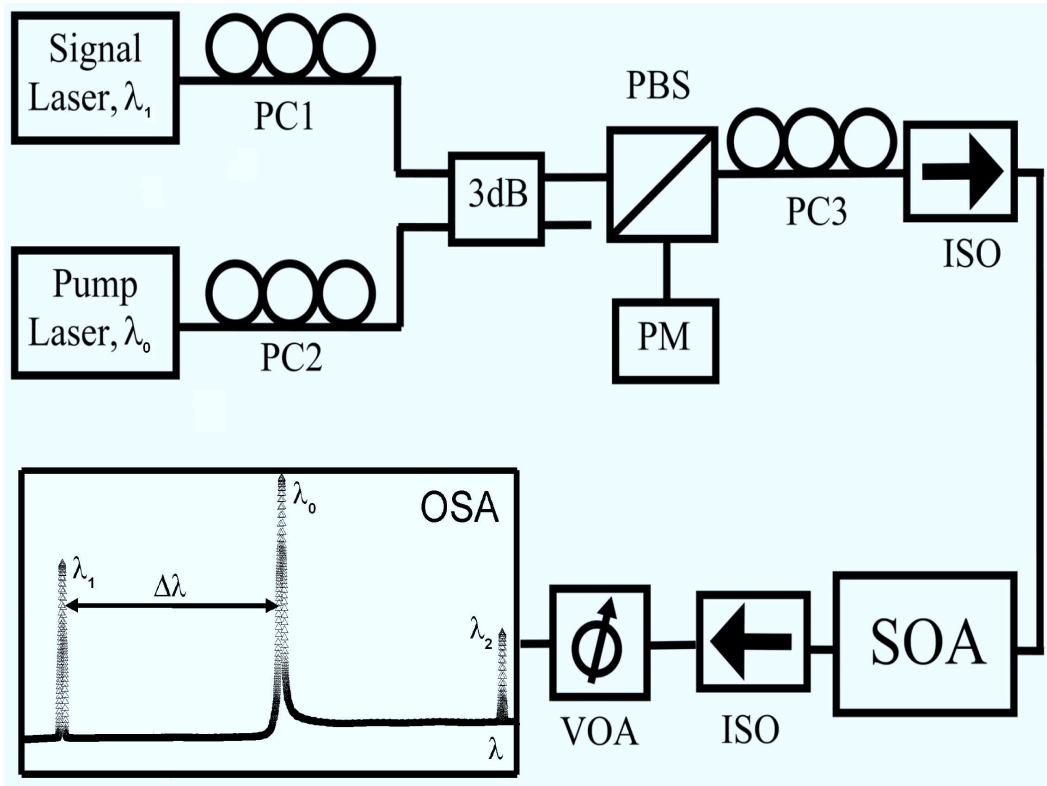


Figure 5.1: Experimental setup used for studying interband FWM. PC: polarization controller; PBS: polarization beam splitter; PM: power meter; ISO: isolator; VOA: variable optical attenuator; OSA: optical spectrum analyzer;  $\Delta\lambda$ : pump-signal detuning.

## 5.2 Experimental Setup

In Chapter 3, it was theoretically established that the interband FWM can be used for wavelength conversion over a large range of pump-signal detunings using low input pump powers if SOAs with ASE-accelerated gain recovery time are employed. To verify the reported theoretical predictions and to investigate various trade-offs required for wavelength conversion performance optimization, a series of experiments are performed using the setup illustrated in Fig. 5.1.

In the proposed setup, the pump and signal are combined using a 3 dB coupler

and sent through a PBS whose role is to ensure that pump and signal remain co-polarized throughout the experiment. The exclusive excitation of only the transverse-electric (TE) mode of the SOA is ensured by proper adjustment of polarization controller PC3. The pump wavelength  $\lambda_0$  is fixed at 1574.93 nm to keep it close to the SOA gain peak at 1570 nm. The signal wavelength  $\lambda_1$  is tuned over a wide range on the short wavelength side (blue-shifted). The insertion and coupling losses after the PBS are estimated to be 3 dB. The isolators are used to minimize back reflections. A VOA (Agilent 8156A) was used at the SOA output to ensure that optical powers at the OSA were below its safe limit. It was calibrated using a broadband ASE source and exhibited a 3.3 dB IL, while providing 20 dB attenuation over 1500–1600 nm with a wavelength dependence of  $< 0.2$  dB. The total attenuation at the output end, including output coupling loss and IL of the isolator and optical attenuator, was estimated to be 30.3 dB at 1570 nm; its wavelength dependence was negligible in the wavelength range 1565–1585 nm. The SOA temperature was fixed at 25 °C for all the measurements.

## 5.3 Wavelength Conversion Optimization

### 5.3.1 Device Characterization

Before reporting the FWM results, the measurements performed to characterize the nonlinear SOA are discussed. Figure 5.2(a) shows the ASE spectra at 100, 300 and 500 mA bias currents. The gain peak of the spectrum near 1570 nm shifts towards the blue side with increasing current. Moreover, a considerable increase in the amplitude of rapid oscillations near the gain peak at high drive currents is also observed. These oscillations have a period of 0.3 nm and have their origin in the residual feedback at the two SOA end facets, resulting in FP effects [5]. As discussed in the later part of the text, they constitute a major source of mismatch

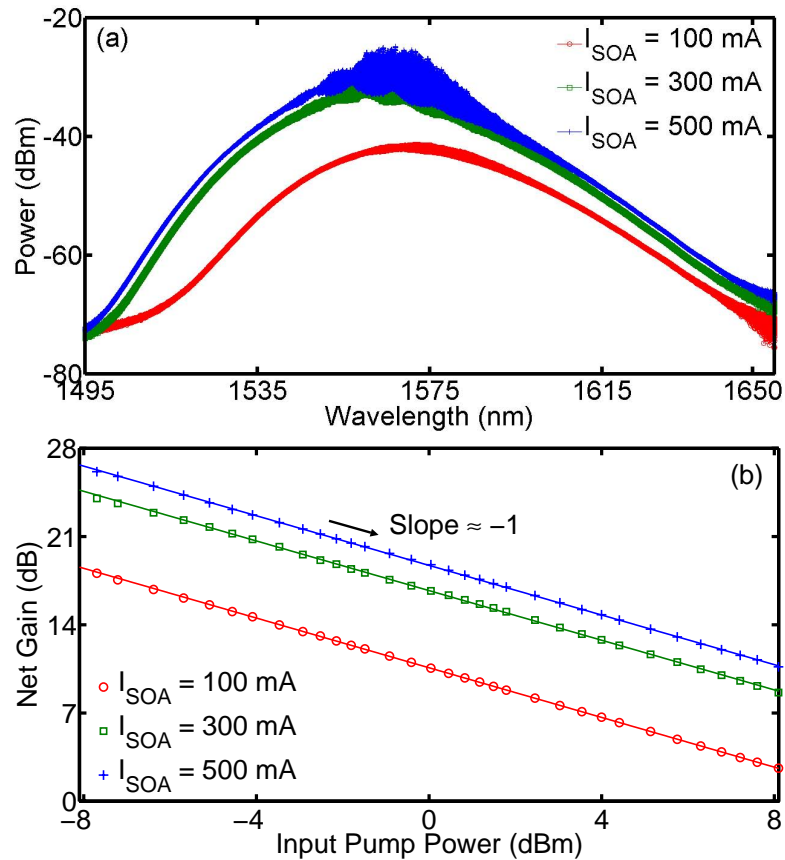


Figure 5.2: (a) The ASE spectra at 100, 300 and 500 mA. (b) Net device gain as a function of pump power. Input signal power and pump-signal detuning  $\Delta\lambda$  were  $-20.3$  dBm and  $2.5$  nm, respectively.

between the theoretical predictions and experimental results.

In Fig. 5.2(b), the net SOA gain is plotted as a function of input pump power at three drive currents. The net gain is defined as the ratio of total output power (sum of pump, signal and idler powers) to total input power (sum of pump and signal power). The solid lines in this Fig. are a linear fit to the experimental data. A negative slope of  $-1$  is expected from the saturation of average gain in Eq. (3.25). A different slope would indicate the onset of intraband effects [5] and is observed in traditional SOAs [159]. These results confirm that the intraband FWM effects are almost negligible in the range of input pump powers used in

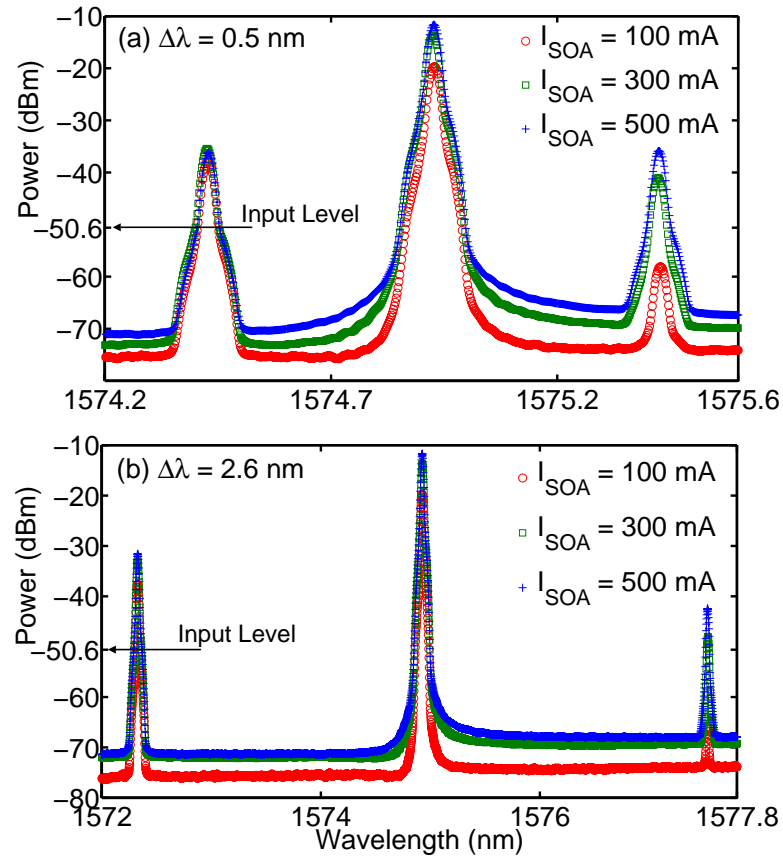


Figure 5.3: FWM spectra measured at three currents for a pump-signal detuning of (a) 0.5 nm and (b) 2.6 nm at a pump power of  $-3.3$  dBm. The input signal level ( $-20.3$  dBm) is marked by an arrow.

these experiments.

### 5.3.2 Drive Current

The impact of increasing the drive current  $I_{\text{SOA}}$  on the FWM process is analyzed here. Figure 5.3 shows the optical spectra at the SOA output for two different pump-signal detunings. The peak on the right side of the pump corresponds to the idler created through interband FWM. For  $\Delta\lambda = 0.5$  nm, the idler is generated at current levels as low as 100 mA, and its power increases by more than 20 dB

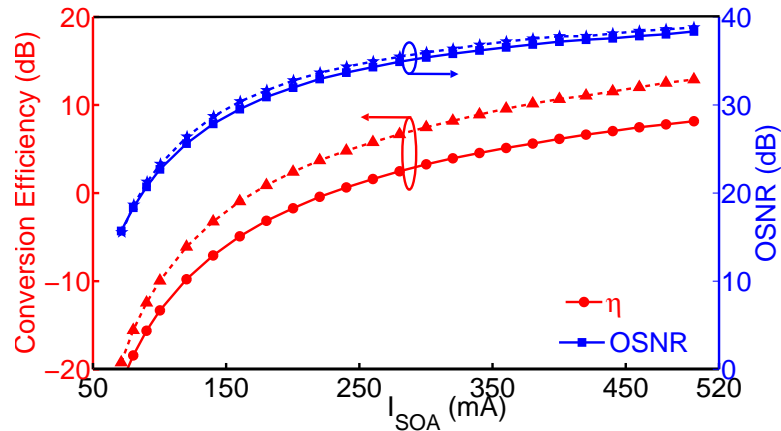


Figure 5.4: Conversion efficiency and OSNR as a function of  $I_{\text{SOA}}$  for  $\Delta\lambda = 0.5$  nm at a pump power of  $-3.3$  dBm (dashed curves) and  $+3.3$  dBm (solid curves). Input signal power was  $-10$  dBm.

as  $I_{\text{SOA}}$  is increased to 500 mA. Multiple signal-idler pairs are observed with increasing  $I_{\text{SOA}}$  (not shown here) in agreement with previously reported results for small  $\Delta\lambda$  [172].

At a large pump-signal detuning of 2.6 nm, negligible FWM occurs at low drive currents ( $<120$  mA). However, the idler is greatly enhanced with increasing  $I_{\text{SOA}}$ , indicating a sharp reduction in the gain recovery time induced by the enhanced ASE [88,90,108,109,172]. From the theory presented in Chapter 3, the magnitude of idler peak corresponds to an effective carrier lifetime of 21 and 10 ps at 300 and 500 mA, respectively (calculated using the method outlined in [90]).

The FWM spectra in Fig. 5.3 show that the ASE noise spectral density near the idler wavelength increases by more than 7 dB as  $I_{\text{SOA}}$  is increased from 100 to 500 mA. Since the ASE power is increasing, it should be ensured that the improvement in the CE  $\eta$  at large  $I_{\text{SOA}}$  is not accompanied with a degradation of the OSNR at the converted wavelength. To understand this issue,  $\eta$  and OSNR as a function of drive current for two different pump powers are plotted in Fig. 5.4. As seen there, OSNR actually increases with increasing current, indicating that the increase in

the in-band ASE noise is more than compensated by the considerable increase in the idler power. An OSNR of  $> 30$  dB along with a reasonable CE ( $\eta > 50\%$ ) can be achieved for  $I_{\text{SOA}} > 160$  mA. At a pump power of  $+3.3$  dBm,  $\eta$  decreases by about 4 dB because of pump-induced gain saturation (discussed in Chapter 3), but the corresponding reduction in OSNR is much smaller ( $< 0.5$  dB). This can be explained by noting that, while the idler power is reduced considerably at higher pump powers, the in-band ASE noise is also reduced because of pump-induced gain saturation.

### 5.3.3 Pump-Signal Detuning $\Delta\lambda$

From the standpoint of designing practical WCs, the relevant issue is how large wavelength shifts are possible if FWM in SOAs with ASE-assisted gain-recovery acceleration is used for wavelength conversion, or alternatively, how large  $\Delta\lambda$  can be while maintaining good CE and OSNR. Figure 5.5 shows the CE  $\eta$  and OSNR as a function of  $\Delta\lambda$  at the same two pump powers. As expected, both degrade as  $\Delta\lambda$  increases, indicating that one should not increase  $\Delta\lambda$  beyond an upper limit. If  $\eta > -10$  dB (10%) is used as an acceptance criterion, this upper limit is  $< 1$  nm at 100 mA but increases to more than 10 nm at 500 mA. Further, at any detuning,  $\eta$  and OSNR are enhanced by more than 20 and 12 dB, respectively, when drive current is increased from 100 to 500 mA. This increase in  $\eta$  and OSNR is observed for both pump powers.

It was demonstrated in Chapter 3 that the enhancement in  $\eta$  is due to faster gain recovery caused by a large increase in the ASE power at high currents. Enhancement in  $\eta$  (or the idler power) with increasing drive current does not translate in its entirety to an increase of OSNR. In Fig. 5.5, a 20 dB enhancement in  $\eta$  translates into an OSNR increase of only about 12 dB as current is increased from 100 to 500 mA. However, the OSNR exceeds 20 dB up to a detuning of about 5 nm at  $-3.3$  dBm pump power at a drive current of 500 mA. With an increase in

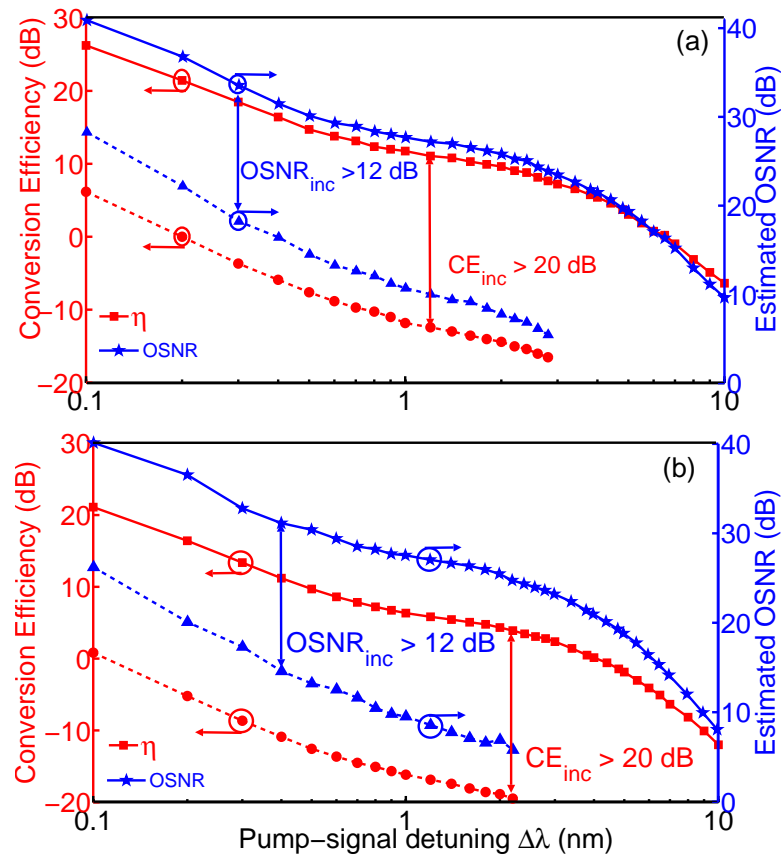


Figure 5.5: Conversion efficiency and OSNR as a function of  $\Delta\lambda$  at a pump power of (a)  $-3.3$  dBm and (b)  $+3.3$  dBm for input signal power of  $-20.3$  dBm. Dashed and solid curves correspond to 100 and 500 mA drive currents, respectively.

input pump power from  $-3.3$  to  $+3.3$  dBm, both  $\eta$  and OSNR are reduced. This indicates that pump power should be optimized suitably.

### 5.3.4 Optimization of Pump and Signal Powers

In this section, the role of input pump power  $P_0$  is investigated by varying it in the range of  $-8$  to  $+8$  dBm. This range corresponds to the range over which the net device gain was measured in Fig. 5.2(b), and over which the intraband FWM effects are negligible. The SOA current is fixed at 500 mA in the following



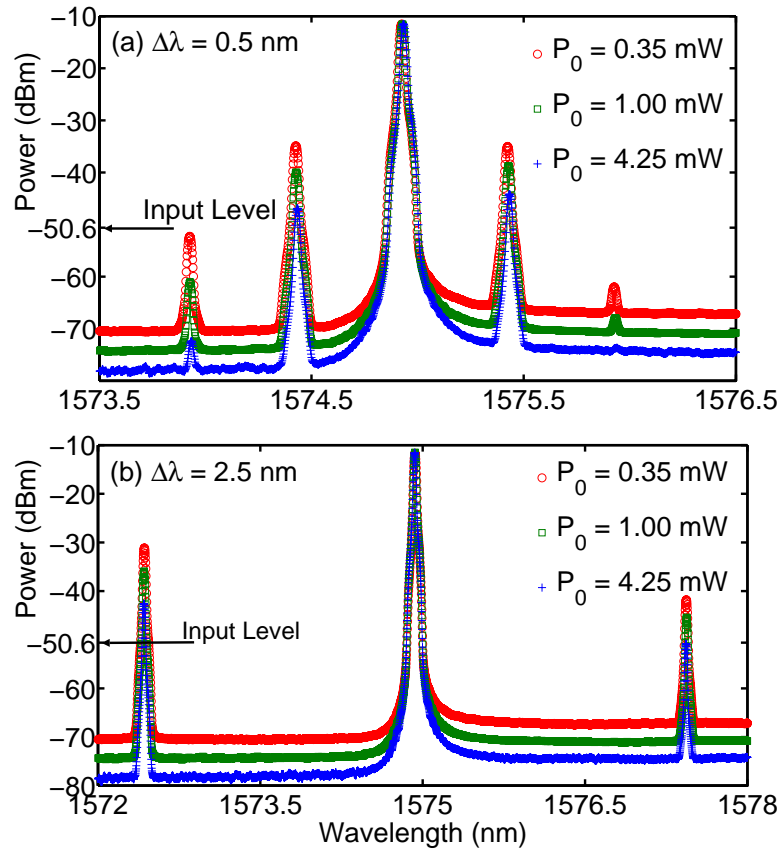


Figure 5.6: FWM spectra observed at three input pump powers for pump-signal detunings of (a) 0.5 nm and (b) 2.5 nm. The SOA current is 500 mA and the signal level ( $-20.3$  dBm) is marked by an arrow.

measurements.

Figure 5.6 shows the FWM spectra at three pump powers for (a)  $\Delta\lambda = 0.5$  nm and (b) 2.5 nm. In both cases, peak heights at the signal and idler wavelengths decrease with increasing pump power, indicating that a higher pump power leads to smaller values of  $\eta$ . The reason for this behavior has been discussed in Chapter 3 in the context of Fig. 3.6(b) and is related to pump-induced gain saturation. As the pump is amplified inside the SOA, its power increases and can become comparable to the ASE power near the output SOA end. At a relatively low input pump power close to 0.1 mW, total ASE power dominates the pump power over

nearly the entire SOA length. However, as input pump power exceeds 1 mW, gain saturation induced by an intense pump decreases the ASE power near the output SOA end, which increases the gain recovery time and reduces the CE. Clearly, high input pump powers should be avoided for WCs based on SOAs making use of ASE-induced gain saturation.

However, the impact on OSNR needs to be investigated before concluding that lower input pump powers are always better. It can be seen from Fig. 5.6 that regardless of the pump-signal detuning, both the in-band ASE spectral density and the peak heights at the idler wavelength are reduced with increasing  $P_0$ . The qualitative behavior of OSNR with increasing pump powers cannot be inferred from this. Therefore, to clearly understand the trade-off associated with increasing the input pump power, the evolution of  $\eta$  and OSNR as a function of  $P_0$  is plotted in Fig. 5.7. We see clearly that, while  $\eta$  decreases monotonically with increasing  $P_0$ , the OSNR exhibits a broad maximum near  $P_0 = -2$  dBm (about 0.6 mW). After this maximum, the OSNR drops when  $P_0$  is increased beyond 2 dBm. The reason is understood by noting that, beyond  $P_0 = 2$  dBm, reduction in the idler power becomes much more severe compared to reduction in the in-band noise. The optimum value of  $P_0$  for a WC is dictated to some extent, by the design requirements. For example, if the requirement is that the OSNR should exceed 23 dB, pump powers as low as to 0.1 mW ( $-10$  dBm) can be used to maximize  $\eta$ .

It should be stressed that the qualitative behavior of  $\eta$  and OSNR in Fig. 5.7 is quite different from that observed when intraband FWM is employed. In that case, it has been shown that both  $\eta$  and OSNR increase linearly with  $P_0$  over a wide range of pump powers [158–160]. This feature can be attributed to the fact that the gain saturation induced either by the pump or by the ASE plays little role in the intraband FWM process in traditional SOAs. Both  $\eta$  and OSNR, therefore, increase monotonically with increasing pump power because the idler power (governed mainly by the device gain) keeps increasing until the pump starts

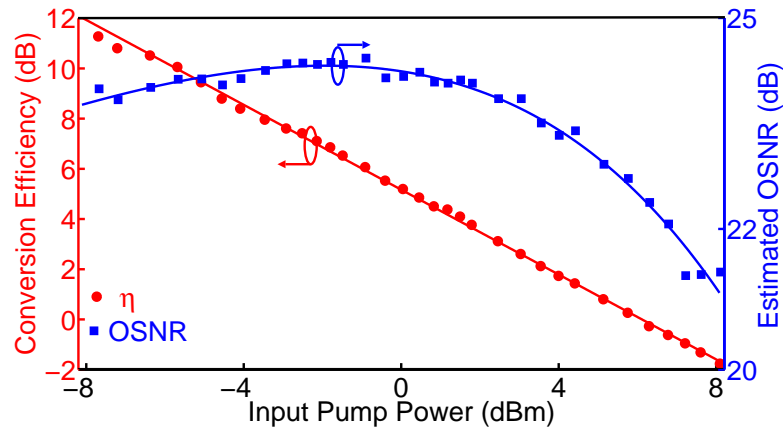


Figure 5.7: Conversion efficiency (circles) and estimated OSNR (squares) measured as a function of  $P_0$  at 500 mA drive current. Solid lines represent a fit to the experimental data. Input signal power was  $10 \mu\text{W}$  at a pump-signal detuning of 2.5 nm.

to reduce the device gain owing to the gain compression effects [159].

The role of input signal power  $P_1$  is considered next. Figure 5.8 shows how  $\eta$  and OSNR vary as function of  $P_1$  at two drive currents (300 and 500 mA) and at pump powers of (a)  $-2.2$  dBm and (b)  $+3.3$  dBm. The first thing to notice is that  $\eta$  remains almost constant until  $P_1$  becomes comparable to  $P_0$  and then, in-turn, starts to saturate the SOA gain. In contrast, OSNR increases linearly with  $P_1$  until it saturates to a value near 35 dB for large values of  $P_1$  near 1 mW. These features can be understood as follows. As long as input signal power  $P_1 \ll P_0$ , the signal and the idler remain weak enough that they do not cause gain saturation, and  $\eta$  remains constant. The situation changes when  $P_1$  becomes comparable to  $P_0$ , and  $\eta$  begins to decrease with increasing  $P_1$ . The OSNR improves with increasing  $P_1$  because of an increase in the output idler power, while the ASE level remains nearly constant. The saturation of OSNR occurs once the idler gain is reduced because of gain saturation induced by the intense signal and idler fields. Practical WCs based on SOAs typically require  $\eta > -10$  dB and OSNR  $> 30$  dB,

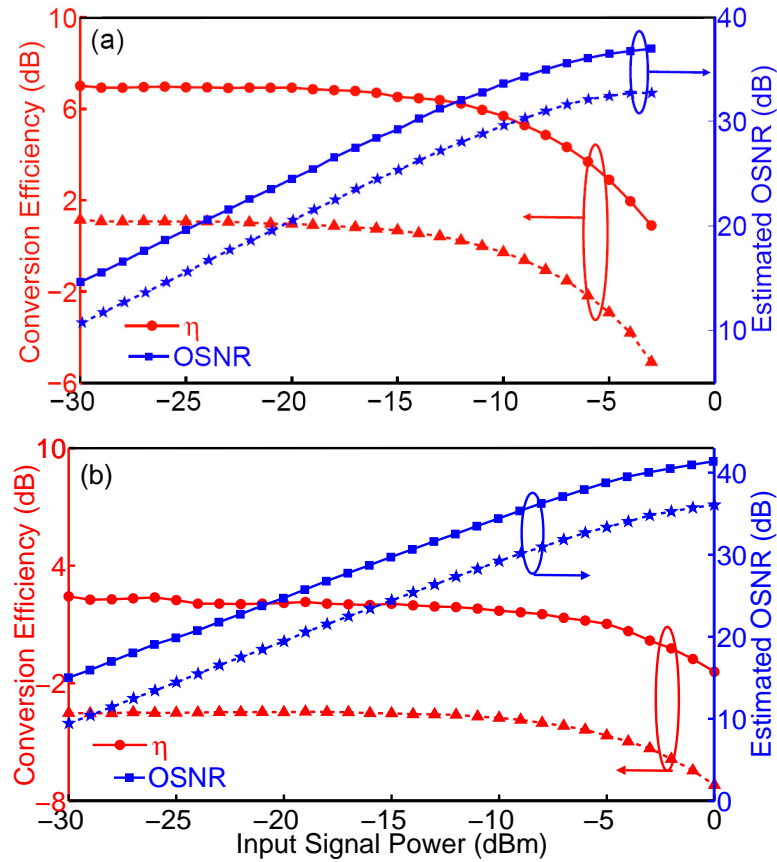


Figure 5.8: Conversion efficiency and OSNR measured as a function of  $P_1$  at (a)  $P_0 = -2.2$  dBm and (b)  $P_0 = +3.3$  dBm for  $\Delta\lambda = 5$  nm. Dashed and solid lines correspond to drive currents of 300 and 500 mA, respectively.

while providing a WS of 10 nm or so [25, 164]. It can be seen from Fig. 5.8, that these conditions can be met for  $P_1/P_0 \approx 0.1$ .

The performance of a WC can be characterized by its power transfer function showing output idler power as a function of input signal power. Figure 5.9 shows this transfer function at two different input pump powers. A WC is usually operated in the linear regime of a power transfer function. Note that the linear regime of the transfer function extends over a wider range of signal powers for a higher input pump power. Although the dynamic range of signal powers is larger at higher pump powers, it comes at the expense of reduced CE. Also, the nonlinear

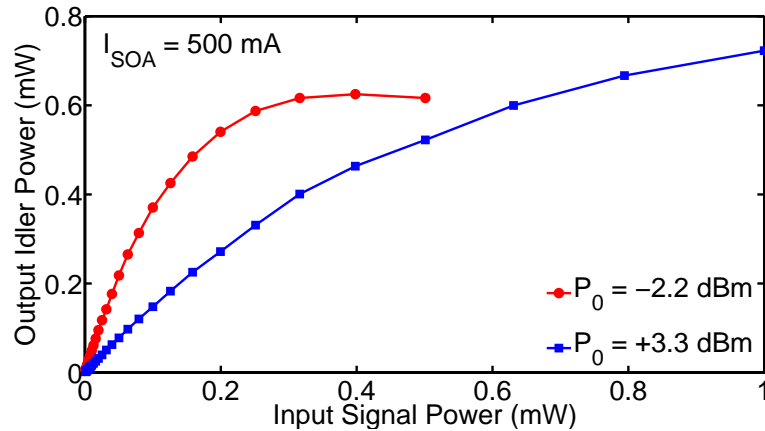


Figure 5.9: Power transfer function for the two pump powers at 500 mA SOA current. The WS is 5 nm.

patterning effects due to slow SOA gain recovery dynamics will come into play at higher pump and signal powers [164]. It is, therefore, likely that the WCs based on interband FWM will be operated at input pump powers close to 0.1 mW to take full advantage of ASE-induced ultrafast gain recovery. This will also ensure low energy footprint of such WCs.

A WC can also act as an all-optical regenerator of a telecommunication channel if its power transfer function has a step-like shape that enables a reduction in signal noise at the converted wavelength [18,38]. As can be seen from Fig. 5.9, the shape of the power transfer function is far from being a step function. Although the plateau-like region at low pump powers may be useful for suppressing power fluctuations in the “1” bits, noise fluctuations in “0” bits cannot be suppressed.

### 5.3.5 Comparison with Theoretical Predictions

In this section, the agreement between experimental results presented in Chapter 4 with the theoretical model of Chapter 3 is studied. The model predicts that relatively large wavelength shifts are possible in SOAs operated at high currents because enhanced ASE forces the carriers to recombine at a rate much faster than

their natural recombination rate set by the carrier lifetime. This prediction indeed holds for this device. A more detailed comparison shows that the experimental results are in agreement with the theoretical predictions qualitatively. A perfect quantitative agreement is not expected because the theoretical model makes following three simplifying assumptions.

1. The effects of ASE are incorporated by assuming that the average ASE power is constant along the SOA length and is related to the carrier density as  $P_{\text{ASE}} = DN^2$  [90]. In reality, ASE power fluctuates in time and also varies along the amplifier length because of the amplified pump induced gain saturation.
2. The SOA acts as a traveling wave amplifier with no reflections at its two end-facets. In reality, there is always residual feedback at the end-facets, resulting in some FP effects. These effects manifest as the spectral fringes in the ASE spectra shown in the inset of Fig. 5.2(a). As seen there, the fringe amplitude becomes relatively large at 500 mA drive current. Most of the measurements reported in this chapter were carried out at this drive current.
3. The third simplification consists of neglecting the wavelength dependence of the SOA gain over the wavelength range occupied by the the pump, signal, and idler. This is a reasonable assumption for small pump-signal detunings ( $\Delta\lambda < 5$  nm), given that the gain bandwidth of the SOA is close to 35 nm. However, this assumption is unlikely to hold for larger detunings.

As a check on the accuracy of the numerical predictions, the theoretical predictions and experimental observations are compared in Fig. 5.10 by plotting the CE as a function of pump-signal detuning when the SOA is operated at 100 and 300 mA drive currents. The agreement is not expected to be perfect because the numerical model completely ignores the FP effects resulting from the residual facet

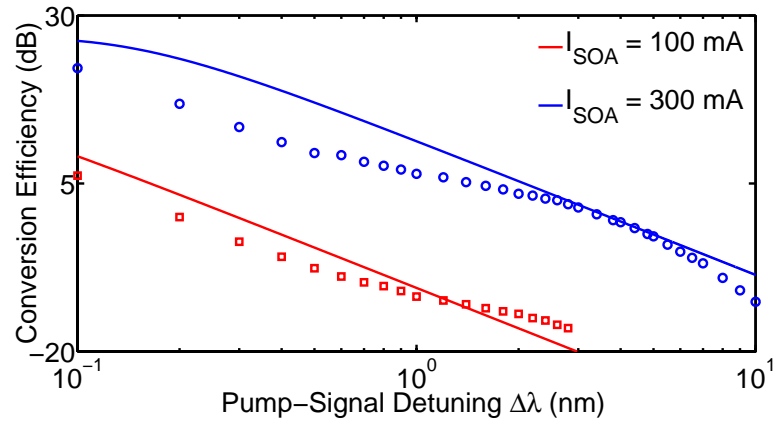


Figure 5.10: Conversion efficiency as a function of  $\Delta\lambda$  at SOA currents of 100 and 300 mA. Solid lines are obtained from the numerical model, whereas symbols represent experimental data.  $P_0$  and  $P_1$  are  $-3.3$  and  $-20.3$  dBm, respectively.

feedback. These effects become worse at higher drive currents, and consequently the numerical model also becomes less accurate quantitatively. However, it still makes reasonable qualitative predictions. As an example, Table 5.1 compares the experimentally observed values with the theoretically calculated pump-signal detunings for which 100% CE is obtained (output idler power equals input signal power) in the case of 0.47 mW input pump power.

Table 5.1: Calculated and Observed Values of  $\Delta\lambda$  for  $\eta = 1$  and  $P_0 = 0.47$  mW

SOA Current	Theory	Experiment
100 mA	0.24 nm	0.20 nm
300 mA	3.20 nm	3.6 nm
500 mA	7.14 nm	6.6 nm

It is possible to improve the numerical model by including the ASE effects more accurately. One approach divides the ASE spectrum into multiple frequency

bins and writes for each spectral slice of the ASE two Eqs. corresponding to the propagation in the forward and backward directions and solve them together with the Eqs. for the pump, signal and idler fields. Up to 45 Eqs. need to be solved simultaneously to accurately calculate the gain and the carrier density at each point of the amplifier [109]. The inclusion of end-facet reflections adds additional complexity as one has to consider the forward and backward propagation of the pump, signal and idler fields as well. Even a small reflection due to residual facet reflectivity can be greatly amplified within the device, especially at high currents when the device gain is high.

## 5.4 10 Gb/s, Sub-mW Input-Optical Pump, L-Band Wavelength Converter

Practical wavelength converters based on intraband FWM in SOAs have attracted a lot of attention recently due to their ease of implementation, data transparency and bit rate independence [25, 41, 170]. They however suffer from poor CE (10% or less). This in turn adversely affects the converted OSNR which is compensated for by either amplifying the pump or the probe which adds to the power consumption of the scheme [170]. Use of holding beam to improve the performance of FWM-based wavelength converter has been investigated in detail [168]. However, typical holding beam powers required to improve the wavelength converter performance exceed 15 dBm. In this section, a wavelength converter for 10 Gb/s, L-Band, RZ signals with 50% duty cycle, based on ASE-assisted interband FWM in SOA is experimentally demonstrated. Using the theoretical and experimental optimization results for CW signals, efficient wavelength conversion ( $CE > 0$  dB) for wavelength-shifts upto 1000 GHz is observed. Typical input optical pump-power required for the implementation of this wavelength convertor is less than 0 dBm ( $< 1$  mW) and no external assist beam was used. The issue of optimum



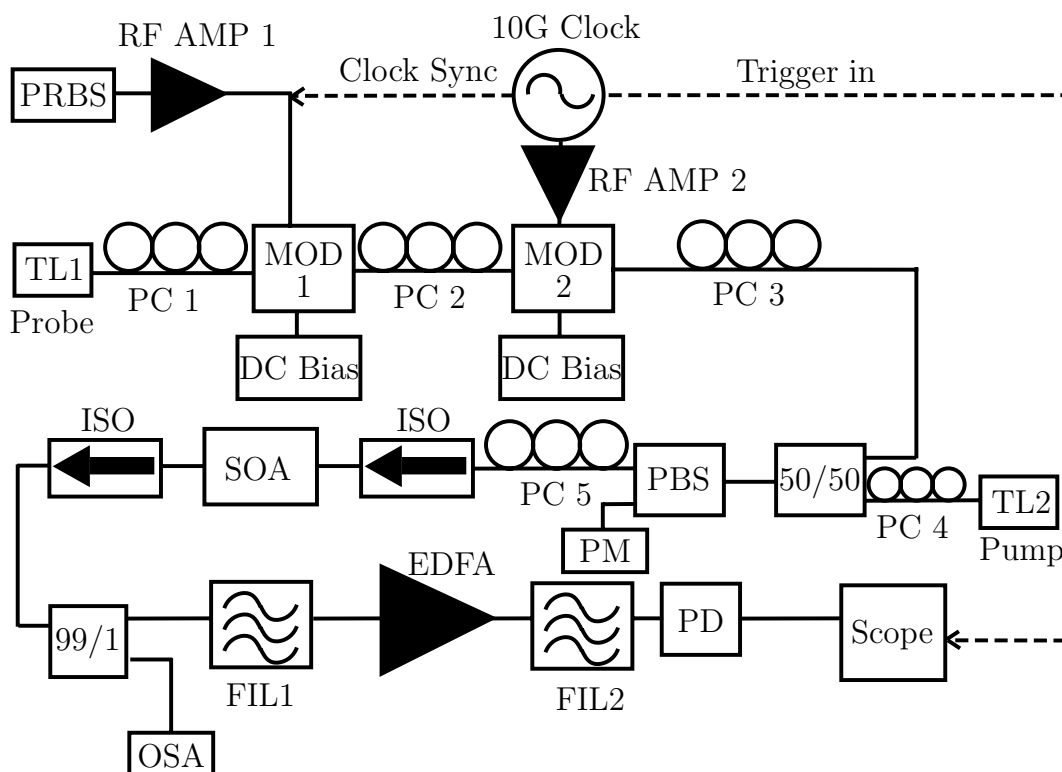


Figure 5.11: Experimental setup used for proof of concept demonstration of 10 Gb/s wavelength converter for RZ-50 signals based on ASE-assisted interband FWM in SOA. PC: Polarization Controller; PBS: Polarization Beam Splitter; PM: Power Meter; 50/50: 3 dB Splitter; 99/1: 1% power tap; RF AMP: RF Amplifier; EDFA: Erbium-Doped Fiber Amplifier; FIL: Optical Filter; MOD: 10 Gb/s Intensity Modulator; VOA: Variable Optical Attenuator; ISO: Isolator; OSA: Optical Spectrum Analyzer.

input pump power ( $P_0$ ) from the standpoint of CE and OSNR is examined in detail.

### 5.4.1 Experimental Setup

Figure 5.11 shows the experimental setup used for proof of concept demonstration of 10 Gb/s wavelength convertor for L-Band, RZ-OOK signal with 50% duty cycle, based on ASE-assisted interband FWM inside a SOA. Similar to the setup used for CW signals [Fig. 5.1], in this setup as well, the pump and signal are combined using a 3 dB coupler and sent through a PBS whose role is to ensure that pump and signal remain copolarized throughout the experiment. This is achieved by individually adjusting the PC3 and PC4 so that the power detected by the power meter is minimum ( $-30$  dBm or less). This power meter also serves as a monitor to ensure the accuracy of input pump ( $P_0$ ) and probe ( $P_1$ ) powers going into the SOA for the duration of the experiment. A significant difference from the CW experiment is in the probe section which has an added 10 Gb/s, LiNbO<sub>3</sub> dual Mach-Zehnder modulator (MZM) [177]. In this experiment RZ pulses with 50% duty cycle are 'carved' from the NRZ data at the output of MOD 1 by modulating MOD 2 with a sinusoidal voltage at 10 Gb/s [4]. Further details on the generation of the NRZ data, 'carving' of RZ pulses, the experimental setup and the optimization of the data pulses are discussed in Appendix C.

The probe power and the SOA drive current were fixed at  $-11.7$  dBm and 500 mA respectively. Exclusive excitation of only the TE mode of the SOA is ensured by proper adjustment of polarization controller PC5. The pump wavelength  $\lambda_0$  is fixed at 1574.54 nm to keep it close to the SOA gain peak at 1570 nm. Further, this wavelength corresponds to the channel no. 45 (ch45) of the L-Band dense wavelength division multiplexed (DWDM) International Telecommunication Union (ITU) Grid, with 100 GHz channel spacing [178]. Another key difference in this experiment is that the signal wavelength  $\lambda_1$  is tuned over a wide range on the long wavelength side (red-shifted) as opposed to the blue shifted configuration used in CW experiments. This was done to achieve the best converted OSNR. The insertion and coupling losses after the PBS are estimated to

be 3 dB. The isolators at the input and output of the SOA are used to minimize back reflections.

At the isolator output, a 1% power tap serves two purposes. The first is to ensure that optical powers at the OSA were below its safe limit. The second is to facilitate simultaneous acquisition of the spectral and temporal data. The total attenuation in the OSA branch, including output coupling and IL of the isolator, 99/1 splitter and OSA, was estimated to be 26.7 dB at 1575 nm. The wavelength dependence of these losses was negligible in the wavelength range of interest (1565–1585 nm). In the PD arm, the output filter FIL1 is the Alnair Labs BVF–200, with its tunable bandwidth set to 0.5 nm and its center wavelength set at converted wavelength ( $\lambda_2$ ). This filter has out of band suppression in excess of 50 dB which effectively eliminates the entire out of band ASE added by the SOA. This however comes at a price. The IL for this filter exceeds 5 dB and therefore an EDFA had to be used as a preamplifier to boost the power level of the converted signal. An OBPF with a 3 dB bandwidth of 1 nm (FIL2) was used to reject the out of band portion of ASE noise added by the EDFA. In the absence of a photoreceiver, a PD with a 22 GHz bandwidth was used to detect the incoming data stream at the converted wavelength. The temporal signal was then captured by a 70 GHz sampling scope (resolution 1.25 ps). The SOA temperature was fixed at 25 °C for all the measurements.

### 5.4.2 Spectral Analysis

In this section the spectral impact of ASE-assisted FWM on pump, probe and the converted signal is investigated. Figure 5.12(a)–(c) shows the FWM spectra for L-Band wavelength conversion measured at the 1% power tap for four different input pump powers and corresponding to three different wavelength shifts. The pump wavelength corresponds to channel no. 45 of L-Band ITU grid with 100 GHz grid spacing [178]. Parts (a), (b) and (c) correspond to 200, 400 and 1000

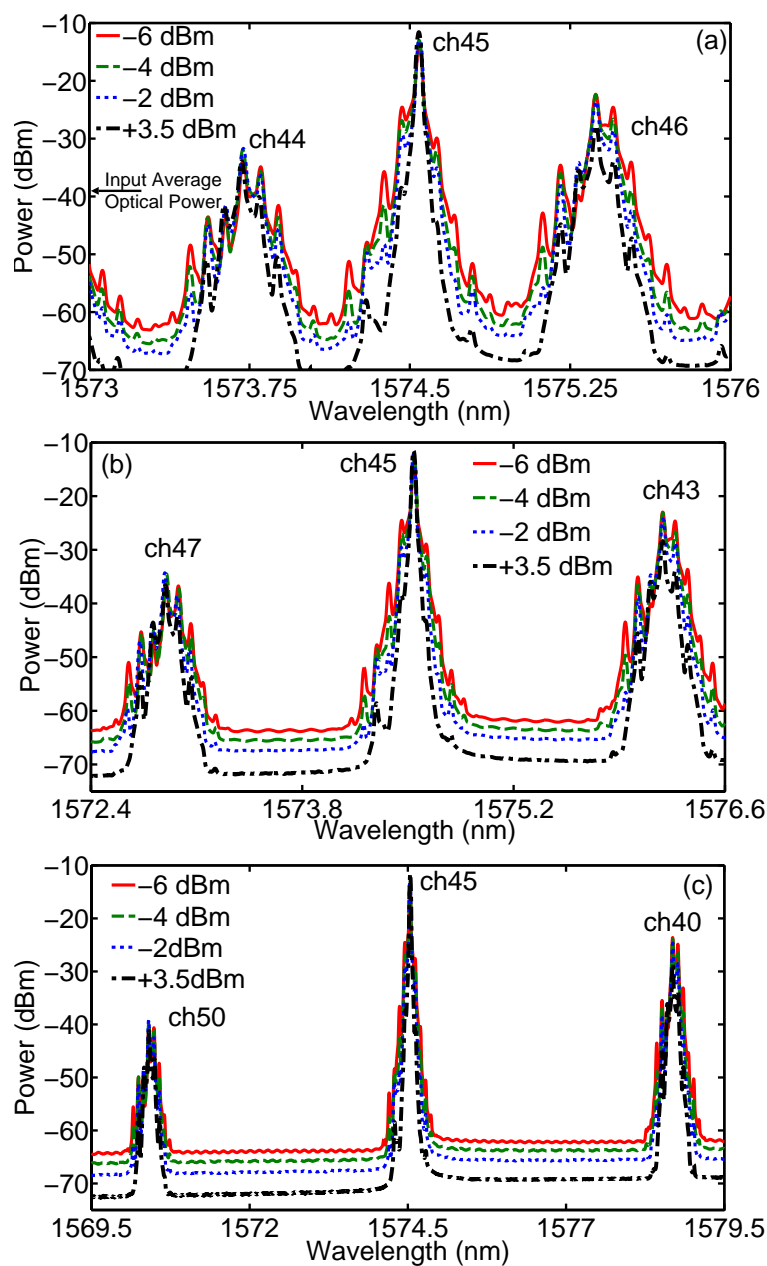


Figure 5.12: FWM spectra for L-Band wavelength conversion measured at the 1% power tap for four different input pump powers. The pump wavelength corresponds to channel no. 45 of L-Band ITU grid with 100 GHz grid spacing [178]. Part (a) corresponds to wavelength conversion from channel no. 44 to 46, (b) channel no. 43 to 47, and (c) channel no. 40 to 50.

GHz wavelength shifts respectively. Comparing the spectra in Fig. 5.12 to those for CW pump and probe (Fig. 5.6), it can be seen that for intensity modulated signals, reduction in  $P_0$  not only enhances the FWM CE, but also causes spectral broadening and chirping at pump, probe and conjugate wavelengths.

The physical mechanism behind this can be explained as follows: At low pump powers, there is significant internal ASE power in the device. As explained in Chapter 3, this increased internal ASE drives up the CE which in turn increases the average optical power at the converted wavelength ( $P_2$ ). As a result, pulses at the converted wavelength suffer SPM induced by the SOA gain dynamics. Further, at low  $P_0$ , the pump, probe and the converted signal powers are of the same order of magnitude. This causes the probe to impose an additional chirp at the pump wavelength due to cross-gain modulation (XGM) and XPM. Further there is also power-transfer between one 10G side-lobe to another due to interband FWM with the carrier frequency acting as the pump. This FWM-induced power transfer between the side lobes is seen at pump, probe and conjugate wavelengths. These observed nonlinear effects are also reduced with increasing WS. At a fixed  $P_0$ , as the WS is increased, the FWM efficiency is reduced [Eq. (3.26)] and as a consequence the impact of other nonlinear effects is also reduced. Clearly, high internal ASE not only increases FWM efficiency, it also enhances SPM induced spectral broadening and chirping due to XPM. Also, these effects are observed at wavelength shifts and input optical pump-powers of practical interest.

Since the additional spectral broadening due to SPM and XPM decreases with both increasing input pump power as well increasing input pump-probe detuning, this implies that other than optimizing the input pump power from the standpoint of CE and OSNR of the converted signal, the extent and the nature of spectral broadening suffered by the converted signal under different input conditions needs to be understood and minimized. To do so, the converted signal spectra measured at the output of FIL1 and FIL2 are plotted in Fig. 5.13(a) and (b) respectively.

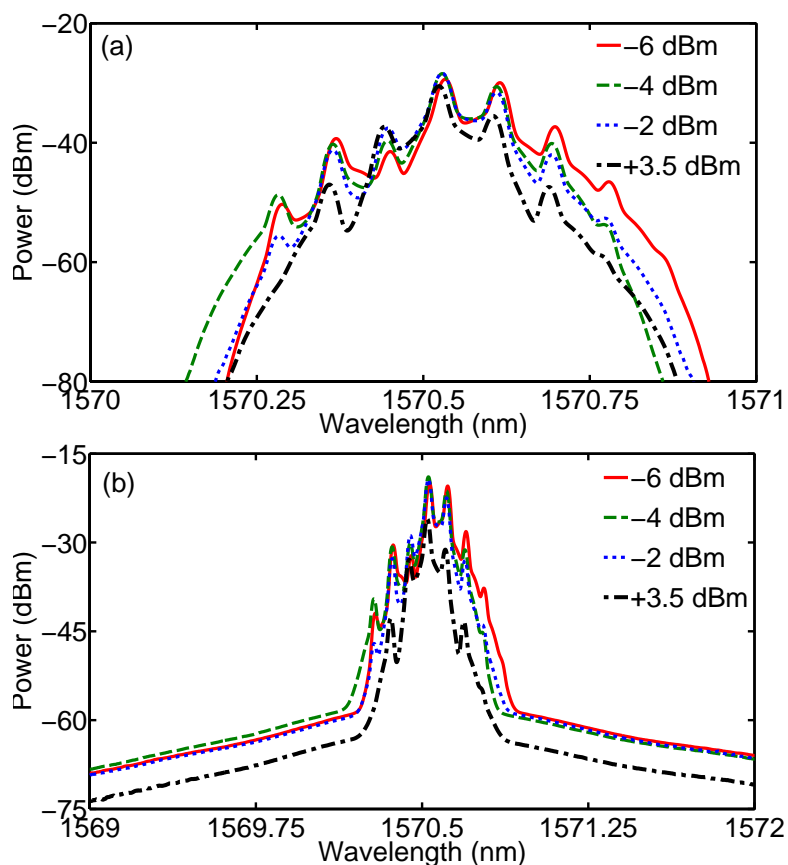


Figure 5.13: Converted signal spectra measured at the output of (a) Output Filter (b) ASE Filter corresponding for four different input pump powers at 1000 GHz WS (corresponding to Fig. 5.12(c)).

These converted spectra correspond to 1000 GHz WS [Fig. 5.12(c)]. The fact that at any WS, the extent of spectral broadening suffered by the converted data pulses is reduced with increasing input pump power can be clearly seen in these two figures. However, the reduction in spectral broadening is much more severe when the input pump power is increased from  $-6$  to  $-2$  dBm as compared to when it is increased from  $-2$  to  $+3.5$  dBm. Clearly at 1000 GHz WS, input optical pump power in the vicinity of  $-2$  dBm is optimum from the standpoint of extent of spectral broadening suffered by the converted data pulses.

At larger wavelength shifts ( $\geq 400$  GHz), the dominant nonlinear effect re-

sponsible for spectral broadening suffered by converted data pulses is SPM. In section 3.2.2, it was demonstrated that the chirp imposed on an optical pulse due to ASE-assisted SPM in a SOA is positive and nearly linear across the pulse and can therefore potentially be compensated optically using well known dispersion compensation techniques [34]. In section 5.3.4, the optimization of input pump power from the standpoint of CE and converted OSNR for CW pump and probe was discussed. It was concluded that the converted OSNR has a broad maximum in the vicinity of  $-2$  dBm input pump power whereas the CE decreases monotonically with increasing pump power. This assertion is valid for low  $P_1$  such that the probe and the converted signal do not significantly saturate the amplifier gain. It will be interesting to see whether this assertion holds true for this wavelength convertor design. This issue is investigated next.

### 5.4.3 Experimental Results

Figure 5.14 shows the CE and the OSNR measured as a function of  $P_0$  at  $P_1 = -11.7$  dBm and 500 mA SOA drive current. The solid lines correspond to 200 GHz, the dashed lines 400 GHz and the dotted lines 1000 GHz WS respectively. The CE and OSNR were measured at the 1% power tap using the dual trace function of the OSA [179]. Comparing the evolution of CE and converted OSNR for data pulses [Fig. 5.14] with the CW case [Fig. 5.7], it can be seen that there is a deviation from the expected behavior at low input pump powers. This deviation can be explained as follows: The power at the converted wavelength is measured using an OSA with its resolution set at 0.2 nm which is typically used to measure the fully integrated power level for 10 Gb/s signals [179]. At low pump powers, the enhanced spectral broadening implies that 0.2 nm resolution is no longer sufficient to accurately estimate the converted signal power. This explains the reduction in measured CE at low  $P_0$  which in turn accounts for the deviation observed in the evolution in OSNR. It is however interesting to note that  $-2$  dBm is the optimum

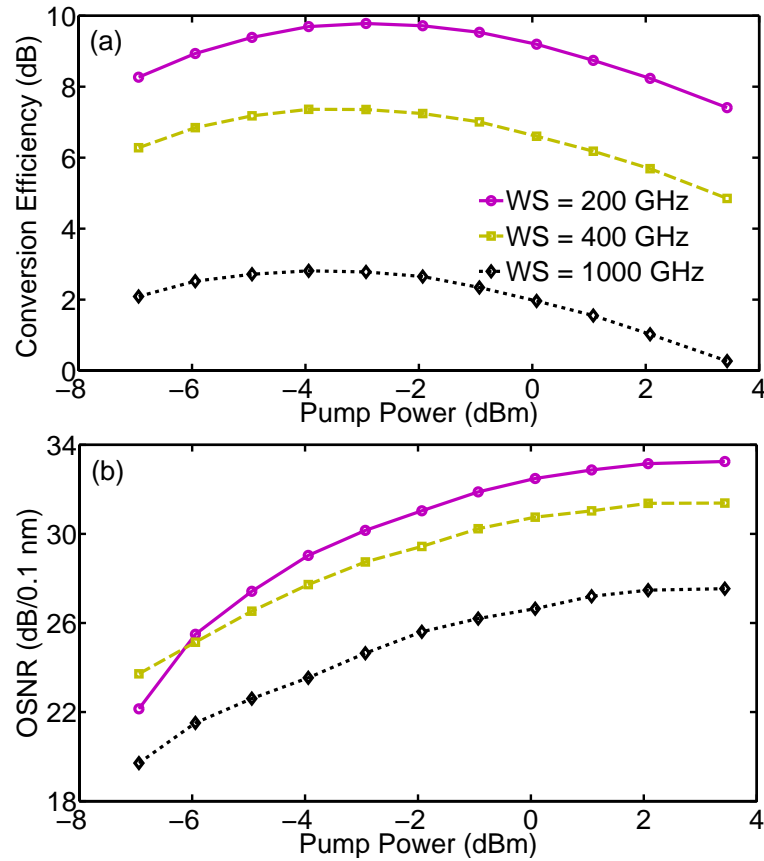


Figure 5.14: (a) Conversion efficiency and (b) OSNR measured as a function of  $P_0$  at  $P_1 = -11.7$  dBm and 500 mA drive current. The solid lines correspond to 200 GHz, the dashed lines 400 GHz and the dotted lines 1000 GHz WS respectively.

$P_0$  both from the standpoint of both CE and converted OSNR over a broad range of wavelength shifts.

These two curves provide design guidelines for optimizing wavelength convertor performance. At wavelength shifts of practical importance (200–1000 GHz), CE in excess of 3 dB and converted OSNR in excess of 26 dB can be achieved for sub-mW pump and probe powers. Depending on the requirements imposed by a particular application, at any WS, some improvement in OSNR can be achieved at the cost of CE. Further, no holding beam is required for facilitating wavelength conversion which significantly reduces the footprint of this technique.



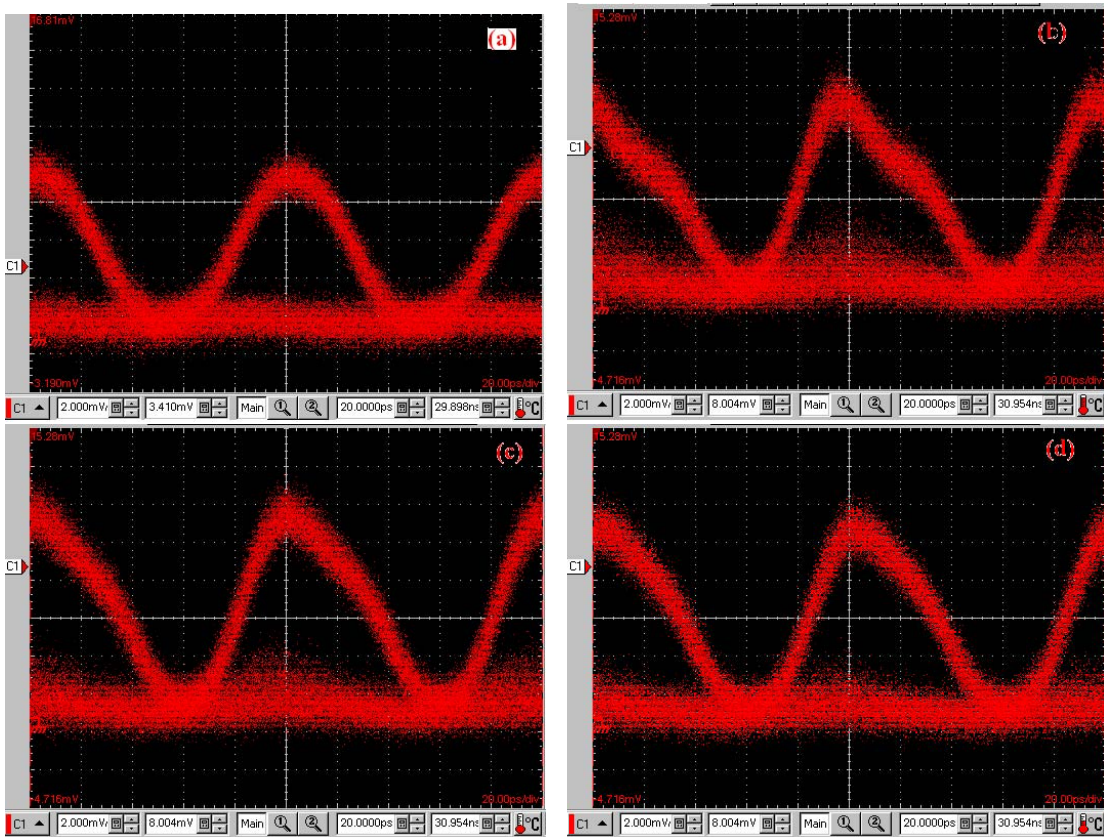


Figure 5.15: (a) Eye-diagram for input data channel ( $P_1 = -11.7$  dBm). Eye diagrams for converted data channel at  $P_0 =$  (b)  $-6$  dBm, (c)  $-4$  dBm, and (d)  $-2$  dBm. The converted data channel was measured at the output of FIL2 and corresponds to 1000 GHz WS.

While CE and OSNR are the two most commonly used FOMs associated with a wavelength converter, bit error rate curves and converted eye diagrams are routinely used for qualitative and quantitative assessment of wavelength converter performance [41, 168, 170]. In the absence of a telecom grade photoreceiver in the lab, the converted signals were detected using a standard 22 GHz discovery PD with a responsivity of 0.6 A/W at 1575 nm. The converted data channel corresponding to 1000 GHz WS was measured at different  $P_0$ . The corresponding converted average optical power at the isolator output varied between  $-9$  and

$-11.5$  dBm depending on  $P_0$ . While typical telecom grade DWDM filters have IL less than 1 dB [180], the filter used in the experiments [FIL1] had an IL in excess of 5 dB. Consequently, the measured converted average optical power at the output of FIL 1 was between  $-18$  and  $-20$  dBm depending on  $P_0$ . An EDFA therefore had to be used as a preamplifier to boost up the optical signal. A further 3.5 dB loss due to the ASE rejection filter meant that the EDFA was barely able to compensate for the output losses and on top of it additional ASE noise was added to the converted signal [Fig. 5.13(b)]. The bit error rate curves at the converted wavelength therefore could not be plotted. The eye diagrams corresponding to the converted data channel were measured and are shown in Fig. 5.15.

Part (a) of Fig. 5.15 shows the input data channel corresponding to  $-11.7$  dBm average optical power at the SOA input. The channel was measured at the output of PBS at which point the measured average optical power was  $-9$  dBm. Parts (b)–(d) show the eye-diagrams for converted data channel corresponding to 1000 GHz WS at  $P_0 = -6$ ,  $-4$ , and  $-2$  dBm respectively. The converted data channel at  $P_0 = +3.5$  dBm could not be measured due to the inability of the EDFA to sufficiently amplify the data channel at the output of FIL1. It can be seen that with increasing  $P_0$  the quality of converted data channel increases progressively. Due to corresponding reduction in CE as well as lack of proper equipment, this trend could not be verified for  $P_0 > -2$  dBm. Further, at low  $P_0$  ( $\leq -4$  dBm), there is significant distortion in the converted data channel due to SPM and XPM as discussed in the previous section. At  $P_0 = -2$  dBm good quality eyes are obtained for converted data channel indicating that this pump power is indeed optimum for wavelength conversion using ASE-assisted FWM.

## 5.5 Concluding Remarks

In this chapter, it has been experimentally demonstrated that the interband FWM can be used for wavelength conversion in SOAs driven at currents so high that the ASE itself begins to saturate the SOA gain. Conversion efficiency and OSNR are used as the two FOMs to characterize the wavelength conversion process. Across a broad range of wavelength shifts (as large as 20 nm), an increase in the CE of over 20 dB, and a corresponding increase in the OSNR of over 12 dB is observed, as the SOA current was increased from 100 to 500 mA. The experimental observations are in qualitative agreement with the theoretical predictions reported in Chapter 3. As seen in Fig. 5.5(a), wavelength shifts ( $2\Delta\lambda$ ) close to 15 nm are possible at high drive current levels that reduce the gain recovery time to near 10 ps, while maintaining a high CE ( $\eta = 1$ ) and a high OSNR close to 25 dB. If 10% CE is considered acceptable for a WC, wavelength shifts  $> 25$  nm are possible.

A major advantage of the ASE-enhanced interband FWM scheme is that input pump powers required for wavelength conversion are much lower ( $P_0 < 0.5$  mW) than those employed in the case of intraband FWM. This feature reduces the electrical power consumption for such WCs by more than a factor of 10. The issue of optimum pump power has been discussed in detail and it has been determined that the high conversion efficiencies over a broad range of input signal powers are possible even at pump powers as low as 0.1 mW. However, the OSNR of the converted signal at such pump levels may be below 25 dB because input signal power in this case must be considerably less than 0.1 mW. If the design criterion requires an OSNR of 30 dB or more, input signal power should be close to 0.1 mW, and this requires an input pump power close to 1 mW.

A realistic WC for WDM systems must operate on pulsed signals at a bit rate of 10 Gb/s or more. The conclusions based on CW experiments are expected to hold for pulsed data channels, with minor modifications, as far as CE and OSNR

are concerned. In the case of OOK, a partial recovery of the SOA gain during successive pulses will introduce the nonlinear patterning effects. This problem would be less severe for formats based on phase modulation. Another practical issue is related to the polarization dependence of FWM efficiency. This problem can be solved to a large extent if two orthogonally polarized pumps are employed. However, the performance of such a WC is likely to degrade if the total pump power increases considerably.

Based on the conclusions derived from theoretical results (Chapter 3) and the experimental results for CW pump and probe, a 10 Gb/s L-Band wavelength convertor for RZ-OOK signals with 50% duty cycle was demonstrated. It was concluded that high internal ASE not only drive up the FWM CE but also enhances the other nonlinear effects (SPM, XPM and XGM) which causes significant spectral broadening the the converted data channel. The extent of spectral broadening decreases with increasing wavelength shifts and increasing  $P_0$ . At any WS, CE, converted OSNR, and the spectral broadening of the converted signal can be optimized through suitable selection of  $P_0$ . For the design studied in this thesis, the optimum value of  $P_0$  was  $-2$  dBm and at this pump power, the CE was 3 dB and the converted OSNR was 26 dB/0.1 nm.

# 6 Empirical VCSEL Thermal Model and Applications

## 6.1 Introduction

VCSELs are key components for communication and sensing applications due to their ease of fabrication and testing, low power consumption, high beam quality, and high modulation speeds [122, 133]. In particular, VCSELs operating in the 850 nm wavelength band constitute an important class of VCSELs. This can be attributed to the availability of commercial multimode fibers that employ VCSELs operating near 850 nm for short haul communication links in data centers and high-performance computing systems. Further, such VCSELs have shown the potential to play an important role in future high-speed optical interconnects and consumer electronics [122–125].

In this chapter, the development of an empirical thermal model to study self-heating effects in VCSELs is outlined. The model incorporates the temperature dependence of different macroscopic VCSEL parameters such as series resistance, threshold current, thermal impedance, internal optical loss, and internal quantum efficiency. The temperature dependence of VCSEL parameters is extracted from measurements of output optical power  $P_{\text{opt}}$ , bias voltage  $V_b$ , and emission wavelength  $\lambda$  of the fundamental mode as a function of bias current  $I_b$ , over an ambient

temperature range of 15–100°C. The parameters are extracted by performing reliable single parameter numerical fits to the measurements. This in-turn is used to calculate various contributions to self-heating, responsible for an increase in the device temperature. This model is applied to an oxide-confined 850 nm VCSEL, fabricated with 9  $\mu\text{m}$  inner aperture diameter and optimized for high speed operation.

At room temperature (25°C), as the bias current is increased from threshold to thermal rollover, the saturation of the output power is caused by a 70°C rise in the internal device temperature, which causes the threshold current and internal optical loss to increase by 85% and 43%, respectively, and the internal quantum efficiency to decrease by 20%. Further, for this particular device, at any ambient temperature and bias current, linear power dissipation exceeds the quadratic power dissipation. In addition to quadratic power dissipation, internal optical loss and carrier leakage are the main factors limiting the thermal performance. The method proposed in this chapter can potentially be applied to any VCSEL design to pinpoint the factors limiting the thermal performance and assess the impact of steps taken to ameliorate them.

## 6.2 Theoretical Model

There are several mechanisms by which power is dissipated inside a VCSEL [144, 181]. The power dissipated across its series resistance  $R_s$  causes resistive or Joule heating. This mechanism is referred to as quadratic power dissipation (QPD), as its dependence on bias current is quadratic. It is included in the model by using:

$$P_{\text{QPD}} = R_s(T_a, I_b)I_b^2. \quad (6.1)$$

where  $I_b$  is the bias current and  $T_a$  is the ambient temperature. A direct dependence of series resistance on current caused by charge accumulation at the

hetero-interfaces in the DBRs is included; it leads to reduction in resistance with bias current [142, 182].

Other sources of power dissipation, including carrier leakage, carrier thermalization, spontaneous carrier recombination, and internal optical loss linearly depend on  $I_b$ , both below and above the threshold. The sum of these mechanisms is referred to as linear power dissipation (LPD) and is included through:

$$P_{\text{LPD}} = K(T)I_b. \quad (6.2)$$

where  $K(T)$  is the LPD coefficient whose value also depends on the device temperature, and therefore on both ambient temperature and current. In these Eqs.,  $T = T_a + \Delta T$  is the sum of the ambient temperature  $T_a$ , and the increase in temperature  $\Delta T$ , caused by bias current induced self-heating. Henceforth, the value of a particular device parameter is defined at a fixed  $T_a$  and  $I_b$  unless specified otherwise.

To model  $P_{\text{LPD}}$ , it is important to understand the physical process behind each of the constituent LPD mechanisms. Figure 6.1 schematically depicts the capture and leakage of carriers injected into the active region of a VCSEL. The proposed theoretical model assumes that a fraction  $\eta_i$  (the internal quantum efficiency) of charge carriers carried by the bias current  $I_b$  is captured by the QWs; remaining carriers, which constitute carrier leakage, recombine in the barriers and the SCH surrounding the QWs to generate heat proportional to the dissipated power  $P_{\text{leak}}$ . Carriers captured by the QWs lose energy through various scattering mechanisms [183](carrier thermalization) and produce the dissipated power  $P_{\text{therm}}$ . Upon losing energy through thermalization, carriers recombine spontaneously through radiative and non-radiative mechanisms. Since, only a small fraction of spontaneously emitted photons couple to the cavity modes, or escape the laser cavity by other means, it is, therefore, assumed that all spontaneous recombination events produce heat with the dissipated power  $P_{\text{rec}}$  [184]. Above

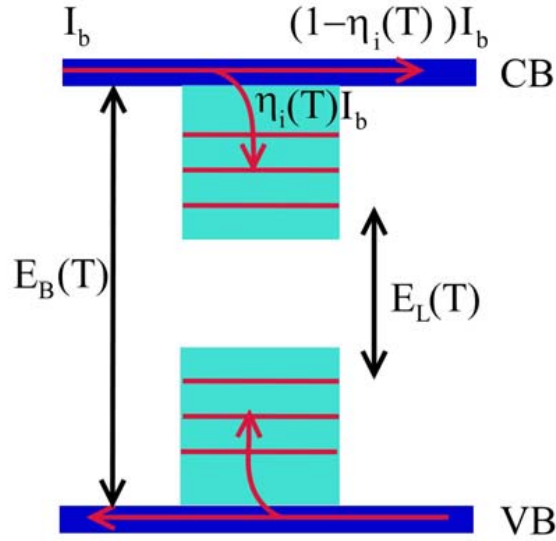


Figure 6.1: Schematic illustration of the capture  $\eta_i(T)I_b$  and leakage  $(1-\eta_i(T))I_b$  of injected carriers in strained InGaAs quantum wells.  $E_B(T)$ ,  $E_L(T)$  and  $\eta_i(T)$  are the temperature dependent barrier bandgap energy, lasing bandgap energy and internal quantum efficiency, respectively. This Fig. depicts three out of the four LPD mechanisms; absorption losses in the top and the bottom DBRs are not shown here.

threshold, a certain fraction of photons generated by stimulated emission are absorbed within the two DBRs forming the VCSEL cavity (internal optical loss). This absorption also produces heat with a dissipated power  $P_{\text{abs}}$ . Taking all these mechanisms into account, the current dependence of the various power dissipation mechanisms can be written as:

$$P_{\text{leak}} = E_B(T)[1 - \eta_i(T)]I_b/q, \quad (6.3)$$

$$P_{\text{therm}} = [E_B(T) - E_L(T)]\eta_i(T)I_b/q, \quad (6.4)$$

$$P_{\text{rec}} = \begin{cases} E_L(T)\eta_i(T)I_b/q & ; \quad I_b < I_{\text{th}}, \\ E_L(T)\eta_i(T)I_{\text{th}}(T)/q; & I_b > I_{\text{th}}, \end{cases} \quad (6.5)$$

$$P_{\text{abs}} = \frac{\eta_i(T)[I_b - I_{\text{th}}(T)][\alpha_i(T) + \alpha_m^B(T)]E_L(T)}{q[\alpha_m^T(T) + \alpha_m^B(T) + \alpha_i(T)]}; \quad I_b > I_{\text{th}}. \quad (6.6)$$



It is assumed that  $P_{\text{abs}} = 0$  for  $I_b < I_{\text{th}}$  as not many photons exist inside the VCSEL cavity below threshold. In these Eqs.,  $E_B(T)$  and  $E_L(T)$  are the temperature dependent barrier bandgap energy and laser photon energy (in eV), respectively,  $q$  is the electron charge,  $I_{\text{th}}$  is the threshold current,  $\alpha_m^T(T)$  and  $\alpha_m^B(T)$  are the transmission loss rates through the top and bottom DBRs, respectively, and  $\alpha_i(T)$  is the internal optical loss rate. Eq. (6.5) takes into account clamping of the spontaneous recombination rate at the lasing threshold, and Eq. (6.6) assumes that light emitted through the bottom DBR is also absorbed and therefore produces heat. The temperature dependence and consequently the bias current dependence of most parameters in Eqs. (6.3)–(6.6) should be noted.

When AlGaAs is used as the barrier material in 850 nm VCSELs, the temperature dependence of the barrier bandgap  $E_B(T)$  is determined from the Varshni Eqs. [185–187] for the temperature dependence of the direct bandgap of AlAs and GaAs:

$$E_g(\text{AlAs}) = 3.099 - \frac{0.885 \times 10^{-3} T_k^2}{T_k + 530}, \quad E_g(\text{GaAs}) = 1.519 - \frac{0.5405 \times 10^{-3} T_k^2}{T_k + 204}. \quad (6.7)$$

where  $T_k$  is the device temperature in Kelvin. The interpolation formula for the barrier bandgap of  $\text{Al}_x\text{Ga}_{1-x}\text{As}$  is known to be [186]:

$$E_g^x(\text{Al}_x\text{Ga}_{1-x}\text{As}) = xE_g(\text{AlAs}) + (1-x)E_g(\text{GaAs}) - x(1-x)(-0.127 + 1.310x). \quad (6.8)$$

Temperature dependence of the photon energy  $E_L$  is estimated from temperature dependence of the lasing wavelength of the fundamental  $LP_{01}$  mode.

Above lasing threshold, where self-heating becomes significant, the total  $P_{\text{LPD}}$  can be written as:

$$\begin{aligned} P_{\text{LPD}} &= P_{\text{therm}} + P_{\text{rec}} + P_{\text{leak}} + P_{\text{abs}} \\ &= \frac{1}{q} E_B(T) I_b - \frac{1}{q} E_L(T) \eta_i(T) [I_b - I_{\text{th}}(T)] \left[ 1 - \frac{\alpha_i(T) + \alpha_m^B(T)}{\alpha_i(T) + \alpha_m^T(T) + \alpha_m^B(T)} \right], \end{aligned} \quad (6.9)$$

Combining Eqs (6.2) and (6.9), the LPD coefficient  $K(T)$  can be written as:

$$K(T) = \frac{1}{q}E_B(T) - \frac{1}{q}E_L(T)\eta_i(T)[1 - \{I_{\text{th}}(T)/I_b\}] \left[ 1 - \frac{\alpha_i(T) + \alpha_m^B(T)}{\alpha_i(T) + \alpha_m^T(T) + \alpha_m^B(T)} \right], \quad (6.10)$$

Further, the total dissipated power ( $P_{\text{tot}}$ ) is given by:

$$P_{\text{tot}} = P_{\text{QPD}} + P_{\text{LPD}} = \frac{dV_b(T, I_b)}{dI_b} I_b^2 + P_{\text{LPD}}, \quad (6.11)$$

where the series resistance has been replaced by the differential resistance ( $R_s = dV_b/dI_b$ ) at the given bias point and  $V_b$  denotes the applied voltage. The device temperature  $T$ , is subsequently obtained using the thermal impedance  $R_{\text{th}}$  which relates the change in device temperature to the dissipated power and can be written as [122, 140]

$$T = T_a + \Delta T = T_a + R_{\text{th}}(T)P_{\text{tot}}. \quad (6.12)$$

Note that  $R_{\text{th}}$  also depends on temperature through temperature dependence of the thermal conductivities of various materials in the VCSEL structure [143]. It is important to note that the series (or differential) resistance in Eq. (6.1) and the LPD coefficient in Eq. (6.2) depend strongly on temperature and therefore, also on the bias current. The consequences of this are strong deviations from quadratic and linear dependencies of  $P_{\text{QPD}}$  and  $P_{\text{LPD}}$ , respectively, on the bias current for the VCSELs operating under continuous bias current.

Finally, the optical power emitted through the top DBR, at a given current and ambient temperature, is calculated using [184]:

$$P(T, I_b) = \frac{\eta_i(T)[I_b - I_{\text{th}}(T)]\alpha_m^T(T)}{\alpha_m^T(T) + \alpha_m^B(T) + \alpha_i(T)} \left( \frac{hc}{q\lambda(T)} \right). \quad (6.13)$$

where  $\lambda(T)$  is the emission wavelength of the fundamental mode,  $c$  is the speed of light and  $h$  is the Planck constant.

### 6.2.1 Extraction of Parameters from Measurements

In the preceding analysis, the Eqs. used to relate the dissipated power  $P_{\text{tot}}$ , device temperature  $T$ , and output power  $P_{\text{opt}}$  to the bias current were derived. These Eqs. contain a number of parameters whose temperature dependence needs to be quantified. To achieve this, the output power, voltage and emission wavelength as a function of the bias current over a range of  $T_a$  (15–100 °C) is measured. The measurements are performed under continuous or low duty cycle pulsed operation.

The measurements for extracting the temperature dependence of VCSEL parameters are performed over a range of bias currents close to the lasing threshold. Any bias current-induced increase in temperature,  $\Delta T$ , depends on the ambient temperature  $T_a$  due to the temperature dependence of thermal impedance [Eq. (6.12)] and the increasing difficulty faced in stabilizing high stage temperatures against room temperature. At low ambient temperatures ( $T_a \leq 50^\circ\text{C}$ ), the error in the extracted parameter values corresponds to a bias current induced increase in the device temperature ( $\Delta T \leq 2^\circ\text{C}$ ). As discussed in the next section, this corresponds to the resolution limit of the device thermometer [122]. With increasing ambient temperature,  $\Delta T$  increases. The corresponding errors in the reported parameter values at room temperature ( $T_a = 25^\circ\text{C}$ ) are summarized in Tables 6.1 and 6.2, assuming a worst case value of  $5^\circ\text{C}$  uncertainty at  $T_a = 100^\circ\text{C}$ .

The temperature dependence of the emission wavelength,  $\lambda(T)$ , is found by measuring the wavelength of the fundamental mode ( $\text{LP}_{01}$ ) as a function of ambient temperature [122]. For GaAs-based 850 nm VCSELs, the value of  $\Delta\lambda/\Delta T$  is typically around  $0.06 \text{ nm}/^\circ\text{C}$ . This quantity is also used to estimate the device temperature at various values of  $T_a$  and  $I_b$ .

The temperature dependence of the threshold current,  $I_{\text{th}}(T)$ , is extracted from power versus current ( $P_{\text{opt}}-I_b$ ) measurements recorded at different ambient temperatures [122].

The internal optical loss,  $\alpha_i(T)$ , is extracted from the measured dependence of output power on bias current just above threshold for VCSELs with different top DBR reflectivities. This reflectivity is varied by changing the thickness of the top layer (using dry etching), which controls the phase of the surface reflection. The method is described in [127]. By performing these measurements at different ambient temperatures, the temperature dependence of  $\alpha_i(T)$  is obtained. Other methods for carrying out these measurements for any VCSEL have been previously reported [188].

The temperature dependence of the internal quantum efficiency,  $\eta_i(T)$ , is also extracted from the measured  $P_{\text{opt}}-I_b$  curves. The slope efficiency (SE) is extracted from the  $P_{\text{opt}}-I_b$  curves at different ambient temperatures by averaging the slope  $dP_{\text{opt}}/dI_b$  over optical powers in the range of  $P_1$  and  $P_2$ . The choice of  $P_1$  and  $P_2$  is constrained such that the increase in the device temperature over this range should be negligible ( $\Delta T \leq 5^\circ\text{C}$ ). Therefore,  $P_1$  is chosen as emitted power at the lasing threshold at a particular ambient temperature and  $P_2$  is chosen as 10% of the maximum emitted power at room temperature. The external differential quantum efficiency is then calculated using [181, 184]:

$$\eta_d(T) = \frac{q\lambda(T)}{hc} \text{SE}(T). \quad (6.14)$$

We then calculate  $\eta_i(T)$  using the relation:

$$\eta_d(T) = \frac{\eta_i(T)\alpha_m^T(T)}{[\alpha_m^T(T) + \alpha_m^B(T) + \alpha_i(T)]}. \quad (6.15)$$

Here, the temperature dependence of the transmission loss rates through the top and bottom DBRs is accurately calculated using an effective index model that takes into account the temperature dependence of the refractive index of the constituent layers of the DBRs [127, 189].

Finally, temperature dependence of the thermal impedance,  $R_{\text{th}}(T)$ , is estimated by measuring the change in the emission wavelength and therefore, the

increase in the device temperature, with increasing dissipated power in the current range,  $I_b < 2I_{th}$ , at different ambient temperatures [131,143]. This is done so that temperature increase due to bias current induced self-heating is negligible.

## 6.3 Impact of Ambient Temperature on Thermal Rollover Mechanisms

### 6.3.1 Device Under Test

The structure of the VCSEL used for the experiments is schematically depicted in Fig. 6.2. The VCSEL operates at wavelengths near 850 nm. It is grown on a GaAs substrate and employs an oxide-confined configuration optimized for high speed modulation [190]. The top and bottom DBRs are fabricated with graded interfaces and modulation doping to reduce their electrical resistance [122]. The bottom DBR is partly composed of binary (AlAs) material to lower its thermal impedance [127]. The active region is made of five strained InGaAs QWs to improve its differential gain [126] and is surrounded by a SCH designed for efficient carrier trapping and low gain compression [128,190]. As indicated with dark shading in Fig. 6.2, six AlGaAs layers in the lower part of the top DBR are composed of high Al content, (98% for the bottom two and 96% for the remaining four) to form a small oxide aperture (9  $\mu\text{m}$  diameter) for current and optical confinement and a larger oxide aperture (18  $\mu\text{m}$  diameter) for reducing device capacitance [127]. In a second dry-etching process, the bottom contact layer is reached and the n-contact layer is evaporated. The etched mesas are embedded in a low-k dielectric (Benzo-Cyclo-Butene) to further reduce the parasitic capacitance [122, 129, 133].

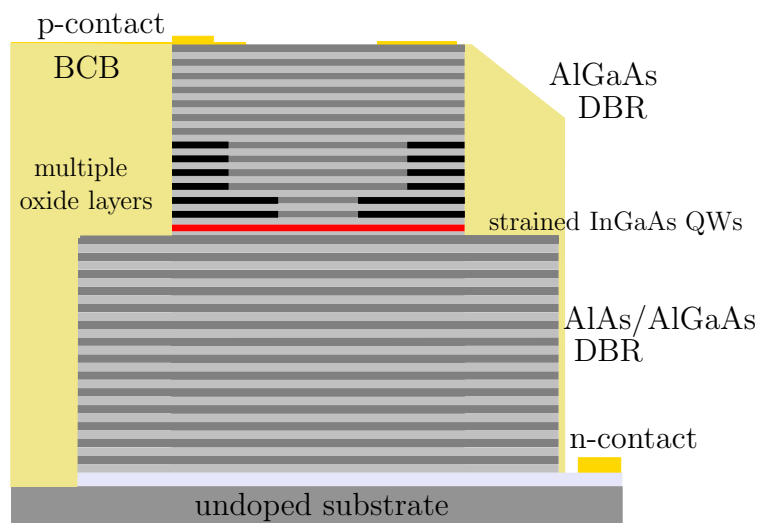


Figure 6.2: Schematic cross section of the high-speed 850 nm VCSEL used in the experiment. Benzo-Cyclo-Butene is employed to reduce parasitic capacitance. Six layers are used for forming an oxide aperture (dark shading region). Other details of the device design can be found in Ref. [190].

### 6.3.2 Experimental Setup and Measurements

For measuring the emitted optical power and voltage as a function of bias current, the VCSEL was placed on a copper stage with active temperature control and stabilization. The light emitted by the VCSEL was detected by a calibrated, large area PD (UDT Sensors PIN-10D) for accurate power measurement. Measurements were performed over an ambient temperature range of 15–100°C. For spectral measurements, the light was coupled to a multimode fiber connected to an OSA. All spectral measurements were performed with 0.1 nm resolution. As a result, device temperatures deduced from spectral data were accurate to within 1.6°C.

Experimental data from measurements are presented in Fig. 6.3. Part (a) shows the emitted optical power versus bias current  $I_b$  under CW operation at different ambient temperatures  $T_a$ . Clearly, the SE decreases and the threshold current  $I_{th}$  increases with increasing  $T_a$ . The corresponding dependence of voltage

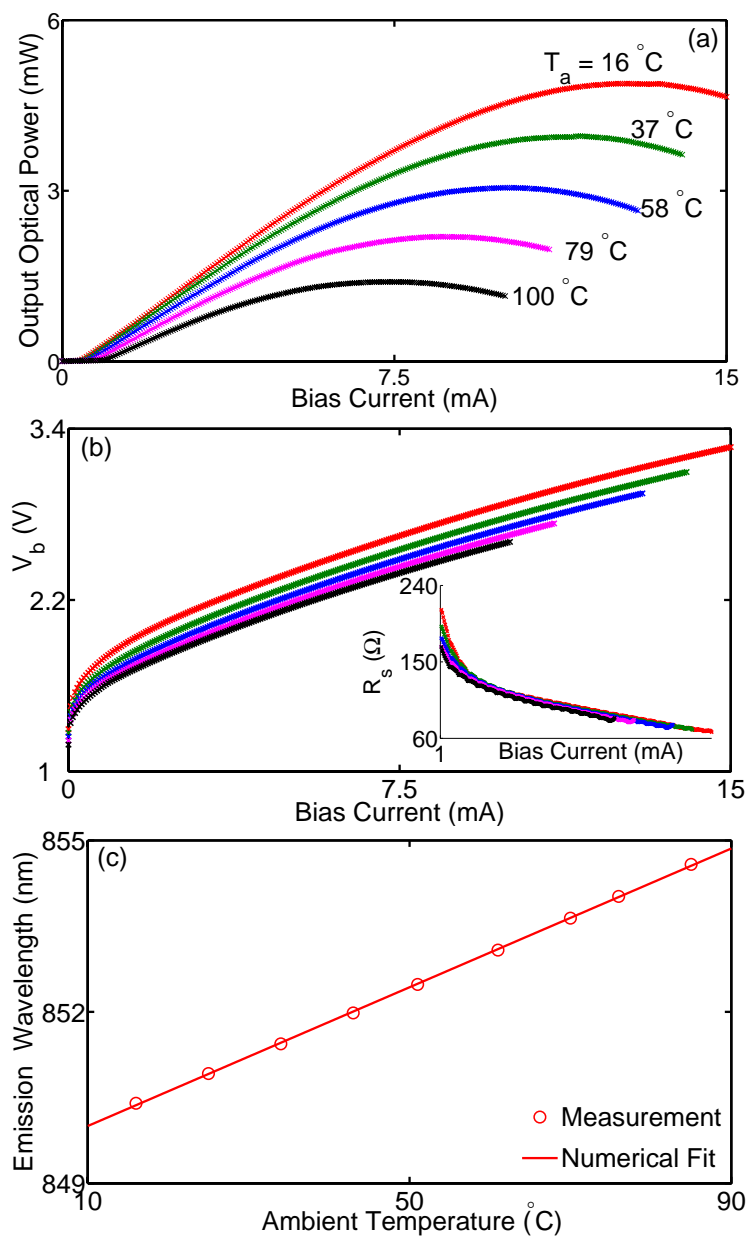


Figure 6.3: Measurements used to extract temperature dependence of VCSEL parameters. (a) Output power and (b) voltage as a function  $I_b$  at five ambient temperatures. The inset in (b) shows variations of differential resistance  $R_s$  with  $I_b$ . (c) Wavelength of the ( $\text{LP}_{01}$ ) mode versus  $T_a$  (circles); the linear fit is used to estimate the device temperature.

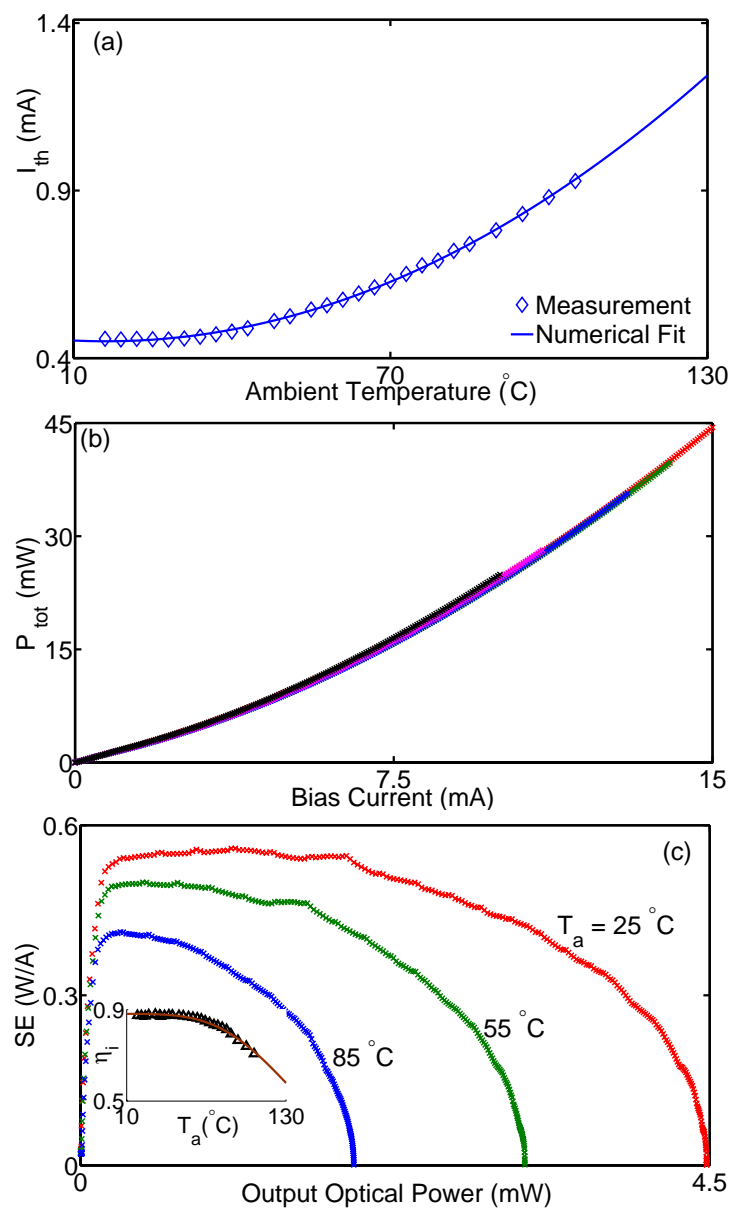


Figure 6.4: (a) Threshold current as a function of  $T_a$ ; the numerical fit is used in the thermal model. (b) Dissipated power as a function of  $I_b$  for five  $T_a$  values used in Fig. 6.3(a). (c) SE versus output power at three different  $T_a$  values. The inset shows the derived dependence of  $\eta_i$  on temperature; the numerical fit is used in the thermal model.



Table 6.1: Room Temperature Values of VCSEL Parameters

Parameter	Value
$\lambda$	$850.9 \pm 0.31$ nm
$R_{th}$	$1.965 \pm 0.029^\circ\text{C mW}^{-1}$
$\alpha_i$	$(7.0 \pm 0.21) \times 10^{-2}$ ps $^{-1}$
$\alpha_m^T$	$5.89 \times 10^{-2}$ ps $^{-1}$
$\alpha_m^B$	$6.27 \times 10^{-3}$ ps $^{-1}$

$V_b$  on  $I_b$  at different  $T_a$  is shown in part (b). At a given  $I_b$ ,  $V_b$  decreases with increasing  $T_a$  due to reduction of the bandgap and improved carrier transport through the DBRs at higher temperatures. The inset Fig. shows the dependence of differential resistance ( $R_s$ ) on  $I_b$  at different  $T_a$ . It can be seen that  $R_s$  decreases much more rapidly with increasing  $I_b$ , as opposed to increasing  $T_a$ . This can be attributed to an increase in charge accumulation at DBR interfaces with increasing bias current [142,182]. The dependence of  $R_s$  on  $I_b$  and  $T_a$  is used to calculate  $P_{\text{QPD}}$  at any combination of current and  $T_a$ . Figure 6.3(c) shows the emission wavelength of the fundamental LP $_{01}$  mode at different  $T_a$ , measured close to lasing threshold to avoid self-heating. The deduced linear dependence of wavelength on temperature is subsequently used to find the device temperature at any combination of  $T_a$  and  $I_b$  under CW operation.

### 6.3.3 Extraction of VCSEL Parameters

Plots used for extracting the temperature dependence of various parameters are shown in Fig. 6.4. Part (a) shows the dependence of  $I_{\text{th}}$  on device temperature, with minimum  $I_{\text{th}}$ , occurring at the temperature for which the gain peak is spec-

trally aligned with the cavity resonance (30°C for the device under test) [181]. Here, a two-segment line-fit is used to calculate threshold current at any ambient temperature from the corresponding  $P_{\text{opt}}-I_b$  curve. This method is relatively insensitive to changes in SE [184]. A parabolic numerical fit is used to model the dependence of  $I_{\text{th}}$  on  $T_a$ . The maximum error in the calculated value of  $I_{\text{th}}$  is less than 2% at any  $T_a$ . Part (b) shows the dependence of dissipated power,  $P_{\text{tot}} = I_b V_b - P_{\text{opt}}$ , on  $I_b$  at different ambient temperatures. At any bias current, a slight increase in dissipated power with increasing  $T_a$  is observed. The reason behind this will be discussed in detail a little later in this chapter. Part (c) shows the dependence of SE on output power at different  $T_a$ . Following the procedure outlined in Section 6.2.1 and using Eqs. (6.14) and (6.15), the dependence of the internal quantum efficiency ( $\eta_i$ ) on the device temperature is deduced and plotted in the inset of Fig. 6.4(c). The  $\eta_i$  is nearly constant and close to 88% at low device temperatures, but it decreases quite rapidly as the device temperature is increased beyond 50°C. A polynomial fit is used to represent  $\eta_i(T)$ . The maximum calculated error in the extracted value of  $\eta_i$  is less than 1% at any  $T_a$ . To enable the calculation of  $\eta_i(T)$  from Eq. (6.15), the values for the internal optical loss obtained using the method outlined in [127] and briefly described in Section 6.2.1 are used. The internal optical loss was found to increase linearly with ambient temperature from 0.070 ps<sup>-1</sup> at 25°C to 0.097 ps<sup>-1</sup> at 85°C. This is consistent with the linear dependence of the free carrier absorption coefficient on temperature [127].

Tables 6.1 and 6.2 list several device parameters, the value of which was found to vary linearly with temperature. Table 6.1 lists the room temperature values while table 6.2 lists the slope of linear temperature dependence. These tables also summarize the error in the measured values of VCSEL parameters. The origin of this error has been discussed in Section 6.2.1. Since  $\alpha_m^T(T)$  and  $\alpha_m^B(T)$  are calculated numerically, their values are assumed to be accurate. Physical

Table 6.2: Linear Temperature Dependence of VCSEL Parameters ( $\Delta = \frac{\partial}{\partial T}$ )

Parameter	Value
$\Delta\lambda$	$(6.07 \pm 0.13) \times 10^{-2} \text{ nm}^\circ\text{C}^{-1}$
$\Delta R_{th}$	$(5.4 \pm 0.4) \times 10^{-3} \text{ mW}^{-1}$
$\Delta\alpha_i$	$(4.167 \pm 0.11) \times 10^{-4} \text{ ps}^{-1}\circ\text{C}^{-1}$
$\Delta\alpha_m^T$	$-3.622 \times 10^{-5} \text{ ps}^{-1}\circ\text{C}^{-1}$
$\Delta\alpha_m^B$	$-5.705 \times 10^{-6} \text{ ps}^{-1}\circ\text{C}^{-1}$

explanation behind the temperature dependence as well as previously reported room temperature values for these parameters can be found in [122, 127, 143, 189].

### 6.3.4 Performance Predictions from Thermal Model

Powered by the deduced temperature dependence of all the VCSEL parameters from the experimental data, the empirical thermal model should be able to reproduce measured VCSEL characteristics. The procedure outlined in Section 6.2, with the parameters listed in tables 6.1 and 6.2, is used to numerically calculate various contributions to the dissipated power. Parts (a) to (c) of Fig. 6.5 show the measured and simulated output powers, total dissipated powers and device temperatures as a function of  $I_b$  at three ambient temperatures ( $T_a = 25, 55$  and  $85^\circ\text{C}$ ). The theoretical predictions based on Eqs. (6.11)–(6.13) are found to be in good agreement with the measured data for all values of  $I_b$ . This agreement depicts the optical, electrical and thermal consistency of the thermal model besides the underlying accuracy of the extracted temperature dependence of various VCSEL parameters.

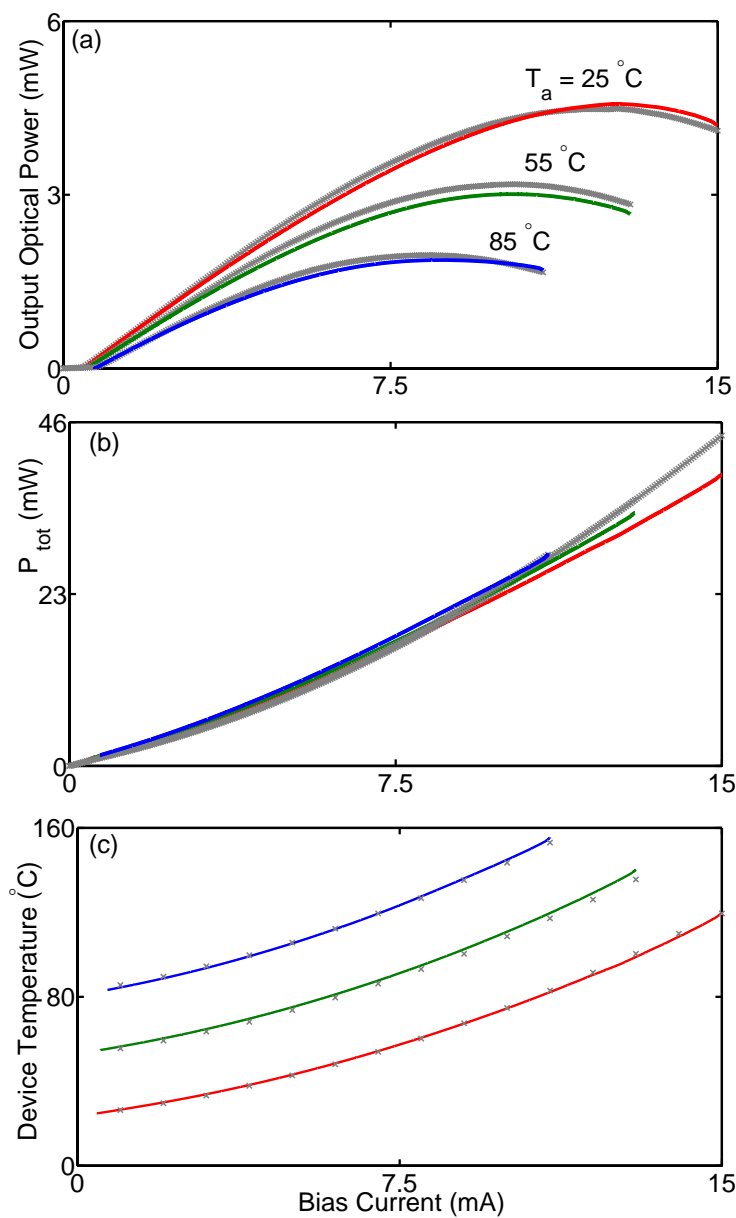


Figure 6.5: Comparison of simulated (solid lines) and measured (symbols) values of (a) output power, (b) total dissipated power, and (c) device temperature as a function of  $I_b$  at three different ambient temperatures  $T_a = 25, 55$  and  $85^\circ\text{C}$ .

The reason behind the saturation of output power at high bias currents can be understood by plotting in Figs. 6.6 and 6.7 the evolution of selected VCSEL parameters with bias current at  $T_a = 25, 55,$  and  $85^\circ\text{C}$ . Figure 6.6(a) shows

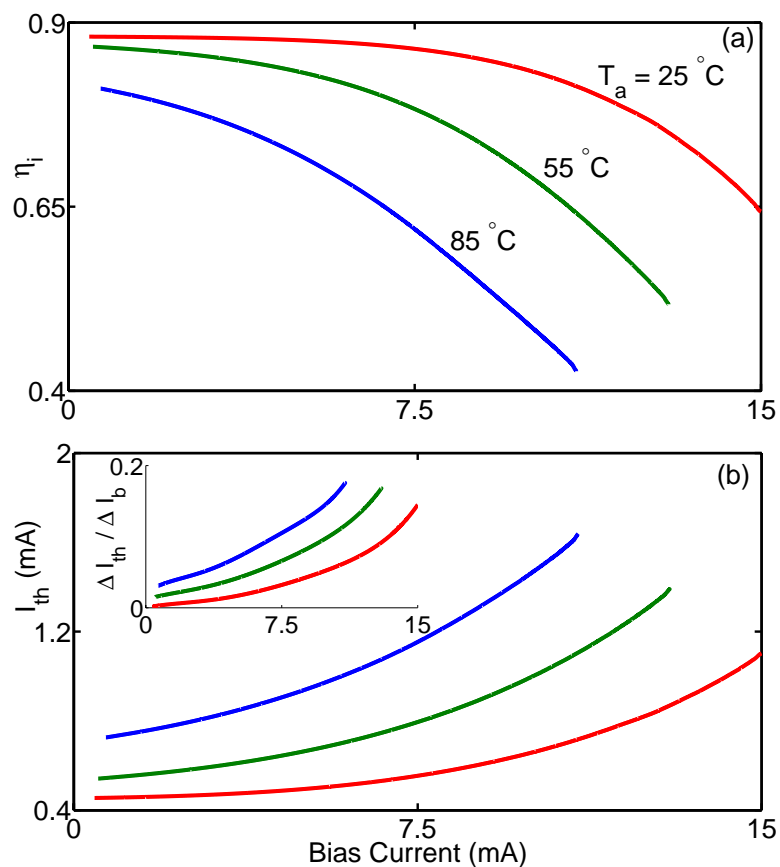


Figure 6.6: (a) Internal quantum efficiency and (b) threshold current as a function of  $I_b$ . The inset in (b) shows the derivative  $dI_{\text{th}}/dI_b$

variation of  $\eta_i$  with  $I_b$ . At  $25^\circ\text{C}$  ambient temperature,  $\eta_i$  is reduced from 88% at threshold to 70% at thermal rollover where the device temperature is close to  $100^\circ\text{C}$  as shown in Fig. 6.5(c). The reduction in  $\eta_i$  becomes more severe at higher ambient temperatures. For example, when  $T_a = 85^\circ\text{C}$ ,  $\eta_i$  is reduced to less than 50% at thermal rollover. Figure 6.6(b) shows the evolution of  $I_{\text{th}}$  with  $I_b$ . As expected, the threshold current increases with bias current because of current-induced self-heating. The inset plots the derivative  $dI_{\text{th}}/dI_b$  as a function of  $I_b$  and shows that this derivative becomes so large near thermal rollover that the rate of increase of  $I_{\text{th}}$  is 0.2 times the change in  $I_b$ . Ideally, threshold current insensitive to  $I_b$  over a wide range of device temperatures is desired, from the standpoint of

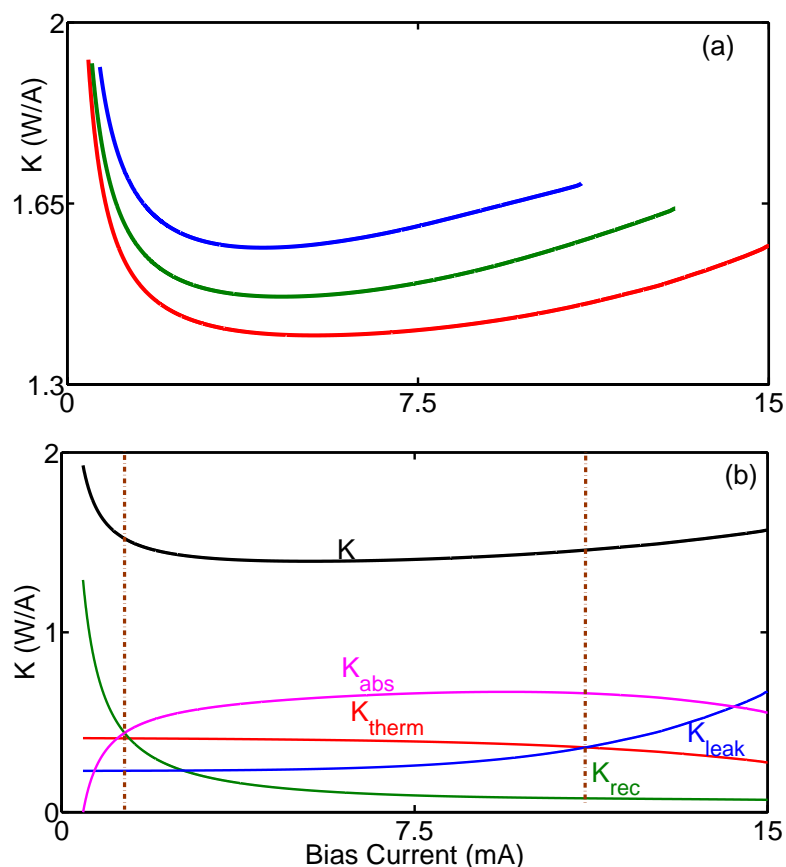


Figure 6.7: (a) LPD coefficient  $K$  versus bias current at three ambient temperatures. (b) Dependence of four individual LPD coefficients on bias current at 25°C. Total  $K$  is also shown for comparison. Vertical dotted lines mark the region where  $K$  is relatively small.

improving the device thermal performance. This can be achieved by optimizing wavelength detuning between the gain peak and the cavity resonance at which the VCSEL operates [181].

The VCSEL thermal saturation behavior can now be explained as follows: at any  $T_a$ , as  $I_b$  increases, the power dissipated within the VCSEL increases [Eq. (6.11)]. The corresponding increase in temperature [Eq. (6.12)] reduces  $\eta_i$  and increases  $I_{th}$  and  $\alpha_i$ , which eventually causes the thermal rollover. To delay the onset of thermal rollover, the rate of increase of  $T$  with respect to  $I_b$  must

be reduced. Traditionally, this has been achieved by reducing series resistance  $R_s$  [122, 129, 130] and  $R_{th}$  [131, 143]. However, the work presented in this chapter, is focussed towards identifying and quantifying the relative contributions to linear power dissipation ( $P_{LPD}$ ) in the device with an aim to formulate design strategies to reduce them. For this purpose, the LPD coefficient  $K$  introduced in Eq. (6.2) is plotted. The three curves in Fig. 6.7(a) show the total  $K$  representing the sum of four individual contributions at three ambient temperatures [ $T_a = 25, 55,$  and  $85^\circ\text{C}$ ]. As seen there,  $K$  initially decreases with increasing  $I_b$ , reaches a minimum value, and then starts increasing as  $I_b$  approaches the bias current corresponding to thermal rollover. It is this increase of  $K$  with current that causes a rapid increase in internal temperature of the VCSEL, which in turn causes the thermal rollover behavior.

To understand the peculiar behavior of  $K(I_b)$ , the LPD coefficient is decomposed into individual coefficients for the four constituent LPD mechanisms. We attach a subscript to  $K$  and introduce  $K_d = P_d/I_b$ , where  $d$  is the subscript label used in Eqs. (6.3)–(6.6) that identifies the specific LPD mechanism in question. Four individual  $K$  parameters are calculated from Eqs. (6.3)–(6.6) by simply dividing the four Eqs. with  $I_b$ . In Fig. 6.7(b), these individual LPD coefficients are plotted as a function of bias current at  $T_a = 25^\circ\text{C}$ . The total  $K$  is also plotted for comparison.

The LPD coefficients representing heating due to carrier leakage and thermalization are fairly constant over a large range of  $I_b$  but the other two change considerably. First, heating due to the carrier recombination governed by  $K_{rec}$  is considered. This parameter is large at low bias currents and decreases as  $I_b$  increases. This can be understood by noting that heating due to spontaneous recombination is high below laser threshold as most injected carriers recombine spontaneously to produce heat. It is reduced near and beyond the laser threshold because of clamping of the carrier density. Next, heating due to internal optical

loss (absorption of photons produced by stimulated emission) governed by  $K_{\text{abs}}$  should be considered. This heating mechanism starts at laser threshold and its contribution increases with  $I_b$  due to an increase in the number of stimulated photons generated inside the laser cavity. The net effect of  $K_{\text{rec}}$  and  $K_{\text{abs}}$  is an initial reduction of  $K(I_b)$  with increasing  $I_b$  around threshold.

The region bounded by the two vertical dotted lines in Fig. 6.7(b) corresponds to the region where total  $K$  takes its relatively low values. In this region, the coefficients representing thermalization and absorption heating are nearly constant while the coefficients representing spontaneous recombination and carrier leakage are slowly decreasing and increasing, respectively. The net effect is a nearly constant  $K$  in this region, implying a linear increase of  $P_{\text{LPD}}$  with current [Eq. (6.2)]. Beyond the second dotted line, the coefficient representing carrier leakage increases, causing an increase in  $K$  and a corresponding super-linear increase of  $P_{\text{LPD}}$  with increasing bias current. This is due to rapid reduction of  $\eta_i$  at high bias currents [Fig. 6.6(a)] corresponding to an internal device temperature increase in excess of 70°C [Fig. 6.5(c)]. Furthermore, the coefficient representing internal optical loss saturates at the thermal rollover current, which is consistent with the saturation of the photon density in the laser cavity.

This analysis suggests that, for the particular device under consideration, carrier leakage and internal optical absorption are the dominant factors among all the contributions to linear power dissipation. It also suggests that a rapid reduction of internal quantum efficiency at high bias currents and ambient temperatures, causing a rapid increase in  $P_{\text{leak}}$ , is the dominant contributor to the thermal rollover.

## 6.4 Thermal Analysis

In this section, the contributions from all the heat sources (linear and quadratic) to the total heat load are quantified. Their impact on the increase of device tem-



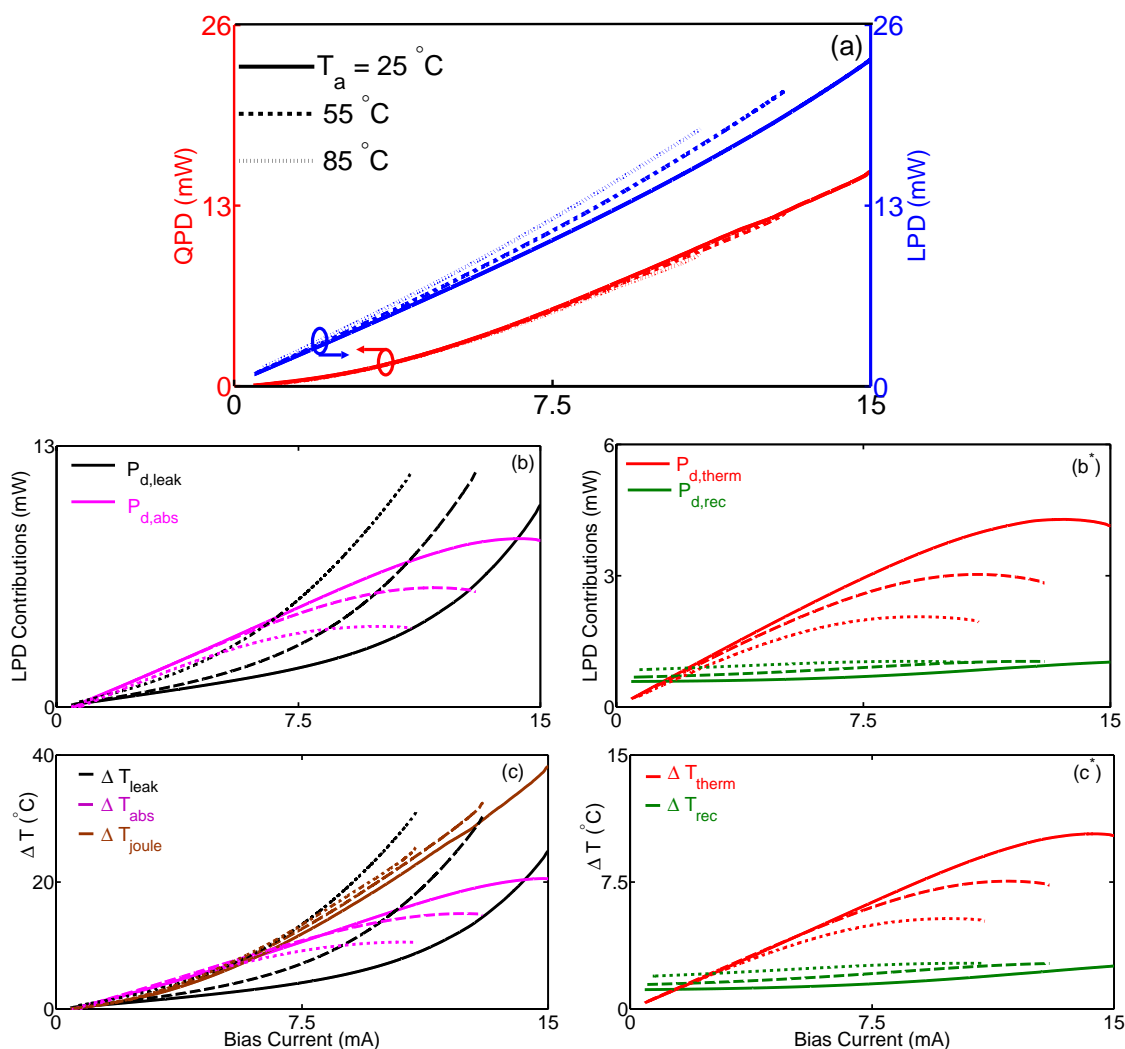


Figure 6.8: Comparison of the various VCSEL heating mechanisms at three ambient temperatures. (a) Total LPD and QPD as a function of  $I_b$ , (b) dependence of individual LPD contributions on  $I_b$ , and (c) contributions of LPD and QPD mechanisms to the increase in device temperature as a function  $I_b$ . The Figs. with asterisk\* refer to the fragments of the corresponding part. These Figs. have been split into two to achieve desired clarity

perature with bias current is also investigated. Figure 6.8(a) shows the individual contributions of  $P_{LPD}$  and  $P_{QPD}$  to  $P_{tot}$  at  $T_a = 25, 55, \text{ and } 85^\circ\text{C}$ . At any  $T_a$ ,  $P_{LPD}$  exceeds  $P_{QPD}$ . This may seem counterintuitive. However, the proportionality

constants ( $R_s$  and  $K$ , respectively) in Eqs. (6.1) and (6.2) themselves depend on temperature, and therefore on  $I_b$ , as seen in the inset of Figs. 6.4(b) and 6.6(c), respectively. Further, with increasing  $T_a$ ,  $P_{\text{QPD}}$  is slightly reduced while  $P_{\text{LPD}}$  increases progressively at any bias current.

The individual contributions of  $P_{\text{leak}}$ ,  $P_{\text{therm}}$ ,  $P_{\text{rec}}$ , and  $P_{\text{abs}}$  to  $P_{\text{LPD}}$  as a function of  $I_b$  are shown in Fig. 6.8(b) at  $T_a = 25, 55, \text{ and } 85^\circ\text{C}$ . At a low ambient temperature ( $25^\circ\text{C}$ ), internal optical loss (optical absorption) and carrier leakage are the two dominant power dissipation mechanisms. With increasing  $I_b$ , power dissipation due to optical absorption saturates and eventually rolls over, whereas power dissipation due to carrier leakage is enhanced significantly. The rollover of the absorption heating is consistent with the rollover of the photon density while the significant increase of the leakage heating is consistent with the rapid reduction of the internal quantum efficiency at high temperatures. The reduction in  $\eta_i$  also causes a saturation and subsequent rollover of the power dissipation due to carrier thermalization. Finally, the slight increase of recombination heating with  $I_b$  is consistent with the increase of  $I_{\text{th}}$ , and therefore of the carrier density in the quantum wells, with increasing  $I_b$ . However, its overall contribution is negligible at any  $T_a$  and  $I_b$ . This analysis points to carrier leakage (reduction of  $\eta_i$  with increasing device temperature) as being the single most dominant contributor to  $P_{\text{LPD}}$  limiting the VCSEL thermal performance, especially at high ambient temperatures.

Figure 6.8(c) displays the contributions to current-induced self-heating as a function of  $I_b$  at  $T_a = 25, 55, \text{ and } 85^\circ\text{C}$ . At a low  $T_a$  of  $25^\circ\text{C}$ , temperature increase due to  $P_{\text{QPD}}$  (Joule heating) exceeds that due to heating from optical absorption and carrier leakage. However, at high ambient temperatures ( $85^\circ\text{C}$ ), increase in device temperature due to carrier leakage exceeds that due to other mechanisms. Also, at any  $T_a$ , heating due to carrier leakage increases most rapidly at high bias currents. This again shows that the reduction of internal quantum efficiency with

increasing device temperature sets the ultimate limit for thermal performance of this device.

Based on the preceding analysis, the following conclusions are drawn regarding design modifications for improving thermal performance of this device. First, to delay the onset of carrier leakage,  $P_{\text{QPD}}$  and  $P_{\text{abs}}$  must be minimized. In a conventional VCSEL with current injection through doped DBRs, this involves a trade-off since higher doping levels lead to reduced resistance and increased free carrier absorption [130, 184]. More effective is the use of an intra-cavity contact and a dielectric top DBR [123] as both resistance and optical absorption can be reduced. In addition, it has been shown that reducing the photon lifetime through increased transmission through the top DBR can reduce internal optical absorption, thereby delaying thermal rollover and improving dynamic performance [127]. The impact of photon lifetime on the thermal degradation mechanisms in 850 nm VCSELs will be examined in detail in the next section. Second, the thermal impedance should be reduced, thereby reducing the increase of device temperature for a given amount of dissipated power. This involves the use of mounting and packaging techniques for improving thermal management and the use of more novel techniques such as integration of on-chip metallic heat spreaders [131]. Finally, further improvements are expected with active region designs that prevent an excessive increase of carrier leakage at high temperatures. This involves the design of quantum wells and barriers as well as the design of the surrounding separate confinement heterostructure [122, 127, 128]. It may also involve the use of e.g. carrier blocking layers [185].

## 6.5 Concluding Remarks

In this chapter, a simple, empirical thermal model to study relative roles of various thermal rollover mechanisms inside VCSELs has been presented. The param-

eters required by this model are deduced experimentally through measurements of output power, voltage and emission wavelength as a function of bias current at different ambient temperatures. The method presented is quite general and can potentially be applied to any VCSEL. Specifically, in this chapter, the method has been used for analyzing the thermal performance of an oxide-confined, 850 nm VCSEL designed with a 9  $\mu\text{m}$  inner aperture diameter and optimized for high speed operation. The model shows that the thermal saturation behavior is caused by a rapid increase of device temperature with bias current, which causes a reduction in the internal quantum efficiency, an increase in the threshold current and increase in the internal optical loss.

An in depth analysis of various thermal rollover mechanisms for this device has been carried out from the standpoint of understanding the power-saturation behavior. Our approach relates macroscopic VCSEL parameters to various thermal rollover mechanisms and makes an accurate estimate, both qualitatively and quantitatively, of various power dissipation mechanisms from the total power dissipation in the device. It was concluded that, at any bias current and ambient temperature, power dissipation due to carrier leakage, carrier thermalization, spontaneous carrier recombination and internal optical absorption together exceeds the power dissipated across the series resistance (Joule heating). This may seem counterintuitive given the fact that the basic dependence of Joule heating on current is quadratic while that of other heat sources is linear. However, the constants of proportionality ( $R_s$  and  $K$ , respectively) depend themselves on the internal device temperature, and change in opposite directions, as the bias current is increased close to thermal rollover. Still, quadratic power dissipation is a major source of device heating, having a significant impact on the thermal performance of the VCSEL.

A careful analysis of the interplay among various thermal rollover mechanisms yields useful conclusions from the standpoint of improving the device design for

improved thermal performance. Even though carrier leakage sets the ultimate limit for the thermal performance of this particular device, directly addressing it by only improving the internal quantum efficiency at high temperature is less advantageous as opposed to delaying the onset of its reduction. This can be achieved by reducing the series resistance, reducing the internal optical loss and reducing the thermal impedance, which leads to reduction of the rate of increase of device temperature with bias current. Further modifying the active region design for improved internal quantum efficiency at high temperatures may lead to a VCSEL design with superior performance in terms of both increased output optical power and speed at elevated temperatures.

# 7 Dimensional Analysis of Thermal Effects in 850 nm VCSELs

## 7.1 Introduction

850 nm is the standard wavelength for various data communication protocols. Further, commercial multimode fibers and polymer waveguides are optimized for the 850 nm wavelength band [191]. This has fueled the development of high-speed, 850 nm VCSELs with data rates as high as 40 Gb/s [121, 192] for diverse applications including high-performance computing, optical interconnects, and consumer electronics [121, 123].

Compared to VCSELs operating in the wavelength range of 980–1100 nm [193–195], pushing the data rate of 850 nm VCSELs beyond 40 Gb/s has posed several technological challenges and has required considerable development effort [122, 126–131]. For example, a high differential gain has required the use of strained quantum wells (QWs) by adding Indium to the GaAs material. This causes a red shift of the gain peak, which in turn has to be compensated by increasing the Al content in the barrier layers and by reducing the QW width [126]. However, a reduced QW width enhances carrier leakage [196], the magnitude of which

worsens with increasing device temperatures, thereby limiting the high speed operation [197].

High speed operation of VCSELs is achieved by reducing the cavity photon lifetime [127], increasing the differential gain [122], and reducing the gain compression coefficient by optimizing the SCH for a short carrier capture time [128]. High speed oxide confined VCSELs commonly employ multiple oxide layers [127] for reducing the oxide capacitance. Pad capacitance is reduced by using low-K dielectric material such as Benzo-Cyclo-Butene [129] or Polyimide [130, 131]

In the current state-of-the art 850 nm VCSELs, self-heating effects are the biggest hurdle in improving the modulation bandwidth beyond 23 GHz [192]. Self-heating manifests itself as premature rollover of the optical power with increasing bias current, under CW operation. The subsequent saturation of the photon density within the active region limits VCSEL's modulation speed. Traditionally, self-heating effects have been ameliorated by reducing series resistance [122, 129] together with thermal impedance [122, 131]. However, it is equally important to understand the interplay between various power dissipation mechanisms [198, 199] for optimizing the device design from the standpoint of improving the device thermal performance.

In the previous chapter, a method for assessing the relative importance of various thermal rollover mechanisms in VCSELs from basic CW measurements and empirical modeling was presented. That method was applied to a specific 850 nm VCSEL, optimized for high speed operation, and it was demonstrated that in that device power dissipation resulting from linear mechanisms (optical absorption, carrier thermalization, carrier leakage, and spontaneous carrier recombination) exceeded the quadratic power dissipation resulting from series resistance at all ambient temperatures and bias currents. It was further concluded that the carrier leakage worsened with increasing ambient temperature. In fact, carrier leakage was the most dominant contributor to thermal rollover for that particular

device.

In this chapter, the thermal performance of four different 850 nm high-speed VCSELs is compared using the numerical model presented in Chapter 6. These devices have very different cavity design and consequently, in this chapter, it is demonstrated that the model presented in Chapter 6 is universally applicable with reasonable accuracy. In this chapter, the aim is to study the impact of device parameters, such as inner aperture diameter and the cavity photon lifetime, on various thermal rollover mechanisms. In VCSELs where cavity photon lifetime is controlled by the top DBR reflectivity, a trade-off between optical absorption and carrier leakage is demonstrated in the sense that overcompensating for one worsens the other. Further, increasing inner aperture diameter (leading to a reduction in thermal impedance and series resistance) and reducing photon lifetime, both have the same impact of delaying the onset of the rapid increase in carrier leakage, which in turn delays the onset of thermal rollover. Therefore, carrier leakage places the ultimate limit on the thermal performance for this entire class of 850 nm devices. Useful design optimization strategies for mitigating carrier leakage are also discussed.

## 7.2 CW Measurements for the Four VCSELs

The details of the empirical thermal model used to study the thermal degradation mechanisms in the four VCSELs can be found in Chapter 6. Further, the basic structure, common to all four 850 nm VCSELs are shown in Fig. 6.2 and described in Section 6.3.1. That description is repeated here for the sake of clarity. The devices are grown on undoped GaAs substrates and employ an oxide-confined configuration optimized for high speed modulation [190]. The top and bottom DBRs are fabricated with graded interfaces and modulation doping to reduce their electrical resistance [122]. The bottom DBR is partly composed of AlAs



Table 7.1: Summary of Devices Under Test

Device	Inner aperture diameter	Surface etch
A	9 $\mu\text{m}$	0 nm
B	6 $\mu\text{m}$	55 nm
C	9 $\mu\text{m}$	55 nm
D	14 $\mu\text{m}$	55 nm

to lower its thermal impedance [127]. The active region is made of five strained InGaAs quantum wells for improved differential gain [126] and is surrounded by a SCH designed for efficient carrier trapping and low gain compression [128,190]. As indicated with dark shading in Fig. 6.2, six AlGaAs layers in the lower part of the top DBR are composed of high Al content (98% for the bottom two and 96% for the remaining four) to form a small oxide aperture for current and optical confinement and a larger oxide aperture (twice the inner aperture diameter) for reducing device capacitance [127]. After the bondpad sputtering, a shallow surface etch is made in selected VCSELs to optimize top DBR reflectivity (and consequently the cavity photon lifetime).

Table 7.1 summarizes the design elements of the four VCSELs investigated in this thesis. Device A has no surface etch in the top DBR whereas devices B, C and D have 55 nm surface etch in their top DBRs. The purpose of this surface-etch is to control the device photon-lifetime. The photon lifetime  $\tau_p$  of a VCSEL is given by [127]:

$$\tau_p = \frac{1}{\alpha_i(T) + \alpha_m^T(T) + \alpha_m^B(T)}. \quad (7.1)$$

This expression shows that changing the top-DBR reflectivity can have a significant impact on the cavity photon lifetime of the VCSEL. While this technique has been described in detail in Ref. [127], a brief description of how the top-DBR

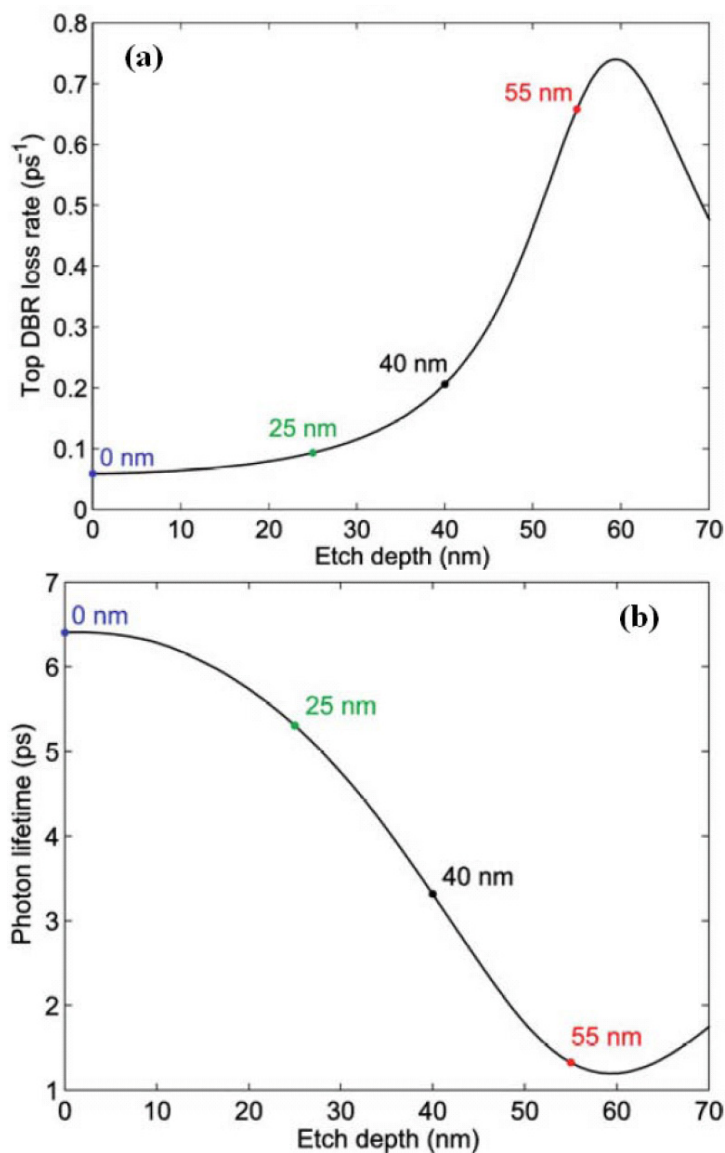


Figure 7.1: Calculated (a) top DBR loss rate and (b) photon lifetime as a function of etch depth into the top DBR. The experimental etch depths are indicated using dots and correspond to 0, 25, 40 and 55 nm. These Figs. have been adapted from Ref. [127].

reflectivity varies with etch-depth and its impact on photon lifetime is presented here. In this physical description the temperature dependence of, internal optical loss rate, top and bottom DBR loss rates are ignored. The top DBR loss rate

( $\alpha_m^T$ ), and the corresponding photon lifetime  $\tau_p$  at 25 °C (calculated using an effective index model [189] and established room temperature values for the free carrier absorption coefficients respectively) are plotted against etch depth ( $d_{\text{etch}}$ ) in Fig. 7.1(a) and (b), respectively. The experimental etch depths are indicated using dots and correspond to 0, 25, 40 and 55 nm. These Figs. have been adapted from Ref. [127]. Physically, with increasing surface etch-depth, the reflection at the semiconductor/air interface becomes increasingly out-of-phase with the reflections from the lower DBR stacks. This is in-turn, decrease the reflectivity and increases the loss rate respectively, of the top DBR and consequently, the photon lifetime is reduced. It is important to note that 0 nm surface etch corresponds to completely in-phase reflection and 60 nm surface etch corresponds to completely out of phase reflection at the semiconductor/air interface. The corresponding room temperature photon lifetime values are 6.4 and 1.1 ps respectively [Fig. 7.1(b)].

This technique of changing the top-DBR reflectivity has previously been successfully used for enhancing the single-mode output power of 850 nm VCSELs [200] as well as reducing the output beam divergence of the VCSELs [201]. This technique is more appropriate for reducing photon-lifetime as compared to removing entire layer pairs in the top-DBR stack as DBR-pair removal causes an increase in the device series resistance due to current crowding [127].

### 7.2.1 Experimental Setup and Measurements

To perform CW measurements, each VCSEL was placed on a copper stage with active temperature control. The emitted optical power was detected by a calibrated, large area PD (UDT Sensors PIN-10D) for accurate measurements. Measurements were performed over an ambient temperature range of 15–100°C. For spectral measurements, the light was coupled into a multimode fiber connected to an optical spectrum analyzer. All spectral measurements were performed with

0.1 nm resolution. As a result, device temperatures deduced from the spectral data are accurate to within 1.6 °C.

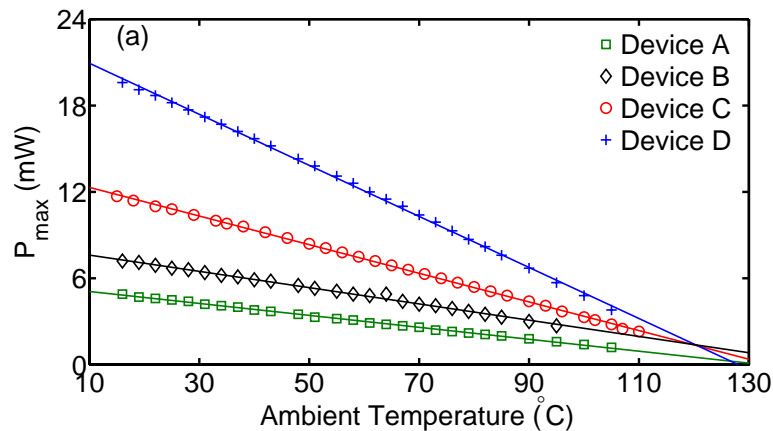


Figure 7.2: (a)  $P_{\max}$  as a function of  $T_a$  for the four VCSELs.

Experimental data from CW measurements is presented in Figs. 7.2 and 7.3. Figure 7.2 shows the maximum emitted optical power ( $P_{\max}$ ) as a function of  $T_a$ . A straight line can be fitted for each case. At  $T_a$  corresponding to  $P_{\max} = 0$ , each VCSEL stops lasing. It is important to note that the internal device temperature under such conditions is higher than  $T_a$ . Our VCSELs are projected to stop lasing between 128 and 145 °C. This indicates that the cut-off temperature strongly depends on VCSEL cavity design. From this point on, only measurements and simulations corresponding to  $T_a = 55$  °C are presented. This is a moderately high  $T_a$  for which the  $P_{\max}$  of all the devices exceeds a few mWs and device temperatures exceed 120 °C at bias currents corresponding to thermal rollover.

Parts (a)–(c) of Fig. 7.3 show  $P_{\text{opt}}$ ,  $V_b$  and  $P_{\text{tot}}$  as a function of  $I_b$ , respectively, under CW operation at  $T_a = 55$  °C. Comparing devices A and C with the same inner aperture diameter (9  $\mu\text{m}$ ), as the shallow surface etch in the top DBR is increased from 0 to 55 nm, the transmission loss rate increases from 0.058 to 0.653  $\text{ps}^{-1}$ . As shown in Fig. 7.3(a), this in turn causes  $P_{\max}$  and  $I_b$  corresponding to  $P_{\max}$  to increase by 150% and 30% respectively. Electrically, these two devices

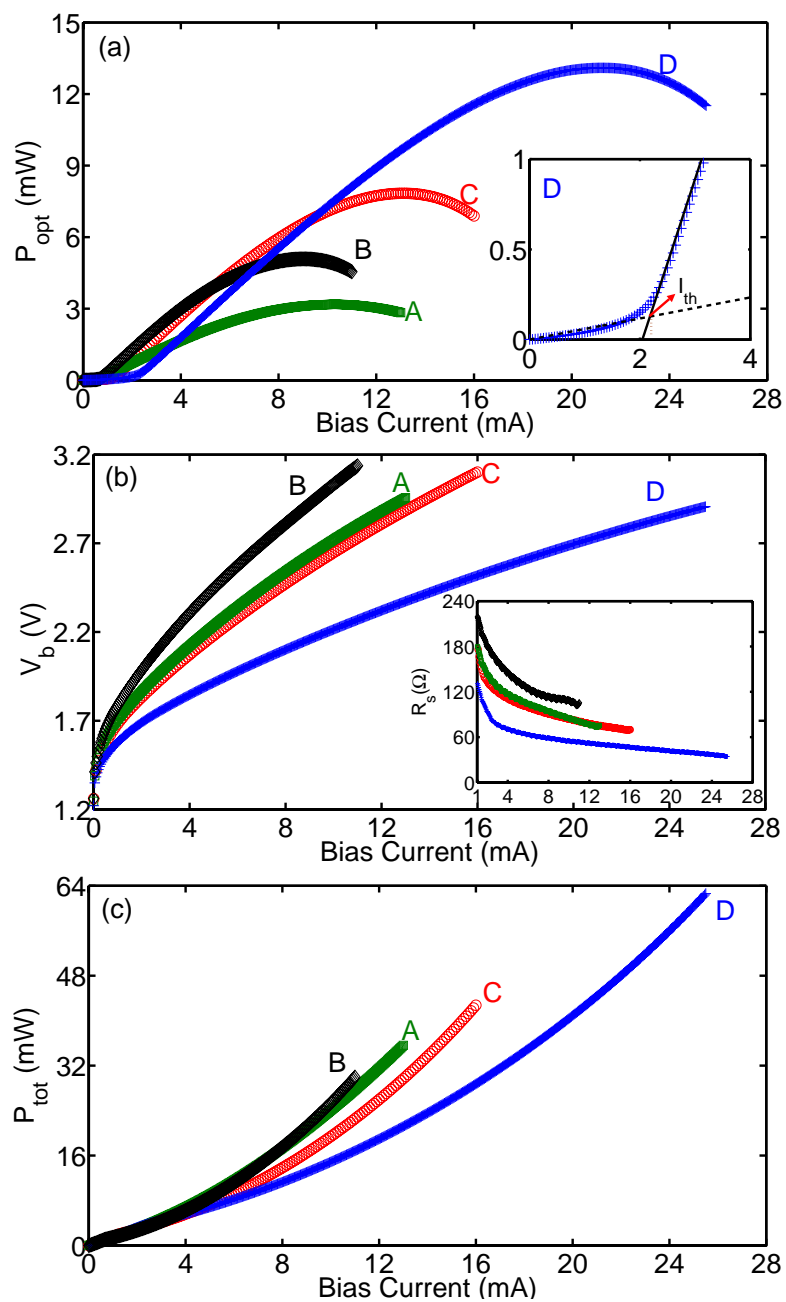


Figure 7.3: (a)  $P_{\text{opt}}$ , (b)  $V_b$  and (c)  $P_{\text{tot}}$  as a function of  $I_b$  at  $T_a = 55$  °C. The inset in (a) shows a two-segment line-fit on device D for estimating threshold current and inset in (b) shows the differential resistance  $R_s$ .

are identical (a shallow surface etch in the top DBR has an insignificant effect on electrical properties). This leads to almost identical  $R_s$  for the two devices over the entire range of  $I_b$ , as shown in the inset of Fig. 7.3(b). Finally, comparing the rate of increase of  $P_{\text{tot}}$  with  $I_b$  for the two devices [Fig. 7.3(c)], it can be seen that power dissipated as heat in device A exceeds that in device C. In subsequent sections, the origin of this excess power dissipation will be discussed.

Comparing devices B, C and D, for which inner aperture diameter increases from 6 to 14  $\mu\text{m}$ , both  $R_{\text{th}}$  and  $R_s$  are reduced [184]. This in turn, progressively increases  $P_{\text{max}}$  and  $I_b$  corresponding to  $P_{\text{max}}$ , as seen in Fig. 7.3(a). The series resistance  $R_s$  plotted in the inset of Fig. 7.3(b), is reduced with increasing aperture diameter. As the diameter is increased, the rate of increase of  $P_{\text{tot}}$  with  $I_b$  is reduced [see Fig. 7.3(c)]. Since the rate of increase of  $P_{\text{tot}}$  is proportional to rate of increase of device temperature [see Eq. 1.5)], clearly inner aperture diameter strongly influences the VCSEL thermal properties.

Table 7.2 summarizes the values of VCSEL parameters at  $T_a = 55^\circ\text{C}$  deduced from the measurements for the four VCSELs. The errors in the measured values of VCSEL parameters are also summarized in table 7.2. It is important to understand the sources of errors in the extracted device parameters values. The uncertainty in the value of  $\alpha_m^T$  is related to the  $\pm 2$  nm uncertainty in the surface etch depth. For the analysis presented here, it is ignored [127]. This fact is also reflected in table 7.1 where absolute values of surface etch depths are assumed. Bias current induced increase in device temperature [199] is a prominent source of error in the parameter values. It depends on the ambient temperature  $T_a$  owing to the temperature dependence of thermal impedance [see Eq. (1.5)] and increasing difficulty in stabilizing high stage temperatures against room temperature. At low ambient temperatures, the error in the extracted parameter values corresponds to the resolution limit of the device thermometer which is limited by the resolution of the optical spectrum analyzer [122, 199]. Assuming a worst case value of  $5^\circ\text{C}$

Table 7.2: Parameter values at  $T_a = 55$  °C for the four VCSELs and their linear temperature dependence ( $\Delta = \frac{\partial}{\partial T}$ ).

Device	A	B	C	D
$\lambda$ (nm)	$852.7 \pm 0.33$	$853.8 \pm 0.33$	$853.9 \pm 0.32$	$853.8 \pm 0.31$
$R_{th}$ (°C/mW)	$2.07 \pm 0.035$	$2.88 \pm 0.03$	$1.97 \pm 0.022$	$1.27 \pm 0.036$
$\alpha_i$ (ps <sup>-1</sup> )	$(8.3 \pm 0.22) \times 10^{-2}$	$(8.3 \pm 0.22) \times 10^{-2}$	$(8.3 \pm 0.22) \times 10^{-2}$	$(8.3 \pm 0.22) \times 10^{-2}$
$\alpha_m^T$ (ps <sup>-1</sup> )	0.0578	0.653	0.653	0.653
$\alpha_m^B$ (ps <sup>-1</sup> )	$6.08 \times 10^{-3}$	$6.08 \times 10^{-3}$	$6.08 \times 10^{-3}$	$6.08 \times 10^{-3}$
$\Delta\lambda$ (nm/°C)	$(6.077 \pm 0.13) \times 10^{-2}$	$(6.198 \pm 0.20) \times 10^{-2}$	$(6.199 \pm 0.14) \times 10^{-2}$	$(6.151 \pm 0.15) \times 10^{-2}$
$\Delta R_{th}$ (mW <sup>-1</sup> )	$(5.4 \pm 0.4) \times 10^{-3}$	$(5.8 \pm 0.2) \times 10^{-3}$	$(3.0 \pm 0.3) \times 10^{-3}$	$(2.0 \pm 0.6) \times 10^{-3}$
$\Delta\alpha_i$ (ps <sup>-1</sup> /°C)	$(4.167 \pm 0.11) \times 10^{-4}$	$(4.167 \pm 0.11) \times 10^{-4}$	$(4.167 \pm 0.11) \times 10^{-4}$	$(4.167 \pm 0.11) \times 10^{-4}$
$\Delta\alpha_m^T$ (ps <sup>-1</sup> /°C)	$-3.622 \times 10^{-5}$	$-3.643 \times 10^{-4}$	$-3.643 \times 10^{-4}$	$-3.643 \times 10^{-4}$
$\Delta\alpha_m^B$ (ps <sup>-1</sup> /°C)	$-5.705 \times 10^{-6}$	$-5.705 \times 10^{-6}$	$-5.705 \times 10^{-6}$	$-5.705 \times 10^{-6}$
$T_{cr}$ (°C)	153	154	145	142
$T_{max}$ (°C)	135	133	145	129

at  $T_a = 100$ °C for all the devices, the corresponding worst case errors in the parameter values are given in Table 7.2.

Temperature dependencies of internal quantum efficiency and threshold current ( $I_{th}$ ) were estimated from the measured  $P_{opt}$ - $I_b$  curves [184].  $I_{th}$  was calculated using a two-segment line-fit at any ambient temperature for all the devices. This method is relatively insensitive to changes in SE [184]. The inset of Fig. 7.3(a) applies this method to device D for calculating  $I_{th}$  at 55 °C ambient temperature. A parabolic fit to measurements at different ambient temperatures is used to model the dependence of  $I_{th}$  on device temperature [199]; maximum error in  $I_{th}$  is less than 2% for any device.

The method for extracting temperature dependence of internal quantum effi-

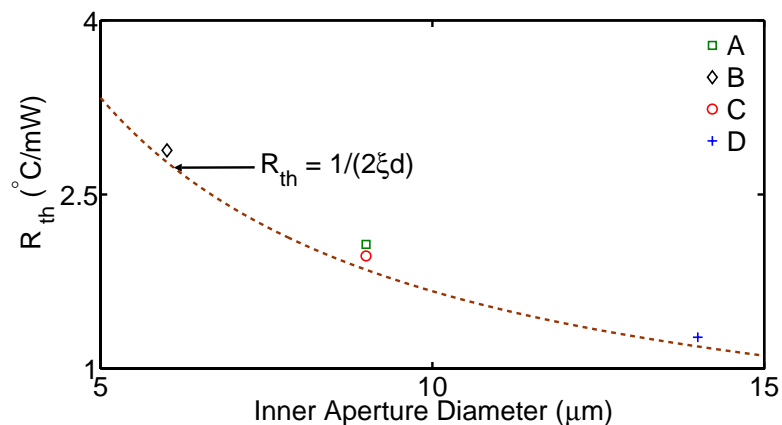


Figure 7.4: Thermal impedance as a function of inner aperture diameter. The dashed line represents analytical prediction and symbols correspond to values extracted using the thermal model presented in Chapter 6.

ciency is described in [199] and also discussed in detail in Chapter 6. A function of the form  $\eta_i(T) = \eta_i(RT)/[1 + (T/T_{cr})^4]$  is used to numerically fit to the measurements;  $\eta_i(RT)$ , where  $RT$  stands for room temperature, can be measured independently [127, 188] and  $T_{cr}$  is used as the fitting parameter. The values of  $T_{cr}$  are also summarized in Table 7.2. It is important to note that  $T_{cr}$  for any device is quite close to  $T_{max}$ , the temperature at which the corresponding VCSEL is projected to stop lasing [Fig. 7.2]. The maximum calculated error in the extracted value of  $\eta_i$  is less than 1%. Transmission losses through the top and the bottom DBR were calculated numerically using an effective index model [189]. Additional details on the method used to extract temperature dependence of various VCSEL parameters from CW measurements, the origin of errors in their values, physical explanations behind the temperature dependence, and previously reported room temperature values can be found in [122, 127, 199].

Since the dimensional dependence of thermal impedance follows a simple analytical expression [184],  $R_{th} = 1/(2\xi d)$ , where  $\xi$  is the effective thermal conductivity and  $d$  is the inner aperture diameter, the validity of the extraction method for



this particular parameter can be checked by comparing its deduced value with the analytical estimate. The expression used to extract  $R_{\text{th}}$  can be written as [122]:

$$R_{\text{th}} = \frac{\Delta T}{\Delta P_{\text{tot}}} = \frac{\partial \lambda / \partial P_{\text{tot}}}{\partial \lambda / \partial T}. \quad (7.2)$$

The average values of  $\partial \lambda / \partial T$  used are given in Table 7.2. The value of  $\xi$  is estimated to be 30 W/(m·K) at 55°C [184]. Figure 7.4 shows an excellent agreement between the analytical result (dashed line) and the extracted values of thermal impedance (solid dots).

### 7.3 Thermal Modelling

In this section, the parameter values extracted from CW measurements (see Table 7.2) are used to study how these parameters influence the thermal rollover mechanisms. The evolution of selected VCSEL parameters with increasing bias current is studied and the influence of this evolution on thermal rollover behavior is investigated. Using the procedure outlined in Chapter 6, together with the parameters listed in Table 7.2, the basic VCSEL characteristics are simulated. Figure 7.5 shows the measured and predicted values of  $P_{\text{opt}}$ ,  $P_{\text{tot}}$ , and  $T$ , respectively, as a function of  $I_{\text{b}}$  at  $T_{\text{a}} = 55^{\circ}\text{C}$  for the four VCSELs. It can be seen in parts (a) and (b) that the quantitative agreement is not the same for all devices. However, even for the worst case (Device D), the mismatch is less than 10%. It can therefore be concluded that the theoretical predictions based on the numerical model presented in Chapter 6 are in reasonable agreement with the measured data for all devices across the entire range of  $I_{\text{b}}$ . This depicts the optical, electrical, and thermal consistency of the thermal model, quantifies the underlying accuracy of the derived temperature dependence of VCSEL parameters and depicts the universal applicability of the method described in Chapter 6.

Next, the changes in selected VCSEL parameters with bias current are considered to gain some insight into the origins of the thermal rollover. In Fig. 7.6(a),

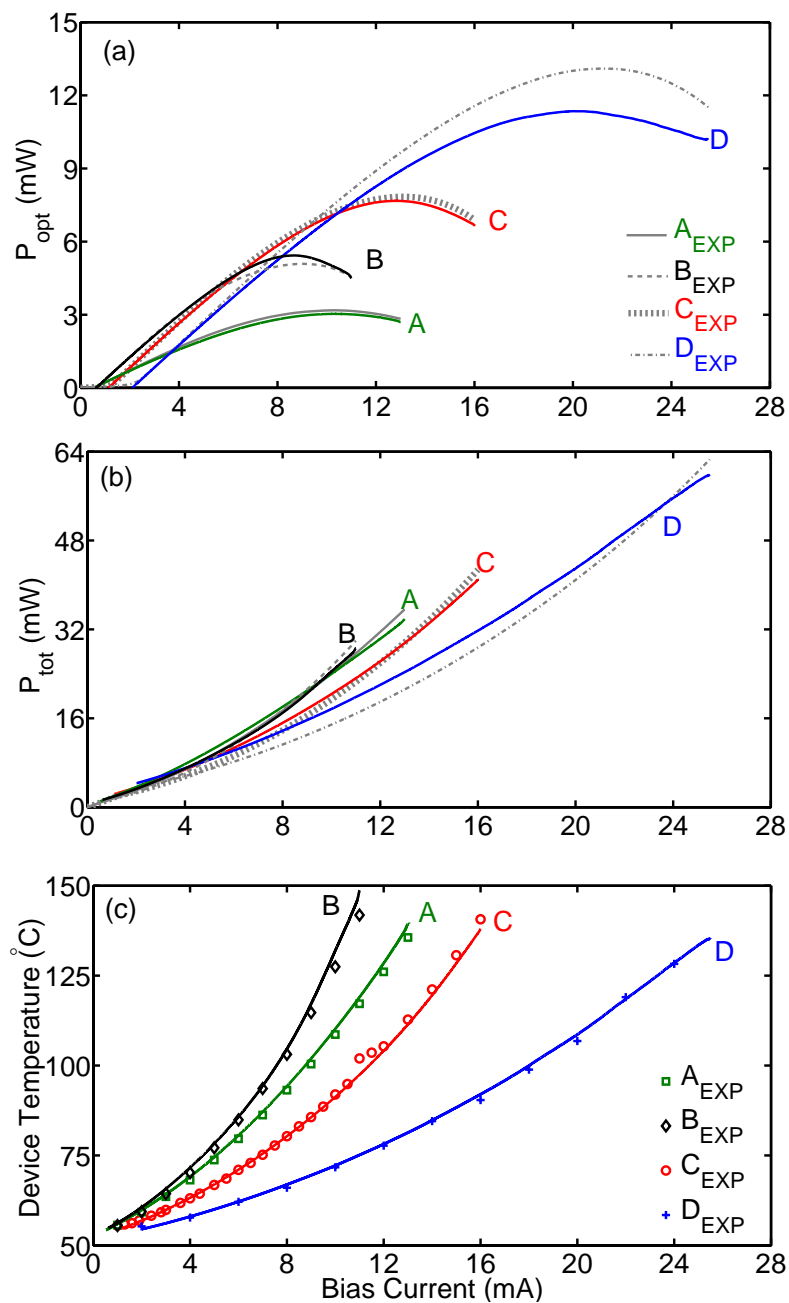


Figure 7.5: Comparison of predicted (colored lines) and measured values (indicated by gray lines and symbols) of (a)  $P_{\text{opt}}$ , (b)  $P_{\text{tot}}$ , and (c)  $T$  as a function of  $I_b$  at  $T_a = 55^{\circ}\text{C}$  for the four VCSELs.

the variation of  $\eta_i$  and  $I_{th}$ , with  $I_b$  is plotted for the four VCSELs. Devices B, C, and D have similar  $\eta_i$  values (about 75 %) at low bias currents, whereas device A has a significantly higher value of 86 %. The physical reason behind this difference will be discussed in the next section. It can be clearly seen that, at high  $I_b$  corresponding to the onset of thermal rollover, there is a sharp decrease in the values of  $\eta_i$  and a corresponding increase in the values of threshold current. The rapid decrease in the value of  $\eta_i$  at high device temperatures [Fig. 7.5(c)] is responsible for the onset of thermal rollover. Since the emitted optical power is  $\propto (I_b - I_{th})$ , an increase in the threshold current reinforces the sharp reduction in the value of  $\eta_i$  and hastens the output power saturation. However, the deleterious effect of threshold current can be independently mitigated by optimizing wavelength detuning between the gain peak and the cavity resonance at which the VCSEL operates [181].

Figure 7.6(b) depicts how the LPD coefficient  $K$  [Eq. (6.10)] varies with  $I_b$  for 4 VCSELs at  $T_a = 55^\circ\text{C}$ . Close to  $I_{th}$ , the value of  $K$  is close to 2 W/A but it decreases quite rapidly as the drive current is increased. It takes a minimum value and begins to increase gradually on further increase in  $I_b$ . Interestingly, this peculiar evolution is common to all the VCSELs and can be understood as follows [199]: Consider first heating due to the carrier recombination which is high below the lasing threshold. This is due to the fact that a significant percentage of the injected carriers recombine spontaneously to produce heat. It is reduced near and beyond the laser threshold because of the clamping of the carrier density. Further, the recombination heating coefficient scales with  $I_{th}/I_b$  [199].

Optical absorption (absorption of photons produced by stimulated emission in the VCSEL cavity) starts at the lasing threshold and its contribution increases with  $I_b$  due to an increase in the number of stimulated photons. The net effect of carrier recombination and optical absorption is an initial reduction of  $K$  with increasing  $I_b$  around threshold. It is important to note that carrier thermalization

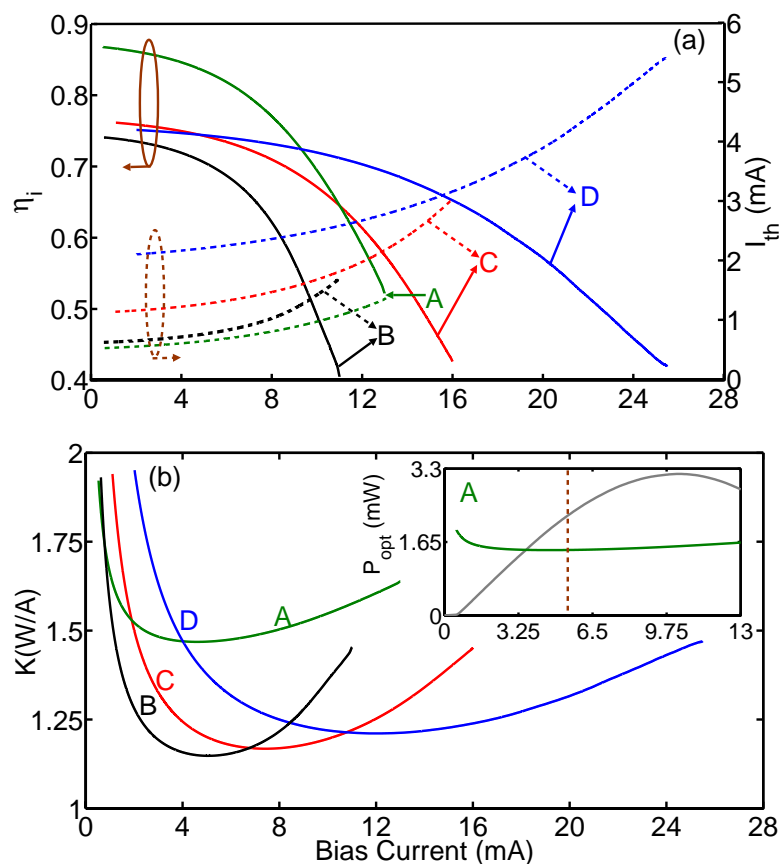


Figure 7.6: (a) Changes in  $\eta_i$  (solid lines) and  $I_{th}$  (dashed lines, right scale) with bias current at  $T_a = 55$  °C for four VCSELs. (b) LPD coefficient  $K$  versus  $I_b$  for four VCSELs; inset shows  $K$  and  $P_{opt}$  for device A as a function of  $I_b$ . An increase in  $K$  marks the onset of thermal rollover.

and carrier leakage are low and nearly constant over these low bias currents and hence do not have a significant impact on the evolution of  $K$ .

With further increase in  $I_b$ ,  $K$  in Fig. 7.6(b) takes its relatively low values for all four VCSELs. For these  $I_b$  values, carrier thermalization and absorption heating are nearly constant while spontaneous recombination and carrier leakage are slowly decreasing and increasing, respectively. The net effect is a nearly constant  $K$ . With a further increase in bias current, increase in carrier leakage dominates, causing an increase of  $K$  and a corresponding super-linear increase of  $P_{LPD}$ . Fur-

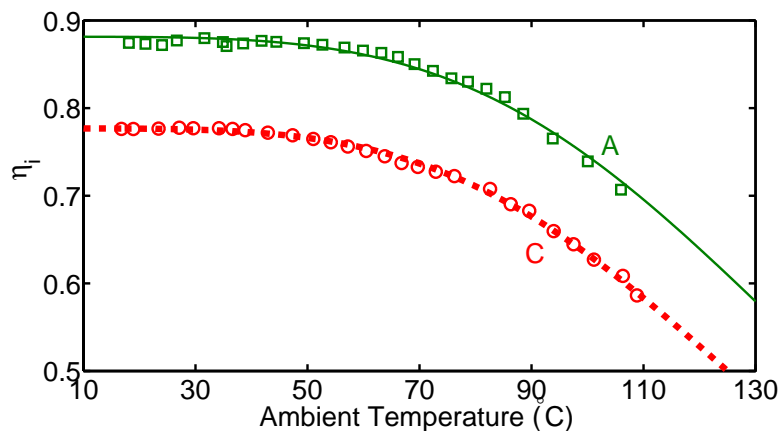


Figure 7.7: Internal quantum efficiency  $\eta_i$  as a function of  $T_a$  for device A (solid lines) and device C (dotted lines). The lines show a numerical fit to the measured data.

ther, absorption heating saturates at  $I_b$  corresponding to  $P_{\max}$ , which is consistent with the saturation of the stimulated photon density in the laser cavity.

To impress the importance of LPD mechanisms on the thermal performance of these devices,  $P_{\text{opt}}$  and  $K$  as a function of  $I_b$  for device A at  $T_a = 55^\circ\text{C}$ , are plotted in the inset of Fig. 7.6(b). As indicated by the vertical dashed line, as  $I_b$  is increased beyond 5.5 mA, the LPD coefficient increases, whereas the emitted optical power begins to saturate. All devices exhibit this behavior. The LPD coefficient therefore, has a profound influence on thermal saturation behavior of all VCSELs. If by some design modification, the onset of increase in LPD coefficient can be delayed, then both the static and dynamic performance can be improved considerably for this class of devices. This issue is investigated in detail in the next section.

## 7.4 Impact of Device Parameters

In this section, the impact of device parameters on thermal rollover mechanisms is studied. As seen in Table 7.1 and discussed in detail in section 7.2, devices A and C are used to study the impact of photon lifetime because they differ due to optical losses introduced by a shallow surface etch in the top DBR. Devices B, C, and D have the same surface etch depth (55 nm) and are used to study the impact of inner aperture diameter  $d$ .

### 7.4.1 Photon Lifetime

For device A (no surface etch),  $\tau_p$  is 6.8 ps. This value reduces to near 1.4 ps for devices B, C, and D with the 55 nm surface etch. It has been demonstrated that a shorter photon lifetime improves the high speed performance of 850 nm VCSELs [127]. Here, the impact of photon lifetime on thermal rollover behavior is investigated. For this purpose, it is important to analyze the impact of surface etch on the internal quantum efficiency  $\eta_i$  of a VCSEL. Ideally, a shallow surface etch should not drastically alter  $\eta_i$ . Indeed, the impact on  $\eta_i$  is insignificant for up to a 40 nm surface etch [127]. However, beyond 40 nm, increased cavity losses lead to an increase in the threshold carrier density, which in turn increases carrier leakage, causing a reduction in  $\eta_i$ .

Following the method for extracting  $\eta_i$  from  $P_{\text{opt}}$  versus  $I_b$  measurements discussed in detail in Chapter 6,  $\eta_i$  as a function of  $T_a$  for devices A and C is plotted in Fig. 7.7. The continuous lines (solid and dotted) correspond to a numerical fit of the data (squares and circles respectively) calculated following the procedure described in Section 7.2.1. At any  $T_a$ ,  $\eta_i$  for device C (with 55 nm etch) is about 10% smaller than that of device A (no etch).

In Figs. 7.8(a)–(c), solid lines correspond to device A and dotted lines to device C. Figure 7.8(a) shows the contributions of  $P_{\text{LPD}}$  and  $P_{\text{QPD}}$  to  $P_{\text{tot}}$  at  $T_a = 55^\circ\text{C}$ .

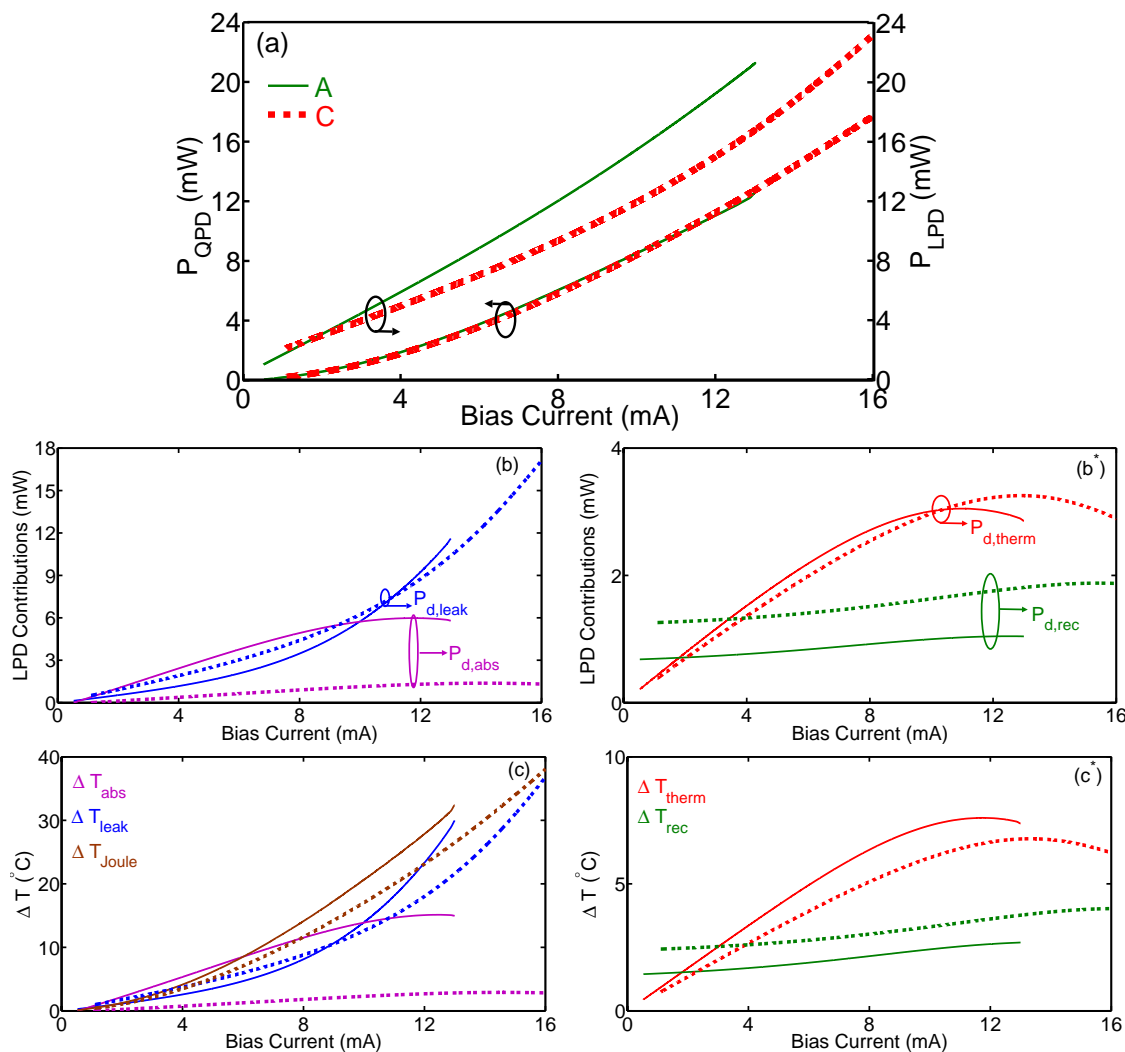


Figure 7.8: Impact of photon lifetime on the LPD and QPD mechanisms. (a)  $P_{LPD}$  and  $P_{QPD}$  as a function of  $I_b$ , (b) individual LPD contributions versus  $I_b$ , and (c) contributions of LPD and QPD mechanisms to  $\Delta T$  for device A (solid lines) and device C (dotted lines). The Figs. with asterisk\* refer to the fragments of the corresponding part. These Figs. have been split into two to achieve desired clarity.

For both these devices,  $P_{LPD}$  exceeds  $P_{QPD}$ . This can be attributed to the fact that  $R_s$  and  $K$  in Eqs. (6.1) and (6.2) themselves depend on temperature, and therefore on  $I_b$ . As discussed earlier, beyond a certain  $I_b$ , while  $K$  increases with

$I_b$  [Fig. 7.6(b)],  $R_s$  decreases with  $I_b$  [Fig. 7.3(c)]. Since similar evolution of  $K$  and  $R_s$  has been found for all devices, it can be concluded that  $P_{\text{LPD}}$  is the dominant contributor to the self-heating effects in all four devices. Devices A and C are electrically identical, and therefore the power dissipated across series resistance is identical for both these devices. Since  $P_{\text{LPD}}$  for device A is significantly higher than that for device C at any  $I_b$ , it can be concluded that a higher  $P_{\text{LPD}}$  in device A is limiting its thermal performance.

To understand the reason behind higher  $P_{\text{LPD}}$  for device A, the dependence of individual LPD contributions on  $I_b$  is plotted in Fig. 7.8(b). It can immediately be seen that  $P_{\text{abs}}$  is much higher for device A as compared to device C for which  $P_{\text{abs}}$  is almost negligible. This implies that a surface etch reduces the photon lifetime which not only reduces the damping [127, 184] but also significantly reduces absorption heating which delays the onset of carrier leakage. However, it is important to note that  $P_{\text{leak}}$  for device C is higher than that for device A at low bias currents.

While a 55 nm deep surface etch minimizes absorption heating, it does so at the cost of increased carrier leakage at low  $I_b$ . On the other hand, the use of a carrier blocking layer [185] for reducing carrier leakage will increase absorption heating owing to a corresponding increase in the internal quantum efficiency at high bias currents. Therefore, a trade-off exists between absorption heating and carrier leakage in devices that control photon lifetime through a shallow surface etch in the top DBR. This trade-off is different from that observed in conventional VCSELs involving absorption heating and Joule heating [130, 199]. A general design guideline for this class of devices is that photon lifetime should be optimized to the point where there is an insignificant increase in the threshold carrier density required for lasing. Indeed, devices with a 40 nm surface etch depth have been found to have superior high speed performance [127]. The residual carrier leakage can then be managed using other techniques such as reducing series re-



sistance [129], thermal impedance [122], and even employing an electron blocking layer [185]. The impact of series resistance and thermal impedance on thermal rollover is discussed later in this section.

Figure 7.8(c) shows the contribution of various power dissipation mechanisms to the total heat load. Again, the dominant contribution to increase in device temperature comes from Joule heating and carrier leakage. In device A, absorption heating also contributes significantly to the total heat load.

## 7.4.2 Inner Aperture Diameter

Inner aperture diameter,  $d$ , is an important VCSEL design parameter from the standpoint of thermal rollover [199]. This is due to the fact that both series resistance ( $R_s \propto 1/d^2$ ) and the device thermal impedance ( $R_{th} \propto 1/d$ ) are reduced with increasing inner aperture diameter [184]. Devices B, C and D are used to study the impact of inner aperture diameter on thermal rollover mechanisms.

Figure 7.9(a) shows  $P_{LPD}$  and  $P_{QPD}$  vs.  $I_b$  at  $T_a = 55$  °C for the three devices. The increase in  $d$  causes a reduction in  $R_s$  at any  $I_b$  [Fig. 7.3(c)], which in turn causes a reduction in  $P_{QPD}$ . Comparing the linear power dissipation for these devices, it can be seen that at low  $I_b$ , device D has the largest  $P_{LPD}$  followed by device C and then device B. However the situation is reversed at high bias currents close to the onset of thermal rollover.

To understand the evolution of  $P_{LPD}$  in devices with different  $d$ , the dependence of individual LPD contributions on  $I_b$  is plotted in Fig. 7.9(b). Since the three devices have identical surface etch depths, this implies that at low  $I_b$ ,  $P_{abs}$  will be identical for them. Further, the contribution of absorption heating to  $P_{LPD}$  is negligible. With increasing  $I_b$ ,  $P_{abs}$  saturates and rolls over. Similar evolution is observed for  $P_{therm}$ . For identical surface etch depths, threshold current increases with increasing inner aperture diameter [184]. Above lasing threshold,

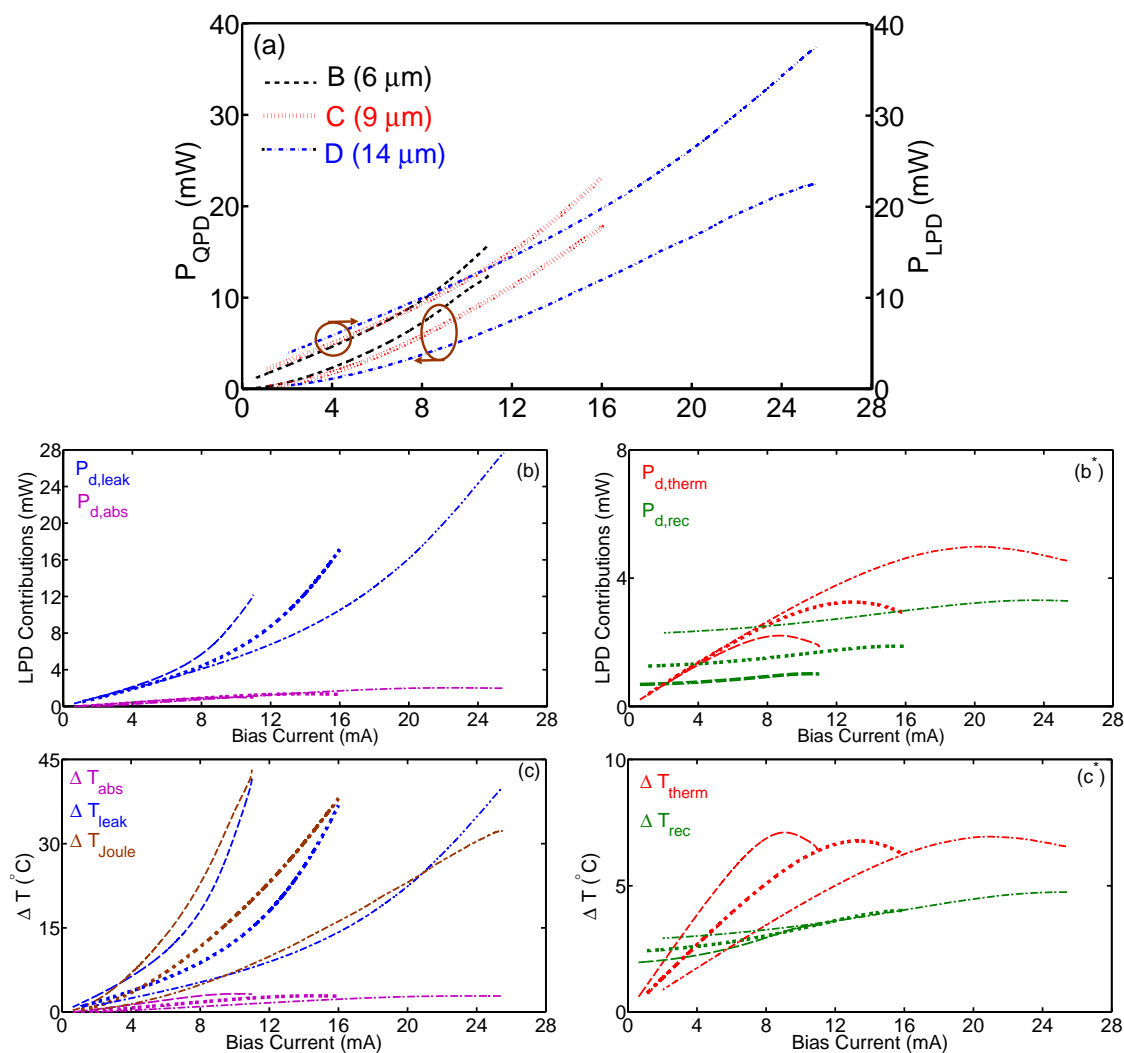


Figure 7.9: Impact of inner aperture diameter on the LPD and QPD mechanisms. (a)  $P_{\text{LPD}}$  and  $P_{\text{QPD}}$  as a function of  $I_b$ , (b) individual LPD contributions versus  $I_b$ , and (c) contributions of LPD and QPD mechanisms to  $\Delta T$  for device B (dashed lines), device C (dotted lines), and device D (dot-dashed lines). The Figs. with asterisk\* refer to the fragments of the corresponding part. These Figs. have been split into two to achieve desired clarity.

$P_{\text{rec}} \propto I_{\text{th}}$  [199]. Since the dominant LPD mechanism at low bias currents is recombination heating for all devices, the device with the largest inner aperture will have the highest  $P_{\text{LPD}}$  at low bias currents. The situation gets reversed at high

bias currents close to the onset of thermal rollover. At those bias currents, with increasing aperture diameter, the onset of increase in carrier leakage is delayed. This in turn delays the onset of thermal rollover [Fig. 7.5(a)]. For example, as the inner aperture diameter is increased from 6 to 14  $\mu\text{m}$ ,  $I_b$  at  $P_{\text{max}}$  and  $P_{\text{max}}$  itself both increase by 135% and 160%, respectively. This clearly indicates that VCSELs with a larger inner aperture diameter ( $\geq 7 \mu\text{m}$ ) exhibit superior CW performance because of a delayed onset of carrier leakage resulting from a reduced series resistance and thermal impedance, which reduces the rate of increase in device temperature with  $I_b$ . For the devices investigated in this work, this assertion has been tested for up to 13  $\mu\text{m}$  inner aperture diameters. However, it is important to understand that an increasing inner aperture diameter does not translate into superior high speed performance. As is well known, high speed performance of a VCSEL is related to the photon density inside its cavity, which decreases with increasing inner aperture diameters [190].

Figure 7.9(c) shows the contributions to increase in the device temperature ( $\Delta T$ ) as a function of  $I_b$  at  $T_a = 55 \text{ }^\circ\text{C}$ . Both  $P_{\text{QPD}}$  (Joule heating) and  $P_{\text{leak}}$  dominate the increase in device temperature for all devices and at any  $I_b$ . This assertion holds at any ambient temperature [199]. A higher  $R_{\text{th}}$  for the device with a smaller inner aperture further exacerbates the situation. The device temperatures rapidly increase, reaching rollover temperatures at lower  $I_b$  for smaller aperture devices. It can therefore be concluded that reducing series resistance and thermal impedance in devices where absorption heating has been reduced can delay the onset of carrier leakage. Reduction in series resistance can be achieved by using intra-cavity contacts [202] whereas thermal impedance can be reduced by using a binary material in the bottom DBR [122] or by employing metallic heat spreading layers [131].

## 7.5 Concluding Remarks

In this chapter, the simple empirical thermal model introduced in Chapter 6 is applied to study the impact of design parameters on thermal performance of 850 nm VCSELs optimized for high speed operation. Four VCSELs, three with different inner aperture diameters (6, 9 and 14  $\mu\text{m}$ ) and two with different photon lifetimes (6.8 and 1.4 ps) corresponding to 0 and 55 nm surface etch in the top DBR in devices with 9  $\mu\text{m}$  inner aperture diameter were analyzed.

Our empirical model requires the temperature dependence of macroscopic VCSEL parameters such as threshold current, internal quantum efficiency, internal optical loss, series resistance and thermal impedance. Adopting a consistent procedure, the temperature dependence is deduced through CW measurements of output power, voltage and emission wavelength as a function of bias current over an ambient temperature range of 15–100°C. It is important to note that the methods used in this work can potentially be applied to any VCSEL design. As a consequence, aside from some minor modifications in the relations for the barrier bandgap energy, lasing energy, and internal quantum efficiency, the empirical thermal model developed in Chapter 6 is generally applicable for a wide class of VCSELs. It is demonstrated that the thermal model can reproduce the measured VCSEL characteristics with reasonable accuracy ( $< 10\%$  error) for the four VCSELs used in this study, indicating that the model is consistent from the standpoint of optical, electrical, and thermal performance. Such an agreement speaks of the underlying accuracy of the extracted temperature dependence of various VCSEL parameters. A careful analysis of changes in the threshold current and internal quantum efficiency shows that thermal rollover occurs because of a bias current induced increase in the device temperature which increases the threshold current and causes a sharp reduction in the value of internal quantum efficiency.

The LPD coefficient  $K$  [Eq. (1.4)] shows a similar behavior for all VCSELs.

Close to  $I_{\text{th}}$ ,  $K$  is quite high because recombination heating dominates in this region. Its rapid reduction with increasing bias current is due to a reduction in recombination heating and simultaneous increase in absorption heating. These two effects reinforce each other. It assumes a minimum value and with further increase in bias current and then begins to increase gradually. This increase in the value of  $K$  is singularly dominated by carrier leakage as both absorption and carrier thermalization heating saturate and rollover at these bias currents. It is also shown that the onset of the optical power saturation coincides with the bias current at which the LPD coefficient  $K$  begins to increase. The onset of power saturation in this class of VCSELs can be delayed if the corresponding onset of increase in LPD coefficient is delayed.

An analysis of the evolution of various power dissipation mechanisms with bias current in the four VCSELs yields interesting conclusions. For this entire class of devices, linear power dissipation  $P_{\text{LPD}}$  exceeds the power dissipated across a series resistance ( $P_{\text{QPD}}$ ). This can be attributed to the fact that, beyond a certain bias current, the proportionality constant for  $P_{\text{LPD}}$  increases with bias current, whereas the series resistance decreases with bias current. Further, carrier leakage places the ultimate limit on the thermal performance of all these devices.

A comparative thermal analysis of devices A and C, which differ in their cavity photon lifetime, shows a trade-off between absorption heating and carrier leakage. Overcompensating for absorption heating can cause an increase in carrier leakage and vice versa. In these devices, absorption heating is reduced by a shallow surface etch in the top DBR. Beyond a certain etch-depth, cavity losses become so high that a very high carrier density is needed to achieve threshold gain which in-turn increases carrier leakage. Increasing inner aperture diameter reduces the series resistance and thermal impedance. These two effects reinforce each other and this in turn delays the onset of carrier leakage and as consequence, a delay in the onset of thermal rollover. However, an indiscriminate increase in the inner

aperture diameter does not translate into a continuing improvement in the high speed performance of these devices.

## 8 Concluding Remarks

### 8.1 Overview

This thesis has explored three photonic devices (HNLFs, SOAs, and VCSELs) from the standpoint of reducing the power consumption of optical signal processing techniques based on these devices. In this chapter the research endeavors presented in this thesis are summarized. The current state of the art in fiber-based all-optical signal processing, wavelength conversion using FWM in SOAs and high-speed VCSEL design is discussed. Finally, in each of the section, the major findings presented in this thesis are reviewed and directions for future research into this area are suggested.

### 8.2 Optical Signal Processing Based on HNLFs

Optical signal processing is a broad term which incorporates various functionalities including but not limited to: optical regenerators, wavelength converters, optical amplifiers, optical switches, pulse compressors and dispersion compensators [34]. Fiber Raman amplifiers (both discrete and distributed) have traditionally been used in long haul optical communication links [39, 67] and more recently their

applications in the passive optical network (PON) domain as a broadband optical amplifier for both upstream and downstream traffic have been explored [203]. Dispersion compensating fibers have been a key enabler behind ultra-long haul optical transport systems operating at bit rates of 10 Gb/s per channel [4]. Optical regenerators and wavelength converters based on HNLFs for telecom signals have been investigated in great detail [8, 10, 12–21, 34, 37–39]. In particular, 2R regenerators based on SPM induced spectral broadening followed by spectrally offset filtering in HNLFs (MTR), has received a lot of attention due to its simple architecture and ease of implementation [13]. While various aspects of this particular device have been optimized [17–19], the impact of fiber dispersion on its performance had been largely ignored.

To that end, in Chapter 2, a scaling parameter  $\mathcal{S}$  was presented. This parameter accounts for the interplay between fiber dispersion and nonlinearity in a 2R regenerator. It was also demonstrated that this parameter can be used to optimize fiber dispersion which in-turn leads to reduction in optimum input optical power required for signal regeneration. In fact, it was demonstrated that through careful dispersion optimization a significant reduction (upto 30%) in input optical power for optimum signal regeneration can be achieved without significantly altering the regenerator performance.

Even with additional dispersion optimization, watt level input optical powers are needed for the implementation of MTR. This makes this technique unattractive for future Green Optical Communication Systems [1, 2]. One potential solution to mitigate this problem is the integration of the optical gain and nonlinear propagation in a single optical fiber [204]. This can be achieved by the integration of raman gain with the MTR architecture. Preliminary theoretical results reported in [204] indicate a strong reduction in the input optical power required for signal regeneration. However, clearly this area awaits future research, both experimental as well as theoretical, before these “Active Mamyshev Regenerators” can become



practically realizable devices.

### 8.3 ASE-Assisted Nonlinear Effects in SOAs

Compared to optical signal processing based on HNLFs, SOA-based optical signal processing techniques offer the promise of reduced electrical footprint and input optical power requirements. However, their slow gain recovery dynamics severely limit their usability at high data rates (Section 1.5 and 1.7). While interferometric methods do cancel out these slow gain recovery dynamics (Section 1.5), they add a fair bit of complexity to the overall device design, stability becomes an issue and the overall device performance still remains constrained by the recovery speed of an individual SOA [27, 97–102].

A relatively recent method for achieving gain recovery acceleration in SOAs, which offsets some of the disadvantages listed above, involves using the internal ASE as the holding beam, which saturates the SOA gain and reduces its gain recovery time [40, 88, 90, 108, 109]. Such SOAs are now available commercially with a gain recovery time as short as 10 ps. They are designed carefully so that they can be driven at high drive currents (up to 500 mA), and high ASE and short gain recovery times are realized only at these high operating currents [88, 108]. Since these devices are fairly recent, ASE-induced enhancement in the nonlinear effects is a fairly unexplored area. What makes this area even more interesting is the fact that when these SOAs are used as part of an optical signal processor, the internal ASE will tie itself to the signal OSNR which is not the case with the previously known holding beam method [111–113]. A significant portion of this thesis is therefore devoted to investigation of enhancement of the nonlinear effects mediated by internal ASE in SOAs.

In Chapter 3, a numerical model was developed, which was used to study the impact of ASE on the nonlinear effects (SPM and FWM) in SOAs. The CW gain

measurements were used along with a detailed theoretical model to deduce how ASE shortens the effective gain recovery time of the SOA under consideration to near 10 ps. The model assumed that the total ASE power is constant along the length of the amplifier and increases with the current injected into the SOA. This is an approximate numerical model which makes fairly accurate predictions on ASE-enhanced nonlinear effects in SOAs.

The current dependence of  $\tau_{\text{eff}}$  and the SOA gain was incorporated into the proposed model which was used to study the impact of ASE on the SPM induced spectral broadening of picosecond pulses inside the SOA. It was demonstrated that a shorter gain recovery time affects the SPM induced spectral broadening in several ways. The SPM induced nonlinear phase shift becomes more symmetric and, consequently, frequency chirp becomes much more linear across the pulse. These features are attractive for designing SOA-based all-optical signal processing devices such as WCs, regenerators, and switches.

The shape and spectrum of the optical pulses was calculated over a range of drive currents to study how they change with shortening of the gain recovery time. The pulse shape becomes much more symmetric at high drive currents because a reduction in the value of  $\tau_{\text{eff}}$  causes the gain to recover fast enough that both the leading and trailing edge of the pulse experience nearly the same dynamic gain profile. For the same reason, the output spectrum becomes more symmetric and resembles that obtained in the case in optical fibers where SPM occurs due to a nearly instantaneous Kerr nonlinearity.

The numerical model developed for studying SPM was further extended to study interband FWM in SOAs driven at currents high enough that ASE itself begins to saturate the SOA gain. Across a broad range of wavelength shifts (as large as 20 nm), an increase in the CE of over 20 dB is observed, as the SOA current was increased from 100 to 500 mA. The impact of pump power, pump-signal detuning and  $\tau_{\text{eff}}$  on FWM CE is investigated. A trade-off between average

device gain  $\bar{g}$  and the bandwidth of gain modulations, mediated by a dimensionless parameter  $r' = \tau_c/\tau_{\text{eff}}$ , is demonstrated. The increase in pump-signal detuning over which interband FWM dominates comes at the cost of reduced device small signal gain.

In Chapter 4, it is experimentally demonstrated that the ASE-induced gain saturation changes the gain dynamics in such a way that the SPM features in SOAs begin to resemble those found in optical fibers, but they occur at peak power levels that are three orders of magnitude lower than those required for optical fibers. Theoretical predictions from Chapter 3 are verified with an experiment in which the output optical pulse spectra of gain-switched, input optical pulses is measured at different bias currents. The experimental results agree well with the theoretical predictions. While the study presented in this thesis has been done for one particular device length ( $L = 1 \text{ mm}$ ), the impact of this important device parameter can be understood by noting that increasing device length increases the ASE power which potentially can further reduce the recovery speed. A trade-off between improvement in spectral symmetry and the extent of spectral broadening associated with SPM has also been demonstrated. Understanding this trade-off is important for designing ultrafast, SOA-based, signal processing techniques for OOK signals such as wavelength conversion and regeneration.

In Chapter 5, it has been experimentally demonstrated that the interband FWM can be used for wavelength conversion in SOAs driven at currents so high that the ASE itself begins to saturate the SOA gain. Conversion efficiency and OSNR are used as the two FOMs to characterize the wavelength conversion process. Across a broad range of wavelength shifts (as large as 20 nm), an increase in the CE of over 20 dB, and a corresponding increase in the OSNR of over 12 dB is observed, as the SOA current was increased from 100 to 500 mA. The experimental observations are in qualitative agreement with the theoretical predictions reported in Chapter 3. As seen in Fig. 5.5(a), wavelength shifts ( $2\Delta\lambda$ ) close to

15 nm are possible at high drive current levels that reduce the gain recovery time to near 10 ps, while maintaining a high CE ( $\eta = 1$ ) and a high OSNR close to 25 dB. If 10% CE is considered acceptable for a WC, wavelength shifts  $> 25$  nm are possible.

## 8.4 Wavelength Conversion in SOAs

A major advantage of the ASE-enhanced interband FWM scheme is that input pump powers required for wavelength conversion are much lower ( $P_0 < 0.5$  mW) than those employed in the case of intraband FWM. This feature reduces the electrical power consumption for such WCs by more than a factor of 10. The issue of optimum pump power has been discussed in detail and it has been determined that the high conversion efficiencies over a broad range of input signal powers are possible even at pump powers as low as 0.1 mW. However, the OSNR of the converted signal at such pump levels may be below 25 dB because input signal power in this case must be considerably less than 0.1 mW. If the design criterion requires an OSNR of 30 dB or more, input signal power should be close to 0.1 mW, and this requires an input pump power close to 1 mW.

Future research in this area can explore low pump power wavelength conversion using ASE-assisted interband FWM in SOAs. Due to the advent of coherent modulation formats [25], wavelength conversion techniques which are modulation format independent and lend themselves easily to polarization diversity will become quite important. To that end, FWM in SOAs is extremely important as it preserves phase information and with some design optimization to polarization multiplexed signals as well [25]. SOA-based wavelength converter results reported in the literature use assist beam in excess of 50 mW [111]. Multiple pumps [25,170] or a single pump with pump power in excess of 10 dBm [41] have also been used. The CW results presented in Chapter 5 point to the fact that practical wave-

length conversion can be achieved using ASE-enhanced interband FWM in SOAs at pump powers as low as 1 mW.

A realistic WC for WDM systems must operate on pulsed signals at a bit rate of 10 Gb/s or more. The conclusions presented Chapter 5 based on CW experiments are expected to hold for pulsed data channels, with minor modifications, as far as CE and OSNR are concerned. However this needs to be experimentally studied. To that end, this thesis explores a 10 Gb/s L-Band wavelength convertor with sub-mW pump for RZ-OOK signals with 50% duty cycle (Chapter 5.4). It was concluded that high internal ASE not only drives up the FWM CE but also enhances the other nonlinear effects (SPM, XPM and XGM) which causes significant spectral broadening of the converted data channel. The extent of spectral broadening decreases with increasing wavelength shifts and increasing pump power. At any WS, CE, converted OSNR, and the spectral broadening of the converted signal can be optimized through suitable selection of pump power. For the design studied in this thesis, the optimum value of pump power was  $-2$  dBm and at this pump power, the CE was 3 dB and the converted OSNR was 26 dB/0.1 nm. The problem of spectral broadening and chirping observed with OOK signals is expected to be less severe for formats based on phase modulation (such as differential phase-shift keying). However, this needs to be investigated in detail and is an exciting avenue for future research into modulation-format transparent, energy-efficient optical wavelength converters.

## 8.5 Self-Heating Effects in VCSELs

ASE-enhanced nonlinear effects in SOAs relax the requirements on input signal powers thereby reducing the optical power consumption associated with the technique. However, SOA-based wavelength converters are not amenable to multicasting [170] which means in a DWDM scenario, each optical carrier would have

to be de-multiplexed and would need a separate wavelength converter. The power consumption associated with a single SOA-based wavelength converter makes such an implementation impractical.

VCSEL or VC-SOA based wavelength converters can be potentially used to implement energy efficient wavelength converters. These devices are more suitable for uncooled operation and hence suffer from deleterious self-heating effects which have been identified as the major factors limiting their static and dynamic performance [122, 127, 137, 138]. An in-depth understanding of these self-heating effects and relating them to the VCSEL design parameters is a key-step towards realization of VCSEL-based optical signal processing.

To that end, a simple, empirical thermal model useful for studying relative roles of various thermal rollover mechanisms inside VCSELs has been presented in this thesis. The parameters required by this model can be deduced experimentally through measurements of output power, voltage and emission wavelength as a function of current at different ambient temperatures. The method proposed in this thesis is quite general and can potentially be applied to any VCSEL. In this thesis, this method has been used for analyzing the thermal performance oxide-confined, 850 nm VCSELs optimized for high-speed operation. In total, four different devices with different photon lifetimes and inner aperture diameters were studied over the ambient temperature range of 15–100 °C. The model predicts that in this class of devices, the thermal saturation behavior is caused by a rapid increase of device temperature with bias current, which causes a reduction in the internal quantum efficiency, an increase in the threshold current and increase in the internal optical loss.

For all the devices, an in-depth analysis of various thermal rollover mechanisms was carried out, from the standpoint of understanding the power-saturation behavior. The approach proposed in this thesis relates macroscopic VCSEL parameters to various thermal rollover mechanisms and makes an accurate estimate,

both qualitatively and quantitatively, of various power dissipation mechanisms from the total power-dissipation in the device. Based on our analysis, it can be concluded that for all the devices, at any bias current and ambient temperature, power dissipation due to carrier leakage, carrier thermalization, spontaneous carrier recombination and internal optical absorption together exceeds the power dissipated across the series resistance (Joule heating). This may seem counter-intuitive given the fact that the basic dependence of Joule heating on current is quadratic while that of other heat sources is linear. However, the constants of proportionality ( $R_s$  and  $K$ , respectively) depend themselves on the internal device temperature, and change in opposite directions as the bias current is increased close to thermal rollover. Still, quadratic power dissipation is a major source of device heating, having a significant impact on the thermal performance of the VCSEL. Carrier leakage, caused due to rapid reduction in the value of internal quantum efficiency at elevated internal device temperatures, places the ultimate limit on the thermal performance of all these devices.

In devices where the photon lifetime is controlled by the top DBR reflectivity, a trade-off between absorption heating and carrier leakage is demonstrated in that overcompensating for absorption heating can cause an increase in carrier leakage and vice versa. In these devices, absorption heating is reduced by a shallow surface etch in the top DBR. Beyond a certain etch-depth, cavity losses become so high that a very high carrier density is needed to achieve threshold gain which in-turn increases carrier leakage. Increasing inner aperture diameter reduces the series resistance and thermal impedance. These two effects reinforce each other and this, in turn, delays the onset of carrier leakage, and as consequence a delay in the onset of thermal rollover. While a larger inner-aperture diameter increases the total number of photons inside the cavity, the photon density is actually reduced, resulting in a poorer high-speed performance.

This simple, empirical thermal model can potentially be extended to VCSELs

based on different material systems to study the heat load distribution due to the various thermally-induced power saturation mechanisms. It can also be potentially used to study the impact of various VCSEL design parameters such as aperture diameter, photon lifetime or top DBR design, substrate design and carrier blocking layer on the thermally induced power saturation mechanisms. Based on the work presented in this thesis, these statements are only true in principle and need further validation.

For the specific case of 850 nm VCSELs, optimized for high speed operation, it was demonstrated that carrier leakage places the ultimate limit on the device thermal performance. Comparison between 850 nm InGaAs VCSELs investigated in this thesis and the traditional 850 nm GaAs VCSELs from the standpoint of carrier leakage lends insight into interesting device-design trade-offs. 850 nm InGaAs VCSELs can potentially have higher carrier leakage at high device temperatures due to the fact that thickness of the QWs in these device had to be reduced by a factor of 2 as compared to the traditional GaAs VCSELs to ensure that the emission wavelength is in the vicinity of 850 nm [126]. However the barrier bandgap energy for InGaAs VCSELs with 37% Al content is about 5% higher than that for traditional 850 nm GaAs VCSELs with 30% Al content. These two design parameters act in the opposite directions with regards to carrier leakage which makes it difficult to qualitatively predict whether traditional GaAs VCSELs have less carrier leakage as compared to InGaAs VCSELs. However, one thing that can be said with certainty is that the Indium-induced strain is required for high differential gain, and therefore for the case of 850 nm InGaAs VCSELs, the accompanying reduction in quantum-well thickness and the associated carrier leakage ends up becoming a necessary evil. This can at best be managed through careful design-optimization.

It is interesting to note that for VCSELs emitting at longer wavelengths (such as 980 and 1060 nm), addition of Indium to the GaAs quantum wells does not



have to be accompanied by reduction in quantum well thickness. This implies that VCSEL designs optimized to emit at these wavelengths will have, among other things, lower power dissipation due to carrier leakage (especially at high device temperatures) and consequently superior uncooled high-speed performance. This has indeed been experimentally demonstrated [193–195].

Based on the analysis presented in this thesis, carrier leakage can be mitigated by careful optimization of absorption heating which is achieved by a shallow surface-etch in the top DBR. The etch-depth should be optimized so that it causes an insignificant increase in the threshold carrier density required for lasing. Removing entire DBR pairs will potentially have the same effect on absorption heating. However the resulting current-crowding effects will increase electrical resistance [117]. Further delay in the onset of carrier leakage can be achieved through the reduction of series resistance and thermal impedance. Reduction in series resistance can be achieved by using intracavity contacts [202] whereas thermal impedance can be reduced by using a binary material in the bottom DBR [122] or by employing metallic heat spreading layers [131]. Incorporating a carrier blocking layer to improve carrier leakage at elevated device temperatures can also be explored [185]. Including all these design nuances in a single VCSEL structure is extremely challenging from the standpoint of device fabrication and is an exciting avenue for future research into extending the reach of 850 nm VCSELs operating uncooled at data rates in excess of 40 Gb/s.

## 8.6 Summary of Contributions

This thesis investigated the signal-processing capabilities of HNLFs, SOAs and VCSELs from the standpoint of reducing electrical footprint associated with signal processing devices based on these nonlinear elements. In particular, this thesis focussed on reducing the power consumption associated with optical wavelength converters and 2R-regenerators. Here the contributions of this thesis in the areas of HNLf-dispersion optimization for optimum optical signal regeneration, understanding the basic physics behind ASE-assisted nonlinear effects in SOAs and modeling thermally induced optical power saturation effects in 850 nm, oxide-confined, high-speed VCSELs are summarized:

- Developed and demonstrated a simple scaling rule that is useful for studying the combined effects of fiber dispersion and nonlinearity on the MTR performance.
- Demonstrated the effectiveness of the scaled parameter  $\mathcal{S}$  in predicting the MTR performance.
- Through careful optimization of the HNLf dispersion, Demonstrated a 30% reduction in optimum input optical peak power required for optical signal regeneration.
- Developed a simple numerical model to study the impact of ASE on the nonlinear effects (SPM and FWM) in SOAs
- Predicted fiber-like SPM due to fast gain saturation and recovery mediated by high internal ASE. This prediction was verified experimentally.
- Experimentally demonstrated that the ASE-induced gain saturation limits the SBF at the same time it improves spectral symmetry by reducing the

gain-recovery time. This trade-off between SBF and spectral symmetry cannot be avoided in SOAs that employ ASE for faster gain recovery.

- Investigated experimentally and theoretically, the applicability of ASE-assisted interband FWM in SOAs for practical wavelength conversion.
- Demonstrated efficient wavelength conversion (0 dB CE) over wavelength shifts in excess of 15 nm and converted OSNR in excess of 25 dB/0.1nm.
- Demonstrated significant reduction in the input optical pump power required for wavelength conversion. Typical input pump power required for ASE-assisted interband FWM was in the vicinity of 0.5 mW compared to 10s of milliwatts required for traditional intraband FWM.
- Demonstrated a 10 Gb/s L-Band wavelength convertor for RZ-OOK signals with 50% duty cycle.
- Developed a simple, empirical thermal model which is useful for studying the relative roles of various thermal rollover mechanisms inside VCSELs.
- Applied the method developed for analyzing the thermal performance of four oxide-confined, high-speed, 850 nm VCSELs.
- Demonstrated a trade-off between absorption heating and carrier leakage in devices which achieve a reduction in absorption heating through a shallow surface etch in the top DBR

These contributions can potentially reduce the electrical footprint associated with optical signal processing techniques. This in-turn will allow these functionalities to be incorporated in the future, high-speed, transparent optical networks.

# A Optiwave OptiSystem Software

Optiwave OptiSystem is an optical communication system simulation package that designs, tests, and optimizes a broad variety of optical links in the physical layer of optical networks. The simulation results presented in Chapter 2 were carried out using version 6.0. Currently version 10.0 is commercially available which has all the features of version 6.0 with some add-ons pertaining to fiber-optic access networks, advanced visualization for coherent communications and other advanced photonic devices and sub-systems [205]. The Optiwave Optisystem software is very intuitive to use and it comes with good online-help and other documentation. OptiSystem is a mature software package and is used by a number of universities for education and research. In addition to that, many companies in the optical communication industry rely on this software for power budget and OSNR calculations [205, 206]. Here a brief tutorial into this commercial software package is presented to give an overview of its capabilities. Particular emphasis is placed on the features used for deriving the results presented in chapter 2. For additional details, the reader is referred to the two references [205, 206] from which the content of this tutorial is adapted.

## A.1 Description and Capabilities of OptiSystem

### 6.0

OptiSystem is a system level simulator based on realistic modeling of fiber-optic communication systems [206]. It possesses a powerful new simulation environment and a truly hierarchical definitions of components and systems. A robust graphical user interface controls the optical component layout, component models, and presentation graphics. An extensive library of active and passive components includes realistic, wavelength dependent parameters. Parameter sweeps allow the user to investigate the effect of particular device specifications on system performance. This particular parameter sweep feature was extensively used to formulate the scaling rule presented in Chapter 2 and also for optimizing the HNLFF dispersion for optimum signal regeneration.

A brief overview of the main features of OptiSystem software is presented below:

- OptiSystem Component Library includes hundreds of validated components. Users can customize by entering parameters that can be measured from real devices. Users can also incorporate new components based on subsystems and user-defined libraries.
- Integration with Optiwave software tools at the subsystem and component level: OptiAmplifier, OptiBPM, OptiGrating, and OptiFiber.
- OptiSystem handles mixed signal formats for optical and electrical signals in the Component Library, and calculates the signals using the appropriate algorithms related to the required simulation accuracy and efficiency.
- System performance is predicted by calculating BER and Q-Factor using numerical analysis or Semi-analytical techniques for systems limited by inter

symbol interference and noise.

- Advanced visualization tools produce OSA Spectra, Oscilloscope, and Eye diagrams. Also included are WDM analysis tools listing signal power, gain, NF, and OSNR.
- Simulations can be repeated with an iteration variation of the parameters. OptiSystem can also optimize any parameter to minimize or maximize any result or can search for target results. Users can combine multiple parameter sweeps and multiple optimizations.

## A.2 Optiwave Tutorial

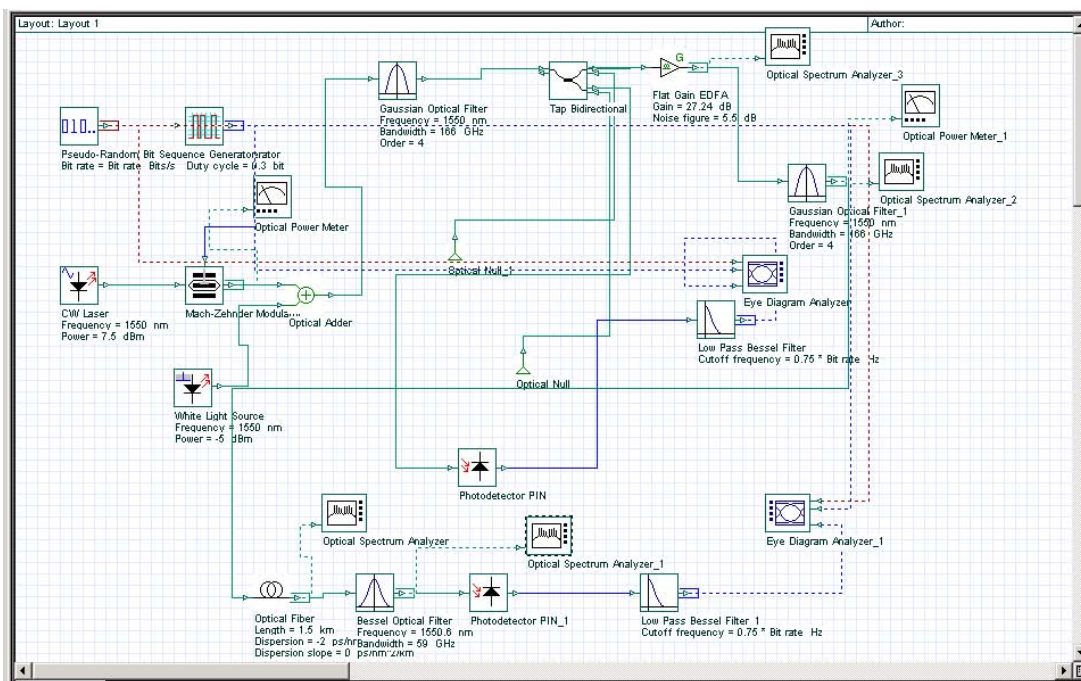


Figure A.1: OptiSystem implementation of the simulation schematic shown in Fig. 2.2.

In this section a brief tutorial of Optiwave OptiSystem software is presented. This tutorial is aimed at providing an insight into how the simulations reported in Chapter 2 were carried out. In the process, it is hoped that the reader will gain an insight into the powerful simulation capabilities afforded by this software. For a more in-depth tutorial on this subject, the readers are referred to the user manuals accompanying this software as well as other references listed in this text.

Figure A.1 shows the OptiSystem layout of the setup used for simulating numerically the operation of an MTR shown in Fig. 2.2. Creating this layout in the layout window is fairly straightforward. First the OptiSystem software needs to be initiated, which can be done by starting the following action [205]:

- From the Start menu, select Programs > Optiwave Software > OptiSystem 6 > OptiSystem. OptiSystem loads and the graphical user interface (GUI) appears

Project Layout shown in Fig. A.1 is the main working area of the OptiSystem GUI where components are inserted into the layout, can be edited, and connections between the components can be created. The components used to create the schematic shown in Fig A.1, can be accessed from the component library, which appears on the top left corner of the OptiSystem GUI [205]. Creating connections in the project layout window is also easy. In fact, the software has an in-built connecting tool which automatically connects two components whose inputs and outputs are compatible (Optical In to Optical Out, Electrical In to Electrical Out and so forth).

For the particular case of the simulation schematic shown in Fig A.1, a CW laser source emitting light at 1550 nm was connected to the MZM which was in-turn driven by an RZ pulse-generator module built into the OptiSystem component library. In the simulations, the performance of the modulator is set by assigning a particular value to the output extinction ratio. For the results reported

in Chapter 2, this value was selected to be 25 dB. The RZ-signal and the output from the White Light Source are then combined using an ideal optical adder. The White Light Source generates Gaussian distributed white noise bins or sampled signals at the specified power level. A Gaussian noise distribution around the center frequency (a user defined parameter) is assumed [205], and the Power parameter specifies the total output of the White Light Source. It is important to note that this White Light Source simulates the Q-factor degradation of the input bit-stream and the extent of degradation is governed by a combination of White Light Source power and the bandwidth of the Gaussian OBPF.

A non-ideal optical power-tap (Tap-Bidirectional component) is used for studying the electrical properties of the optical signal going into the MTR. This component has a wavelength-dependent tap percentage, IL and return loss that is user specified. The corresponding values for simulations reported in this thesis are 15% (130 nm bandwidth), 0 and 65 dB respectively. A Flat Gain EDFA module is used to simulate optical amplification. Its performance is governed by Optical Gain and NF parameters. The NF was fixed at 5.5 dB and the optical gain was selected for suitable amplification of input optical signal. The Optical Fiber component simulates the propagation of an optical field in a single-mode fiber with the dispersive and nonlinear effects taken into account by a direct numerical integration of the modified nonlinear Schrödinger Eq. [205]. All the fiber parameters such as the length, attenuation, group velocity dispersion, polarization mode dispersion, fiber nonlinearity etc are user specified. For the purposes of simulation reported in this thesis, third order dispersion was ignored. Other relevant fiber parameters have been reported in Chapter 2.

Once all the components are placed on the project layout, the Global Parameters need to be set to commence simulations. Figure A.2 shows the snapshot of the window used to set the Global Simulation Parameters. These parameters are common to all OptiSystem simulations. In this particular case, the simulation



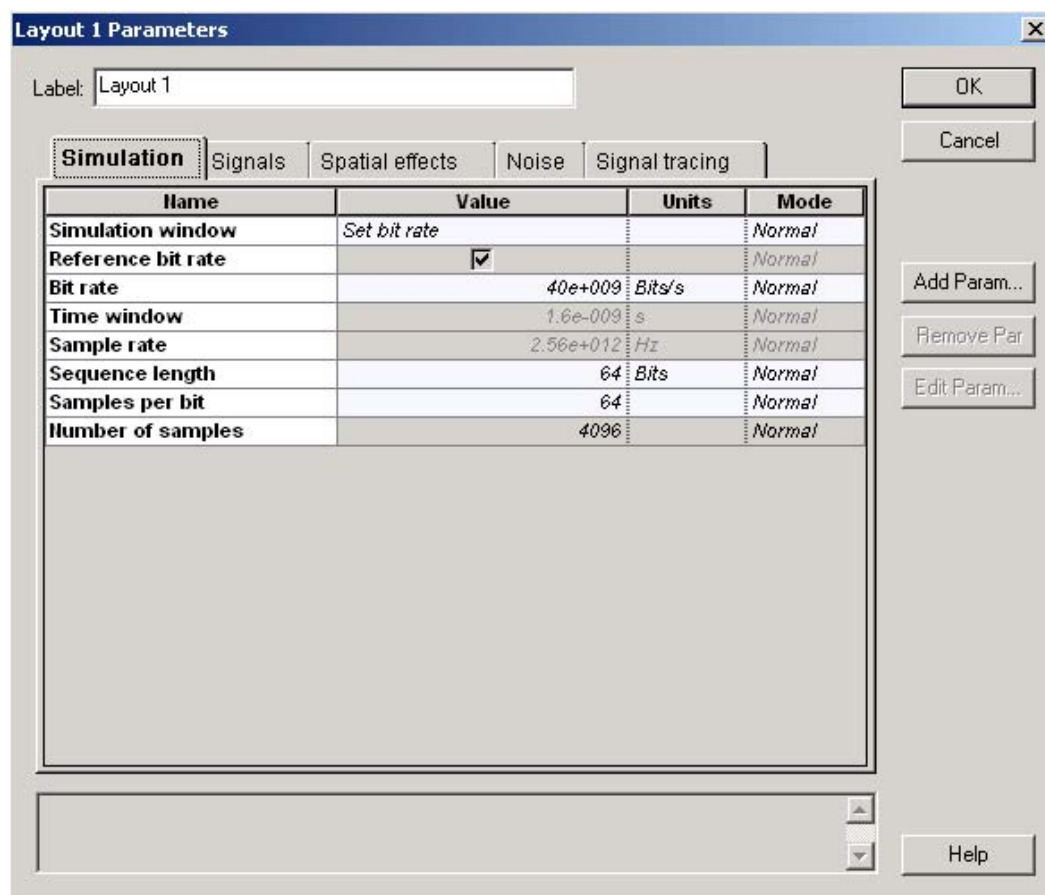


Figure A.2: Setting the global simulation parameters in OptiSystem Software.

time window, the number of samples, and the sample rate are indirectly defined using the following three parameters:

- Bit Rate
- Bit Sequence Length
- Number of Samples per Bit

These parameters are then used to calculate the time window, sample rate, and the number of samples as follows:

- Time window = Sequence length \* 1/Bit rate

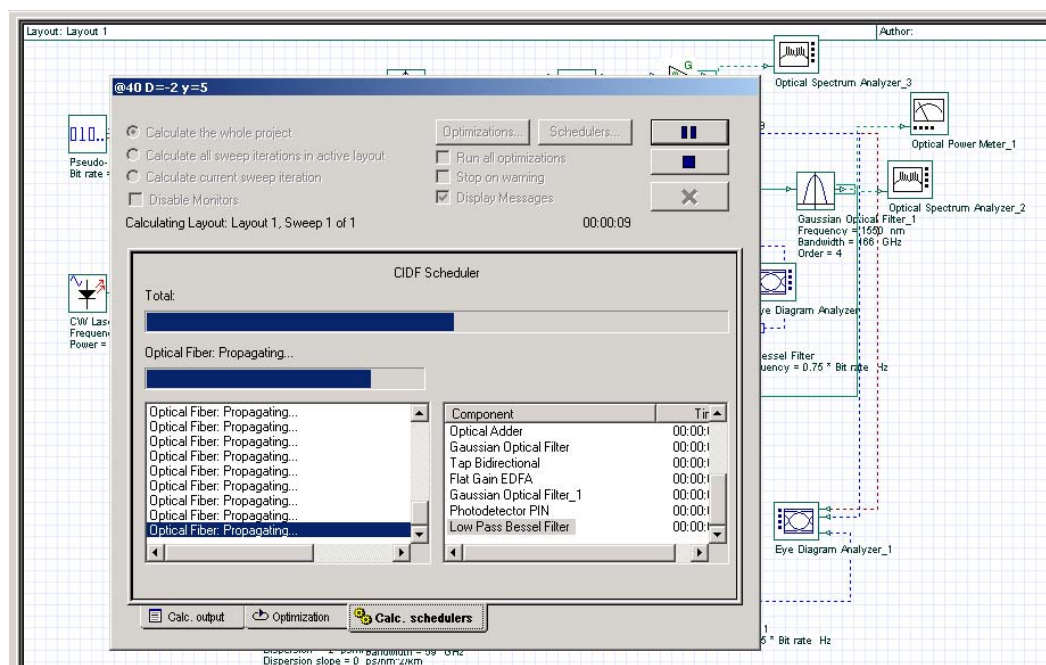


Figure A.3: Calculation Output Window for the OptiSystem Software.

- Number of samples = Sequence length \* Samples per bit
- Sample rate = Number of samples / Time window

The corresponding values for 40 Gb/s simulations are shown in Fig A.2. OptiSystem shares these parameters with all components.

Once all the components are connected, their values specified and the global parameters chosen, it is time to run the simulation. To run a simulation, from the File menu, the Calculate command is selected which opens the OptiSystem Calculation dialog box [205]. In the OptiSystem Calculations dialog box, the Run button needs to be clicked which opens the Calculation Output window shown in Fig A.3. The calculation output appears in the Calculation Output window, and the simulation results appear below the components that were included in the simulation.

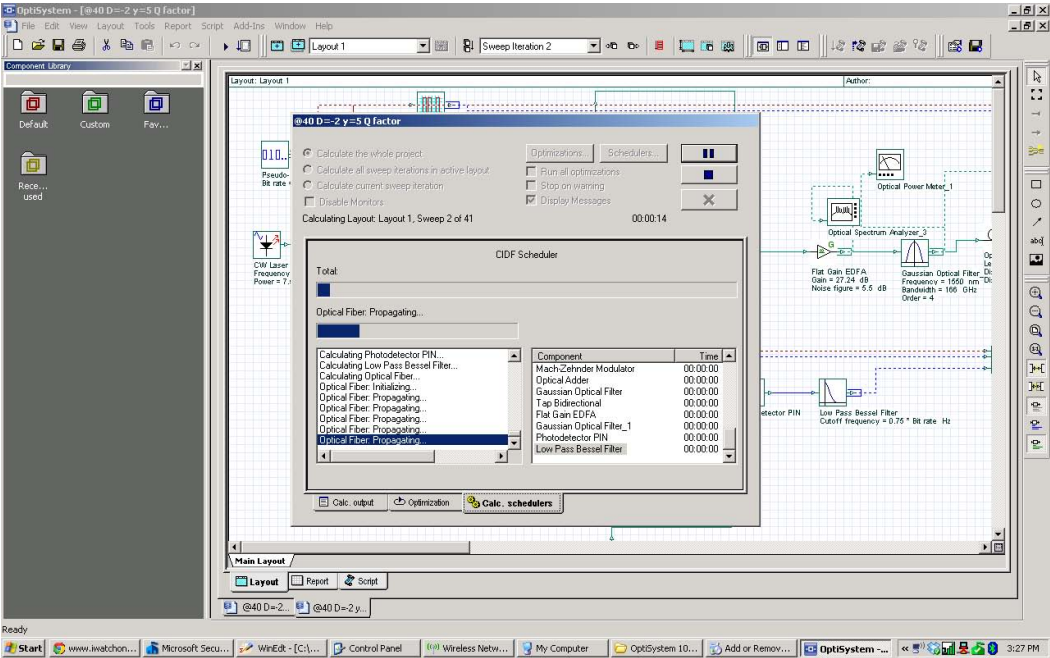


Figure A.4: Calculation Output Window for the OptiSystem Software while running a parameter sweep.

### A.3 Parameter Sweeps

One of the most important feature of the OptiSystem software which greatly aided in generating all the curves presented in Chapter 2 is the parameter sweep feature. Parameter sweeps and optimizations feature built in the OptiSystem software allows for the simulations to be repeated with an iterated variation of the selected parameter(s). OptiSystem can also optimize any parameter to minimize or maximize any result or can search for target results. Multiple parameter sweeps and multiple optimizations can also be potentially combined [205].

When a parameter is in sweep mode, the value of the parameter changes through sweep iterations. The parameter sweep version can be selected for display in the project layout window. In order to change a parameter value across sweep iterations, the total number of sweep iterations and the parameter values corresponding to each iteration needs to be defined.

To set the total number of sweep iterations, the following procedure needs to be performed [205]:

1. Click the Set Total Sweep Iterations button on the Layout toolbar. The Total Parameter Sweep Iterations dialog appears displaying the current values.
2. Enter the total number of sweep iterations.
3. Click OK

Assigning parameter values corresponding to each iteration is relatively simple and can be achieved in many ways. Manual discrete assignment is one possibility. However, OptiSystem allows for a lot of flexibility in assigning these values. Linear, Exponential, Log, User Defined Formula, Gaussian, LogNormal etc. are the in-built methods for assigning parameter values for each sweep iteration. All these distributions require the user to define a start and an end value and then select the preferred distribution. For all the simulations reported in Chapter 2, a linear distribution was assumed for all the parameter sweeps.

Once both the number of sweep iterations and the parameter value for each iteration is specified, again from the File menu, the Calculate command is selected which opens the OptiSystem Calculation dialog box [205]. Pressing the run button in the calculation box initiates the parameter sweep as shown in Fig A.4. For generating all Figs. presented in Chapter 2, linear sweep iterations were used. In particular, for both the parts of Figs. 2.3 and 2.7, the gain of flat gain EDFA module was varied between 15 and 31 dB. For generating the Q-factor improvement curves as a function of input Q-factor, the power of the white light source was varied between  $-14$  and  $+8$  dBm etc. This concludes a brief overview of the simulation capability of the Optiwave OptiSystem software as applied to the research presented in Chapter 2 of this thesis.

## B Gain-Switching in Semiconductor Lasers

Gain switching is known to be the simplest of the picosecond pulse generation schemes because no external cavity or careful alignment of optical components is required. The pulses can be wavelength tunable and can be modulated at any arbitrary repetition rate. In this method, the gain of a semiconductor laser diode is modulated by an input RF signal which results in a train of pulses at a repetition rate which is exactly the same as the frequency of the input RF signal. Gain switching pulses are the first peaks of the relaxation oscillations [207] and can be up to 10 times shorter than the applied electrical signal. Gain-switching in semiconductor lasers is a phenomenon that has been researched both experimentally and theoretically for over two decades [5, 176, 207–210]. The purpose of this brief tutorial is to present the theoretical and experimental work done to build a gain switched pulse source to be used in ASE-assisted SPM experiments presented in Chapter 4.

To study the impact of ASE-mediated gain dynamics on the spectral broadening suffered by picosecond optical pulses propagating in the SOA, it was desirable that a source be built that send out optical pulses with  $\text{FWHM} > 2\tau_{\text{eff}}$  at 500 mA drive current. Further, the repetition rate of the pulses should be low enough to allow the SOA gain to recover to its equilibrium value. Gain switching fits the bill on both the criteria and in the next two sections, theoretical and experimental

optimization efforts for this pulse source are described.

## B.1 Numerical Model

The basic rate Eqs. for a single mode laser can be written as [5]:

$$\frac{dP}{dt} = GP + R_{sp} - \frac{P}{\tau_p} \quad (\text{B.1})$$

$$\frac{dN}{dt} = \frac{I}{q} - \frac{N}{\tau_c} - GP, \quad (\text{B.2})$$

where  $P$  and  $N$  are the number of photons and electrons respectively inside the active region. Further,  $G$  is the rate of stimulated emission defined as  $G = G_N(N - N_0)$ ,  $N_0$  is the number of carriers at gain transparency,  $R_{sp}$  is the rate of spontaneous emission,  $\tau_p$  is the photon lifetime and  $\tau_c$  is the carrier lifetime.

To study gain-switching in semiconductor lasers, the bias current  $I$  needs to have a time dependent form. In particular, an RF signal, which is usually used for gain switching, can be expressed as:

$$I = I_b + I_m \sin(2\pi F_0 t) \quad (\text{B.3})$$

Here  $I_b$  is the bias current,  $I_m$  is the modulation current, and  $F_0$  is the frequency of the RF signal. This parameter also sets the repetition rate of the gain-switched pulses. Further, gain compression effects need to be included phenomenologically. This is achieved by modifying the gain  $G$  as:

$$G = G_N(N - N_0)(1 - \epsilon_{nl}P). \quad (\text{B.4})$$

Finally, time-dependent variation in the optical gain in a semiconductor laser, leads to time dependent changes in refractive index. The resulting phase modulation has to be included through the Eq. [5]:

$$\frac{d\phi}{dt} = \frac{1}{2}\beta_c[G_N(N - N_0) - \frac{1}{\tau_p}], \quad (\text{B.5})$$

where  $\beta_c$  is the linewidth enhancement factor. Combining Eqs. (B.1)–(B.5), coupled Eqs. describing the modulation response of the semiconductor laser can be written as:

$$\frac{dP}{dt} = G_N(N - N_0)(1 - \epsilon_{nl}P)P + R_{sp} - \frac{P}{\tau_p} \quad (\text{B.6})$$

$$\frac{dN}{dt} = \frac{I_b + I_m \sin(2\pi F_0 t)}{q} - \frac{N}{\tau_c} - G_N(N - N_0)(1 - \epsilon_{nl}P)P \quad (\text{B.7})$$

$$\frac{d\phi}{dt} = \frac{1}{2}\beta_c[G_N(N - N_0) - \frac{1}{\tau_p}]. \quad (\text{B.8})$$

For numerically solving Eqs. (B.6)–(B.8), these Eqs. were normalized using the following quantities:

$$P_e = \left(\frac{1}{2}v_g\alpha_{mir}\hbar\omega\right)P \quad I_{th} = \frac{qN_{th}}{\tau_c} \quad (\text{B.9})$$

$$N' = \frac{N}{N_{th}} \quad \tau = \frac{t}{T_0} \quad (\text{B.10})$$

$$a = \frac{I_b}{I_{th}} \quad b = \frac{I_m}{I_{th}}. \quad (\text{B.11})$$

Here  $P_e$  is the emitted power,  $v_g$  is the group velocity,  $\alpha_{mir}$  is the mirror loss,  $I_{th}$  is the threshold current,  $N_{th} = N_0 + (G_N\tau_p)^{-1}$  is the carrier population at the lasing threshold, and  $T_0$  is the inverse of RF signal frequency  $F_0$ . Combining Eqs. (B.6)–(B.8) and Eqs. (B.9)–(B.11), the normalized laser rate Eqs. can be written as:

$$\frac{dN'}{d\tau} = \frac{T_0}{\tau_c}[(a + b \sin(2\pi\tau) - N')] - \frac{T_0 G_N}{k} P_e \left(1 - \frac{\epsilon_{nl} P_e}{k}\right) \quad (\text{B.12})$$

$$\frac{dP_e}{d\tau} = G_N T_0 N_{th} \left(N' - \frac{N_0}{N_{th}}\right) \left(1 - \frac{\epsilon_{nl} P_e}{k}\right) P_e + k T_0 R_{sp} - P_e \frac{T_0}{\tau_p} \quad (\text{B.13})$$

$$\frac{d\phi}{d\tau} = \frac{G_N T_0 \beta_c}{2} \left(N' - \frac{N_0}{N_{th}}\right) - \frac{\beta_c T_0}{2\tau_p}. \quad (\text{B.14})$$

In writing the preceding set of Eqs. a parameters  $k$  was introduced which can be written as:

$$k = \frac{1}{2}v_g\alpha_{mir}\hbar\omega \quad (\text{B.15})$$

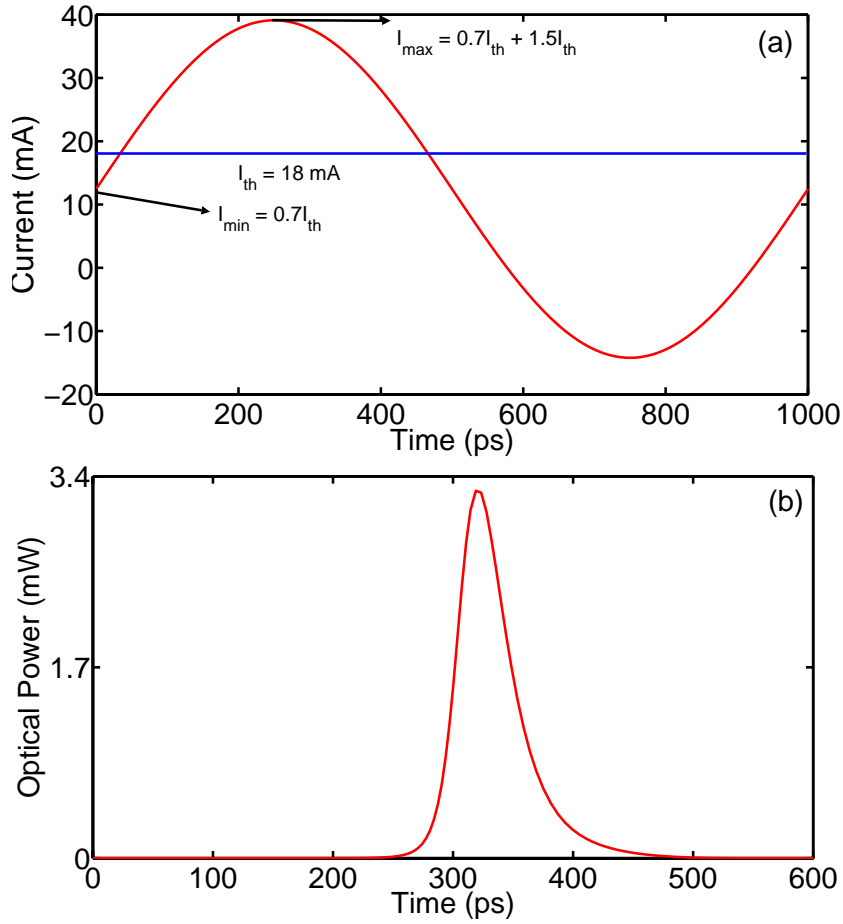


Figure B.1: Gain-switching simulations snapshot. Part (a) shows the total current applied to the diode laser in one RF-signal cycle. Part (b) shows the simulated gain-switched pulse with  $T_{FWHM} = 44$  ps.

To solve Eqs. (B.12)–(B.14), the following laser parameters were used [5]:

$$\beta_c = 5 \quad v_g = \frac{c}{4} \quad \lambda = 1.59 \mu m \quad (\text{B.16})$$

$$T_0 = 1 \text{ ns} \quad \tau_p = 3 \text{ ps} \quad \tau_c = 0.9 \text{ ns} \quad (\text{B.17})$$

$$R_{sp} = \frac{2}{\tau_P} \quad a \approx 0.6 - 0.99 \quad b \approx 1.5 - 3.5 \quad (\text{B.18})$$

$$G_N = 10^4 \text{ s}^{-1} \quad N_0 = 10^8 \quad \epsilon_{nl} = 10^{-7} \quad (\text{B.19})$$

It is important to note that these parameters vary quite a bit for different



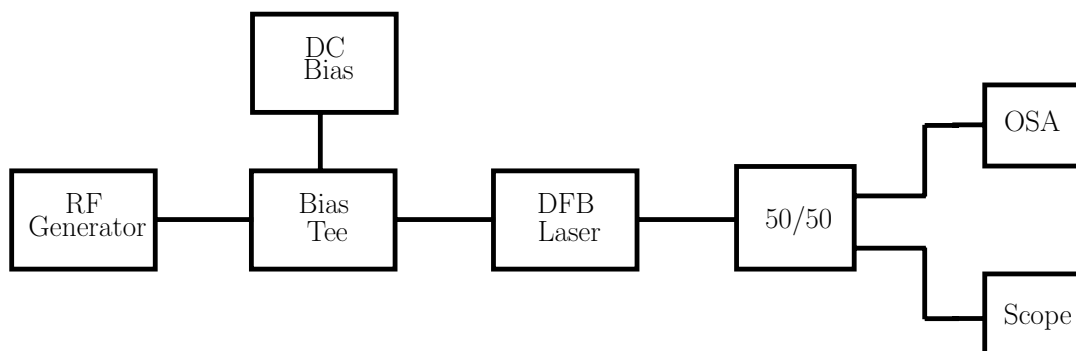


Figure B.2: Experimental setup used for characterizing gain-switched pulse source.

semiconductor lasers and the simulation results based on this model and the selected parameters can only serve as a reference point to get an idea of what kind of pulsewidths one can expect from the source. Extensive simulations were carried out and as an example, one example of simulations is presented here [Fig. B.1], which shows that by biasing a semiconductor laser at 12.6 mA and by applying an RF signal with 27 mA amplitude and 1 GHz frequency, pulses with 40 ps FWHM can be produced at the 1 GHz repetition rate. The threshold current for this laser was calculated to be 18 mA. In the next section, we use the parameters obtained from the numerical model to experimentally optimize the gain-switched source

## B.2 Gain-Switching Experiments

Figure B.2 shows the experimental setup used for characterizing gain-switched pulse source. It consists of an RF generator and a DC bias source which are combined using the bias-T circuitry of an ILX lightwave mount (LDM-4984RF) [211]. This mount accepts RF signals up to 2.5 GHz. The laser diode module is placed on this mount. The laser diode used in the gain-switched source is an Agere D2526-G880 wavelength-selected direct modulated isolated DFB laser module [212]. A 50/50 splitter was employed at the output of the DFB laser to send the gain-

switched simultaneously into an optical spectrum analyzer (OSA) with resolution of 0.01 nm and into a PD with a 22 GHz bandwidth. The temporal signal was then captured by a 70 GHz sampling scope (resolution 1.25 ps). For all these experiments, the temperature of the DFB laser was stabilized at 25 °C.

Optimizing the pulses from a gain-switched source involves optimizing the bias current and the modulation current at the fixed repetition rate. The goal is to capture only the first peak of the relaxation oscillation and effectively suppress the other peaks. This is achieved by terminating the RF signal before the onset of the next relaxation oscillation spike [210]. It was deduced from the simulations that most effective way to achieve this is to bias the laser close to  $0.7 \times I_{th}$  and then apply modulation current with an amplitude in the range of  $1.5\text{--}2.5 \times I_{th}$ . To experimentally verify this assertion, the DFB laser was biased at currents ranging from  $0.6\text{--}0.84 \times I_{th}$  and the applied modulation currents were varied from  $1.5\text{--}2.5 \times I_{th}$ . As an example, pulse shape and spectra at  $0.6 \times I_{th}$  bias current and four different modulation currents is shown in Fig. B.3.

In Fig. B.3(a), the modulation amplitudes are expressed in terms of peak to peak voltages. That is because those values are directly measured using a low bandwidth oscilloscope. The series resistance of the LDM-4984RF is 50  $\Omega$ . The values of modulation current are simply the corresponding values of peak to peak voltages divided by the series resistance. Further, from fig. B.3(a), it can clearly be seen that, at a fixed bias current, increasing the modulation current initially increases the peak power and simultaneously reduces the pulse width. After a while though, the pulse saturates whereas the peak power keeps on increasing. At the maximum modulation current, the second relaxation oscillation spike shows up. Though not shown here, at a fixed RF current, increasing the bias current fairly quickly saturates the output power due to the onset of higher order relaxation oscillation peaks. These observations are consistent with the previously reported results [210].

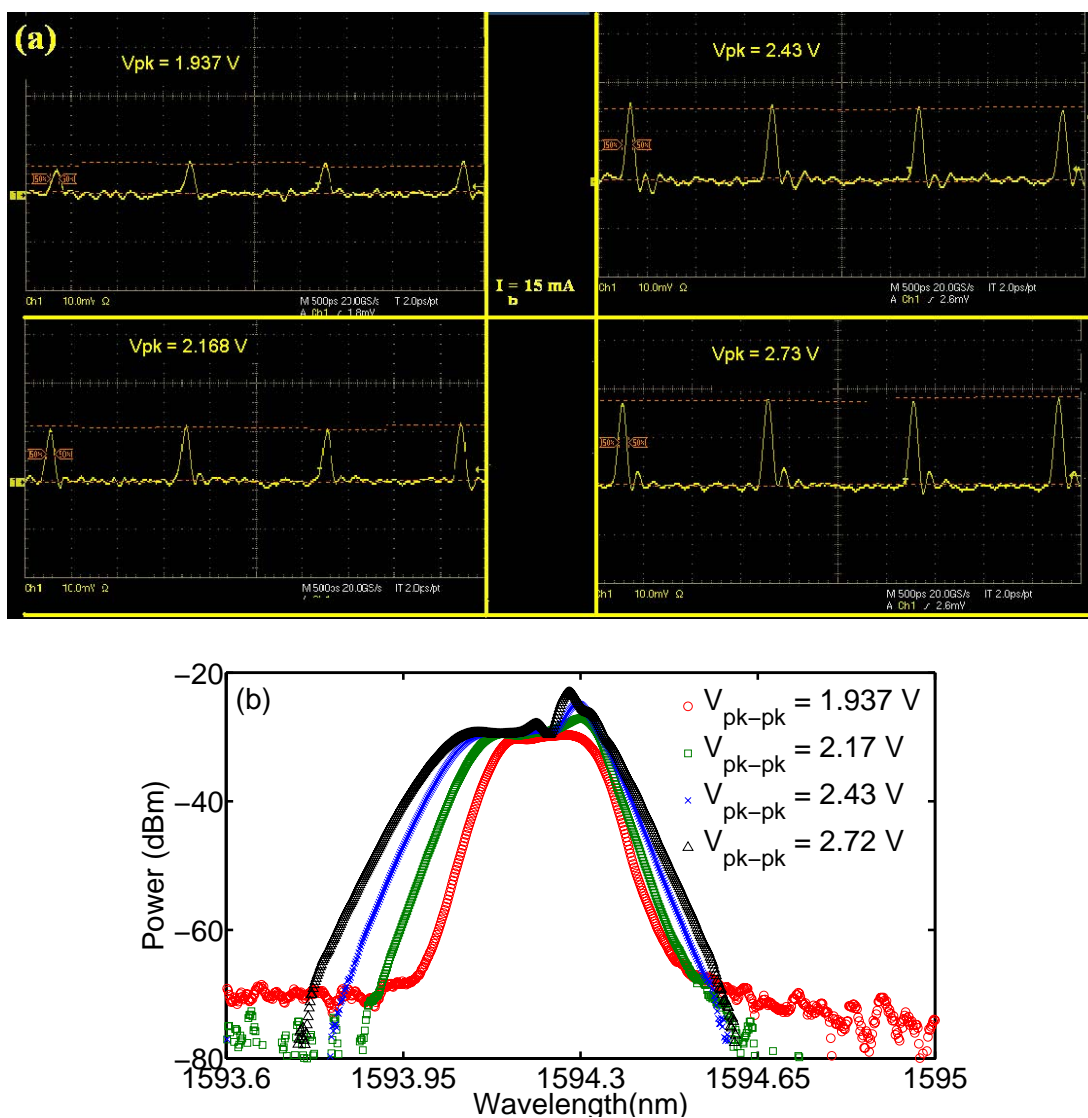


Figure B.3: (a) Shapes and (b) spectra of the picosecond optical pulses from the gain-switched source. For all these measurements, the DFB laser is biased at 15 mA. The series resistance of the mount is 50  $\Omega$ . The modulation currents corresponding to the four peak-to-peak voltages are 38.8, 43.4, 48.6, and 55 mA, respectively.

To optimize the gain switched source for the experiments reported in Chapter 4, it was important to bias the DFB laser at a reasonable current (close to  $0.6 \times I_{th}$ ) and then increase the modulation current to maximize the output optical power

while capturing only the first relaxation oscillation peak. To that end, the DFB laser was biased slightly below 15 mA at 14.8 mA and the modulation current was optimized at 64 mA. The corresponding pulse shape and spectra are shown in Fig. 4.1(b) and (c).

## C 10 Gb/s NRZ and RZ OOK data generation.

NRZ and RZ are the two types of amplitude-shift-keying modulation formats. In the NRZ format, optical pulses can occupy the entire bit slot whereas in the RZ format, optical pulses occupy only a part of the bit slot [4]. Since each “1” bit occupies the entire bit slot, the pulses in an NRZ bit stream do not have the same width and in-fact, the pulse width varies with the bit pattern. In the RZ format, since the optical pulse occupies only a part of the bit slot, all pulses in an RZ bit stream have the same pulse width. Further, the RZ format gives an additional degree of freedom to the lightwave system designers in that the fraction of the bit slot occupied by the optical pulse, also known as the duty cycle, can be varied depending on the level of cross-talk that can be tolerated by the lightwave system [4].

Traditionally, NRZ modulation format has been the more widely used format due to the fact that it was used exclusively for microwave communications. Further it requires half the bandwidth of that required for RZ modulation format [4]. However, RZ format is more efficient from the standpoint of suppressing deleterious nonlinear interactions and which is why this modulation format (more specifically RZ-50 format) was used for wavelength conversion experiments described in Chapter 5.

Commercially available 10 Gb/s PRBS generators such as the Centellax TG1B1 – A 10 Gb/s bit-error rate tester use NRZ modulation format for 10-Gb/s PRBS pattern generation [213]. The easiest way to convert a NRZ bit stream into a RZ bit stream is to cascade two modulators. The first modulator is driven by the electrical PRBS signal and the second modulator is driven by a sinusoidal clock at the data bit-rate. Depending on the amplitude, frequency and phase of the clock with respect to the PRBS data, RZ pulses with different pulse-widths can be generated [4]. This transmitter configuration, known as the “pulse-carver” has been widely researched both experimentally and theoretically [4,177,214–216]. Therefore this fairly robust configuration was used for generation of our RZ-50 bit stream. Experimental setup used for generation of 10 Gb/s RZ bit stream and its optimization is described next.

## C.1 Experimental Setup

Figure C.1 shows the experimental setup used for generating 10 Gb/s NRZ and RZ-50 bit streams. For generating 10 Gb/s NRZ bit-stream, MOD2 is swapped out of the setup. For the series of experiments reported here, the tunable laser wavelength is fixed at 1575 nm and the optical power is fixed at 14.1 dBm. The PRBS unit is part of the Centellax TG1B1-A 10 Gbit/s PRBS generator and bit error tester. It drives a JDSU 10 Gb/s, LiNbO<sub>3</sub> MZM (MOD1). This device has the maximum rated input optical power at +27 dBm. However, its IL is 6 dB. While generating RZ-50 bit stream, the output of MOD1 goes into MOD2 which is a EOSPACE 10 Gb/s X-cut LiNbO<sub>3</sub> MZM. This device has a maximum rated optical power of +13 dBm and 4 dB IL. It is driven by Centellax TG1C1-A 13G Clock Synthesizer. Because of their rated maximum optical input and insertion losses, MOD1 and MOD2 were used as data modulator and pulse carver respectively. The polarization controllers PC1 and PC2, control the polarization of the light

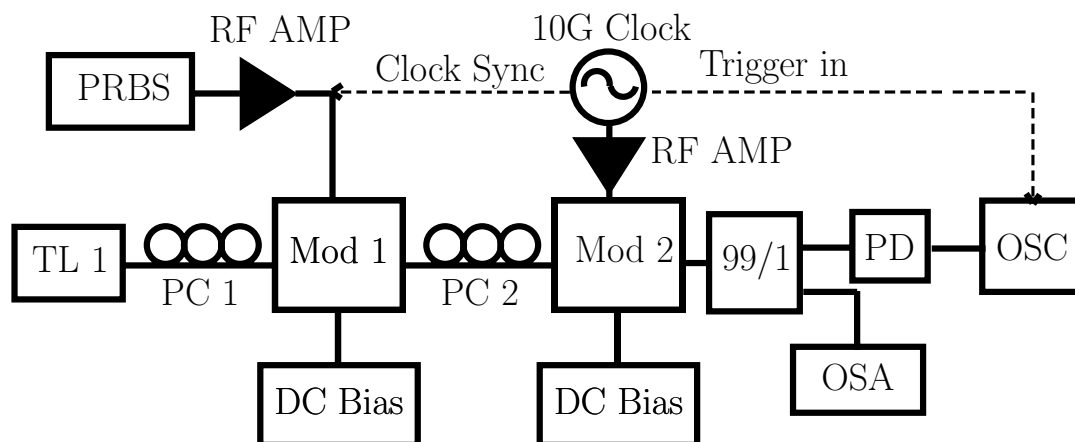


Figure C.1: Experimental setup used for generating 10 Gb/s NRZ and RZ-50 bit streams. For generating 10 Gb/s NRZ bit-stream, MOD2 is swapped out of the setup. PC: Polarization Controller; PRBS: Pseudo Random Bit Sequence Generator; 99/1: 1% power tap; RF AMP: RF Amplifier; TL: Tunable Laser; MOD1: 10 Gb/s Data Modulator; MOD2: Synchronous Pulse Carver; OSA: Optical Spectrum Analyzer; PD: Photodiode; OSC: Sampling Scope.

going into the data modulator and the pulse carver. The polarization of the light must be perfectly aligned with the axis of the  $\text{LiNbO}_3$  crystals in the MZM or else the output extinction ratios become severely degraded. The RF amplifiers were biased to operate at maximum gain and they converted input peak-peak voltages between 0.6-0.7 V to 5.5-6 V at the output with negligible distortion.

To “carve-out” RZ-50 pulses from 10 Gb/s NRZ data, the sinusoidal clock unit is driven at  $(V_\pi|_{AC})/4$  amplitude and at 10 GHz frequency. Here  $V_\pi$  is an MZM characteristic parameter and is different for RF and DC signals [4]. Further, the DC bias applied to the SPC is adjusted at  $(V_\pi|_{DC})/2$  [4]. Further, the BERT unit runs as a slave to the clock unit. To do that, the units need to be connected in the configuration described below. For the nomenclature used, the reader is referred to the manual of the two units [213]:

1. Connect TrigO output in the TG1C1-A to the EXT CKI input in the TG1B1-A.
2. Remove the shorts between TXCKI and TXCKO and RXCKI and RXCKO in the TG1B1-A.
3. Connect L.F. TrigO to the Oscilloscope.
4. Channel 2 OUT in the front panel of the TG1C1-A goes to the RX1 in the TG1B1-A.
5. Channel 2  $\overline{OUT}$  in the front panel of the TG1C1-A goes to the TX1 in the TG1B1-A.
6. In the TG1B1-A, go to the CONFIG STATE menu. Keep on pressing the CONFIG STATE button till SYNTH menu shows up. Then press the ADJUST CONFIG button to set SYNTH value to “0”.

At the output of MOD2, a 1% power tap facilitate simultaneous acquisition of the spectral and temporal data. In the absence of a photoreceiver, a PD with a 22 GHz bandwidth was used to detect and characterize the incoming data stream. The temporal signal was then captured by a 70 GHz sampling scope (resolution 1.25 ps).

## C.2 Experimental Results

Figure C.2 shows the experimentally optimized 10 Gb/s NRZ and RZ-50 optical bit streams. For generating the NRZ bit stream, the JDSU modulator was biased at 3.29 V and the peak to peak voltage at the input to RF amplifier was fixed at 0.7 V. The spectrum of NRZ bit stream is plotted in Fig. C.2(a) and it resembles the previously recorded spectra for NRZ bit-stream. It has a characteristic peak



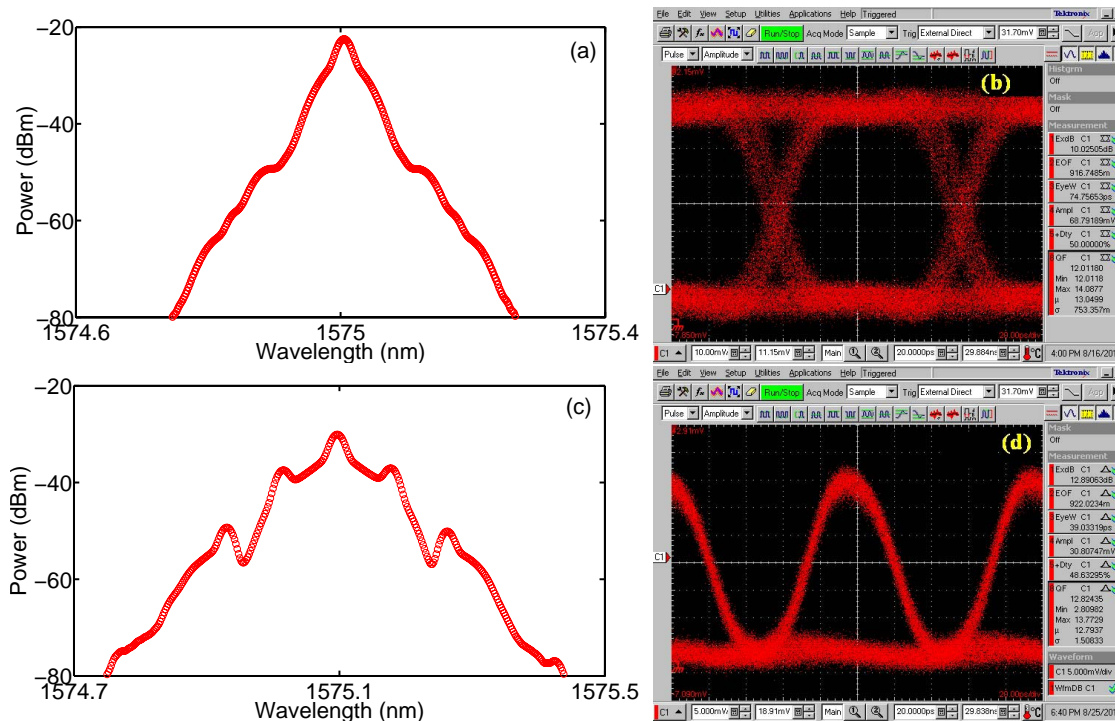


Figure C.2: Experimentally optimized 10 Gb/s NRZ and RZ-50 optical bit streams. (a) Spectrum (b) Eye Diagram for 10 Gb/s NRZ bit stream. (c) Spectrum and (d) Eye Diagram for 10 Gb/s RZ-50 bit stream.

at the center frequency and a broad pedestal due to the NRZ modulation [4]. Figure C.2(b) shows the optical eye detected by a pin PD and visualized using a sampling oscilloscope. The measured Q-factor of the NRZ bit stream exceeded 12 dB.

For generating the RZ-50 bit stream, the JDSU MZM was left as it is, the EOSPACE MZM was biased at 9.41 V, and the peak-to-peak voltage at the input to RF amplifier was fixed at 0.6 V. This RF amplifier seemed to have a higher gain than the RF amplifier used with the data modulator because 0.6 V was enough to drive the amplifier to saturation. The measurement and characterization of RF amplifiers was carried out using a robust low-bandwidth oscilloscope and low frequency (1 GHz) RF signals. The spectrum of 10 Gb/s RZ-50 bit stream is

plotted in Fig. C.2(c) and it resembles the previously recorded spectra for RZ-50 bit-stream [4]. It has a characteristic peak at the center frequency and modulation side bands at 10 and 20 GHz offset. Figure C.2(d) shows the detected optical eye. The measured Q-factor of the RZ-50 bit stream also exceeded 12 dB, however the peak amplitude was about 40% of the peak amplitude of NRZ bit stream. This is consistent with 4 dB IL as specified in the datasheet of EOSPACE MZM.

## Bibliography

- [1] R. S. Tucker, “Green optical communications—Part I: Energy limitations in transport,” *IEEE J. Sel. Top. Quantum Electron.* **17**, 245–260 (2011).
- [2] R. S. Tucker, “Green optical communications—Part II: Energy limitations in networks,” *IEEE J. Sel. Top. Quantum Electron.* **17**, 261–274 (2011).
- [3] J. Baliga, R. Ayre, K. Hinton, W. V. Sorin, and R. S. Tucker, “Energy consumption in optical IP networks,” *J. Lightw. Technol.* **27**, 2391–2403 (2009).
- [4] G. P. Agrawal, *Lightwave Technology: Telecommunication systems*, (Hoboken, Wiley, 2005).
- [5] G. P. Agrawal, *Lightwave Technology: Components and Devices*, (Hoboken, Wiley, 2004).
- [6] J. C. Simon, L. Billes, A. Dupas, B. Kowalski, M. Henry, and B. Landousies, “All-optical regeneration,” in *Proc. Eur. Conf. Optical Communication (ECOC98)*, (Madrid, Spain, 1998), 467–469.
- [7] S. Bigo, O. Leclerc, P. Brindel, G. Vendrome, E. Desurvire, P. Doussiere, and T. Ducellier, “All-optical regenerator for 20 Gbit/s transoceanic transmission,” *Electron. Lett.* **33**, 975–976 (1997).

- [8] C. Ito and J. C. Cartledge, "Polarization independent all-optical 3R regeneration based on the Kerr effect in highly nonlinear fiber and offset spectral slicing," *IEEE J. Sel. Top. Quantum Electron.* **14**, 616–624 (2008).
- [9] A. Bogoni, P. Ghelfi, M. Scaffardi, and L. Poti, "All-optical regeneration and demultiplexing for 160-Gb/s transmission systems using a NOLM-based three-stage scheme," *IEEE J. Sel. Top. Quantum Electron.* **10**, 192–196 (2004).
- [10] S. Radic, C. J. McKinstrie, R. M. Jopson, J. C. Centanni, and A. R. Chraplyvy, "All-optical regeneration in one- and two-pump parametric amplifiers using highly nonlinear optical fiber," *IEEE Photon. Technol. Lett.* **15**, 957–959 (2003).
- [11] C. Finot, S. Pitois, and G. Millot, "Regenerative 40 Gbit/s wavelength converter based on similariton generation," *Opt. Lett.* **30**, 1776–1778 (2005).
- [12] E. Ciaramella, and S. Trillo, "All-optical signal reshaping via four-wave mixing in optical fibers," *IEEE Photon. Technol. Lett.* **12**, 849–851 (2000).
- [13] P. V. Mamyshev, "All-optical data regeneration based on self-phase modulation effect," in *Proc. Eur. Conf. Optical Communication (ECOC98)*, (Madrid, Spain, 1998), 475–476.
- [14] M. Vasilyev, and T. I. Lakoba, "All-optical multichannel 2R regeneration in a fiber-based device," *Opt. Lett.* **30**, 1458–1460 (2005).
- [15] M. Matsumoto, "Efficient all-optical 2R regeneration using self-phase modulation in bidirectional fiber configuration," *Opt. Exp.* **14**, 11018–11023 (2006).

- [16] T. N. Nguyen, M. Gay, L. Bramerie, T. Chartier, J. C. Simon, and M. Joindot, “Noise reduction in 2R-regeneration technique utilizing self-phase modulation and filtering,” *Opt. Exp.* **14**, 1737–1747 (2006).
- [17] T. H. Her, G. Raybon, and C. Headley, “Optimization of pulse regeneration at 40 Gb/s based on spectral filtering of self-phase modulation in fiber,” *IEEE Photon. Technol. Lett.* **16**, 200–202 (2004).
- [18] L. Provost, C. Finot, P. Petropoulos, T. Mukasa, and D. J. Richardson, “Design scaling rules for 2R-optical self-phase modulation-based regenerators,” *Opt. Exp.* **15**, 5100–5113 (2007).
- [19] C. Finot, T.N. Nguyen , J. Fatome, T. Chartier, S. Pitois , L. Bramerie, M. Gay, and J. C. Simon, “Numerical study of an optical regenerator exploiting self-phase modulation and spectral offset filtering at 40 Gbit/s,” *Opt. Commun.* **281**, 2252–2264 (2008).
- [20] A. G. Streigler, and S. Schmauss, “Analysis and Optimization of SPM-Based 2R Signal Regeneration at 40 Gb/s,” *J. Lightw. Technol.* **24**, 2835–2843 (2006).
- [21] G. Raybon, Y. Su, J. Leuthold, R. Essiambre, T.-H. Her, C. Joergensen, P. Steinvurzel, K. Dreyer, and K. Feder, “40 Gb/s pseudo-linear transmission over one million kilometers,” in *Proc. Optical Fiber Communications (OFC’02)* (Anaheim ,CA, 2002), paper FD01.
- [22] M. Rochette, L. Fu, V. Taeed, D. J. Moss, and B. J. Eggleton, “2R optical regeneration: an all-optical solution for BER improvement,” *IEEE J. Sel. Top. Quantum Electron.* **12**, 736–744 (2006).
- [23] J. H. Lee, T. Nagashima, T. Hasegawa, S. Ohara, N. Sugimoto, Y. G. Han, S. B. Lee, and K. Kikuchi, “Output performance investigation of

- self-phase-modulation-based 2R regenerator using bismuth oxide nonlinear fiber,” *IEEE Photon. Technol. Lett.* **18**, 1296–1298 (2006).
- [24] P. Petropoulos, T. M. Monro, W. Belardi, K. Furusawa, J. H. Lee, and D. J. Richardson, “A highly nonlinear holey fiber and its application in a regenerative optical switch,” in *Proc. Optical Fiber Communications (OFC’01)*, (Anaheim CA, 2001), paper TuC3.
- [25] G. Contestabile, L. Banchi, M. Presi, and E. Ciaramella, “Investigation of transparency of FWM in SOAs to advanced modulation formats involving intensity, phase, and polarization multiplexing,” *J. Lightw. Technol.* **27**, 4256–4261 (2009).
- [26] D. N. Maywar, “All-optical processing of optical-network signals using distributed feedback amplifiers”. Ph.D. dissertation, University of Rochester, 2000.
- [27] J. Leuthold, R. Ryf, D. N. Maywar, S. Cabot, J. Jacques, and S. S. Patel, “Nonblocking all-optical cross connect based on regenerative all-optical wavelength converter in a transparent demonstration over 42 nodes and 16800 km,” *J. Lightw. Technol.* **21**, 2863–2870 (2003).
- [28] Y. C. Foo, S. F. Chien, A. L. Y. Low, and C. F. Teo, “New strategy for optimizing wavelength converter placement,” *Opt. Exp.*, **13**, 545–551 (2005).
- [29] K. Roy, and M. K. Naskar, “Genetic evolutionary algorithm for optimal allocation of wavelength converters in WDM optical networks,” *Photon. Netw. Commun.* **16**, 31–42 (2008).
- [30] I. Cristiani, V. Degiorgio, L. Socci, F. Carbone, and M. Romagnoli, “Polarization-insensitive wavelength conversion in a lithium niobate waveguide by the cascading technique,” *IEEE Photon. Technol. Lett.* **14**, 669–671 (2002).

- [31] W. Mathlouthi, H. Rong, and M. Paniccia “Characterization of efficient wavelength conversion by four-wave mixing in sub-micron silicon waveguides,” *Opt. Exp.* **16**, 16735–16745 (2008).
- [32] L. Jia, M. Geng, L. Zhang, L. Yang, P. Chen, Y. Liu, Q. Fang, and M. Yu, “Effects of waveguide length and pump power on the efficiency of wavelength conversion in silicon nanowire waveguides,” *Opt. Lett.* **34**, 3502–3504 (2009).
- [33] A. Pasquazi, R. Ahmad, M. Rochette, M. Lamont, B. E. Little, S. T. Chu, R. Morandotti, and D. J. Moss, “All-optical wavelength conversion in an integrated ring resonator,” *Opt. Exp.* **18**, 3858–3863 (2010).
- [34] G. P. Agrawal, *Applications of Nonlinear Fiber Optics 2nd ed.*, (San Diego, Academic Press, 2008).
- [35] T. Sakamoto, F. Futami, K. Kikuchi, S. Takeda, Y. Sugaya, and S. Watanabe, “All-optical wavelength conversion of 500-fs pulse trains by using a nonlinear-optical loop mirror composed of a highly nonlinear DSF,” *IEEE Photon. Technol. Lett.* **13**, 502–504 (2001).
- [36] T. Tanemura, J. H. Lee, D. Wang, K. Katoh, and K. Kikuchi, “Polarization-insensitive 160-Gb/s wavelength converter with all-optical repolarizing function using circular-birefringence highly nonlinear fiber,” *Opt. Exp.* **14**, 1408–1412 (2006).
- [37] S. Radic, C. J. McKinstire, R. M. Jopson, J. C. Centanni, Q. Lin, and G. P. Agrawal, “Record performance of parametric amplifier constructed with highly nonlinear fiber,” *Electron. Lett.* **39**, 838–839 (2003).
- [38] S. Radic, C. J. McKinstire, R. M. Jopson, J. C. Centanni, and A. R. Chraplyvy, “All-optical regeneration in one- and two-Pump parametric amplifiers using highly nonlinear optical fiber,” *IEEE Photon. Technol. Lett.* **15**, 957–959, (2003).

- [39] M. Hirano, T. Nakanishi, T. Okuno, and M. Onishi, "Silica-based highly nonlinear fibers and their application," *IEEE J. Sel. Topics Quantum Electron.*, **15**, 103–113 (2009).
- [40] P. P. Baveja, D. N. Maywar, G. P. Agrawal, "Interband four-wave mixing in semiconductor optical amplifiers with ASE-enhanced gain recovery," *IEEE J. Sel. Topics Quantum Electron.*, (Accepted for Publication).
- [41] C. M. Gallep, H. J. S. Dorren, and O. Raz, "Four-wave-mixing-based dual-wavelength conversion in a semiconductor optical amplifier," *IEEE Photon. Technol. Lett.*, **22**, 957–959 (2010).
- [42] P. Runge, C-A Bunge, and K. Petermann, "All-optical wavelength conversion with extinction ratio improvement of 100 Gb/s RZ-signals in ultralong bulk semiconductor optical amplifiers," *IEEE J. Quantum Electron.* **46**, 937–944 (2010).
- [43] D. Nielsen, and S. L. Chuang, "Four-wave mixing and wavelength conversion in quantum dots," *Phys. Rev. B* **81**, 035305/1-11 (2010).
- [44] A. Capua, S. ÓDuill, V. Mikhelashvili, G. Einstien, J. P. Reithmaier, A. Somers, A. Forchel, "Cross talk free multi channel processing of 10 Gbit/s data via four wave mixing in a 1550 nm InAs/InP quantum dash amplifier," *Opt. Express* **16**, 19072–19077 (2008).
- [45] H. Simos, I. Stamataki, and D. Syvridis, "Relative intensity noise performance of wavelength converters based on four-wave mixing in semiconductor optical amplifiers," *IEEE J. Quantum Electron.* **43**, 370–377 (2007).
- [46] H. Liu, P. Shum, and M. S. Kao, "Design and analysis of VCSEL based two-dimension wavelength converter," *Opt. Express* **11**, 1659–1668 (2003).



- [47] A. Keating, A. Black, A. Karim, Y.-J. Chiu, Member, Pat. Abraham, C. Harder, E. Hu, and John Bowers, “High-temperature optically pumped 1.55- $\mu\text{m}$  VCSEL operating at 6 Gb/s,” *IEEE Photon. Technol. Lett.* **12**, 116–118 (2000).
- [48] L. Yin, and G. P. Agrawal, “Impact of two-photon absorption on self-phase modulation in silicon waveguides,” *Opt. Lett.* **32**, 2031–2033 (2007).
- [49] E. M. Dianov and A. M. Prokhorov, “Medium-power CW Raman fiber lasers,” *IEEE J. Sel. Topics Quantum Electron.* **6**, 1022–1028 (2000).
- [50] S. P. Smith, F. Zarinetchi, and S. Ezekiel, “Narrow-linewidth stimulated Brillouin fiber laser and applications,” *Opt. Lett.* **16**, 393–395 (1991).
- [51] M. E. Marhic, K. K.-Y. Wong, L. G. Kazovsky, and T.-E. Tsai, “Continuous-wave fiber optical parametric oscillator,” *Opt. Lett.* **27**, 1439–1441 (2002).
- [52] N. Nishizawa and T. Goto, “Widely wavelength-tunable ultrashort pulse generation using polarization maintaining optical fibers,” *IEEE J. Sel. Topics Quantum Electron.* **7**, 518–524 (2001).
- [53] M. D. Pelusi, V. G. Táeed, L. Fu, Eric Mägi, M. R. E. Lamont, S. Madden, D.-Y. Choi, D. A. P. Bulla, B. L.-Davies, and B. J. Eggleton, “Applications of highly-nonlinear chalcogenide glass devices tailored for high-speed all-optical signal processing,” *IEEE J. Sel. Topics Quantum Electron.* **14**, 529–539 (2008).
- [54] K. Igarashi, and K. Kikuchi, “Optical signal processing by phase modulation and subsequent spectral filtering aiming at applications to ultrafast optical communication systems,” *IEEE J. Sel. Topics Quantum Electron.* **14**, 551–565 (2008).

- [55] M. P. Fok, and C. Shu, “Recent advances in optical processing techniques using highly nonlinear bismuth oxide fiber,” *IEEE J. Sel. Topics Quantum Electron.* **14**, 587–598 (2008).
- [56] G. P. Agrawal, *Nonlinear Fiber Optics, 4th ed.*, (San Diego, Academic, 2007).
- [57] T. Okuno, T. Nakanishi, M. Hirano, and M. Onishi, “Practical considerations for the application of highly nonlinear fibers,” *Proc. Optical Fiber Communications (OFC 07)*, (Anaheim CA, 2007), paper OTuJ1.
- [58] J. H. Lee, T. Tanemura, K. Kikuchi, T. Nagashima, T. Hasegawa, S. Ohara, and N. Sugimoto, “Experimental comparison of a Kerr nonlinearity figure of merit including the stimulated Brillouin scattering threshold for state-of-the-art nonlinear optical fibers,” *Opt. Lett.* **30**, 1698–1700 (2005).
- [59] E. Myslivets, C. Lundström, J. M. Aparicio, S. Moro, A. O. J. Wiberg, C.-S. Bres, N. Alic, P. A. Andrekson, and S. Radic, “Spatial equalization of zero-dispersion wavelength profiles in nonlinear fibers,” *IEEE Photon. Technol. Lett.* **21**, 1807–1809 (2009).
- [60] N. Holonyak Jr., “The semiconductor laser: A thirty-five-year perspective,” *Proc. IEEE* **85**, 1678–1693 (1997).
- [61] N. Holonyak, Jr., and S. F. Bevacqua, “Coherent (visible) light emission from  $\text{GaAs}_{(1-x)}\text{P}_x$  junctions,” *Appl. Phys. Lett.* **1**, 82–83 (1962).
- [62] N. Holonyak, R. Kolbas, R. Dupuis, and P. Dapkus, “Quantum-well heterostructure lasers,” **16**, 170–186 (1980).
- [63] M. J. Connelly, *Semiconductor Optical Amplifiers*, (Secaucus, Kluwer, 2002).
- [64] T. Saitoh, and T. Mukai, “1.5  $\mu\text{m}$  GaInAsP traveling-wave semiconductor laser amplifier,” *IEEE J. Quantum Electron.* **23**, 1010–1020 (1987).

- [65] N. A. Olsson, "Lightwave systems with optical amplifiers," *J. Lightw. Technol.* **7**, 1071–1082 (1989).
- [66] E. Desurvire, *Erbium-Doped Fiber Amplifiers: Principles and Applications*, (Wiley, New York, 1994).
- [67] C. Headly and G. P. Agarwal, *Raman Amplification in Fiber Optical Communication Systems*, (Academic, San Deigo, 2005).
- [68] J. Leuthold, B. Mikkelsen, R. E. Behringer, G. Raybon, C. H. Joyner, and P. A. Besse, "Novel 3R regenerator based on semiconductor optical amplifier delayed-interference configuration," *IEEE Photon. Technol. Lett.* **13**, 860–862 (2001).
- [69] T. Fjelde, D. Wolfson, A. Kloch, B. Dagens, A. Coquelin, I. Guillemot, F. Gaborit, F. Poingt and M. Renaud, "Demonstration of 20 Gbit/s all-optical logic XOR in integrated SOA-based interferometric wavelength converter," *Electron. Lett.* **36**, 1863–1864 (2000).
- [70] H. J. S. Dorren, X. Yang, A. K. Mishra, Z. Li, H. Ju, H. de Waardt, G.-D. Khoe, T. Simoyama, H. Ishikawa, H. Kawashima, and T. Hasama, "All-optical logic based on ultrafast gain and index dynamics in a semiconductor optical amplifier" *IEEE J. Sel. Topics Quantum Electron.* **10**, 1075–1093 (2004).
- [71] Z. Li and Guifang Li, "Ultrahigh-speed reconfigurable logic gates based on four-wave mixing in a semiconductor optical amplifier," *IEEE Photon. Technol. Lett.* **18**, 1341–1343 (2006).
- [72] R. J. Manning, A. D. Ellis, A. J. Poustie, and K. J. Blow, "Semiconductor laser amplifiers for ultrafast all-optical signal processing," *J. Opt. Soc. Am. B* **14**, 3204–3216 (1997).

- [73] D. N. Maywar, G. P. Agrawal, and Y. Nakano, “Robust control of an optical-amplifier-based flip-flop,” *Opt. Exp.* **6**, 75–80 (2000).
- [74] N. Ogasawara, and R. Ito, “Static and dynamic properties of nonlinear semiconductor laser amplifiers,” *Jpn. J. Appl. Phys.* **25**, 739–742 (1986).
- [75] D. N. Maywar, G. P. Agrawal, and Y. Nakano, “All-optical hysteresis control by means of cross-phase modulation in semiconductor optical amplifiers,” *J. Opt. Soc. Am. B* **18**, 1003–1013 (2001).
- [76] K. Mishina, A. Maruta, S. Mitani, T. Miyahara, K. Ishida, K. Shimizu, T. Hatta, K. Motoshima, and K. Kitayama, “NRZ-OOK-to-RZ-BPSK modulation-format conversion using SOA-MZI wavelength converter” *J. Lightw. Technol.* **24**, 3751–3758 (2006).
- [77] W. Astar, and G.M. Carter, “10 Gbit/s RZ-OOK to BPSK format conversion by cross-phase modulation in single semiconductor optical amplifier,” *Electron. Lett.* **42**, 1472–1474 (2006).
- [78] J. Leuthold, P. A. Besse, J. Eckner, E. Gamper, Marcus Dülk, and Hans Melchior, “All-optical space switches with gain and principally ideal extinction ratios,” *IEEE J. Quantum Electron.* **34**, 622–633 (1998).
- [79] R. P. Schrieck, M. H. Kwakernaak, Member, H. Jäckel, and H. Melchior, “All-optical switching at multi-100-GB/s data rates with Mach-Zehnder interferometer switches,” *IEEE J. Quantum Electron.* **38**, 1053–1061 (2002).
- [80] K. Suzuki, K. Iwatsuki, S. Nishi, and M. Saruwatari, “Error-free demultiplexing of 160 Gbit/s pulse signal using loop mirror including semiconductor laser amplifier,” *Electron. Lett.* **30**, 1501–1503 (1994).

- [81] J. P. Sokoloff, P. R. Prucnal, I. Glesk, and M. Kane, "A terahertz optical asymmetric demultiplexer (TOAD)," *IEEE Photon. Technol. Lett* **5**, 787–790 (1993).
- [82] C. Schubert, C. Schmidt, S. Ferber, R. Ludwig, and H. G. Weber, "Error-free all-optical add-drop multiplexing at 160 Gbit/s," *Electron. Lett.* **39**, 1074–1075 (2003).
- [83] C. Bintjas, N. Pleros, K. Yiannopoulos, G. Theophilopoulos, M. Kalyvas, H. Avramopoulos, and G. Guekos, "All-optical packet address and payload separation," *IEEE Photon. Technol. Lett.* **14**, 1728–1730 (2002).
- [84] C. de Dios, and H. Lamela, "Compression and reshaping of gain-switching low-quality pulses using a highly nonlinear optical loop mirror," *IEEE Photon. Technol. Lett.* **22**, 377–379 (2010).
- [85] N. A. Olsson, G. P. Agrawal, and K. W. Wecht, "16 Gbit/s, 70 km pulse transmission by simultaneous dispersion and loss compensation with 1.5  $\mu\text{m}$  optical amplifiers," *Electron. Lett* **25**, 603–604 (1989).
- [86] A. M. Kaplan, G. P. Agrawal, and D. N. Maywar, "Optical square-wave clock generation based on an all-optical flip-flop," *IEEE Photon. Technol. Lett.* **22**, 489–491 (2010).
- [87] O. Kamatani and S. Kawanishi, "Ultrahigh-speed clock recovery with lock loop based on four-wave mixing in a traveling-wave laser diode amplifier," *IEEE J. Quantum Electron.* **14**, 1757–1767 (1996).
- [88] A. Borghesani, "Semiconductor optical amplifiers for advanced optical applications," *Proc. 8th Int. Conf. Transparent Opt. Netw. (ICTON 2006)*, (Nottingham, U.K., 2006), pp. 119–122.

- [89] L. Zhang, I. Kang, A. Bhardwaj, N. Sauer, S. Cabot, J. Jaques, and D. T. Nielson, "Reduced recovery time semiconductor optical amplifiers using p-type-doped multiple quantum wells," *IEEE Photon. Technol. Lett.* **18**, 2323–2325 (2006).
- [90] P. P. Baveja, D. N. Maywar, G. P. Agrawal, "Self-phase modulation in semiconductor optical amplifiers: Impact of amplified spontaneous emission," *IEEE J. Quantum Electron.* **46**, 1396–1403 (2010).
- [91] T. Ito, N. Yoshimoto, K. Magari, K. Kishi, and Y. Kondo, "Extremely low power consumption semiconductor optical amplifier gate for WDM applications," *Electron. Lett.* **33**, 1791–1792 (1997).
- [92] C. H. Henry, "Theory of the linewidth of semiconductor lasers," *IEEE J. Quantum Electron.*, **18**, 259–264 (1982).
- [93] G. P. Agrawal, and N. A. Olsson, "Self-phase modulation and spectral broadening of optical pulses in semiconductor laser amplifiers," *IEEE J. Quantum Electron.* **25**, 2297–2306 (1989).
- [94] G. P. Agrawal and N. K. Dutta, *Semiconductor Lasers 2nd ed.*, (Van Nostrand Reinhold, New York, 1993).
- [95] M. J. Adams, D. A. O. Davies, M. C. Tatham, and M. A. Fisher, "Non-linearities in semiconductor laser amplifiers," *Opt. Quantum Electron.* **27**, 1-13 (1995).
- [96] R. G.-Castrejón and A. Filios, "Pattern-effect reduction using a cross-gain modulated holding beam in semiconductor optical in-line amplifier," *J. Lightw. Technol.* **24**, 4912–4917 (2006).
- [97] Y. Ueno, S. Nakamura, and K. Tajima, "Nonlinear phase-shifts induced by semiconductor optical amplifiers with control pulses at repetition frequen-

- cies in the 40-160 GHz range for use in ultrahigh-speed all-optical signal processing,” *J. Opt. Soc. Am. B*, **19**, 2573–2589 (2002).
- [98] J. Leuthold, B. Mikkelsen, G. Raybon, C.H. Joyner, J.L. Pleumeekers, B.I. Miller, K. Dreyer and R. Behringer, “All-optical wavelength conversion between 10 and 100 Gb/s with SOA delayed-interference configuration,” *Opt. Quantum Electron.* **33**, 939–952 (2001).
- [99] Y. Liu, E. Tangdionga, Z. Li, H. de Waardt, A. M. J. Koonen G. D. Khoe, X. Shu, I. Bennion, H. J. S. Dorren, “Error-free 320 Gb/s all-optical wavelength conversion using a single SOA,” *J. Lightw. Technol.* **25**, 103–108 (2007).
- [100] J. Dong, X. Zhang, S. Fu, J. Xu, P. Shum, D. Huang, “Ultrafast all-optical signal processing based on single semiconductor optical amplifier and optical filtering,” *IEEE J. Sel. Topics Quantum Electron.* **14**, 770–778 (2008).
- [101] D. A. Reid, A. M. Clarke, X. Yang, R. Maher, R. P. Webb, R. J. Manning, and L. P. Barry, “Characterization of SOA turbo-switch SOA wavelength converter using spectrographic pulse measurement,” *IEEE J. Sel. Topics Quantum Electron.* **14**, 841–848 (2008).
- [102] R. J. Manning, X. Yang, R. P. Webb, R. Giller, F. C. G. Gunning, and A. D. Ellis, “The turbo-switch: A novel technique to increase the high-speed response of SOAs for wavelength conversion,” in *Proc. Optical Fiber Communications (OFC’06)*, (Anaheim, CA, 2006), paper OWS8.
- [103] M. A. Dupertuis, J. L. Pleumeekers, T. P. Hessler, P. E. Selbmann, B. Deveaud, B. Dagens, and J. Y. Emery, “Extremely fast high-gain and low-current SOA by optical speed-up at transparency,” *IEEE Photon. Technol. Lett.* **12**, 1453–1455 (2000).

- [104] J. Pleumeekers, M. Kauer, K. Dreyer, C. Burrus, A. G. Dentai, S. Shunk, J. Leuthold, and C. H. Joyner, "Acceleration of gain recovery in semiconductor optical amplifiers by optical injection near transparency wavelength," *IEEE Photon. Technol. Lett.* **14**, 12–14 (2002).
- [105] G. Talli and M. J. Adams, "Gain recovery acceleration in semiconductor optical amplifiers employing a holding beam," *Opt. Commun.* **245**, 363–370 (2005).
- [106] F. Girardin, G. Guekos, and A. Houbavlis, "Gain recovery of bulk semiconductor optical amplifiers," *IEEE Photon. Technol. Lett.* **10**, 784–786 (1998).
- [107] F. Ginovart and J.C. Simon, "Gain dynamics studies of a semiconductor optical amplifier," *J. Opt. A-Pure Appl. Opt.* **4**, 283–287 2002.
- [108] R. Giller, R.J. Manning, G. Talli, R. P. Webb, and M. J. Adams, "Analysis of the dimensional dependence of semiconductor optical amplifier recovery speeds," *Opt. Exp.* **15**, 1773–1782 (2007).
- [109] A. M. de Melo, and K. Petermann, "On the amplified emission noise modelling of semiconductor optical amplifiers," *Opt. Commun.* **281**, 4598–4605 (2008).
- [110] R.J. Manning, D.A.O. Davies, D. Cotter, and J.K. Lucek, "Enhanced recovery rates in semiconductor laser amplifiers using optical pumping," *Electron. Lett.* **30**, 787–788 (1994).
- [111] P. M. Gong, J. T. Hsieh, S. L. Lee, and J. Wu, "Theoretical analysis of wavelength conversion based on four-wave mixing in light-holding SOAs," *IEEE J. Quantum Electron.* **40**, 31–40 (2004).



- [112] R. Inohara, K. Nishimura, M. Tsurusawa, and M. Usami, “Experimental analysis of cross-phase modulation and cross-gain modulation in SOA injecting CW assist light,” *IEEE Photon. Technol. Lett.* **15**, 1192–1194 (2003).
- [113] H. Wang, J. Wu, J. Lin, “Spectral characteristics of optical pulse amplification in SOA under assist light injection,” *J. Lightw. Technol.* **23**, 2761–2771 (2005).
- [114] J. M. Tang, and K. A. Shore, “Strong picosecond optical pulse propagation in semiconductor optical amplifiers at transparency,” *IEEE J. Quantum Electron.* **34**, 1263–1269 (1998).
- [115] G. P. Agrawal, “Population pulsations and nondegenerate four-wave mixing in semiconductor lasers and amplifiers,” *J. Opt. Soc. Am. B* **5**, 147–159 (1988).
- [116] R. S. Grant and W. Sibbett, “Observation of ultrafast nonlinear refraction in an InGaAsP optical amplifier,” *Appl. Phys. Lett.* **58**, 1119–1121 (1991).
- [117] P. Westbergh, “High-speed vertical-cavity surface-emitting lasers for short reach communications,” Ph.D. dissertation, Chalmers University of Technology, 2011.
- [118] H. Soda, K. Iga, C. Kitahara and Y. Suematsu, “GaInAsP/InP surface emitting injection lasers,” *Jpn. J. Appl. Phys.* **18**, 2329–2330 (1979).
- [119] K. Iga, F. Koyama, and S. Kinoshita, “Surface emitting semiconductor lasers,” *IEEE J. Quantum Electron.* **24**, 1845–1855, (1998).
- [120] J. K. Guenter, R. A. Hawthorne, D. N. Granville, M. K. Hibbs-Brenner and R.A. Morgan, “Reliability of proton-implanted VCSELs for data communications,” in *Proc. SPIE vol. 2683*, (Bellingham, WA, 1996).

- [121] J. Tatum, “VCSEL proliferation,” in *Proc. SPIE*, vol. 6484, (Bellingham, WA, 2007).
- [122] P. Westbergh, J. Gustavsson, Å. Haglund, M. Skold, A. Joel, and A. Larsson, “High-speed, low-current-density 850 nm VCSELs,” *IEEE J. Sel. Topics Quantum Electron.* **15**, 694–703 (2009).
- [123] J. S. Harris, T. Ó Sullivan, T. Sarmiento, M. M. Lee, and S. Vo, “Emerging applications for vertical cavity surface emitting lasers,” *Semicond. Sci. Technol.* **26**, 014010 (2011).
- [124] B. Ciftcioglu, R. Berman, J. Zhang, Z. Darling, S. Wang, J. Hu, J. Xue, A. Garg, M. Jain, I. Savidis, D. Moore, M. Huang, E. G. Friedman, G. Wicks, and H. Wu, “A 3-D integrated intrachip free-space optical interconnect for many-core chips,” *IEEE Photon. Technol. Lett.* **23**, 164–166 (2011).
- [125] I. A. Young, E. M. Mohammed, J. T. S. Liao, Alexandra M. Kern, Samuel Palermo, Bruce A. Block, Miriam R. Reshotko, and Peter L. D. Chang, “Optical technology for energy efficient I/O in high performance computing,” *IEEE Communications Magazine* **48**, 184–191 (2010).
- [126] S. B. Healy, E. P. óReilly, J. S. Gustavsson, P. Westbergh, Å. Haglund, A. Larsson, and Andrew Joel, “Active region design for high-speed 850 nm VCSELs,” *J. Quantum Electron.* **46**, 506–512 (2010).
- [127] P. Westbergh, J. S. Gustavsson, B. Kögel, Å. Haglund, and A. Larsson, “Impact of photon lifetime on high-speed VCSEL performance,” *IEEE J. Sel. Topics Quantum Electron.* **17**, 1603–1613 (2011).
- [128] L. F. Lester, S. S. Ó Keefe, W. J. Schaff, L. F. Eastman, “Multiquantum well strained-layer lasers with improved low frequency response and very low damping,” *Electron. Lett.* **28**, 383–385 (1992).

- [129] Y. Ou, J. S. Gustavsson, P. Westbergh, Å. Haglund, A. Larsson, and A. Joel, “Impedance characteristics and parasitic speed limitations of high-speed 850 nm VCSELs,” *IEEE Photon. Technol. Lett.* **21**, 1840–1842 (2009).
- [130] A. N. Al-Omari, and K. L. Lear, “Polyimide-planarized, vertical-cavity surface emitting lasers with 17.0-GHz bandwidth,” *IEEE Photon. Technol. Lett.* **16**, 969–971 (2004).
- [131] A. N. Al-Omari, and K. L. Lear, “VCSELs with a self-aligned contact and copper-plated heatsink,” *IEEE Photon. Technol. Lett.* **17**, 1225–1227, (2005).
- [132] E. Kapon, and A. Sirbu, “Long-wavelength VCSELs: Power-efficient answer,” *Nature Photon.* **3**, 27–29 (2009).
- [133] W. Hofmann, “High-speed buried tunnel junction vertical-cavity surface-emitting lasers,” *IEEE Photon. J.* **2**, 802–815, (2010).
- [134] M. Huang, Y. Zhou, and C. Chang-Hasnain, “A surface-emitting laser incorporating a high-index-contrast subwavelength grating,” *Nature Photon.*, **1**, 119–122 (2007).
- [135] M. Müller, W. Hofmann, T. Gründl, M. Horn, P. Wolf, R. D. Nagel, E. Rönneberg, G. Böhm, D. Bimberg, and M.-C. Amann, “1550-nm high-speed short-cavity VCSELs,” *IEEE J. Sel. Topics Quantum Electron.* **17**, 1158–1166 (2011).
- [136] R. Rodes, J. Estaran, B. Li, M. Mueller, J. B. Jensen, T. Gründl, M. Ortseifer, C. Neumeier, J. Roskopf, K. J. Larsen, M.-C. Amann, and I. T. Monroy, “100 Gb/s single VCSEL data transmission link,” in *Proc. National Fiber Optic Engineers Conference (NFOEC) 2012* (Los Angeles, CA, 2012), paper PDP5D.

- [137] Y. Ding, W.J. Fan, D.W. Xu, C.Z. Tong, Y. Liu, L.J. Zha, “Low threshold current density, low resistance oxide-confined VCSEL fabricated by a dielectric-free approach,” *Appl. Phys. B* **98**, 773–778 (2010).
- [138] C. Ji, J. Wang, D. Söderström, and L. Giovane, “20-Gb/s 850 nm oxide VCSEL operating at 25°C-70°C,” *IEEE Photon. Technol. Lett.* **22**, 670–672 (2010).
- [139] Y. Liu, W.-C. Ng, K. D. Choquette, and K. Hess, “Numerical investigation of self-heating effects of oxide-confined vertical-cavity surface-emitting lasers,” *IEEE J. Quantum Electron.* **41**, 15–25 (2005)
- [140] P. V. Mena, J. J. Morikuni, S.-M. Kang, A. V. Harton, and K. W. Wyatt, “A simple rate-equation-based thermal VCSEL model,” *J. Lightw. Technol.* **17**, 865–872 (1999).
- [141] J. W. Scott, R. S. Geels, S. W. Corzine, and L. A. Coldren, “Modeling temperature effects and spatial hole burning to optimize vertical-cavity surface-emitting laser performance,” *IEEE J. Quantum Electron.* **29**, 1295–1308 (1993)
- [142] G. Hasnain, K. Tai, L. Yang, Y. H. Wang, R. J. Fischer, J. D. Wynn, B. Weir, N. K. Dutta, and A. Y. Cho, “Performance of gain-guided surface emitting lasers with semiconductor distributed bragg reflectors,” *IEEE J. Quantum Electron.* **27**, 1377–1385 (1991)
- [143] W. Nakwaski and M. Osinski, “On the thermal resistance of vertical-cavity surface-emitting lasers,” *Opt. and Quantum. Electron.* **29**, 883–892 (1997).
- [144] P. Debernardi, A. Kroner, F. Rinaldi, and R. Michalzik, “Surface relief versus standard VCSELs: A comparison between experimental and hot-cavity model results,” *IEEE J. Sel. Topics Quantum Electron.* **15**, 828–837 (2009).

- [145] <http://www.nuphoton.com/edfa-ase.html>
- [146] <http://www.ciphotonics.com/products/soa/soa-nl-c-14-fca/>
- [147] A.M. Kaplan, G.P. Agrawal and D.N. Maywar, “All-optical flip-flop operation of VCISOA,” *Electron. Lett.* **45**, 127–128 (2009).
- [148] E.S. Björilin, T. Kimura, Q. Chen, C. Wang and J.E. Bowers, “High output power 1540 nm vertical cavity semiconductor optical amplifiers,” *Electron. Lett.* **40**, 121–123 (2004).
- [149] G. D. Cole, E. S. Björilin, C. S. Wang, N. C. MacDonald, and J. E. Bowers, “Widely tunable bottom-emitting vertical-cavity SOAs,” *IEEE Photon. Technol. Lett.* **17**, 2526–2528 (2005).
- [150] O. V. Sinkin, R. Holzlohner, J. Zweck, and C. R. Menyuk, “Optimization of the split-step Fourier method in modeling optical-fiber communications systems,” *J. Lightw. Technol.* **21**, 61–68 (2003).
- [151] S. Bischoff, M. L. Nielsen, and J. Mørk, “Improving the all-optical response of SOAs using a modulated holding signal,” *J. Lightw. Technol.* **22**, 1303–1308 (2004).
- [152] P. Morel and A. Sharaiha, “Wideband time-domain transfer matrix model equivalent circuit for short pulse propagation in semiconductor optical amplifiers,” *IEEE J. Quantum Electron.* **45**, 103–114 (2009).
- [153] G. Giuliani and D. D. Alessandro, “Noise analysis of conventional and gain-clamped semiconductor optical amplifiers,” *J. Lightw. Technol.* **18**, 1256–1263 (2000).
- [154] M. P. Dlubek, S. N. Kaunga-Nyirenda, A. J. Phillips, S. Sujecki, I Harrison, and E. C. Larkins, “Experimental verification of the existence of optically induced carrier pulsations in SOAs,” *Opt. Commun.* **283**, 1481–1484 (2010).

- [155] G. P. Agrawal, "Highly nondegenerate four-wave mixing in semiconductor lasers due to spectral hole burning," *Appl. Phys. Lett.* **51**, 302–304 (1987).
- [156] J. Zhou, N. Park, K. J. Vahala, M. A. Newkirk, and B. I. Miller, "Four-wave mixing wavelength conversion efficiency in semiconductor travelling-wave amplifier measured to 65 nm of wavelength shift," *IEEE Photon. Technol. Lett.* **6**, 984–987 (1994).
- [157] A. Mecozzi, S. Scotti, A. d'Ottavi, E. Iannone, and P. Spano, "Four-wave mixing in travelling-wave semiconductor amplifiers," *IEEE J. Quantum Electron.* **31**, 689–699 (1995).
- [158] A. d'Ottavi, E. Iannone, A. Mecozzi, S. Scotti, P. Spano, R. Dall'Ara, J. Eckner, and G. Guekos, "Efficiency and noise performance of wavelength converters based on FWM in semiconductor optical amplifiers," *IEEE Photon. Technol. Lett.* **7**, 357–359 (1995).
- [159] M. A. Summerfield, and R. S. Tucker, "Noise figure and conversion efficiency of four-wave mixing in semiconductor optical amplifiers," *Electron. Lett.* **31**, 1159–1160 (1995).
- [160] M. A. Summerfield, and R. S. Tucker, "Optimization of pump and signal powers for wavelength converters based on FWM in semiconductor optical amplifiers," *IEEE Photon. Technol. Lett.* **8**, 1316–1318 (1996).
- [161] K. Obermann, I. Koltchanov, K. Petermann, S. Diez, R. Luwig, and H. G. Weber, "Noise analysis of frequency converters utilizing semiconductor-laser amplifier," *IEEE J. Quantum Electron.* **33**, 81–88 (1997).
- [162] D. F. Geraghty, R. B. Lee, M. Verdiell, M. Ziari, and K. J. Vahala, "Wavelength conversion for WDM communication systems using four-wave mixing in semiconductor optical amplifiers," *IEEE J. Sel. Topics Quantum Electron.* **3**, 1146–1155 (1997).

- [163] S. Diez, C. Schmidt, R. Ludwig, H. G. Weber, K. Obermann, S. Kindt, I. Koltchanov, and K. Petermann, “Four-wave mixing in semiconductor optical amplifiers for frequency conversion and fast optical switching,” *IEEE J. Sel. Topics Quantum Electron.* **3**, 1131–1145 (1997).
- [164] L. Lu, Y. Dong, H. Wang, W. Cai, and S. Xie, “Bit-error-rate performance dependence on pump and signal powers of wavelength converter based on FWM in semiconductor optical amplifiers,” *IEEE Photon. Technol. Lett.* **12**, 855–857 (2000).
- [165] Z. Li, Y. Dong, J. Mo, Y. Wang, and C. Lu, “Cascaded all-optical wavelength conversion for RZ-DPSK signal based on four-wave mixing in semiconductor optical amplifier,” *IEEE Photon. Technol. Lett.* **16**, 1685–1687 (2004).
- [166] S-L. Lee, P-M. Gong, and C-T Yang, “Performance enhancement on SOA-based four-wave mixing wavelength conversion using an assisted beam,” *IEEE Photon. Technol. Lett.* **14**, 1713–1715 (2002).
- [167] D-Z. Hsu, S-L. Lee, P-M. Gong, Y-M. Lin, S. S. W. Lee, and M. C. Yuang, “High-efficiency wide-band SOA-based wavelength converters by using dual-pumped four-wave mixing and an assist beam,” *IEEE Photon. Technol. Lett.* **16**, 1903–1905 (2004).
- [168] J-T. Hsieh, P-M. Gong, S-L. Lee, and J. Wu, “Improved dynamic characteristic on four-wave mixing wavelength wavelength conversion in light-holding SOAs,” *IEEE J. Sel. Topics Quantum Electron.* **10**, 1187–1196 (2004).
- [169] Y. Hong, P. S. Spencer, and K. A. Shore, “Wide-band polarization-free wavelength conversion based on four-wave mixing in semiconductor optical amplifier,” *IEEE J. Quantum Electron.* **40**, 152–156 (2004).

- [170] C. Politi, D. Klionidis, and M. J. O'Mahony, "Waveband converters based on four-wave mixing in SOAs," *J. Lightw. Technol.* **24**, 1203–1217 (2006).
- [171] F. Girardin, J. Eckner, G. Guekos, R. Dall'Ara, A. Mecozzi, A. D'Ottavi, F. Martelli, S. Scotti, and P. Spano, "Low-Noise and Very High-Efficiency Four-Wave Mixing in 1.5-mm-Long Semiconductor Optical Amplifiers", *IEEE Photon. Technol. Lett.* **9**, 746–748 (1997).
- [172] S. Jarabo, and A. Tomás, "Experimental study on wave-mixing in semiconductor optical amplifiers," *Opt. Commun.* **281** 3872–3877 (2008).
- [173] S. Fu, W. Du, P. Shum, C. Wu, D. Hak, and L. Zhang, "Measurement of SOA linewidth enhancement factor with a Sagnac fiber loop," *IEEE Photon. Technol. Lett.* **18**, 1934–1936 (2006).
- [174] J. Wang, A. Maitra, C. G. Poulton, W. Freude, and J. Leuthold, "Temporal dynamics of alpha factor in semiconductor optical amplifiers," *J. Lightw. Technol.* **25**, 891–900 (2007).
- [175] X. Li, M. J. Adams, D. Alexandropoulos, and I. F. Lealman, "Gain recovery in semiconductor optical amplifiers," *Opt. Commun.* **281**, 3466–3470 (2008).
- [176] K. Y. Lau, "Gain switching of semiconductor injection laser," *Appl. Phys. Lett.* **52**, 257–259 (1988).
- [177] P. J. Winzer, C. Dorrer, R.-J. Essiambre, and I. Kang, "Chirped return-to-zero modulation by imbalanced pulse carver driving signals," *IEEE Photon. Technol. Lett.* **16**, 1379–1381 (2004).
- [178] <http://www.bayspec.com/pdf/ITU-DWDM.pdf>
- [179] [http://www.dmoptics.com/pdf/applications%20pdf/APPLICATION\\_NOTE\\_ON\\_SNR\\_DM\\_Optics.pdf](http://www.dmoptics.com/pdf/applications%20pdf/APPLICATION_NOTE_ON_SNR_DM_Optics.pdf)



- [180] <http://www.fiberdyne.com/products/100-dwdm-filter.html>
- [181] C. Wilmsen, H. Temkin, and L. Coldren, *Vertical-Cavity Surface-Emitting Lasers: Design, Fabrication, Characterization, and Applications*, (Cambridge Univ. Press, Cambridge, U.K., 1999).
- [182] C. J. Chang-Hasnain, C. E. Zah, G. Hasnain, J. P. Harbison, L. T. Florez, N. G. Stoffel, and T. P. Lee, “Effect of operating electric power on the dynamic behavior of quantum well vertical-cavity surface-emitting lasers,” *Appl. Phys. Lett.* **58**, 1247–1249 (1991).
- [183] W. H. Knox, D. S. Chemla, G. Livescu, J. E. Cunningham, and J. E. Henry, “Femtosecond carrier thermalization in dense fermi seas,” *Phys. Rev. Lett.* **61**, 1290–1293 (1988).
- [184] L. A. Coldren and S. W. Corzine, *Diode Lasers and Photonic Intergrated Circuits*, (Wiley, New York, 1995).
- [185] Y.-A. Chang, J.-R. Chen, H.-C. Kuo, Y.-K. Kuo, and S.-C. Wang, “Theoretical and experimental analysis on InAlGaAs/AlGaAs active region of 850 nm vertical-cavity surface-emitting lasers,” *J. Lightw. Technol.* **24**, 536–543 (2006).
- [186] I. Vurgaftman, J. R. Meyer, and L.-R. Ram-Mohan, “Band parameters for III-V compound semiconductors and their alloys,” *Appl. Phys. Rev.* **89**, 5815–5875 (2001).
- [187] Y. P. Varshni, “Temperature dependence of the energy gap in semiconductors,” *Physica* **34**, 149–154 (1967).
- [188] D. V. Kuksenkov, H. Temkin, and S. Swirhun, “Measurement of internal quantum efficiency and losses in vertical cavity surface emitting lasers,” *Appl. Phys. Lett.* **66**, 1720–1722 (1995).

- [189] G. R. Hadley, “Effective index model for vertical-cavity surface-emitting lasers,” *Opt. Lett.* **20**, 1483–1485 (1995)
- [190] A. Larsson, P. Westbergh, J. Gustavsson, Å. Haglund, and Benjamin Kögel, “High-speed VCSELs for short reach communication,” *Semicond. Sci. Technol.* **26**, 014017 (5pp) (2011).
- [191] R. Dangel, C. Berger, R. Beyeler, L. Dellmann, M. Gmur, R. Hamelin, F. Horst, T. Lamprecht, T. Morf, S. Oggioni, M. Spreafico, and B.J. Offrein, “Polymer-waveguide-based board-level optical interconnect technology for datacom applications,” *IEEE Trans. Adv. Packag.* **31**, 759–767 (2008).
- [192] P. Westbergh, J.S. Gustavsson, B. Kögel, Å. Haglund, A. Larsson, A. Mutig, A. Nadtochiy, D. Bimberg and A. Joel, “40 Gbit/s error-free operation of oxide-confined 850 nm VCSEL,” *Electron. Lett.* **46**, 1014–1016 (2010).
- [193] W. H. Hofmann, P. Moser, P. Wolf, A. Mutig, M. Kroh, and D. Bimberg, “44 Gb/s VCSEL for optical interconnects,” in *Proc. Optical Fiber Communications (OFC’2011)*, (Los Angeles, CA, 2011), paper PDPC5.
- [194] W. H. Hofmann, P. Moser, P. Wolf, G. Larisch, W. Unrau, and D. Bimberg, “980-nm VCSELs for optical interconnects at bandwidths beyond 40 Gb/s,” in *Proc. SPIE, vol. 8276*, (Bellingham, WA, 2012).
- [195] T. Suzuki, S. Imai, S. Kamiya, K. Hiraiwa, M. Funabashi, Y. Kawakita, H. Shimizu, T. Ishikawa, and A. Kasukawa, “Reliability study of 1060nm 25Gbps VCSEL in terms of high speed modulation,” in *Proc. SPIE, vol. 8276*, (Bellingham, WA, 2012).
- [196] W. W. Chow, M. H. Crawford, and R. P. Schneider, Jr. “Minimization of threshold current in short wavelength AlGaInP vertical-cavity surface-emitting lasers,” *IEEE J. Sel. Topics Quantum Electron.* **1**, 649–653 (1995).

- [197] Y.-H. Chang, H.-C. Kuo, F.-I. Lai, Y.-A. Chang, C.-Y. Lu, L.-H. Lai, and S.-C. Wang “Fabrication and characteristics of high-speed oxide-confined VCSELs using InGaAsP-InGaP strain-compensated MQWs,” *J. Lightw. Technol.* **22**, 2828–2833 (2004).
- [198] J. Shah, “Hot Carriers in Quasi-2-D Polar Semiconductors,” *IEEE J. Quantum Electron.* **22**, 1728–1743 (1986).
- [199] P. P. Baveja, B. Kögel, P. Westbergh, J. S. Gustavsson, Å. Haglund, D. N. Maywar, G. P. Agrawal, and A. Larsson, “Assessment of VCSEL thermal rollover mechanisms from measurements and empirical modeling,” *Opt. Exp.* **19**, 15490–15505 (2011).
- [200] Å. Haglund, J. S. Gustavsson, J. Vukušić, P. Modh, and A. Larsson, “Single fundamental-mode output power exceeding 6 mW from VCSELs with a shallow surface relief,” *IEEE Photon. Technol. Lett.* **16**, 368–370 (2004).
- [201] H. Martinsson, J. Vukušić, M. Grabherr, R. Michalzik, R. Jäger, K. J. Ebeling, and A. Larsson, “Transverse mode selection in large-area oxide-confined vertical-cavity surface-emitting lasers using a shallow surface relief,” *IEEE Photon. Technol. Lett.* **11**, 1536–1538 (1999).
- [202] N. Suzuki, T. Anan, H. Hatakeyama, and M. Tsuji, “Low resistance tunnel junctions with type-II heterostructures,” *Appl. Phys. Lett.* **88**, 231103 (1-3) (2006).
- [203] P. Iannone, K. Reichmann, C. Brinton, J. Nakagawa, T. Cusick, M. Kimber, C. Doerr, L. L. Buhl, M. Cappuzzo, E. Y. Chen, L. Gomez, J. Johnson, A. M. Kanan, J. Lentz, F. Chang, B. Pálsdóttir, T. Tokle, and L. Spiekman, “Bi-directionally amplified extended reach 40 Gb/s CWDM-TDM PON with burst-mode upstream transmission,” in *Proc. Optical Fiber Communications (OFC’2011)*, (Los Angeles, CA, 2011), paper PDPD6.

- [204] C. Finot, J. Fatome, S. Pitois, G. Millot and E. Pincemin, “Active many-shuv regenerator,” *Opt. Rev.* **18**, 257–263 (2011).
- [205] *OptiSystem 6.0: Getting Started and Tutorials*, (Optiwave Systems Inc., 2007)
- [206] [http://www.lnt.ei.tum.de/mitarbeiter/inan/lehre/OCSLab/documents/optiwave/Optiwave\\_intro.pdf](http://www.lnt.ei.tum.de/mitarbeiter/inan/lehre/OCSLab/documents/optiwave/Optiwave_intro.pdf)
- [207] M. Sayin and M. S. Özyazici, “Effect of gain switching frequency on ultrashort pulse generation from laser diodes,” *Opt. Quantum Electron.* **29**, 627-638 (1997).
- [208] A. Clarke, “Optical pulse processing towards Tb/s high-speed photonic systems,” Ph.D. dissertation, Dublin City University, 2007.
- [209] L. P. Barry, P. Anandarajah, and A. Kaszubowska, “Optical pulse generation at frequencies up to 20 GHz using external-injection seeding of a gain-switched commercial FabryPérot laser,” *IEEE Photon. Technol. Lett* **13**, 1014–1016 (2001).
- [210] P. VasićV, *Ultrafast Diode Lasers; Fundamentals and Applications*, (Artech House, Boston, 1995).
- [211] [http://www.ilxlightwave.com/pdfs/4980\\_brochure.pdf](http://www.ilxlightwave.com/pdfs/4980_brochure.pdf)
- [212] <http://www.oquest.com/getDatasheet/id/5166-324f45960728e4a.pdf>
- [213] <http://www.centellax.com/products/testmeas/10gbert.shtml>
- [214] I. Kang, L. Mollenauer, B. Greene, and A. Grant, “A Novel method for synchronizing the pulse carver and electroabsorption data modulator for ultralong-haul DWDM transmission,” *IEEE Photon. Technol. Lett.* **14**, 1357–1359 (2002).

- [215] J. H. Sinsky, “High-speed data and pulse-carver alignment in dual mach-zehnder modulator optical transmitters using microwave signal processing,” *J. Lightw. Technol.* **21**, 412–423 (2003).
- [216] J. J. Veselka and S. K. Korotky, “Pulse generation for soliton systems using lithium niobate modulators,” *IEEE J. Sel. Topics Quantum Electron.* **2**, 300–310 (1996).